

PHYSICS-BASED DEEP LEARNING METHODS FOR MAGNETIC
RESONANCE DATA SAMPLING, IMAGE RECONSTRUCTION AND
QUANTITATIVE SUSCEPTIBILITY MAPPING

A Dissertation

Presented to the Faculty of the Graduate School
of Cornell University

In Partial Fulfillment of the Requirements for the Degree of
Doctor of Philosophy

by

Jinwei Zhang

August 2023

© 2023 JINWEI ZHANG

ALL RIGHTS RESERVED

**IMPROVED MAGNETIC RESONANCE DATA SAMPLING, IMAGE
RECONSTRUCTION, AND DIPOLE INVERSION USING PHYSICS-
BASED DEEP LEARNING**

JINWEI ZHANG PH.D.

Cornell University 2023

Improved magnetic resonance (MR) data sampling, under-sampled image reconstruction, and dipole inversion can be achieved using physics-based deep learning methods. These methods leverage the physical models of MR imaging processes to improve the quality and accuracy of MR images.

One approach to improving MR data sampling involves optimizing the k-space under-sampling pattern from fully sampled k-space dataset. A pioneering work is called LOUPE [1] which updates the probabilistic density function used to generate binary k-space sampling patterns, and uses a sigmoid approximation to sample from the learned density function.

In addition, physics-based deep learning methods can be used for under-sampled image reconstruction by incorporating the imaging physical models into the deep learning architectures. Pioneering works, such as VarNet [2] and MoDL [3], have incorporated physical models by unrolling iterative reconstruction algorithms with deep learning-based regularizers.

Moreover, physics-based deep learning has also improved the ill-posed problem of

dipole inversion used to extract tissue susceptibility from magnetic field data. QSMnet [4] and DeepQSM [5] are two pioneering works that have tackled this problem by incorporating physical models either into the training loss function or through simulating the training dataset.

This thesis contributes to physics-based deep learning for MRI by: 1) improving LOUPE using a straight-through (ST) estimator and extending the improved LOUPE to multi-echo and multi-contrast scenarios; 2) developing pulse sequence for prospective multi-echo gradient echo under-sampling and customized efficient multi-contrast sampling; 3) designing image reconstruction network architectures aggregating multi-echo and multi-contrast image features; 4) utilizing physical models into the loss function for test time fine-tuning to improve generalization; 5) solving Bayesian posterior estimation of dipole inversion problem using Variational Inference (VI) incorporating physical models.

BIOGRAPHICAL SKETCH

Jinwei Zhang was born in Shanxi, China in Dec 1994. He received the Bachelor of Science degree in Optical Science from Sun Yat-sen University in 2016, and the Dual Bachelor of Science degree in Computational Mathematics in 2017. He joined the graduate program in Biomedical Engineering at Cornell University in Fall 2017 and received the Master of Science degree in Biomedical Engineering in 2020.

This Thesis is Dedicated to My Family,

for Their Support and Encouragement

During My Difficult Times While Pursuing the Thesis.

ACKNOWLEDGEMENTS

First, I'd like to thank my thesis advisor Dr. Yi Wang. Dr. Wang has immense knowledge of MR physics and critical insight on its clinical applications. He always told me to think deep and conduct research based on principles. He shapes the direction of my thesis and always makes sure I'm on the right track.

Second, I will thank Drs. Pascal Spincemaille, Thanh Nguyen, Alexey Dimov and Kelly Gillen. Dr. Spincemaille helped me a lot on different aspects of my PhD study, including providing timely feedback of my research progress, editing my drafts and response letters, and even debugging my code. He is quite a resourceful advisor. Dr. Nguyen is very experienced on MR pulse sequence. His patient and detailed mentoring helped me learn pulse sequence programming efficiently. I cannot finish my pulse sequence programming project without Dr. Nguyen's mentoring. Dr. Dimov's expertise on MR physics helps me gain better understanding of my research. Dr. Gillen always cares about PhD students' mental health and is always supportive whenever I have difficulty.

Third, I will thank my committee members Drs. Mert Sabuncu and Amy Kuceyeski. I have frequent meetings with Dr. Sabuncu during my PhD study. His knowledge on machine learning benefited my research projects a lot. Some of the core ideas in my projects came from his mind and turned into publications. Dr. Kuceyeski invited me to give a talk on the MLiM symposium she organized, which helped me improve my

presentation skills. Besides, when I was a junior PhD student, she suggested me communicate and collaborate effectively with other lab mates. I took the advice and became a good research collaborator during my PhD study.

I also thank all the radiologists I collaborated with, Drs. Shun Zhang, Ilhami Kovanlikaya, Martin Prince, Gary Brittenham and Sujit Sheth. I received input from them from a clinical view which strengthened my research.

I also thank all my lab mates. Zhe and Hang is experienced with deep learning. I learned plenty of deep learning concepts and coding skills from them. Qihao, as both my room and lab mates, helped me pick up pulse sequence programming. Also, his persistence and concentration on academic research always inspires me. Jiahao and Chao work on pulse sequence programming and image reconstruction as well. We always share research ideas and scan together. I also have very joyful time with other lab mates, Carly, Daniel, Dom, Hangwei, Ali, Mert, Renjiu and Ben.

Finally, I will thank my family. My parents and grandparents always encourage me to pursue what I'm passionate about. My little sister always inspires me during our conversation. My dog Jojo is my emotional support. Most importantly, my wife, who is not only my partner but also an inspirer in my research. It's my pleasure to have her on the journey of my life.

TABLE OF CONTENTS

IMPROVED MAGNETIC RESONANCE DATA SAMPLING, IMAGE RECONSTRUCTION, AND DIPOLE INVERSION USING PHYSICS-BASED DEEP LEARNING	iii
BIOGRAPHICAL SKETCH	iii
ACKNOWLEDGEMENTS	v
TABLE OF CONTENTS	vii
LIST OF FIGURES	xiii
LIST OF TABLES	xxvii
LIST OF ABBREVIATION	xxix
LIST OF SYMBOLS	xxxii
CHAPTER 1. INTRODUCTION	1
1.1 MRI Signal Model Basics	1
1.2 Summary of Contribution.....	3
CHAPTER 2. LOUPE-ST: EXTENDING LOUPE FOR K-SPACE UNDER- SAMPLING PATTERN OPTIMIZATIN IN MULTI-COIL MRI.....	7
2.1 Abstract	7
2.2 Introduction.....	7
2.3 Method	9
2.3.1 Unrolled Reconstruction Network.....	11
2.3.2 ST Estimator for Binary Pattern.....	12

2.3.3	Network Architecture.....	14
2.4	Results	15
2.4.1	Dataset and Implementations.....	15
2.4.2	Comparison with LOUPE.....	17
2.4.3	Comparison with Other Pattern.....	18
2.5	Discussion and Conclusion	22

CHAPTER 3. LARO: LEARNED ACQUISITION AND RECONSTRUCTION

OPTIMIZATION TO ACCELERATE QUANTITATIVE SUSCEPTIBILITY

MAPPING 23

3.1	Abstract	23
3.2	Introduction.....	24
3.3	Theory	26
3.3.1	Sampling pattern optimization (SPO).....	29
3.3.2	Temporal feature fusion (TFF) for reconstruction	31
3.3.3	K-space under-sampling sequence design.....	33
3.4	Method	34
3.4.1	Fully sampled acquired k-space data.....	34
3.4.2	Fully sampled synthetic k-space data	35
3.4.3	Under-sampled k-space data in both retrospective and prospective studies....	36
3.4.4	Network architecture.....	37
3.4.5	Training strategy	38
3.4.6	Ablation study.....	39
3.4.7	Performance comparison.....	39
3.4.8	Generalization experiments	41
3.5	Results	44
3.5.1	Sampling patterns	45
3.5.2	Acquired k-space data.....	46
3.5.3	Synthetic k-space data.....	52

3.5.4	Prospective study.....	54
3.5.5	Generalization study.....	55
3.6	Discussion and Conclusion	55
CHAPTER 4. mcLARO: MULTI-CONTRAST LEARNED ACQUISITION		
AND RECONSTRUCTION OPTIMIZATION FOR SIMULTANEOUS		
QUANTITATIVE MULTI-PARAMETRIC MAPPING.....		
		61
4.1	Abstract	61
4.2	Introduction.....	62
4.3	Method	64
4.3.1	Pulse sequence design.....	64
4.3.2	K-space sampling.....	65
4.3.3	Optimized multi-contrast reconstruction.....	65
4.3.4	Optimized multi-contrast sampling pattern.....	67
4.3.5	Data acquisition and processing.....	68
4.3.6	Comparison and statistical analysis.....	69
4.4	Results	73
4.4.1	Retrospectively under-sampled ablation study	73
4.4.2	Prospectively under-sampled reconstruction.....	76
4.5	Discussion and Conclusion	78
CHAPTER 5. FINE: FIDELITY IMPOSED NETWORK EDIT FOR SOLVING		
ILL-POSED IMAGE RECONSTRUCTION		
		82
5.1	Abstract	82
5.2	Introduction.....	83
5.3	Theory	84
5.4	Method	87
5.4.1	QSM.....	88
5.4.2	Under-sampled reconstruction.....	92

5.5	Results	96
5.5.1	QSM.....	96
5.5.2	Under-sampled reconstruction	103
5.6	Discussion and Conclusion	111
CHAPTER 6. HOBIT: HYBRID OPTIMIZATION BETWEEN ITERATIVE		
AND NETWORK FINE-TUNING RECONSTRUCTIONS FOR FAST		
QUANTITATIVE SUSCEPTIBILITY MAPPING		
6.1	Abstract	118
6.2	Introduction.....	119
6.3	Method	121
6.3.1	Issues in FINE.....	121
6.3.2	HOBIT	122
6.4	Results	125
6.4.1	Data acquisition and preprocessing	125
6.4.2	Implementation details and ablation study	128
6.4.3	Simulated ICH.....	130
6.4.4	In vivo ICH.....	131
6.5	Discussion and Conclusion	131
CHAPTER 7. PHYSICS-BASED NETWORK FINE-TUNING FOR ROBUST		
QUANTITATIVE SUSCEPTIBILITY MAPPING FROM HIGH-PASS FILTERED		
PHASE		
	133	
7.1	Abstract	133
7.2	Introduction.....	134
7.3	Method	136
7.3.1	Data acquisition and preprocessing	136
7.3.2	Experiments.....	140

7.4	Results	145
7.5	Discussion and Conclusion	150
CHAPTER 8. PDI: PROBABILISTIC DIPOLE INVERSION FOR ADAPTIVE		
QUANTITATIVE SUSCEPTIBILITY MAPPING		
8.1	Abstract	155
8.2	Introduction.....	156
8.3	Related Work.....	158
8.4	Method	162
8.4.1	Posterior Density Estimation	162
8.4.2	VI Domain Adaptation.....	164
8.4.3	Relation to VAE.....	166
8.4.4	Network Architecture.....	167
8.5	Results	168
8.5.1	Data Acquisition and Preprocessing.....	168
8.5.2	Implementation Details	170
8.5.3	COSMOS Dataset.....	171
8.5.4	Patient Datasets	173
8.5.5	Amortized vs Subject-specific VI.....	174
8.5.6	Uncertainty Map Evaluation.....	176
8.6	Discussion and Conclusion	179
CHAPTER 9. FUTURE DIRECTIONS AND CONCLUSION.....		
9.1	Future Directions	184
9.1.1	LARO for CMRO ₂ mapping.....	184
9.1.2	mcLARO for Susceptibility Source Separation	184
9.1.3	SPARKLING sampling + LARO.....	185
9.1.4	Probabilistic diffusion models + LARO.....	185
9.2	Conclusion.....	185

REFERENCE.....186

LIST OF FIGURES

Figure 2.1. Proposed network architecture consisting of a sampling pattern learning network and a K-rolled reconstruction network.14

Figure 2.2. Reconstruction results on one test slice by four combinations of reconstruction network and sampling pattern optimization network with 10% under-sampling ratio. First row: reconstruction results; second row: 5× absolute error maps (window level: [0, 0.5]). MoDL + BS equipped with ST estimator had the best performance.18

Figure 2.3. Reconstruction results on another test slice using VD and learned sampling patterns with three different reconstruction methods. First two rows: reconstruction results; last two rows: corresponding 5× absolute error maps (window level:[0, 0.5]). For each reconstruction method, the learned sampling pattern produced lower global errors and sharper structural details than VD sampling pattern.20

Figure 3.1. Network architecture of LARO. (a): deep ADMM was used as the backbone for under-sampled k-space reconstruction. (b): a sampling pattern optimization (SPO) module was used to learn the optimal k-space under-sampling pattern. (c): a temporal feature fusion (TFF) module was inserted into deep ADMM to capture the signal evolution along echoes. ...28

Figure 3.2. Illustration of (a): the proposed segmented k-space ordering strategy

of ten echoes and (b): pulse sequence design. In (a), segmented centric k-space ordering is indexed by greyscale level. In a certain TR, sampled ky-kz locations (yellow dots) in current k-space segment (yellow hollow triangles) are exemplified. In (b), additional Gy and Gz gradients (blue solid triangles) are added between two unipolar readouts in Gx to adjust next sampled location in ky-kz plane.30

Figure 3.3. SPO=2 sampling pattern of the first echo (Echo1) and difference maps between two adjacent echoes ($\Delta_{Echo\#}$) in (a): acquired k-space data (acceleration factor $R = 8$) and (b): synthetic k-space data (acceleration factor $R = 4$). Different k-space sampling pattern was generated from the learned probabilistic pattern per echo, introducing additional incoherency along temporal dimension.32

Figure 3.4. Ablation study on acquired k-space dataset with acceleration factor $R = 8$. Reconstruction errors were progressively reduced in magnitude, $R2^*$ and QSM as more modules were added. White matter tracts (insets) were blurry in all reconstructed $R2^*$ and QSMs except LARO (TFF=1, SPO=2). Abbreviation: TFF=0 or 1, with or without temporal feature fusion module; SPO=0, 1 or 2, “without”, “with single-echo”, or “with multi-echo” sampling pattern optimization.44

Figure 3.5. Performance comparison of acquired k-space test dataset under-

sampled by the optimized sampling pattern with acceleration factor $R = 8$ (Figure 3a). LLR (2nd column) had heavy block-like artifacts in RDFs and QSMs with larger errors compared to MoDL (3rd column) and LARO (4th column). Insets in QSMs and R2* showed pronounced noise in MoDL, which were not seen in LARO.45

Figure 3.6. Performance comparison of MS lesion dataset under-sampled by the optimized sampling pattern with acceleration factor $R = 4$ (Figure 3b). MoDL (3rd column) and LARO (4th column) dramatically outperformed LLR (2nd column) in terms of reconstruction accuracy, while LARO was slightly better than MoDL.46

Figure 3.7. TFF reconstructions on prospectively under-sampled raw k-space data of one healthy subject with acceleration factor $R = 8$. Compared to SENSE reconstruction with $R = 2$ as reference, depictions of white matter tracts in R2* maps (insets in R2* maps) were progressively improved from SPO=0, 1 to LARO (SPO=2). Sharpness scores of perivascular spaces inside putamen (insets in QSMs) were 0.0270, 0.0111, 0.0247 and 0.0411 for SENSE, SPO=0, 1 and 2. Abbreviation: TFF= 1, with temporal feature fusion module; SPO=0, 1 or 2, without, with single-echo or with multi-echo sampling pattern optimization.48

Figure 3.8. Performance comparison on the prospectively under-sampled raw k-

space data of one healthy subject with $SPO=2$ and acceleration factor $R = 8$ (Figure 3.3a). SENSE reconstructions with $R = 2$ were used as references. LLR had heavy block-like artifacts in RDFs and QSMs. White matter tracts in $R2^*$ maps (insets in $R2^*$ maps) and vein structures in QSMs (insets in QSMs) were blurrier in MoDL than LARO.49

Figure 3.9. Generalization experiments of LARO with different imaging parameters retrospectively under-sampled by $SPO=2$ sampling pattern. Fully sampled reference of each test dataset was used to compute error maps and quantitative metrics. Magnitude images were not considered for quantitative comparison due to signal intensity variations among scans. LARO performed well without visible artifacts on test datasets with another flip angle (25° , 2nd column), number of echoes (7 echoes, 1st column) and a second MRI scanner from the same manufacturer (GE, 3rd column), but had moderate noise (red arrows in the last column) on another voxel size ($0.75 \times 0.75 \times 1.5 \text{ mm}^3$, last column) and moderate residual aliasing artifacts on a third MRI scanner from another manufacturer (Siemens, 4th column). Reconstructions on these datasets retrospectively under-sampled by $SPO=1$ and 0 were shown in Figures S6 and S7. For each test dataset, reconstruction performance was consistently improved from sampling pattern $SPO=0, 1$ to 2.52

Figure 4.1. a) Schematics of the proposed mcLARO pulse sequence for multi-parametric mapping, which consists of inversion recovery (IR) and T2prep magnetization preparations and single and multi-echo GRE readouts; b) Bloch simulation of the steady state signal of the white matter ($T1/T2 = 855/67$ ms, blue), gray matter ($1264/89$ ms, orange), and CSF ($T1/T2 = 4000/2000$ ms, yellow).70

Figure 4.2. a) Deep unrolled ADMM network of mcLARO multi-contrast reconstruction; b) multi-contrast sampling pattern optimization module to learn an optimized pattern from fully sampled data; c) multi-contrast feature fusion module to aggregate information across contrasts during reconstruction.71

Figure 4.3. Ablation study of the multi-contrast sampling pattern optimization and multi-contrast feature fusion modules in mcLARO with $R = 8$ retrospective under-sampling from the fully sampled data of one representative test subject. For T1 maps (1st row), the noise visible in the fully sampled reconstruction (1st column) was reduced in all under-sampled reconstructions (2nd to 5th columns). Deep grey matter regions in the zoomed in images were blurry without the two modules (mcLARO=00), but were progressively improved when the sampling pattern optimization (mcLARO=01), feature fusion (mcLARO=10) and combined (mcLARO=11)

modules were applied. For T2 and T2 maps, noise in the fully sampled reconstruction was reduced in all under-sampled reconstructions. No visual differences were observed among under-sampled reconstructions of T2, T2* and QSM.73*

Figure 4.4. Bland–Altman plots of regional T1, T2, T2 and QSM ROI values between fully sampled and retrospectively under-sampled reconstructions on the four test subjects. For all the under-sampled reconstructions, negligible bias and narrow 95% limits of agreement were obtained (FS = Fully Sampled, M = mcLARO).75*

Figure 4.5. a) mcLARO and reference multi-parametric maps. Similar multi-parametric maps were derived from mcLARO compared to the reference. b) Bland–Altman plots of regional T1, T2, T2 and QSM values obtained with the proposed mcLARO and reference methods from four test subjects. Small or negligible bias and narrow 95% limits of agreement were achieved by mcLARO.....77*

Figure 5.1. Comparison of QSMs (first row) and the corresponding difference maps (second row) of 2016 QSM challenge data reconstructed by MEDI, U-Net, DLL2 and FINE with COSMOS as ground truth. All methods showed similar performance. b) Comparison of QSMs (first row) and the corresponding difference maps (second row) of one simulated brain with

ICH. Hemorrhage was underestimated in U-Net, but were recovered progressively from DLL2 to FINE. MEDI and FINE had minimal reconstruction errors among all four methods. All images were displayed using a [-0.3, 0.3] ppm window except in insets in the third row, which used [-0.6, 1.5] ppm.97

Figure 5.2. Median relative change of the weights per layer in U-Net structure between weights of U-Net reconstruction (initialization) and FINE reconstruction in Figure 1b. FINE changed predominantly the weights in high-level layers of U-Net (layers 1 through 5 and layers 17 through 21). 98

Figure 5.3. a) representative axial images from two MS patients, showing that FINE improves lesion appearance in reference to MEDI. From left to right: QSMs reconstruction by MEDI, U-Net, DLL2 and FINE, respectively. Lesions (solid arrows) near the ventricle were underestimated in U-Net, but were recovered progressively from DLL2 to FINE. The fine structure of periventricular veins was shown more clearly on FINE and DLL2, as compared to MEDI or U-Net (hollow arrows). Despite the merits, some shadow artifacts near the CSF were introduced in FINE. b) Deming regressions of all patients' lesion mean values between MEDI and the DL based three methods, showing FINE improves the lesion susceptibility accuracy in reference to MEDI. All images were displayed using a [-0.15,

0.15] ppm window..... 100

Figure 5.4. QSM shown in three orthogonal planes in a representative ICH patient. From left to right: QSMs reconstructed by MEDI, U-Net, DLL2 and FINE, respectively. Hemorrhage was underestimated in U-Net, but were recovered progressively from DLL2 to FINE. All images were displayed using a [-0.15, 0.15] ppm window except in insets, which used [-0.6, 1.5] ppm..... 101

Figure 5.5. Reconstruction results of one image with glioma. From left to right: fully sampled ground truth, under-sampled k-space reconstruction by TV, U-Net, DLL2, MoDL and FINE, respectively. a) reconstructed image. b) magnitude of reconstruction error with respect to truth. c) zoomed in regions. TV suffered from modest structural error. U-Net suffered from substantial structural error (failure in the large uniform region of the glioma). DLL2 substantially reduced structural error in U-Net but still suffered modest error. MoDL also suffered modest structural error (arrow). FINE provided the most accurate reconstruction. 102

Figure 5.6. a) PSNR metrics of two types of pre-training dataset with different number of images before and after FINE. b) SSIM metrics of two types of pre-training dataset with different number of images before and after FINE. Given the same size of pre-trained dataset, FINE trained on MR image

dataset had better performance than trained on natural image dataset.

FINE with 2200 MR images for pre-training had nearly identical performance to the one with 8800 MR images for pre-training shown in table 2.....103

Figure 5.7. Reconstructions of one representative image with MS lesions at two noise levels (a: $\sigma = 0.01$, b: $\sigma = 0.05$). All the reconstructions became noisier as test data noise levels increase. Compared to MoDL, FINE reconstructions looked less noisy and had better depicted lesions.105

Figure 5.8. Reconstructions of a representative T2w image without adversarial noise (a) and with adversarial noise (b-c). Artifacts in U-Net output increased as adversarial noise levels increased from (b) to (c). These artifacts were suppressed in both TV regularized and FINE reconstructions (arrows), which appeared more similar to their corresponding ground truth images (first column).109

Figure 6.1. Network architecture in HOBIT. f_{θ} was the dipole inversion network 3D U-Net and g_{ψ} was a slimmer network with five convolutional layers. f_{θ} has a single input b while g_{ψ} has b and f_{θ} 's output χ_0 concatenating together as its input to produce the final output χ_1 . Only g_{ψ} is adapted for each test case after training.125

Figure 6.2. (a): Reconstruction results of two test cases in ablation study ($[-0.15,$

0.15] ppm). DLL2 and HOBIT ($\alpha = 1.0, \rho = 60$) suffered from shadow artifacts surrounding the hemorrhages (red arrows). (b): Fidelity costs of HOBIT with $\alpha = 0.5$ (monotonically decreasing) and $\alpha = 1.0$ (divergent) per ADMM outer loop. 126

Figure 6.3. Reconstruction results of two simulated test cases ($[-0.15, 0.15]$ ppm). MEDI visually looked smooth. Under-estimation inside the hemorrhages in QSMnet was reduced in QSMnet+. QSMnet and QSMnet+ had shadow artifact issue surrounding the hemorrhages (red arrows). FINE, PDI-VI and HOBIT produced qualitatively better QSMs than the other methods. 127

Figure 7.1. Proposed progressive 3D Unet architecture and its fine-tuning using high-pass filtering dipole convolution forward model. QSM prediction is progressively refined after each Unet during forward pass. Fine-tuning backpropagation is deployed only in the last Unet to save computational cost. 141

Figure 7.2. Retrospective HPFP test case with cutoff frequency $FCs = 1/4, 3/8, 1/2, 5/8$ and $3/4$ in Hann filters. $FC = 1/2$ was used in the training dataset as well as fine-tuning loss function Eq. 2. At $FC = 1/2$, visible over-estimation of GP in Unet reconstruction was reduced in Unet-FT, Prognnet and Prognnet-FT reconstructions (red arrows). At $FC = 3/8$, moderate

image blurring and GP over-estimation in Unet and Prognnet reconstructions were mitigated by Unet-FT and Prognnet-FT (red arrows). At $FC = 1/4$, excessive image blurring was observed in Unet, Unet-FT, Prognnet and Prognnet-FT reconstructions. At $FC = 5/8$ and $3/4$, GP over-estimation in Unet was reduced in Unet-FT (red arrows). Slight under-estimation of GP was observed in Prognnet and Prognnet-FT (red arrows).

..... 144

Figure 7.3. Retrospective HPFP test case with isotropic in-plane voxel sizes = 0.577, 0.75, 0.938 and 1.25 mm. Voxel size = 0.75 mm was used for training. At voxel size = 0.75 mm, visible over-estimation of GP in Unet reconstruction was reduced in Unet-FT, Prognnet and Prognnet-FT reconstructions (red arrows). Besides GP over-estimation, increased image blurring were observed in Unet and Prognnet as the test case voxel size increased (0.938 and 1.25 mm), but were reduced in Unet-FT and Prognnet-FT. Prognnet reconstruction was less blurry than Unet. At voxel size = 0.577 mm, slight blurriness was observed in Unet and Prognnet but was reduced in Unet-FT and Prognnet-FT.

..... 147

Figure 7.4. Boxplot of quantitative metrics of two retrospective HPFP test datasets. a): cutoff frequencies $FCs = 1/4, 3/8, 1/2, 5/8$ and $3/4$ in test data Hann filters. b): isotropic in-plane voxel sizes = 0.577, 0.750, 0.938 and

1.25 mm. In a), at $FC = 3/8, 1/2, 5/8$ and $3/4$, the reconstruction accuracy of Unet and Prognnet was improved in Unet-FT and Prognnet-FT. Prognnet slightly outperformed Unet both before and after fine-tuning. At $FC = 1/4$, all methods suffered from performance degradation and fine-tuning resulted in worse accuracy. In b), at all voxel sizes, the reconstruction accuracy of Unet and Prognnet was improved in Unet-FT and Prognnet-FT. Prognnet slightly outperformed Unet both before and after fine-tuning. 149

Figure 7.5. a) predicted QSMs of two prospective HPFP test cases and b) ROIs analysis averaged over 9 test cases. In a), compared to the reference QSMs, blurriness for both cases in Unet and Prognnet was reduced after fine-tuning in Unet-FT and Prognnet-FT. In b), all four methods had slight under-estimation in CN. Unet and Unet-FT had additional under-estimation in GP. 152

Figure 8.1. The network architecture of the proposed method. Two upsampling paths' outputs represent mean and variance maps of susceptibility. The COSMOS dataset was used to perform posterior density estimation in Eq. 8.8. Domain adaptation VI with MC sampling in Eq. 8.10 were applied on other datasets. 170

Figure 8.2. Reconstructions (first row, $[-0.15, 0.15]$ ppm) and absolute error maps (second row, $[0, 0.05]$ ppm) of one COSMOS test subject in one

orientation, with COSMOS as the gold standard. FINE achieved the lowest reconstruction error, while the other methods had comparable results. SD maps of PDI, PDI-VI0 and PDI-VI (third row, $[0, 0.05]$ ppm) showed high uncertainties at the sagittal sinus and globus pallidus, which was consistent with their error maps.170

Figure 8.3. Two MS patient reconstructions (first six columns, $[-0.15, 0.15]$ ppm) and SD maps (last three columns, $[0, 0.05]$ ppm). Lesions indicated by the red arrows near the ventricle had lower susceptibility values in QSMnet and PDI, but were recovered in FINE and PDI-VI. Compared to PDI-VI, lesions reconstructed by PDI-VI0 also had lower susceptibility.172

Figure 8.4. Two ICH patient Reconstructions (first six columns, $[-0.15, 0.15]$ ppm) with the insets ($[-0.6, 1.5]$ ppm) and SD maps (last three columns, $[0, 0.05]$ ppm). Hemorrhage susceptibility was lower on QSMnet and PDI as compared to MEDI. This issue was reduced in FINE and PDI-VI. PDI-VI0 gave comparable hemorrhage reconstructions to PDI-VI. High variance inside the hemorrhage was consistent with high measured noise in the same region.173

Figure 8.5. (a) Reconstructions ($[-0.15, 0.15]$ ppm) with the insets ($[-0.6, 1.5]$ ppm) and SD maps ($[0, 0.05]$ ppm) and (b) KL divergence values of two ICH test patients using amortized and subject-specific VIs. MEDI and FINE

with TV were used for comparison. Although an almost zero amortization gap (Eq. 8.11) was achieved by amortized VI (b) for both cases, reconstruction quality at the hemorrhage center and surrounding hemorrhage was still marginally better for subject-specific VI. FINE with TV and subject-specific VI achieve comparably image quality.174

Figure 8.6. Value changes of three individual terms in Eq. 8.10 of subject-specific VI during iterations, with the value of amortized VI as a reference. The second term of TV regularization was slightly lower in subject-specific VI after convergence, while the other two terms were similar between amortized and subject-specific VIs.175

Figure 8.7. PDI and PDI-VI's average absolute error maps (first two columns, [0, 0.05] ppm) through simulations and predicted SD maps (last two columns, [0, 0.05] ppm) of (a) healthy and (b) hemorrhagic brains. The SD maps resembled the error maps in both cases for PDI and PDI-VI.177

LIST OF TABLES

<i>Table 2.1. Quantitative results of section 2.4.2</i>	21
<i>Table 2.2. Quantitative results of section 2.4.3</i>	22
<i>Table 5.1. RMSE, SSIM and HFEN for various QSM reconstructions averaged among cross-validation experiments in healthy subjects, with COSMOS as the ground truth reference (* denotes statistical significance for the comparison between MEDI/U-Net/DLL2 and FINE; $p < 0.05$).</i>	106
<i>Table 5.2. RMSE, SSIM and HFEN for various QSM reconstructions of 6 simulated ICH brains (* denotes statistical significance for the comparison between MEDI/U-Net/DLL2 and FINE; $p < 0.05$).</i>	107
<i>Table 5.3. PSNR and SSIM for real-valued T2w MS patient test dataset reconstruction. (* denotes statistical significance for the comparison between TV/U-Net/DLL2/MoDL and FINE; $p < 0.05$).</i>	108
<i>Table 5.4. PSNR and SSIM for real-valued T2w Glioma patient test dataset reconstruction. (* denotes statistical significance for the comparison between TV/U-Net/DLL2/MoDL and FINE; $p < 0.05$).</i>	110
<i>Table 5.5. PSNR and SSIM for complex-valued T2w test dataset reconstruction. (* denotes statistical significance for the comparison between TV/U-Net/DLL2/MoDL and FINE; $p < 0.05$).</i>	111
<i>Table 5.6. PSNR and SSIM of MoDL and FINE reconstructions on MS test</i>	

<i>dataset with noise $\sigma = 0.01$ and 0.05. (* denotes statistical significance for the comparison between MoDL and FINE; $p < 0.05$).</i>	112
<i>Table 6.1. Average quantitative metrics of 10 test simulated brains reconstructed by different methods in ablation study. Overall, HOBIT ($\alpha = 0.5, \rho = 30$) performed the best.</i>	129
<i>Table 8.1. Average quantitative metrics of 10 test COSMOS brains reconstructed by different methods. FINE gave the best reconstruction at the expense of significantly increased computational time. The other methods had comparable results.</i>	178

LIST OF ABBREVIATION

ADMM	Alternating Direction Method of Multipliers
CG	Conjugate Gradient
LOUPE	Learning-based Optimization of the Under-sampling Pattern
CS	Compressed Sensing
IR	Inversion Recovery
PI	Parallel Imaging
ST	Straight Through
CNN	Convolutional Neural Network
VD	Variable Density
TGV	Total Generalized Variation
MoDL	Model Based Deep Learning
LLR	Locally Low Rank
LARO	Learned Acquisition and Reconstruction Optimization
TFF	Temporal Feature Fusion

SPO	Sampling Pattern Optimization
PDF	Probabilistic Density Function
mcLARO	multi-contrast Learned Acquisition and Reconstruction Optimization
QSM	Quantitative Susceptibility Mapping
MEDI	Morphology Enabled Dipole Inversion
COSMOS	Calculation Of Susceptibility through Multiple Orientation Sampling
mGRE	multi-echo Gradient Echo
FINE	Fidelity Imposed Network Edit
DLL2	Deep Learning based L2 Regularization
HOBIT	Hybrid Optimization Between Iterative and network fine-Tuning
SWI	Susceptibility Weighted Imaging
HPFP	high-pass filtered phase
PDI	Probabilistic Dipole Inversion
VAE	Variational Auto-Encoder
GAN	Generative Adversarial Network

VI Variational Inference

KL Kullback–Leibler divergence

LIST OF SYMBOLS

b	K-space data or measured local field
$d (D)$	Dipole kernel
x	MR complex image
χ	Susceptibility map
s_j	Multi-echo complex GRE images
P	Probabilistic density function of sampling pattern
W	Noise weighting
F	Fourier transform
U	Binary k-space sampling pattern
S	Coil sensitivity map
n	Measurement noise
N	Network with multiple layers
w	Network weights
h	Hidden state features

$p(q)$ Probabilistic distribution

μ Mean

Σ Standard deviation

CHAPTER 1. INTRODUCTION

1.1 MRI Signal Model Basics

An MRI system consists of several components, including magnet, radiofrequency (RF) and gradient coils and computer system. In MRI, images are produced using a pulse sequence that includes a specific order, timing, and duration of RF and gradient pulses, which are used to manipulate the magnetization of the hydrogen nuclei (also known as protons) in the body's water and fat molecules. Once placed inside a magnetic field, the magnetic moment of spins by the protons emits a signal that can be detected by the MRI system.

The MRI signal model is based on two relaxation times, spin-lattice relaxation time (T1) and spin-spin relaxation time (T2). The Bloch equation governs the magnetic moment of spins (\mathbf{m}) inside the magnetic field (\mathbf{B}):

$$\frac{d\mathbf{m}}{dt} = \gamma (\mathbf{m} \times \mathbf{B}) - \frac{1}{T_1(m_z - m_0)}\hat{z} - \frac{1}{T_2(m_x\hat{x} + m_y\hat{y})} \quad [1.1]$$

where the magnetization \mathbf{m} precesses clockwise around the magnetic field \mathbf{B} with an angular velocity $\boldsymbol{\omega} = \mathbf{m} \times \mathbf{B}$, which is known as the Larmor frequency. The

Larmor frequency is proportional to the strength of the magnetic field \mathbf{B} and the gyromagnetic ratio γ , which is a fundamental property of the nuclei being imaged.

For example, the gyromagnetic ratio of hydrogen nuclei (protons) is approximately

42.58 MHz/T. The solutions to the Bloch equation that correspond to T2 for transverse magnetization (m_{\perp}) and T1 for the longitudinal component (m_z) are given by:

$$m_{\perp}(t) = m_{\perp}(0) e^{-\frac{t}{T_2}} \quad [1.2]$$

$$m_z(t) = m_0 - (m_0 - m_z(0)) e^{-\frac{t}{T_1}} \quad [1.3]$$

“Observed” or “effective” T2, denoted as T2*, takes into account both spin-spin relaxation (T2) and magnetic field inhomogeneities (T2’) caused by factors such as susceptibility effects from tissue interfaces, air-tissue interfaces, and magnetic field gradients:

$$\frac{1}{T_2^*} = \frac{1}{T_2'} + \frac{1}{T_2}. \quad [1.4]$$

Considering T2* decay, Gradient-echo (GRE) signal at time t after gradient ($G(t)$) dephasing and refocus is:

$$s(t) = \int m(\mathbf{r}) e^{-\frac{t}{T_2^*(\mathbf{r})}} e^{-2\pi i \mathbf{k} \cdot \mathbf{r}} d^3\mathbf{r} \quad [1.5]$$

where $\mathbf{k} = \frac{\gamma G(t)t}{2\pi}$ and \mathbf{r} is the location vector. Considering tissue magnetization as a collection of magnetic dipole moments, a unit dipole z-field affecting the spin precession rate is defined as:

$$d(\mathbf{r}) = \frac{1}{4\pi} \frac{3 \cos^2 \theta - 1}{r^3}. \quad [1.6]$$

where θ is the angle between \mathbf{r} and the main magnetic field \mathbf{B} . Then the magnetic field (scaled to \mathbf{B}_0) is the sum of contributions from all dipole moments:

$$\frac{\mathbf{b}(\mathbf{r})}{4\pi} = \mu_0 \int \frac{(3 \cos^2 \theta_{\mathbf{r}\mathbf{r}'} - 1)\mathbf{m}(\mathbf{r}')}{|\mathbf{r} - \mathbf{r}'|^3} d^3\mathbf{r}'. \quad [1.7]$$

After Lorentz sphere correction, we get the following quantitative susceptibility mapping inverse problem [6] given measured field:

$$\mathbf{b}(\mathbf{r}) = (\chi * d)(\mathbf{r}). \quad [1.8]$$

Field contribution to phase can be added to GRE signal equation:

$$s(t) = \int m(\mathbf{r}) e^{-i\omega b(\mathbf{r})t} e^{-\frac{t}{T_2^*(\mathbf{r})}} e^{-2\pi i \mathbf{k} \cdot \mathbf{r}} d^3\mathbf{r} \quad [1.9]$$

1.2 Summary of Contribution

This thesis is focused on improving MR data sampling, under-sampled image reconstruction and quantitatively susceptibility mapping (QSM) using physics-based deep learning methods.

1. LOUPE with Straight-Through (ST) Estimator (LOUPE-ST). In Chapter 2, we extended the LOUPE technique [7] for optimizing k-space under-sampling patterns. A binary stochastic sampling method together with an ST estimator to estimate the gradient of the threshold operation in a neural network was applied [7]. This approach led to better reconstruction performance compared to the

approximate sampling method used in LOUPE during training. Furthermore, the optimized sampling pattern could be applied to other reconstruction methods with similar success.

2. Learned Acquisition and Reconstruction Optimization (LARO). In Chapter 3, we introduced a new framework call LARO [8, 9], which is designed to accelerate multi-echo gradient echo (mGRE) sequence for quantitative susceptibility mapping. LARO achieves this by optimizing a Cartesian multi-echo k-space sampling pattern extended from LOUPE-ST in Chapter 2. This optimized sampling pattern is then implemented in an mGRE sequence for prospective scans. LARO also incorporates a recurrent temporal feature fusion module, which captures signal redundancies along echoes. Experiments show LARO is robust on the test data with new pathologies and different sequence parameters.

3. Multi-contrast Learned Acquisition and Reconstruction Optimization (mcLARO). In Chapter 4, we developed a new pulse sequence that contained an interleaved inversion recovery (IR) prepared single-echo acquisition, a multi-echo gradient echo acquisition and a T2 prepared single-echo acquisition. This allowed to acquire k-space data sensitive to T1, T2, T2* and magnetic susceptibility. A deep learning framework called mcLARO, extended from LARO in Chapter 3, was proposed to optimize both the multi-contrast k-space under-sampling pattern and the image reconstruction based on image feature fusion [10]. The prospective

study showed good agreement on regional T1, T2, T2* and QSM values by mcLARO (5:39 mins) compared to reference scans (40:03 mins in total).

4. Fidelity Imposed Network Edit (FINE). In Chapter 5, we introduced a new method called FINE [11], which aims to improve deep learning image reconstruction by incorporating the physical model into the network for test time adaptation. By doing so, FINE reduces generalization errors in deep learning image reconstruction, leading to better results in tasks such as multiple sclerosis (MS) lesion and hemorrhage susceptibility in deep learning QSM. FINE is also robust to noise and adversarial attack in deep learning under-sampled MRI reconstruction.

5. Hybrid Optimization Between Iterative and network fine-Tuning (HOBIT).

In Chapter 6, we accelerated FINE from Chapter 5 by alternating direction method of multiplier (ADMM), which splits the time-consuming fidelity imposed network update into iterative reconstruction and network update subproblems alternatively in ADMM [12]. For the network update subproblem, only a subnet of the pre-trained network is updated for further acceleration. Compared to FINE, HOBIT achieves both performance gain of reconstruction accuracy and vast reduction of computational time.

6. Application of FINE to solve QSM from high-pass filtered phase (HPFP). In

Chapter 7, we applied FINE from Chapter 5 to tackle two common generalization issues that arise when using a pre-trained network to predict QSM from HPFP: a) data with unseen voxel sizes and b) data with unknown high-pass filters which may be different from training. A network fine-tuning step based on a high-pass filtering dipole convolution forward model is proposed to reduce generalization error of the pre-trained network [13]. A progressive Unet architecture is proposed to improve prediction accuracy without increasing fine-tuning computational cost. The proposed method shows improved robustness compared to the pre-trained network without fine-tuning when test dataset deviates from the training.

7. Probabilistic Dipole Inversion (PDI). In Chapter 8, A learning-based posterior distribution estimation method, PDI, is proposed to solve QSM with uncertainty estimation [14, 15]. In PDI, a deep convolutional neural network (CNN) is used to represent the multivariate Gaussian distribution as the approximate posterior distribution of susceptibility given the input measured field. Such CNN is first trained on healthy subjects via posterior density estimation, then domain adapted to patient data in an unsupervised fashion using variational inference (VI). Based on our experiments, PDI provides additional uncertainty estimation compared to the conventional maximum-a-posteriori (MAP) approach, while addressing the potential issue of the pre-trained CNN when test data deviates from training.

CHAPTER 2. LOUPE-ST: EXTENDING LOUPE FOR K-SPACE UNDER-SAMPLING PATTERN OPTIMIZATION IN MULTI-COIL MRI

2.1 Abstract

In this chapter, we present LOUPE-ST [7], an extension of LOUPE [1] for k-space under-sampling pattern optimization in MRI. A binary stochastic sampling method together with an ST estimator to estimate the gradient of the threshold operation in a neural network was applied. This approach led to better reconstruction performance compared to the approximate sampling method used in LOUPE during training. Furthermore, the optimized sampling pattern could be applied to other reconstruction methods with similar success.

2.2 Introduction

Parallel imaging (PI) [16, 17] and Compressed Sensing MRI (CS-MRI) [18] are widely used techniques for acquiring and reconstructing under-sampled k-space data thereby shortening scanning times in MRI. CS-MRI is a computational technique that suppresses incoherent noise-like artifacts introduced by random under-sampling, often via a regularized regression strategy. Combining CS-MRI with PI promises to make MRI much more accessible and affordable. Therefore, this has been an intense area of research in the past decade [19, 20]. One major task in PI CS-MRI is designing a random under-sampling pattern, conventionally controlled by a variable-density

probabilistic density function (PDF). However, the design of the ‘optimal’ under-sampling pattern remains an open problem for which heuristic solutions have been proposed. For example, [21] generated the sampling pattern based on the power spectrum of an existing reference dataset; [22] combined experimental design with the constrained Cramer-Rao bound to generate the context-specific sampling pattern; [23] designed a parameter-free greedy pattern selection method to find a sampling pattern that performed well on average for the MRI data in a training set.

Recently, with the success of learning based k-space reconstruction methods [2, 3, 11, 24], a data-driven machine learning based approach called LOUPE [1] was proposed as a principled and practical solution for optimizing the under-sampling pattern in CS-MRI. In LOUPE, fully sampled k-space data was simulated from magnitude MR images and retrospective under-sampling was deployed on the simulated k-space data. A sampling pattern optimization network and a modified U-Net [25] as the under-sampled image reconstruction network were trained together in LOUPE to optimize both the k-space under-sampling pattern and reconstruction process. In the sampling pattern optimization network, one sigmoid operation was used to map the learnable weights into probability values, and a second sigmoid operation was used to approximate the non-differentiable step function for stochastic sampling, as the gradient needed to be back-propagated through such layer to update the learnable weights. After training, both optimal sampling pattern and reconstruction network

were obtained. For a detailed description of LOUPE we refer the reader to [1].

In this work, we extended LOUPE in three ways. Firstly, in-house multi-coil in-vivo fully sampled T2-weighted k-space data from MR scanner was used to learn the optimal sampling pattern and reconstruction network. Secondly, modified U-Net [25] as the reconstruction network in LOUPE was extended to a modified unrolled reconstruction network with learned regularization term in order to reconstruct multi-coil data in PI with proper data consistency and reduce the dependency on training data when training cases were scarce. Thirdly, approximate stochastic sampling layer was replaced by a binary stochastic sampling layer with Straight-Through (ST) estimator [26], which was used to avoid zero gradients when back-propagating to this layer. Fully sampled data was acquired in healthy subjects. Under-sampled data was generated by retrospective under-sampling using various sampling patterns. Reconstructions were performed using different methods and compared.

2.3 Method

In PI CS-MRI, given an under-sampling pattern and the corresponding acquired k-space data, a reconstructed image \hat{x} is obtained via minimizing the following objective function:

$$\hat{x} = \operatorname{argmin}_x \sum_j^{N_c} \|UFS_j x - b_j\|_2^2 + R(x) \quad [2.1]$$

where x the MR image to reconstruct, S_j the coil sensitivity map of j -th coil, N_c the number of receiver coils, F the Fourier transform, U the k-space under-sampling pattern, and b_j the acquired under-sampled k-space data of the j -th coil. $R(x)$ is a regularization term, such as Total Variation (TV) [27] or wavelet [28]. The minimization in Eq. 2.1 is performed using iterative solvers, such as the Quasi-Newton method [29], the alternating direction method of multipliers (ADMM) [30] or the primal-dual method [31]. Eq. 2.1 can also be mimicked by learning a parameterized mapping such as neural network from input $\{b_j\}$ to output \hat{x} . We denote the mapping $\{b_j\} \rightarrow \hat{x}$ using either iterative solvers or deep neural networks as $\hat{x} = \mathcal{A}(\{b_j\})$.

Our goal is to obtain an optimal under-sampling pattern \hat{U} for a fixed under-sampling ratio γ from N fully sampled data through retrospective under-sampling. The mathematical formulation of this problem is:

$$\min_U \frac{1}{N} \sum_{i=1}^N L(x_i^*, \hat{x}_i(U)), \text{ subject to } U \in \Omega, \hat{x}_i(U) = \mathcal{A}(\{U b_{ij}^*\}) \quad [2.2]$$

where x_i^* the i -th MR image reconstructed by direct inverse Fourier transform from fully sampled k-space data $\{b_{ij}^*\}$, $L(\cdot, \cdot)$ the loss function to measure the similarity between reconstructed image $\hat{x}_i(U)$ and fully sampled label x_i^* , Ω the constraint set of U to define how U is generated with a fixed under-sampling ratio γ . The bilevel optimization problem [32] of Eq. 2.2 was solved in LOUPE [1] via jointly optimizing

a modified U-Net [25] as $\mathcal{A}(\cdot)$ and an approximate stochastic sampling process as Ω on a large volume of simulated k-space data from magnitude MR images. However, for in-vivo k-space data with multi-coil acquisition as in PI, both U-Net architecture for reconstruction and approximate stochastic sampling for pattern generation could be sub-optimal. Specifically, due to limited training size of in-vivo data and no k-space consistency imposed in U-Net, inferior reconstructions could happen in test and even training datasets. And the approximate stochastic sampling process generated fractional rather than 0–1 binary patterns during training, which might not work well during test as binary patterns should be used for realistic k-space sampling. In view of the above, we extend and improve LOUPE in terms of both reconstruction mapping $\mathcal{A}(\cdot)$ and sampling pattern’s generating process Ω when working on in-vivo multi-coil k-space data in this work.

2.3.1 Unrolled Reconstruction Network

A modified residual U-Net [25] was used as the reconstruction network in LOUPE [1] to map from the zero-filled k-space reconstruction input to the fully-sampled k-space reconstruction output. U-Net works fine with simulated k-space reconstruction when enough training data of magnitude MR images are given, but as for in-vivo multi-coil k-space data, training cases are usually scarce, since fully-sampled scans are time consuming and as a result, only a few fully-sampled cases can be acquired.

To reduce the dependency on training dataset and improve the data consistency of deep learning reconstructed images, combining neural network block for the regularization term in Eq. 2.1 with iterative optimization scheme to solve Eq. 2.1 has been explored in recent years [1, 13, 24], which are called “unrolled reconstruction networks” in general. Prior works showed that such unrolled networks performed well for multi-coil k-space reconstruction task by means of inserting measured k-space data into the network architecture to solve Eq. 2.1 with a learning-based regularization. In light of the success of such unrolled reconstruction networks, we apply a modified MoDL [3] as the reconstruction network in this work. MoDL unrolled the quasi-Newton optimization scheme to solve Eq. 2.1 with a neural network based denoiser as the L_2 regularization term $R(x)$, and conjugate gradient (CG) descent block was applied in MoDL architecture to solve the L_2 regularized problem. Besides, we will show that such unrolled network architecture also works as the skip connections for sampling pattern weights’ updating as the generated pattern is connected to each intermediate CG block to perform L_2 regularized data consistency (Figure 2.1).

2.3.2 ST Estimator for Binary Pattern

In LOUPE , a probabilistic pattern P_m was defined as $P_m = \frac{1}{1+e^{-a \cdot w_m}}$ with hyper-parameter a and trainable weights w_m . The binary k-space sampling pattern U was assumed to follow a Bernoulli distribution $Ber(P_m)$ independently on each k-space

location. U was generated from P_m as $U = \mathbf{1}_{z < P_m}$, where $z \sim U[0,1]^{\dim(P_m)}$

and $\mathbf{1}_x$ the pointwise indicator function on the truth values of x . However, indicator function $\mathbf{1}_x$ has zero gradient almost everywhere when back-propagating through it.

LOUPE addressed this issue by approximating $\mathbf{1}_{z < P_m}$ using another sigmoid

function: $U \approx \frac{1}{1 + e^{-b \cdot (P_m - z)}}$ with hyper-parameter b .

Although the gradient issue was solved in LOUPE, U was approximated as a fraction between $[0, 1]$ on each k-space location instead of the binary pattern deployed in both test phase and realistic MR scan. As a result, binary sampling patterns generated in test phase could yield inferior performance due to such mismatch with training phase.

To address this issue, binary patterns are also needed during training phase, at the same time gradient back-propagating through binary sampling layer should be properly handled. Such binary pattern generation layer can be regarded as the layer with stochastic neurons in deep learning, and several methods have been proposed to address its back-propagation [26, 33]. Here we use straight through (ST) estimator

[26] in the stochastic sampling layer to generate binary pattern U meanwhile

addressing the zero gradient issue during back-propagation. Based on one variant of

ST estimator, U is set as $\mathbf{1}_{z < P_m}$ during forward pass. When back-propagating through

the stochastic sampling layer, an ST estimator replaces the derivative factor $\frac{d\mathbf{1}_{z < P_m}}{dw_m} =$

0 with the following:

$$\frac{d\mathbf{1}_{z < P_m}}{dw_m} = \frac{dP_m}{dw_m} \quad [2.3]$$

In other words, indicator function in the stochastic layer is applied at forward pass but treated as identity function during back-propagation. This ST estimator allows the network to make a yes/no decision, allowing it to picking up the top γ fraction of k-space locations most important for our task.

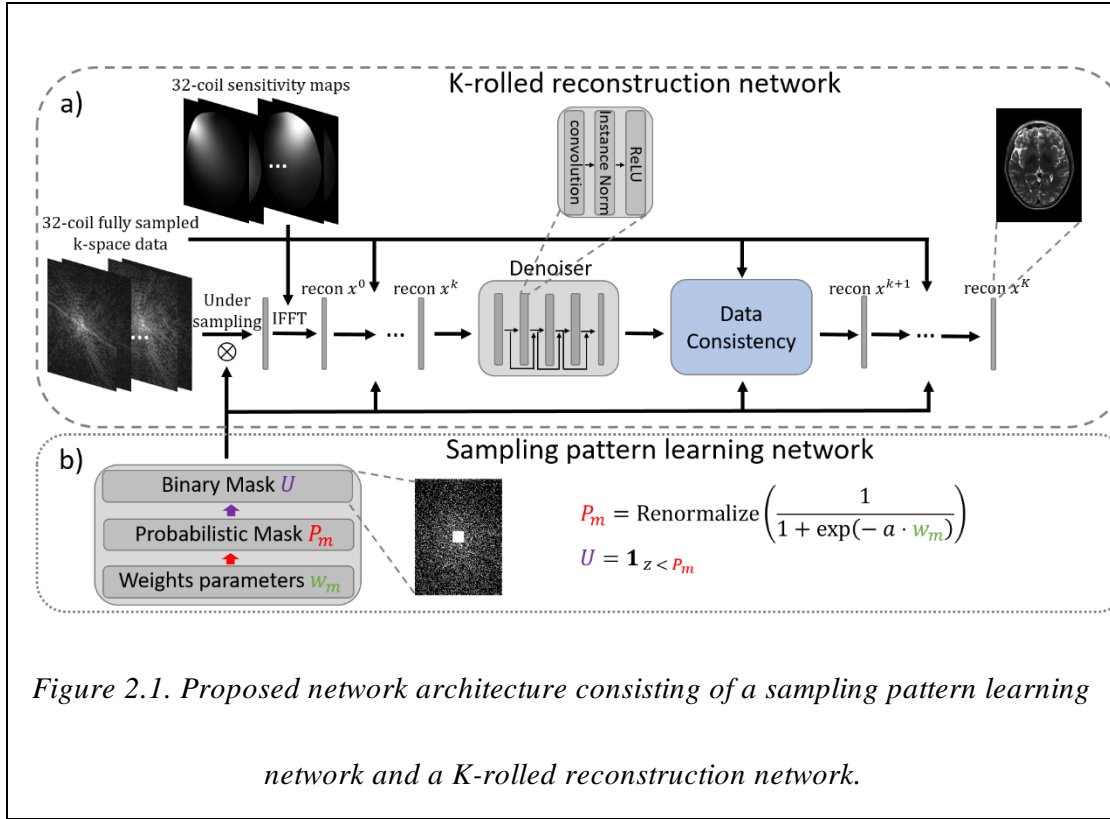


Figure 2.1. Proposed network architecture consisting of a sampling pattern learning network and a K-rolled reconstruction network.

2.3.3 Network Architecture

Figure 2.1 shows the proposed network architecture consisting of two sub-networks: one unrolled reconstruction network and one sampling pattern learning network.

In the sampling pattern learning network (Figure 2.1(b)), $\text{Renormalize}(\cdot)$ is a linear

scaling operation to make sure the mean value of probabilistic pattern is equal to the desired under-sampling ratio γ . The binary pattern U is sampled at every forward pass in the network and once generated, it is used to retrospectively under-sample the fully sampled multi-coil k-space data.

The deep quasi-Newton network (MoDL) as the unrolled reconstruction network architecture is illustrated in Figure 2.1(a). In deep quasi-Newton, Denoiser + Data consistency blocks are replicated K times to mimic K quasi-Newton outer loops of solving Eq. 2.1 in which a neural network denoiser for $R(x)$ is applied. Five convolutional layers with skip connection [34] and instance normalization [35] are used as the denoiser and the weights are shared among blocks. The binary pattern U is used to generate zero-filled reconstruction x^0 as the input of reconstruction network and connected to all the data consistency sub-blocks to deploy regularized optimization, which also works as the skip connection to benefit the training of pattern weights w_m .

2.4 Results

2.4.1 Dataset and Implementations

Data Acquisition and Processing. Fully sampled k-space data were acquired in 6 healthy subjects (5 males and 1 female; age: 30 ± 6.6 years) using a sagittal T2-weighted variable flip angle 3D fast spin echo sequence on a 3T GE scanner with a

32-channel head coil. Imaging parameters were: $256 \times 256 \times 192$ imaging matrix, 1mm^3 isotropic resolution. Coil sensitivity maps of each axial slice were calculated with ESPIRiT [36] using a $25 \times 25 \times 32$ auto-calibration k-space region. From the fully sampled data, a combined single coil image using the same coil sensitivity maps was computed to provide the ground truth label for both sampling pattern learning and reconstruction performance comparison. The central 100 slices of each subject were extracted for the training (300 slices), validation (100 slices) and test (200 slices) dataset. In addition, k-space under-sampling was performed retrospectively in the ky-kz plane for all the following experiments.

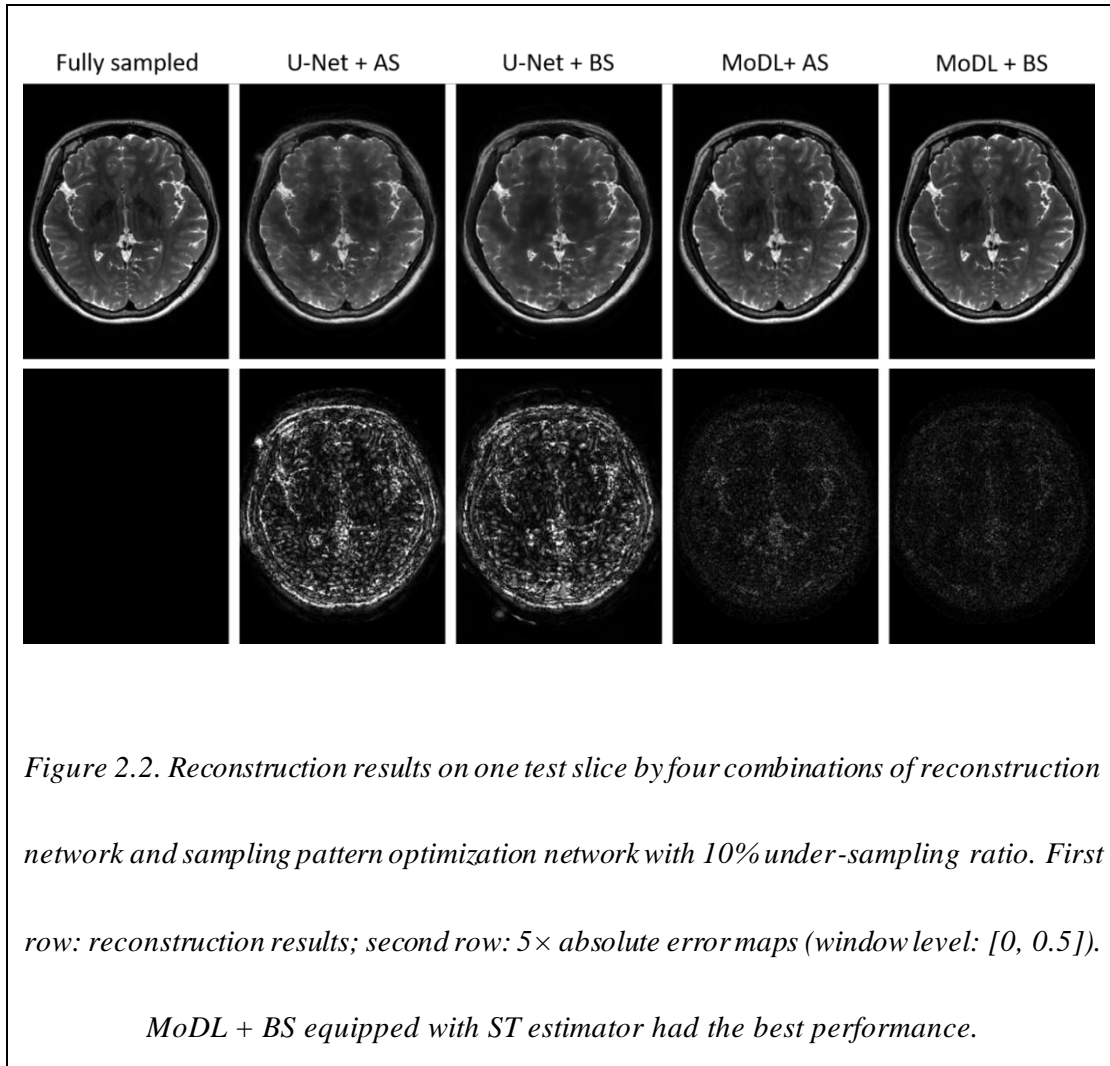
Training Parameters. In the sampling pattern learning network, w_m were initialized randomly, the slope factor $a = 0.25$ and the under-sampling ratio $\gamma = 10\%$. The central 25×25 k-space region remained fully sampled for each pattern. For the baseline LOUPE, a second slope factor $b = 12$ was used to approximate the binary sampling. The sampling pattern learning networks using binary sampling with ST estimator and approximated sampling were denoted as BS (binary sampling) and AS (approximated sampling) in the following experiments. In the unrolled reconstruction network, $K = 5$ replicated blocks were applied and the denoiser was initialized randomly. For the baseline LOUPE, a residual U-Net was applied. All of the learnable parameters in Figure 2.1 were trained simultaneously using the loss

function: $\frac{1}{N} \sum_{i=1}^N \sum_{k=1}^K \|x_i^k - x_i^*\|_1$, where x_i^* the i -th ground truth label in the training

dataset, x_i^k the k -th intermediate reconstruction ($K = 1$ in U-Net). Stochastic optimization with batch size 1 and Adam optimizer (initial learning rate: 10^{-3}) [37] was used to minimize the loss function. The number of epochs was 200. The whole training and inference procedures were implemented in PyTorch with Python version 3.7.3 on an RTX 2080Ti GPU.

2.4.2 Comparison with LOUPE

Figure 2.2 shows the reconstruction results from one of the test subjects to demonstrate the performance improvement of the extended LOUPE over vanilla LOUPE. Four combinations of reconstruction network and sampling pattern optimization network were tested and compared. Binary sampling patterns were generated during test phase. From Figure 2.2, MoDL provided better reconstruction results compared to U-Net, while for both U-Net and MoDL reconstruction networks, BS (binary sampling) gave less noisy reconstructions than AS (approximate sampling) during test phase. Quantitative comparisons in terms of PSNR (peak signal-to-noise ratio) and SSIM (structural similarity index measure [38]) are shown in Table 2.1, where MoDL + BS had the best performance.



2.4.3 Comparison with Other Pattern

To compare the learned sampling pattern (‘learned pattern’ in Figure 2.3, generated from MoDL + BS) with the manually designed one with 10% ratio, a variable density (VD) sampling pattern following a probabilistic density function whose formula is a polynomial of the radius in k-space with tunable parameters was generated (‘VD pattern’ in Figure 2.3). ESPIRiT [36] and TGV [39] as two representative iterative methods for solving PI CS-MRI were also deployed using

both sampling patterns, and the corresponding reconstruction results are shown in Figure 2.3. For each reconstruction method, the learned sampling pattern captured better image depictions with lower global errors than VD pattern and the structural details as zoomed in were also sharper with the learned sampling pattern. PSNR and SSIM in Table 2.2 shows consistently improved performance of the learned sampling pattern over the VD pattern for each reconstruction method.

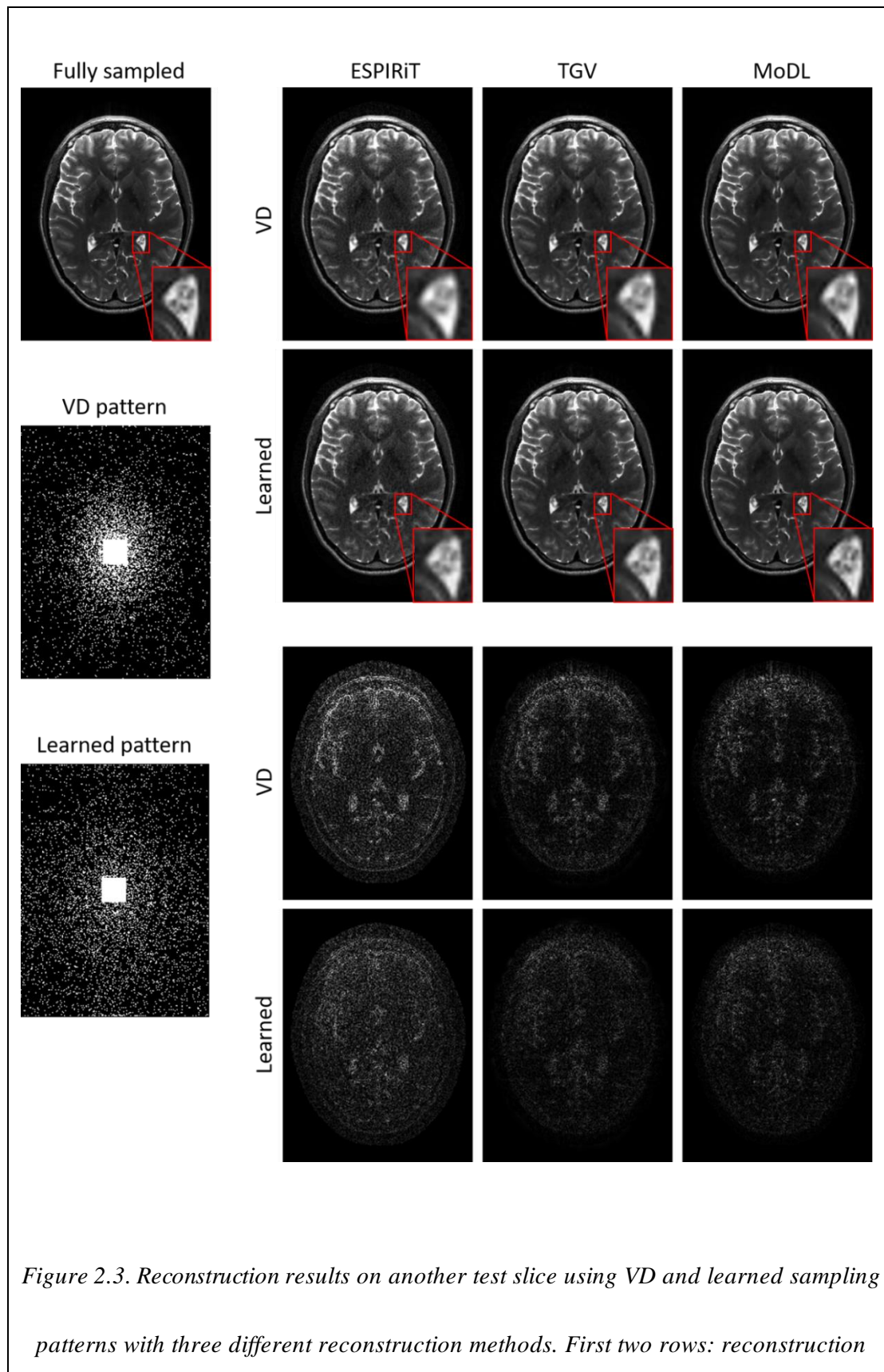


Figure 2.3. Reconstruction results on another test slice using VD and learned sampling patterns with three different reconstruction methods. First two rows: reconstruction

results; last two rows: corresponding $5 \times$ absolute error maps (window level: $[0, 0.5]$). For each reconstruction method, the learned sampling pattern produced lower global errors

and sharper structural details than VD sampling pattern.
Table 2.1. Quantitative results of section 2.4.2

	PSNR (dB)	SSIM
U-Net+AS	32.5 ± 1.0	0.885 ± 0.016
U-Net+BS	33.0 ± 0.6	0.898 ± 0.012
MoDL+AS	41.3 ± 1.2	0.963 ± 0.015
MoDL+BS	42.6 ± 1.1	0.968 ± 0.012

2.5 Discussion and Conclusion

In this work, LOUPE for optimizing the k-space sampling pattern in MRI was extended by training on in-vivo multi-coil k-space data and using the unrolled network for under-sampled reconstruction and binary stochastic sampling with ST estimator for sampling pattern optimization. Experimental results show that the extended LOUPE worked better than vanilla LOUPE on in-vivo k-space data and the learned sampling pattern also performed well on other reconstruction methods. Future work includes implementing the learned sampling pattern in the pulse sequence to

<i>Table 2.2. Quantitative results of section 2.4.3</i>			
Pattern	Method	PSNR (dB)	SSIM
VD	ESPIRiT	37.5 ± 1.0	0.920 ± 0.016
	TGV	40.1 ± 0.9	0.952 ± 0.014
	MoDL	40.4 ± 0.9	0.963 ± 0.010
Learned	ESPIRiT	39.5 ± 1.1	0.932 ± 0.018
	TGV	42.5 ± 1.1	0.959 ± 0.016
	MoDL	42.6 ± 1.1	0.968 ± 0.012

optimize the k-space data acquisition process prospectively.

CHAPTER 3. LARO: LEARNED ACQUISITION AND RECONSTRUCTION OPTIMIZATION TO ACCELERATE QUANTITATIVE SUSCEPTIBILITY MAPPING

3.1 Abstract

Quantitative susceptibility mapping (QSM) involves acquisition and reconstruction of a series of images at multi-echo time points to estimate tissue field, which prolongs scan time and requires specific reconstruction technique. In this paper, we present our new framework, called Learned Acquisition and Reconstruction Optimization (LARO), which aims to accelerate the multi-echo gradient echo (mGRE) pulse sequence for QSM. Our approach involves optimizing a Cartesian multi-echo k-space sampling pattern with a deep reconstruction network. Next, this optimized sampling pattern was implemented in an mGRE sequence using Cartesian fan-beam k-space segmenting and ordering for prospective scans. Furthermore, we propose to insert a recurrent temporal feature fusion module into the reconstruction network to capture signal redundancies along echo time. Our ablation studies show that both the optimized sampling pattern and proposed reconstruction strategy help improve the quality of the multi-echo image reconstructions. Generalization experiments show that LARO is robust on the test data with new pathologies and different sequence parameters.

3.2 Introduction

Quantitative magnetic resonance imaging (MRI) provides biomarkers for clinical assessment of diverse diseases, including T1 and T2 relaxation time [40, 41], fat fraction [42], quantitative susceptibility mapping (QSM) [6], etc. For QSM, a multi-echo gradient echo (mGRE) pulse sequence is used to acquire signals at different echo times. A tissue-induced local magnetic field map can be obtained by fitting the acquired complex multi-echo signals [43, 44]. Then, a tissue susceptibility map can be computed using an inverse problem solver, such as regularized dipole inversion [45].

For QSM, the range of echo times needs to be large enough to cover both small and large susceptibilities in tissue [46], such as in the application of QSM in multiple sclerosis (MS), where QSM has been shown to be sensitive to myelin content as well as iron [46], both of which are modified in MS. However, limited scan time in clinics only allows for mGRE with a compromised spatial resolution, making visualization of smaller MS lesion more challenging. Overcoming this compromise is a major motivation for this work.

The significantly increased scan time of mGRE sequence can be partly overcome using classical acceleration techniques such as Parallel imaging (PI) [16, 17], compressed sensing (CS) [18], or their combination (PI-CS) [19, 20]. Recently, deep

learning has been used to optimize k-space sampling patterns from training data, such as in LOUPE [1] and its extension LOUPE-ST [7], experimental design with the constrained Cramer-Rao bound (OEDIPUS) [22] and greedy pattern selection [23]. Building on these prior works, we propose here to learn an optimal sampling pattern to accelerate QSM acquisition and improve reconstruction quality.

Reconstruction from under-sampled measurements can be solved using regularization to exploit signal redundancies, such as low-rank and/or sparsity constraints [47-49]. More recently, convolutional neural networks have been proposed for compressed sensing reconstruction. One popular neural network technique involves implementing the unrolled iterations of an optimization process, coupled with a learned regularizer, as in MoDL [50] and VarNet [50]. These architectural designs have been applied to single-echo image reconstruction, and extended to dynamic image sequence reconstruction via cascaded [51] and recurrent networks [52]. Recently QSM acquisition was accelerated using 2D incoherent Cartesian under-sampling and deep neural network reconstruction with a variable density sampling pattern manually designed and fixed across echoes [53].

We propose Learned Acquisition and Reconstruction Optimization (LARO) to further optimize the sampling pattern across echoes by inferring the temporal variation through adding a temporal dimension to LOUPE-ST [7] for the multi-echo case.

Images are reconstructed accordingly using an unrolled reconstruction network based

on alternating direction method of multipliers (ADMM) [30] to capture the signal evolution and compensate the aliasing patterns of mGRE images with a temporal feature fusion module.

In this study, the learning based acquisition acceleration is not used to increase the spatial resolution but to instead accelerate the clinical protocol. For LARO training and testing experiments, we used retrospective under-sampling on fully sampled k-space data either simulated from the existing clinical protocol by taking inverse Fourier transform of the clinical mGRE images, or directly acquired from the scanner; the fully sampled k-space data served as ground truth for LARO sampling pattern optimization and under-sampled reconstruction. The optimized sampling pattern was then implemented in a modified mGRE sequence such that prospectively under-sampled data could be acquired and reconstructed with LARO. This work is extended from our conference paper [8] where preliminary retrospective results were shown as a proof of concept of LARO.

3.3 Theory

In QSM data acquisition, multi-echo k-space sampling with multiple receiver coils is modeled as:

$$b_{jk} = U_j F E_k s_j + n_{jk}, \quad [3.1]$$

where b_{jk} is the measured k-space data of the k -th receiver coil at the j -th echo time,

with N_C receiver coils and N_T echo times, U_j is the k-space under-sampling pattern at the j -th echo time, F is the Fourier transform, E_k is the sensitivity map of the k -th coil, s_j is the complex image of the j -th coil to be reconstructed, and n_{jk} is the acquisition noise, assumed to be Gaussian.

Having acquired b_{jk} with fixed U_j , we aim at reconstructing all s_j simultaneously with a cross-echo regularization loss $R(\{s_j\})$. Based on Eq. 3.1, a solution $\{\hat{s}_j\}$ can be obtained by solving the following optimization

$$\{\hat{s}_j\} = \underset{\{s_j\}}{\operatorname{argmin}} E(\{s_j\}) = \underset{\{s_j\}}{\operatorname{argmin}} \sum_{j=1}^{N_T} \sum_{k=1}^{N_C} \|U_j F E_k s_j - b_{jk}\|_2^2 + R(\{s_j\}). \quad [3.2]$$

We denote the iterative reconstruction method solving Eq. 3.2 as $\{\hat{s}_j\} =$

$A(\{U_j\}; \{b_{jk}\})$. With this notation, the sampling pattern optimization problem consists of finding, for a given under-sampling ratio γ and a given set of fully sampled training data $\{b_{jk}^i, s_j^i\}_{i=1\dots N}$, the sampling pattern $\{\hat{U}_j\}$ that solves:

$$\{\hat{U}_j\} = \underset{\{U_j\}}{\operatorname{argmin}} G(\{U_j\}) = \underset{\{U_j\}}{\operatorname{argmin}} \frac{1}{N} \sum_{i=1}^N L(\{\hat{s}_j^i\}, \{s_j^i\}),$$

$$\text{subject to } \{\hat{s}_j^i\} = A(\{U_j\}; \{U_j b_{jk}^i\}) \text{ and } \bar{U}_j = \gamma \text{ for all } i \text{ and } j, \quad [3.3]$$

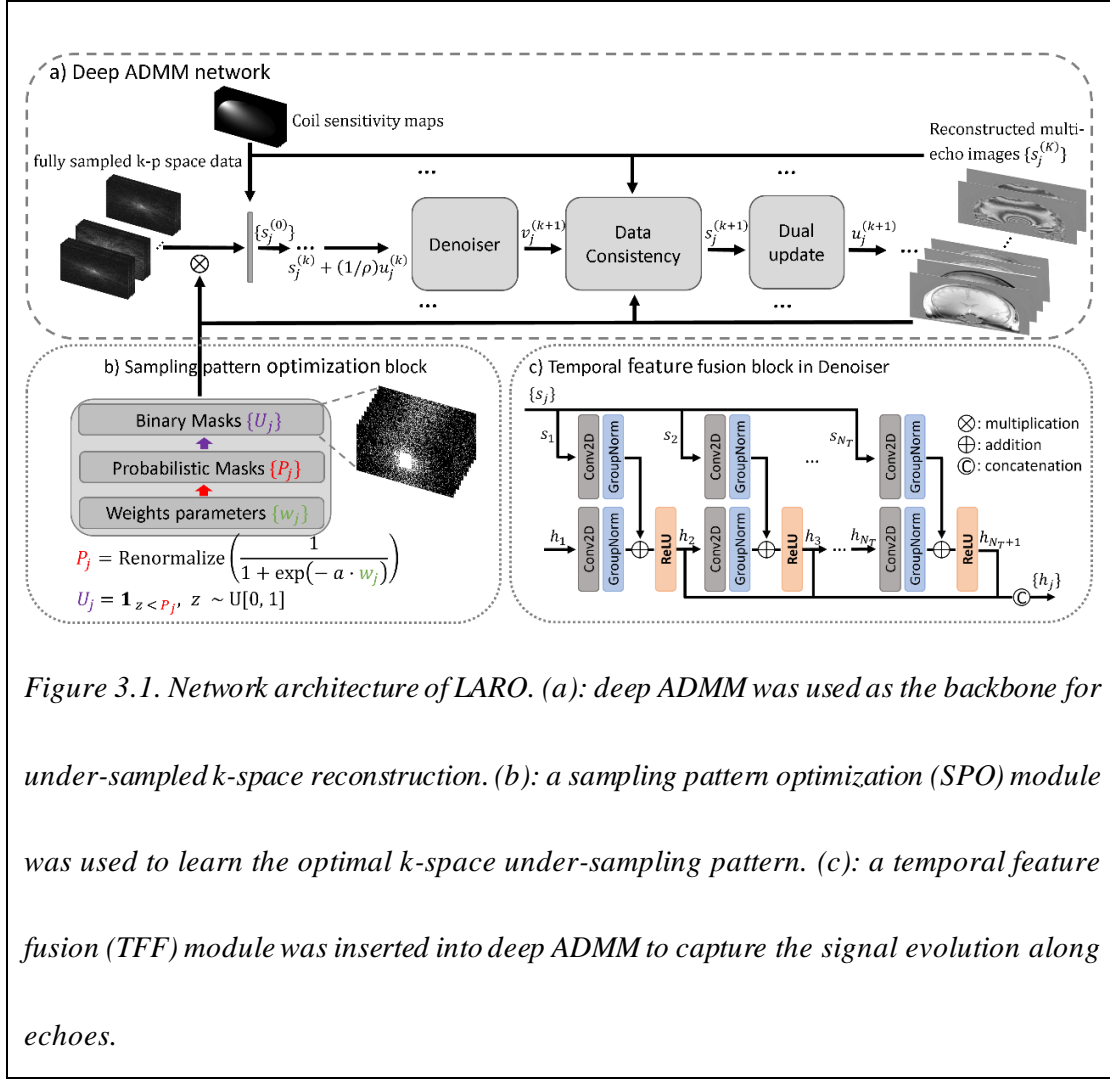


Figure 3.1. Network architecture of LARO. (a): deep ADMM was used as the backbone for under-sampled k-space reconstruction. (b): a sampling pattern optimization (SPO) module was used to learn the optimal k-space under-sampling pattern. (c): a temporal feature fusion (TFF) module was inserted into deep ADMM to capture the signal evolution along echoes.

where N is the total number of samples in the training dataset, $\{s_j^i\}$ is the i -th fully sampled multi-echo image, $\{\hat{s}_j^i\}$ is the i -th reconstructed under-sampled multi-echo obtained using solver $A(\{U_j\}; \{U_j b_{jk}^i\})$ and L is the metric to quantify difference between $\{\hat{s}_j^i\}$ and $\{s_j^i\}$, such as the L_1 loss. In the following section, we will propose a unified framework called LARO (Learned Acquisition and Reconstruction Optimization) to tackle both Eq. 3.2 and 3.3 using deep learning techniques.

3.3.1 Sampling pattern optimization (SPO)

For k-space sampling pattern optimization Eq. 3.3, we extend the previously proposed LOUPE-ST method [7] to the multi-echo setting. We consider 2D variable density Cartesian sampling patterns in the $k_y - k_z$ plane with a fixed under-sampling ratio as shown in Figure 3.1b, in which learnable weights $\{w_j\}$ are used to generate a multi-echo probabilistic pattern $\{P_j\}$ through sigmoid transformation and sampling ratio renormalization:

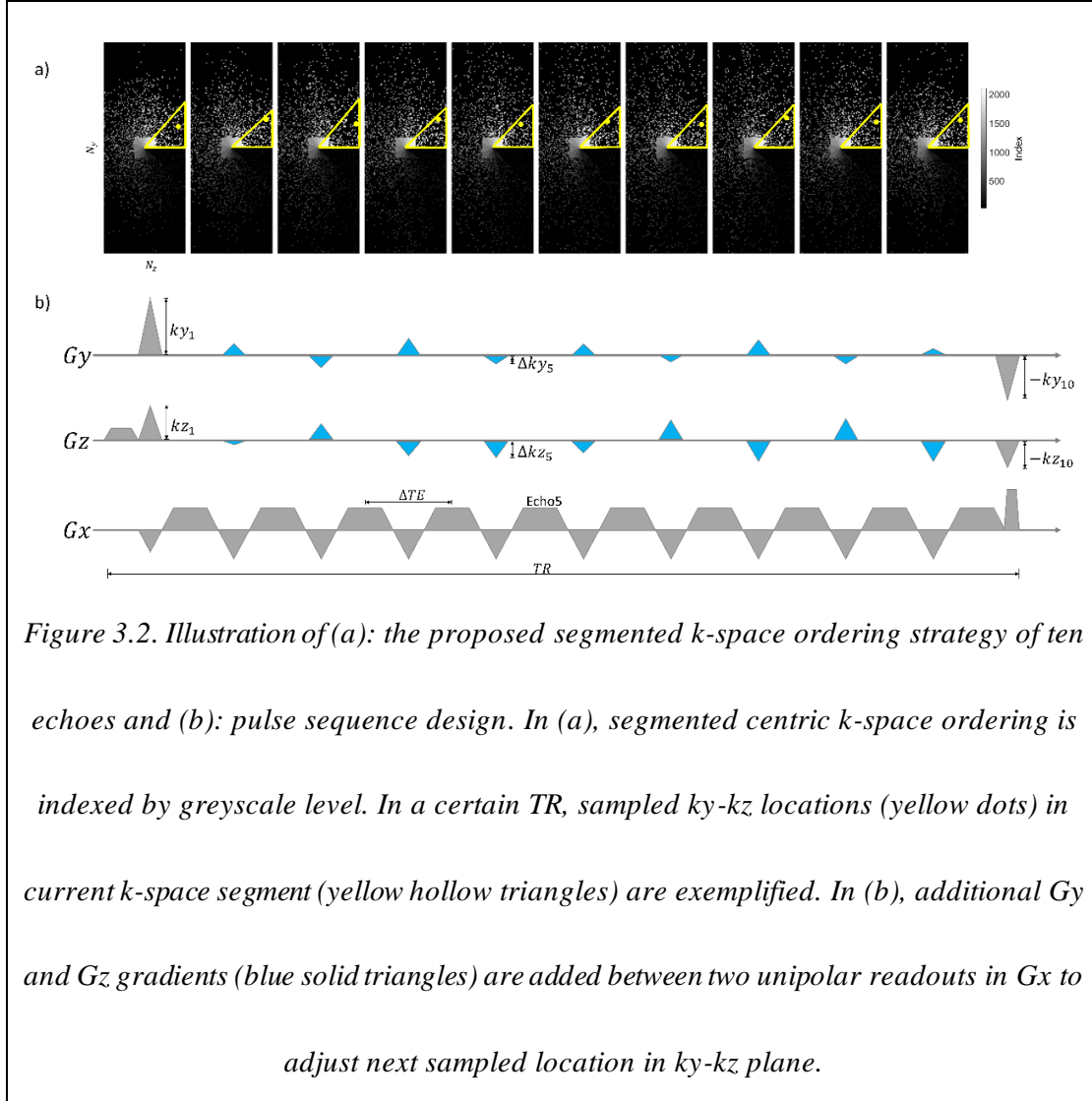
$$P_j = \text{Renorm}\left(\frac{1}{1 + e^{-a \cdot w_j}}\right), \quad [3.4]$$

where a is the slope parameter of the sigmoid function and $\text{Renorm}(\cdot)$ is a linear scaling operation to make sure the mean value of probabilistic pattern is equal to the desired under-sampling ratio [1]. Assuming an independent Bernoulli distribution $Ber(P)$ at each k-space location, a binary under-sampling pattern U_j is generated via stochastic sampling from P_j :

$$U_j = \mathbf{1}_{z < P_j}, \quad [3.5]$$

where $\mathbf{1}_x$ is the indicator function on the truth value of x and z is uniformly distributed between $[0, 1]$. Then $\{U_j\}$ are used to retrospectively acquire $\{b_{jk}\}$ from fully sampled multi-echo k-space data. The stochastic sampling layer in Eq. 3.5 has zero gradient almost everywhere when backpropagating through this layer, which

makes updating $\{w_j\}$ infeasible [54]. To solve this issue, LOUPE-ST implements a



straight-through estimator [26] for backpropagation through the stochastic sampling layer by using the probability distribution P instead:

$$\frac{d\mathbf{1}_{z < P_j}}{dw_j} \rightarrow \frac{dP_j}{dw_j}, \quad [3.6]$$

which solves the zero gradient issue and performs better than other gradient approximations, such as the one implemented in LOUPE [7].

3.3.2 Temporal feature fusion (TFF) for reconstruction

For image reconstruction Eq. 3.2, we propose an unrolled architecture with a temporal feature fusion (TFF) module based on the plug-and-play ADMM [55] strategy. In plug-and-play ADMM, auxiliary variables $v_j = s_j$ for each echo j were introduced and an off-the-shelf image denoiser $\{v_j^{(t+1)}\} = \mathcal{D}(\{\tilde{v}_j^{(t)}\})$, where $\tilde{v}_j^{(t)} = s_j^{(t)} + \frac{1}{\rho} u_j^{(t)}$ with $u_j^{(t)}$ the dual variable of the t -th outer loop and ρ the penalty parameter in ADMM, was applied. We propose to unroll the iterative scheme of plug-and-play ADMM as a data graph which we call “deep ADMM” network as shown in Figure 3.1a, where a CNN denoiser $\mathcal{D}(\{\tilde{v}_j^{(t)}\}; w_D)$ with weights w_D is designed to replace $\mathcal{D}(\{\tilde{v}_j^{(t)}\})$ as:

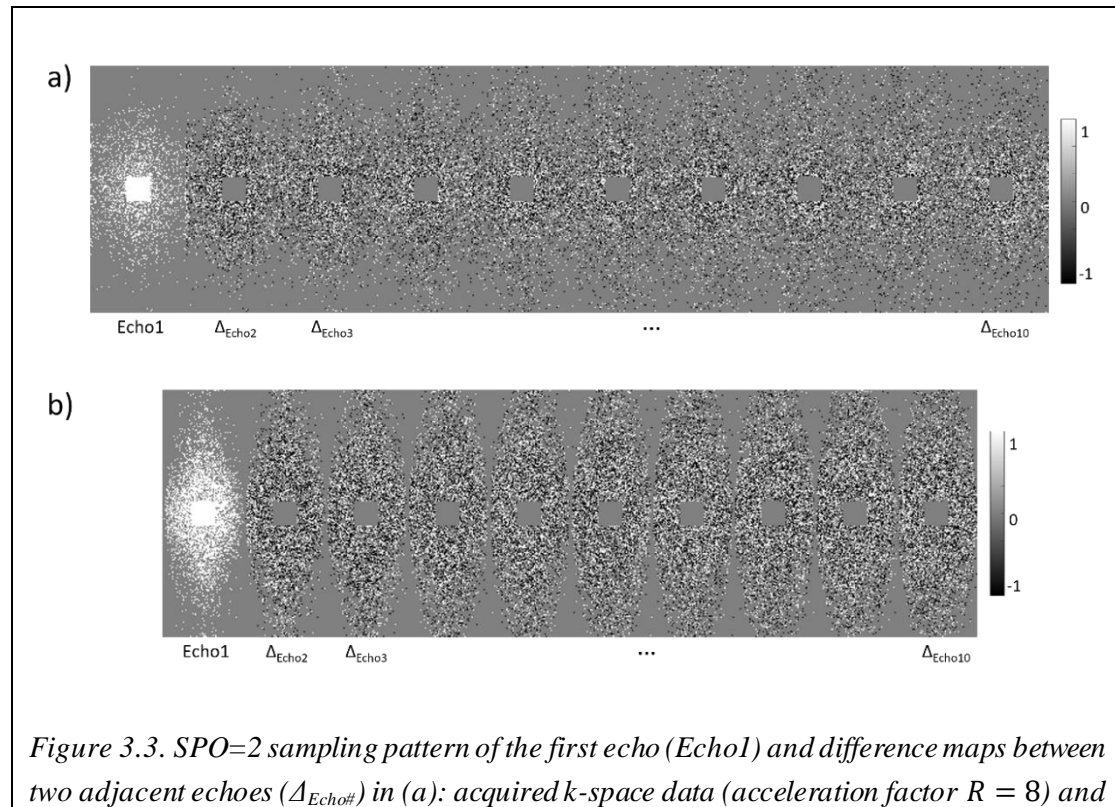
$$v_j^{(t+1)} = \mathcal{D}(\tilde{v}_j^{(t)}; w_D). \quad [3.7]$$

To incorporate the dynamic nature of multi-echo images into $\mathcal{D}(\{\tilde{v}_j^{(t)}\}; w_D)$, we propose a temporal feature fusion (TFF) module as shown in Figure 3.1c. In TFF, a recurrent module is repeated N_T times in which at the j -th repetition (corresponding to the j -th echo), s_j (real and imaginary parts concatenated along the channel dimension) and s_{j-1} 's hidden state feature h_{j-1} are fed into the module to generate s_j 's hidden state feature h_j :

$$h_j = \text{ReLU}(N_s(s_j) + N_h(h_{j-1})), \quad [3.8]$$

where $N_s(\cdot)$ and $N_h(\cdot)$ are convolutional layers for s_j and h_{j-1} , and ReLU is the

Rectified Linear Unit activation function. The learnable weights in $N_s(\cdot)$ or $N_h(\cdot)$ are shared across recurrent repetitions. At the j -th recurrent forward pass shown in Eq. 3.8, feature maps h_j are generated by aggregating s_j and h_{j-1} through convolutions and nonlinear activations, which implicitly capture the echo dynamics and fuses features from the preceding echoes. After a full recurrent pass over echoes, all feature maps h_j are concatenated along the batch dimension and fed into a denoising network to generate $\{v_j^{(t+1)}\}$. The dynamic nature of the signal over echo times is implicitly captured with the recurrent forward process due to the parameter sharing mechanism which attempts to exploit the relationship between a given echo and all earlier echoes.



(b): synthetic k-space data (acceleration factor $R = 4$). Different k-space sampling pattern was generated from the learned probabilistic pattern per echo, introducing additional incoherency along temporal dimension.

3.3.3 K-space under-sampling sequence design

The learned k-space sampling patterns U_j were implemented in an mGRE pulse sequence for prospective data acquisition. Gradient pulses along the phase and slice encoding directions were added between consecutive echoes to allow for the modification of k-space sampling locations echo-by-echo during one TR. To avoid large changes in the phase and slice encoding gradients between two echoes, the following k-space ordering strategy was deployed: for each echo j , the sampled k-space locations U_j were first divided into multiple ordered segments of equal size based on their angle with respect to the positive k_y axis. Within each segment, k-space locations were ordered based on their distance with respect to the k-space center. Using such k-space ordering strategy, sampled locations will follow a similar trajectory for all echoes, avoiding large changes in the phase and slice encoding gradients from echo to echo during one TR. Illustration of the proposed segmented k-space ordering and pulse sequence design is shown in Figure 3.2. In this example, number of echoes $N_T = 10$, acceleration factor $R = 8$, $N_y = 206$, $N_z = 80$, N_s (number of segments) = 11, N_{ind} (number of k-space location per segment) = 188 so that $N_s \times N_{ind} = N_y \times N_z / R$. Figure 3.2a exemplified the sampled k_y - k_z locations

(yellow dots) in current k-space segment (yellow hollow triangles) during a certain TR. Gy and Gz gradients (blue solid triangles) in Figure 3.2b are added between two unipolar readouts in Gx to adjust next sampled location in ky-kz plane.

3.4 Method

Data were acquired following an IRB approved protocol. All images used in this work were de-identified to protect the privacy of human participants.

3.4.1 Fully sampled acquired k-space data

Cartesian fully sampled k-space data were acquired in 13 healthy subjects (3 females, age: 30.7 ± 7.3) using a 3D mGRE sequence on a 3T GE scanner with a 32-channel head coil. Imaging parameters included FA = 15° , FOV = 25.6 cm, TE₁ = 1.972 ms, TR = 36 ms, #TE = 10, ΔTE = 3.384 ms, acquisition matrix = 256×206×80 (readout × phase encoding × phase encoding), voxel size = 1×1×2 mm³, BW = 64 kHz. Total scan time was 9:30 mins per subject. 32-coil k-space data of each echo were compressed into 8 virtual coils using a geometric singular value decomposition coil compression algorithm [56]. After compression, coil sensitivity maps of each echo were estimated with a reconstruction null space eigenvector decomposition algorithm ESPIRiT [36] using a centric 20×20×20 self-calibration k-space region for each compressed coil. From the fully sampled data, coil combined multi-echo images were computed using the obtained coil sensitivity maps to provide the ground truth labels

for both network training and performance comparison. Training, validation and testing has been performed on 2D coronal slices. To this end, the 200 central coronal slices per subject were selected along the readout direction, as these contain mostly brain anatomy to avoid a bias from slices that do not resemble the brain. 8/1/4 subjects (1600/200/800 slices) were used as training, validation, and test datasets, respectively.

To demonstrate the generalization ability of LARO, Cartesian fully sampled k-space data were also acquired in one of the healthy test subjects with the following sequence parameter modifications: another flip angle (25°), number of echoes (7 echoes), voxel size ($0.75 \times 0.75 \times 1.5 \text{ mm}^3$), a second MRI scanner from the same manufacturer (GE, 12-channel head coil) and a third MRI scanner from another manufacturer (Siemens, 64-channel head coil). Same k-space processing was applied to these data to get compressed 8-coil k-space, coil sensitivity maps and ground truth labels.

3.4.2 Fully sampled synthetic k-space data

To demonstrate LARO's improvement on pathologic reconstruction, supplementary synthetic k-space datasets from healthy subjects, multiple sclerosis (MS) and intracerebral hemorrhage (ICH) patients were simulated, considering unavailability of acquired fully sampled k-space data from patients. Multi-echo complex images of 7 healthy subjects, 4 MS patients and 1 ICH patient were acquired using a 3D mGRE

sequence on a 3T GE scanner. Imaging parameters included $FA = 15^\circ$, $FOV = 25.6$ cm, $TE_1 = 6.69$ ms, $TR = 49$ ms, $\#TE = 10$, $\Delta TE = 4.06$ ms, acquisition matrix = $256 \times 206 \times 68$ (readout \times phase encoding \times phase encoding), voxel size = $1 \times 1 \times 2$ mm³, $BW = 64$ kHz. Synthetic single-coil k-space data was generated through Fourier transform of the complex multi-echo images. Retrospective Cartesian under-sampling was applied on the synthetic k-space data along two phase encoding directions. Training, validation and testing has been performed on 2D coronal slices. To this end, the 200 central coronal slices per subject were selected along the readout direction, as these contain mostly brain anatomy to avoid a bias from slices that do not resemble the brain. Data from 6/1 healthy subjects (1200/200 slices) was used as training/validation. Data from the MS (800 slices) and ICH (200 slices) patients was used as two test datasets.

3.4.3 Under-sampled k-space data in both retrospective and prospective studies

For a retrospective study, an acceleration factor $R = 8$ (12.5% under-sampling ratio) was applied on the fully sampled acquired k-space dataset and acceleration factor $R = 4$ (25% under-sampling ratio) was applied on the fully sampled synthetic k-space dataset. For a prospective study, Cartesian under-sampled k-space data was prospectively acquired in 10 healthy test subjects (3 females, age: 28.4 ± 4.1) using a modified 3D mGRE sequence with the same 3T GE scanner and imaging parameters. Different sampling patterns with $R = 8$ were applied during prospective scans and

compared. For the optimized k-space sampling pattern, each echo was divided into 11 segments with 188 locations in each segment, resulting in $188 \times 11 = 2068$ k-space locations to sample in total. Corresponding scan time was 1:20 mins. For reference, the default imaging protocol using the same imaging parameters except for elliptical R=2 uniform under-sampling reconstruction using the SENSE implementation [17] on the scanner was performed on the same subjects.

3.4.4 Network architecture

The proposed network architecture is shown in Figure 3.1. Real and imaginary parts of multi-echo images were concatenated along the channel dimension, yielding 20 channels to represent multi-echo complex images in the network. Under-sampled k-space data was zero-filled and Fourier-transformed to be used as input for deep ADMM (Figure 3.1a) with $N_l = 10$ unrolled iterations. In deep ADMM, the denoiser $\mathcal{D}(\cdot; w_D)$ consisted of five convolutional layers equipped with 320 channels with instance normalization [35] + ReLU activation after convolution for each hidden layer. The TFF module (Figure 3.1c) used 64 channels in both convolutional layers for s_j and h_j . The hidden state feature maps h_j were concatenated along the channel dimension and fed into $\mathcal{D}(\cdot; w_D)$ to generate denoised multi-echo images. The SPO module (Figure 3.1b) was used to learn optimal sampling patterns, where weights $\{w_j\}$ (with matrix size $206 \times 68 \times 10$ for synthetic k-space data and $206 \times 80 \times 10$ for the acquired k-space data) were initialized as zeros and slope parameter a in sigmoid

function was 0.25. After generating binary patterns $\{U_j\}$ from probabilistic patterns $\{P_j\}$, values in central 20×20 locations of $\{U_j\}$ were set as ones for self-calibration.

3.4.5 Training strategy

The training process consists of two phases. In phase one, weights in the deep ADMM network and SPO module were updated simultaneously by maximizing a channel-wise structural similarity index measure (SSIM) [38]: $\frac{1}{N} \sum_i^N \sum_{j=1}^{N_T} SSIM(\hat{s}_j^i, s_j^i)$ with the measure between two windows x and y of common size (10×10) and location in \hat{s}_j^i and s_j^i as:

$$SSIM(x, y) = \frac{(2\mu_x\mu_y + c_1)(2\sigma_{xy} + c_2)}{(\mu_x^2 + \mu_y^2 + c_1)(\sigma_x^2 + \sigma_y^2 + c_2)}, \quad (9)$$

where μ_x , μ_y and σ_x , σ_y are the mean and variance of x and y , σ_{xy} is the covariance between x and y , $c_1 = 0.01^2$ and $c_2 = 0.03^2$. In phase two, the pre-trained deep ADMM network from phase one was fine-tuned with fixed binary sampling patterns $\{U_j\}$ either manually designed using a multi-level sampling scheme [57] or generated from the learned probabilistic patterns $\{P_j\}$ in phase one. We implemented in PyTorch using the Adam optimizer [37] (batch size 1, number of epochs 100 and initial learning rate 10^{-3}) on a RTX 2080Ti GPU. Our code is available at <https://github.com/Jinwei1209/LARO.git>.

3.4.6 Ablation study

An ablation study regarding the effectiveness of TFF and SFO modules were investigated by removing one or more of these modules and quantifying the corresponding loss in performance. First, a manually designed variable density sampling pattern was generated based on a multi-level sampling scheme [57] and used to train a baseline deep ADMM network without TFF or SPO (denoted by TFF=0/SPO=0). Then TFF (denoted as TFF=1), single-echo SPO (optimized sampling pattern was fixed across echoes, denoted as SPO=1) and multi-echo SPO (denoted as SPO=2) were progressively added to the baseline deep ADMM network to check the effectiveness of each module, with LARO representing TFF with multi-echo SPO (i.e., TFF=1, SPO=2). For baseline deep ADMM without TFF, Eq. 3.8 was replaced with $h_j = \text{ReLU}(N_s(s_j))$ by removing $N_h(h_{j-1})$ to show the effectiveness of recurrent forward pass of hidden state features $\{h_j\}$ in TFF, where two 64-channel convolutional layers in $N_s(\cdot)$ were used to match the memory usage of TFF during ablation study.

3.4.7 Performance comparison

Iterative method locally low rank (LLR) [49] and a deep learning method MoDL [50] were used as two benchmark reconstruction methods, where MoDL was modified to reconstruct multi-echo images simultaneously with concatenated real and imaginary

parts of multi-echoes along channel dimension. Manually designed and optimized sampling patterns were applied to all reconstruction methods and compared. From the resulting gradient echo images, $R2^*$ was estimated using ARLO [58] and QSM using morphology enabled dipole inversion with CSF-0 reference [59] from relative difference local field (RDF), which was estimated using nonlinear field estimation [44], phase unwrapping and background field removal [60].

For all retrospectively under-sampled datasets, quantitative comparisons were presented with fully sampled data as reference, where PSNR (Peak Signal-to-Noise Ratio) and SSIM (Structural Similarity Index) [38] metrics per reconstructed coronal slice were used to measure the reconstruction accuracy of the echo-combined magnitude image $\sqrt{\sum_{j=1}^{N_T} |s_j|^2}$, $R2^*$ and RDF maps. RMSE (Root-Mean-Square Error), HFEN (High-Frequency Error Norm) [61] and SSIM [38] per 3D volume were used to measure the reconstruction quality of QSM.

For the MS patient dataset, lesions were manually segmented by an experienced neuroradiologist based on the corresponding T2-weighted FLAIR images which were spatially registered to the magnitude of mGRE data. A linear regression was performed of the mean susceptibility of all lesions between fully sampled and under-sampled test data.

For the prospectively under-sampled dataset, reconstructions were performed by LLR,

MoDL and TFF reconstructions with different sampling patterns. The SENSE reconstruction from the scanner with acceleration factor 2 was used as a reference for comparison. Detailed structures in QSM and R2* such as white matter tracts were qualitatively compared. The perivascular spaces were segmented manually into a single region of interest ROIp. From this ROIp, a border ROIb was computed by dilating ROIp by 1 pixel and removing the original ROIp. The sharpness was defined as the difference of average susceptibility of ROIp and ROIb. Mean QSM and R2* values and standard deviations in manually drawn ROIs including Globus pallidus (GP), Substantia Nigra (SN), Red Nucleus (RN), Caudate Nucleus (CN), Putamen (PU), thalamus (TH), optic radiation (OR) and cerebral cortex (CC, starting from the top of the brain, drawn on the tenth slice of QSMs covering some part of frontal and parietal lobes) were computed and compared.

3.4.8 Generalization experiments

When acquiring the fully sampled test data with sequence parameter modifications, only one parameter was modified in each scan, except for a different voxel size, where increased spatial resolution also increased echo spacing ΔTE to 4.728 ms and acquisition matrix to $320 \times 258 \times 112$ (readout \times phase encoding \times phase encoding). Sampling patterns of this voxel size were obtained by bicubic interpolation of the pre-trained probabilistic sampling distribution P_j with matrix size 206×80 in Eq. 3.4 to P'_j with matrix size 258×112 for the new voxel size. Then the new binary sampling

patterns U_j' were generated using Eq. 3.5: $U_j' = \mathbf{1}_{z < p_j'}$, where $\mathbf{1}_x$ is the indicator function on the truth value of x and z is uniformly distributed between $[0, 1]$. For the test data with 7 echoes, the first 7 sampling patterns were used when applying LARO with SPO=2. Fully sampled data were used as the reference for quantitative

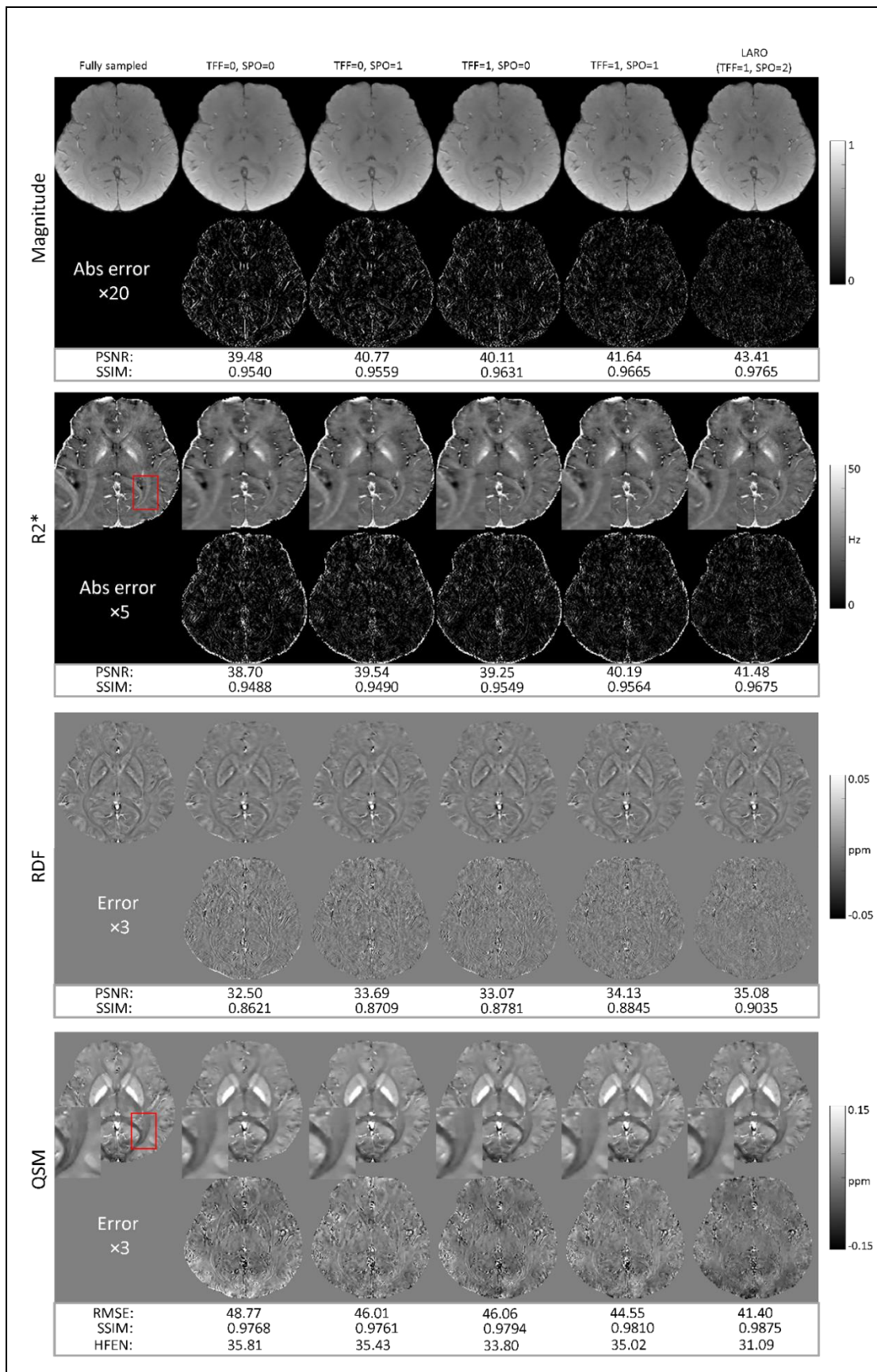
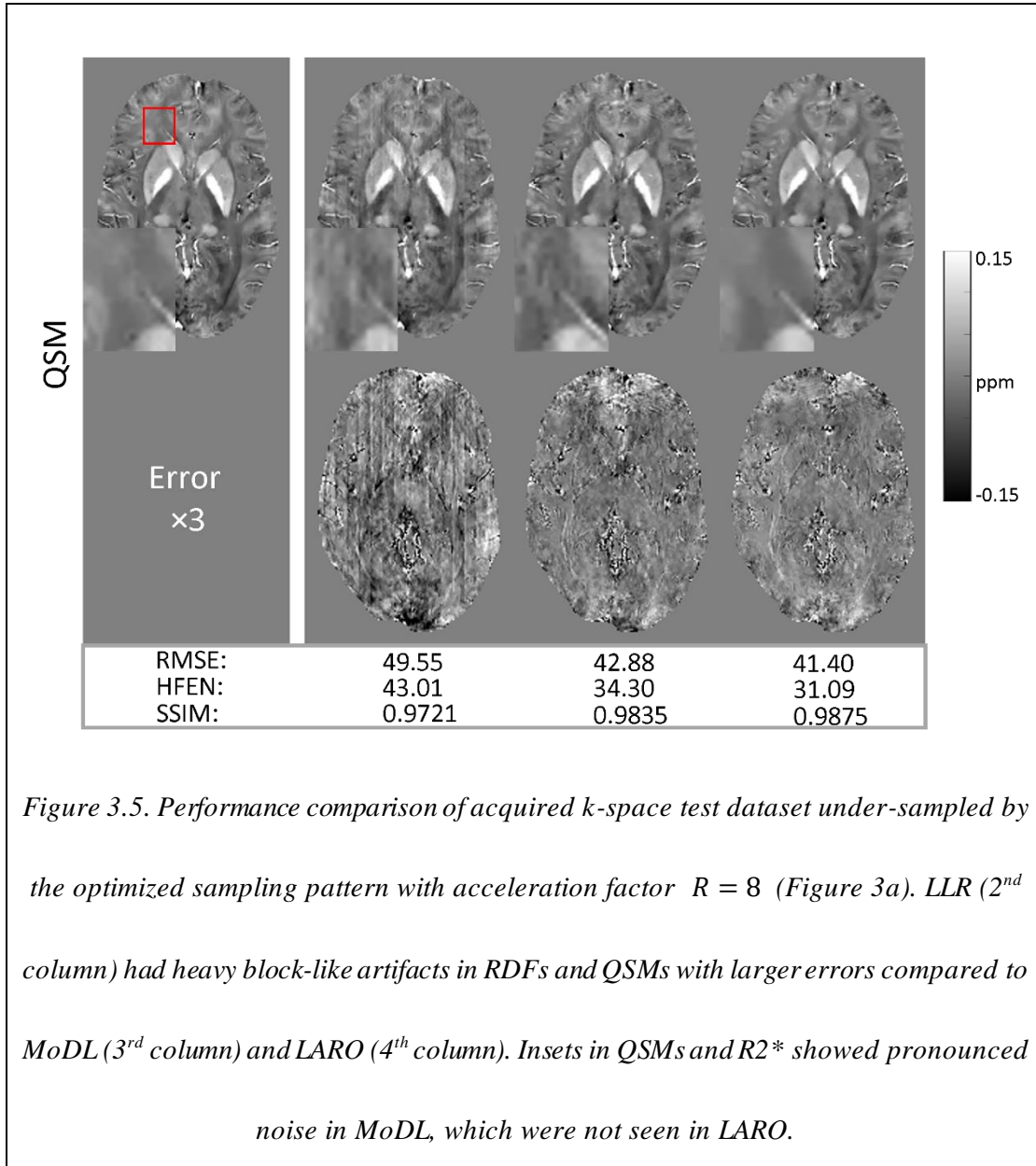


Figure 3.4. Ablation study on acquired k-space dataset with acceleration factor $R = 8$. Reconstruction errors were progressively reduced in magnitude, $R2^$ and QSM as more modules were added. White matter tracts (insets) were blurry in all reconstructed $R2^*$ and QSMs except LARO (TFF=1, SPO=2). Abbreviation: TFF=0 or 1, with or without temporal feature fusion module; SPO=0, 1 or 2, “without”, “with single-echo”, or “with multi-echo” sampling pattern optimization.*

comparison in $R2^*$, RDF and QSM, except in magnitude due to signal intensity variations of different scans.

3.5 Results

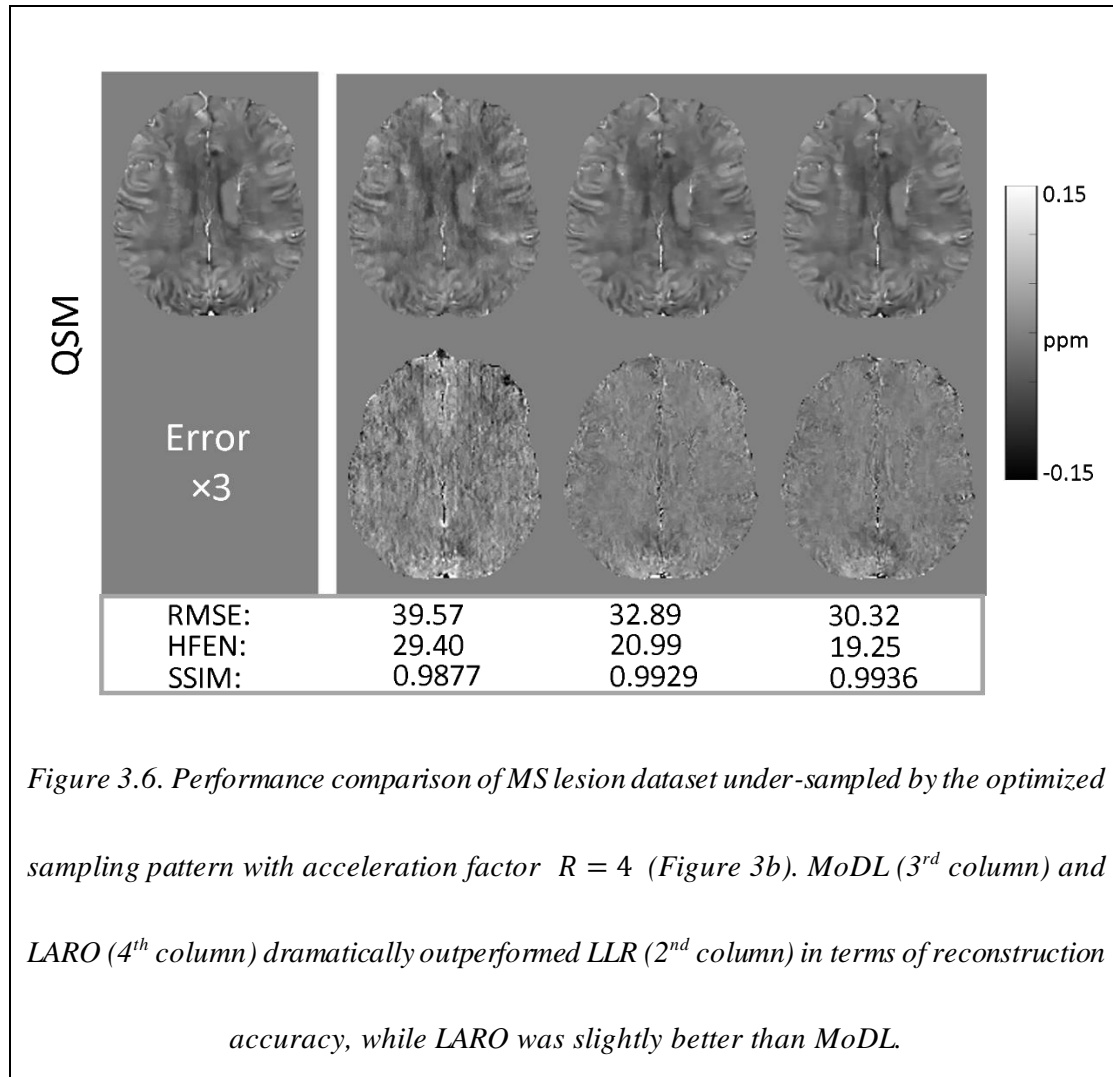
For abbreviations, “TFF=0” or “1” denotes “with” or “without” temporal feature fusion module; “SPO=0”, “1” or “2” denotes “without”, “with single-echo”, or “with multi-echo” sampling pattern optimization. In terms of reconstruction methods, “TFF” denotes the proposed reconstruction with “TFF=1” under different sampling patterns; “LARO” denotes “TFF” reconstruction specifically under “SPO=2” sampling pattern, i.e., the proposed learned acquisition and reconstruction optimization framework.



3.5.1 Sampling patterns

Figure 3.3 shows SPO=2 sampling pattern of the first echo (Echo1) and difference maps between two adjacent echoes ($\Delta_{\text{Echo}\#}$) in (a): acquired k-space data (acceleration factor $R = 8$) and (b): synthetic k-space data (acceleration factor $R = 4$). Different

k-space sampling patterns were generated from the learned probabilistic patterns per echo, introducing additional incoherency along the temporal dimension.



3.5.2 Acquired k-space data

Ablation study

Reconstructed magnitude, R2*, RDF and QSM in one representative slice are shown in Figure 3.4. As TFF and SPO modules were gradually added to the baseline deep

ADMM architecture, reconstruction errors (2nd, 4th, 6th and 8th rows) were progressively reduced in magnitude, R2*, RDF and QSM maps, where LARO (TFF=1, SPO=2) performed the best. Depictions of white matter tracts (insets) in R2* and QSM maps were improved as more modules were added. Quantitative metrics of the ablation study is shown in Table S1. Reconstruction accuracies of magnitude, R2*, RDF and QSM maps were progressively improved as more modules were introduced, where LARO (TFF=1, SPO=2) performed the best.

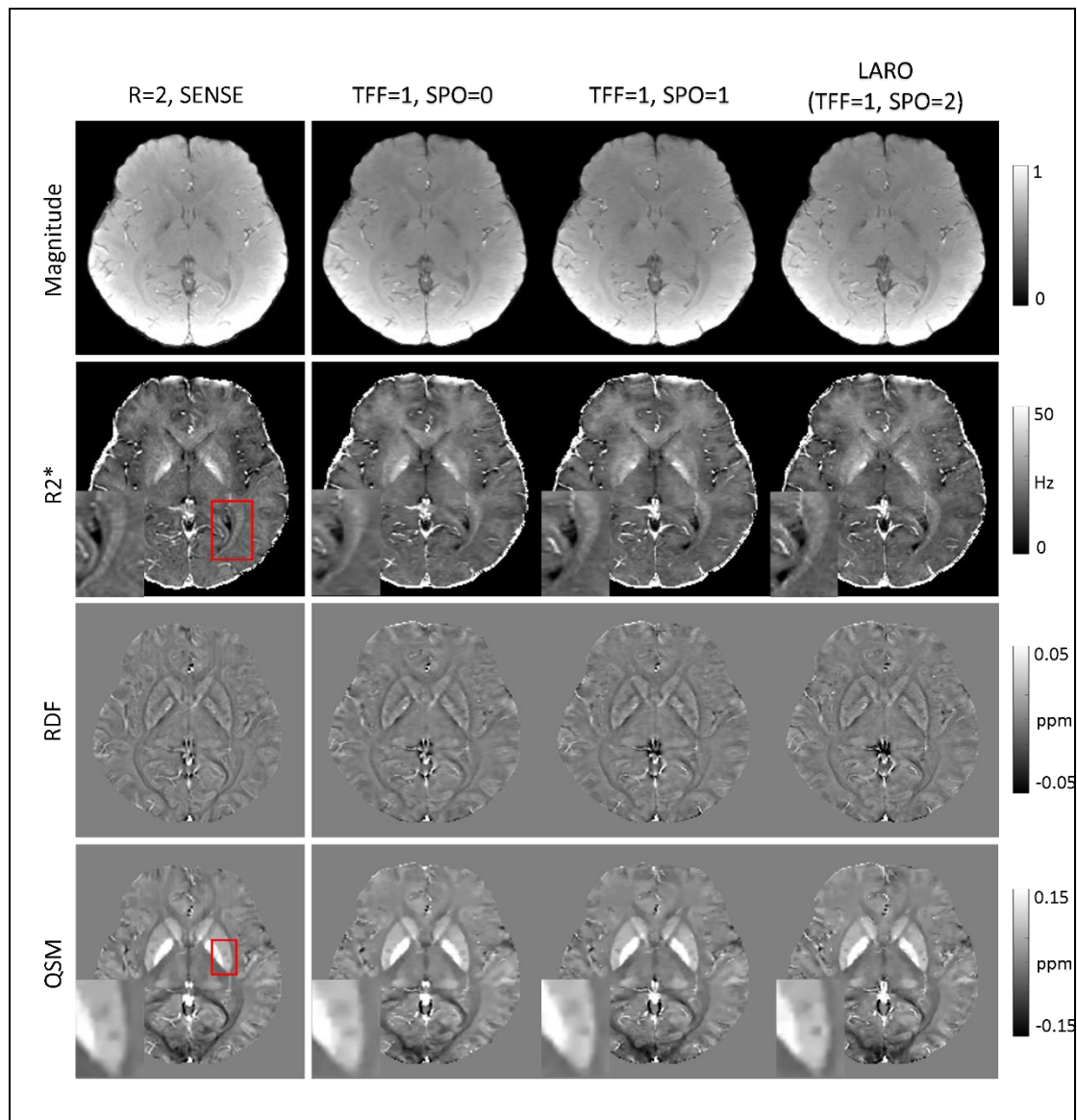
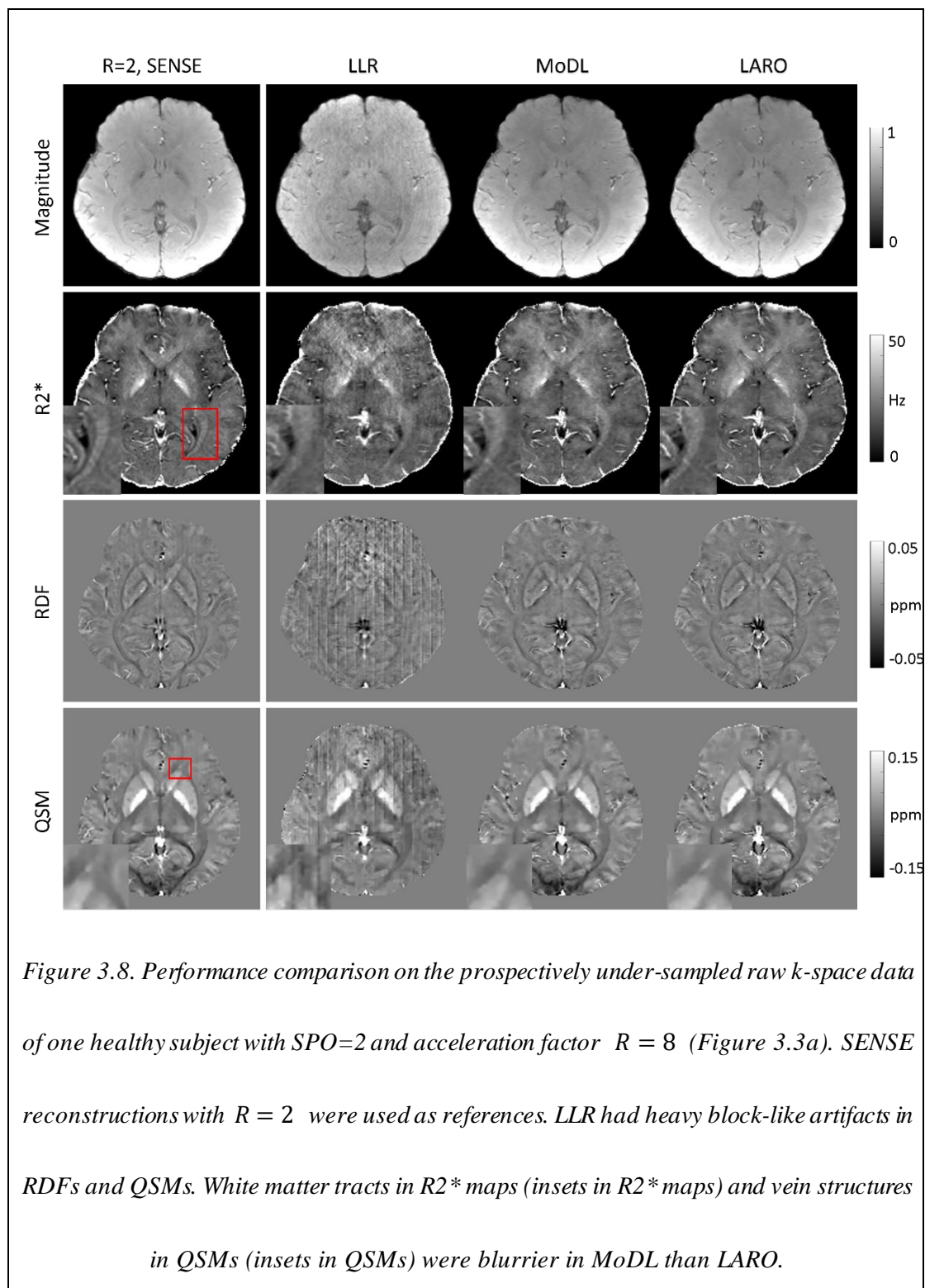


Figure 3.7. TFF reconstructions on prospectively under-sampled raw k-space data of one healthy subject with acceleration factor $R = 8$. Compared to SENSE reconstruction with $R = 2$ as reference, depictions of white matter tracts in $R2^$ maps (insets in $R2^*$ maps) were progressively improved from SPO=0, 1 to LARO (SPO=2). Sharpness scores of perivascular spaces inside putamen (insets in QSMs) were 0.0270, 0.0111, 0.0247 and 0.0411 for SENSE, SPO=0, 1 and 2. Abbreviation: TFF= 1, with temporal feature fusion module; SPO=0, 1 or 2, without, with single-echo or with multi-echo sampling pattern optimization.*

Performance comparison

Reconstructed magnitude, $R2^*$, RDF and QSM with SPO=2 sampling pattern (Figure 3.3a) in one representative slice are shown in Figure 3.5. LLR had larger reconstruction errors with heavy block-like artifacts in RDFs and QSMs compared to MoDL and



LARO. Pronounced noise in QSMs and $R2^*$ (insets) were showed in MoDL, which were not seen in LARO. Reconstructions with $SPO=0$ and 1 sampling patterns are

shown in Figure S1. Quantitative metrics are shown in Table S2. For each method, reconstruction accuracies of magnitude, $R2^*$ and QSM maps were progressively improved from sampling pattern SPO=0, 1 to 2. For each sampling pattern, TFF reconstruction consistently outperformed MoDL and LLR.

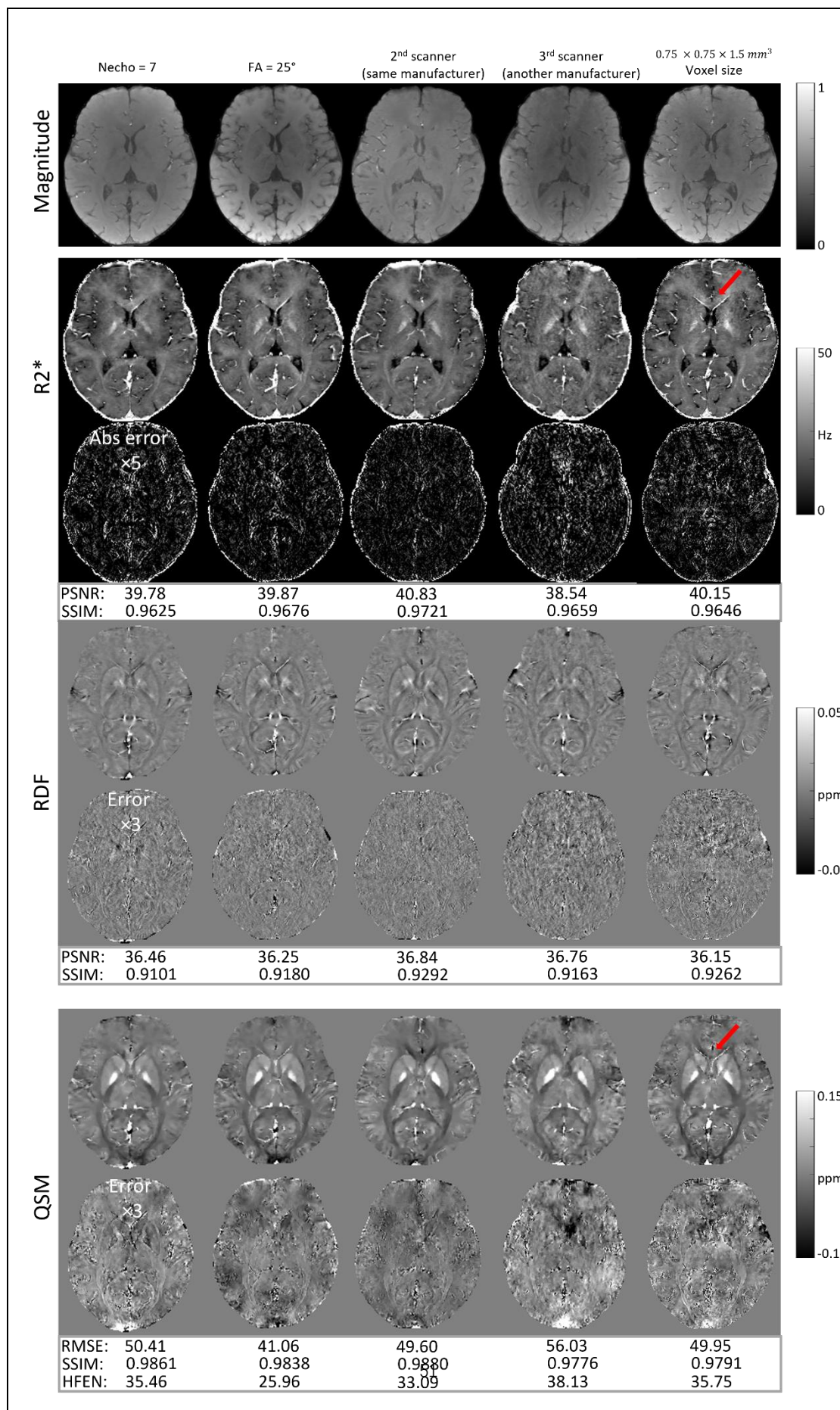


Figure 3.9. Generalization experiments of LARO with different imaging parameters retrospectively under-sampled by SPO=2 sampling pattern. Fully sampled reference of each test dataset was used to compute error maps and quantitative metrics. Magnitude images were not considered for quantitative comparison due to signal intensity variations among scans. LARO performed well without visible artifacts on test datasets with another flip angle (25°, 2nd column), number of echoes (7 echoes, 1st column) and a second MRI scanner from the same manufacturer (GE, 3rd column), but had moderate noise (red arrows in the last column) on another voxel size (0.75 × 0.75 × 1.5 mm³, last column) and moderate residual aliasing artifacts on a third MRI scanner from another manufacturer (Siemens, 4th column). Reconstructions on these datasets retrospectively under-sampled by SPO=1 and 0 were shown in Figures S6 and S7. For each test dataset, reconstruction performance was consistently improved from sampling pattern SPO=0, 1 to 2.

3.5.3 Synthetic k-space data

Ablation study

Reconstructed magnitude, R2*, RDF and QSM at one representative slice of MS test dataset are shown in Figure S2 with quantitative metrics of ablation study in Table S3.

Similar to the acquired k-space data, reconstruction accuracies were progressively improved as more modules were added. In Figure S2, putamen in QSMs (insets in

QSMs) were better depicted as more modules were added.

Performance comparison on MS dataset

Reconstructed magnitude, $R2^*$, RDF and QSM with SPO=2 sampling pattern (Figure 3.3b) in one representative slice are shown in Figure 3.6. LLR had much larger errors compared to MoDL and TFF. TFF slightly outperformed MoDL. Reconstructions with SPO=0 and 1 sampling patterns are shown in Figure S3. Quantitative metrics are shown in Table S4. Both TFF and SPO=2 outperformed other baseline reconstruction methods and sampling patterns.

Linear regressions of lesion-wise mean susceptibility values between fully sampled and reconstructed QSMs are shown in Figure S4. For SPO=0, 1 and 2, linear coefficients for TFF were 1.08, 0.96, and 0.97 with the highest R^2 : 0.95, 0.98 and 0.99 compared to LLR and MoDL under each sampling pattern. LLR had linear coefficients 1.13, 0.98, 0.95 with the lowest R^2 : 0.84, 0.81 and 0.92. MoDL had linear coefficients 1.20, 1.07 and 1.10 with R^2 in between: 0.89, 0.94 and 0.95. Both TFF and SPO=2 outperformed other baselines.

Performance comparison on ICH dataset

The pre-trained models were tested on the ICH patient data with acceleration factor $R = 4$ and compared. Reconstructed magnitude, $R2^*$, RDF and QSM in one representative slice containing hemorrhage are shown in Figure S5. LLR had the highest errors among the three methods. MoDL showed some errors (red solid

arrows) in QSMs which were not seen in TFF. Quantitative metrics show that both TFF and SPO=2 outperformed their baselines.

3.5.4 Prospective study

Prospectively under-sampled scans with acceleration factor $R = 8$ were acquired using the modified sequence (Figure 3.2) with sampling patterns SPO=0, 1 and 2. TFF reconstructions with different sampling patterns are shown in Figure 3.7, where SENSE reconstructions with $R = 2$ were used as reference. Depictions of white matter tracts in $R2^*$ maps (insets in $R2^*$ maps) were progressively improved from SPO=0, 1 to 2. Sharpness scores of perivascular spaces inside putamen (insets in QSMs) were 0.0270, 0.0111, 0.0247 and 0.0411 for SENSE, SPO=0, 1 and 2. LARO achieved comparable image quality with $R=2$ SENSE reference. LLR, MoDL and LARO reconstructions with SPO=2 sampling pattern (Figure 3.3a) are shown in Figure 3.8. LLR had the largest errors with heavy block-like artifacts. LARO outperformed MoDL in the depiction of white matter tracts in $R2^*$ maps (insets) and vein structures in QSMs (insets). ROI analyses are shown in Tables S5 and S6. In Table S5, with $R=2$ SENSE as reference, QSM under-estimations in SN, RN, CN and CC reconstructed by MoDL and TFF were observed when SPO=0 and 1 but were reduced or recovered when SPO=2. LLR had more deviations than MoDL and TFF. In Table S6, $R2^*$ over-estimations in GP, PU and CC were seen when SPO=0 and 1 but were recovered when SPO=2 for LLR, MoDL and TFF.

3.5.5 Generalization study

Reconstructions of different test datasets retrospectively under-sampled by SPO=2 were shown in Figure 3.9. Error maps and quantitative metrics were computed in R2*, RDF and QSM according to their fully sampled references except in magnitude due to signal intensity variations of different datasets. No visible artifacts were seen when applying the pre-trained reconstruction network to the datasets with another flip angle (25°, 2nd column), number of echoes (7 echoes, 1st column) and a second MRI scanner from the same manufacturer (GE, 3rd column). Moderate noise appeared (red arrows in the last column) when tested with another voxel size ($0.75 \times 0.75 \times 1.5 \text{ mm}^3$, last column), while moderate residual aliasing artifacts existed when tested with a third MRI scanner from another manufacturer (Siemens, 4th column). Reconstructions retrospectively under-sampled by SPO=0 and 1 were shown in Figures S6 and S7. For each test dataset, reconstruction performance was consistently improved from sampling pattern SPO=0, 1 to 2.

3.6 Discussion and Conclusion

In this work, we demonstrated the feasibility of learning a sampling pattern and reconstruction process specifically designed to accelerate the acquisition of multi-echo gradient echo data for the purpose of computing a susceptibility map (QSM). R=8 acceleration was achieved while maintaining QSM quality in both healthy

subjects as well as in an MS patient. Both retrospective and prospective acceleration was demonstrated. Finally, reconstruction performance was observed to be superior when compared to previously proposed acceleration techniques.

The original LOUPE [1]/LOUPE-ST [7] learned an optimized variable density sampling pattern from fully sampled single-echo k-space data. In the SPO=1 method in this work, LOUPE-ST was performed to learn a single optimized sampling pattern from fully sampled multi-echo k-space data and the obtained sampling pattern and reconstruction was applied to all echoes. The SPO = 2 method differs from SPO = 1 by learning a sampling pattern for each echo, allowing the introduction of additional sampling incoherency along echoes. LOUPE/LOUPE-ST (SPO = 1) outperformed manually designed variable density patterns (SPO = 0) in that LOUPE/LOUPE-ST optimized the sampling pattern variable density by learning a probabilistic density distribution in Eq. 3.4 that was updated during training to improve the reconstruction performance.

In this work, multi-echo sampling pattern optimization SPO = 2 (Eq. 3.3) was learned, achieving both optimized k-space variable density as in SPO = 1 and additional incoherency along echoes, which may result in better aliasing patterns for gradient echo images of different echoes that can be combined and compensated during reconstruction. SPO=2 sampling pattern distinguishes the proposed framework from another deep learning based mGRE acceleration method [53], where manually

designed 2D variable density sampling pattern (SPO=0) was applied, which may not be optimal for mGRE acquisition. We extend our conference paper [8] by implementing SPO = 2 sampling pattern into the existing mGRE sequence. The proposed multi-echo adaptive fan-beam ordered strategy (Figure 3.2a) prevented large changes in the phase and slice encodings between echoes within one TR, improving image quality [62, 63]. The prospective results in Figures 3.6 and 3.7 show the feasibility of achieving R = 8 factor acceleration using the modified mGRE sequence with QSM image quality comparable to R=2 SENSE.

Our reconstruction architecture (Figure 3.1) was based on unrolling a plug-and-play ADMM iterative scheme [55] and replacing the regularization step with a deep neural network denoiser. This idea is inspired by MoDL [50] where quasi-Newton iterative scheme was unrolled as a network architecture and a five-convolution-layer neural network denoiser was applied. In [53], a MoDL-like architecture (Figure 3.1 in [53]) was proposed but only one repetition of unrolling was applied. As reported in MoDL [50], more iterations/repetitions of the unrolled architecture helped improve reconstruction performance. We used $N_I = 10$ unrolled iterations same as MoDL to ensure good performance.

Recently, using convolutional neural networks to solve inverse problems related to multi-echo MRI signals has been explored in [11, 12, 14, 15, 64-67], where the established U-Net architecture [68] was always applied. LARO is novel here because

it introduces a TFF module (Figure 3.1c) to implicitly capture the multi-echo correlation and effectively compensate temporally incoherent aliasing patterns of the GRE echo signals when $SPO = 2$. The benefit of the TFF module was apparent in our ablation study (Figures 3.4 and S2, Tables S1 and S3) and comparison to MoDL (Figures 3.7, S1, S3 and S5). This distinguishes the proposed framework from [53] as well, since in [53] multi-echo images were only concatenated into channel dimension for convolution.

Pathologies such as hemorrhagic lesions which were not seen in the healthy training data were still effectively reconstructed by LARO and MoDL with low reconstruction error (2nd row in Figure S5). We speculate that the use of the data consistency module in the proposed method allows for accurate image reconstruction of pathologies not seen during training. Generalization experiments of LARO (Figures 3.9, S6 and S7) demonstrate that changing the flip angle, number of echoes or using a different scanner from the same manufacturer led to small image reconstruction errors. At the same time, using a smaller voxel size or a scanner from a different manufacturer led to a moderate increase in image noise (red arrows in the last column of Figure 3.9) or residual aliasing (4th column in Figure 3.9). One potential cause for the decreased performance when changing the voxel size is that it currently requires interpolating the optimal sampling pattern. For optimal performance, LARO may need to be retrained. It is however possible that fine-tuning the existing weights using

a small set of fully sampled data acquired with the new resolution may be sufficient, the details of which should be the subject of future research.

Despite the limitations, pre-trained sampling patterns from SPO=0, 1 to 2 consistently improved the reconstruction performance on all test datasets, which implies that for brain mGRE acquisition, the optimized k-space variable density distribution (Eq. 3.4) may be independent of the scanning parameters/manufacturers and can be generalized effectively. LARO is also independent of the number of receiver coil channels used for scan, as both TFF and denoiser networks are applied to the coil-combined image, which also improves the generalization ability of LARO.

For raw k-space data, fully sampled training dataset was only available on healthy volunteers because of long scan time (9:30 mins), which was not feasible on patients. To incorporate patients' dataset for training, an unrolled reconstruction network may be trained without fully sampled k-space data using self-supervised learning [69], where during training, one portion of the under-sampled k-space data is included in the data consistency module and the remaining k-space data is used in a forward model loss, which promises to achieve test results comparable to supervised training on fully sampled data. The reconstruction network of LARO may be enhanced by incorporating under-sampled patient data with such self-supervised learning strategy.

LARO is applied here to mGRE for accelerating QSM that is useful for studying

tissue magnetism [70], particularly paramagnetic iron [71], and is promising for assessing various diseases [72], such as multiple sclerosis [73]. The proposed combination of sampling and reconstruction optimization can be extended to other mGRE tasks with different organs, such as liver and cardiac QSM [74-76], or other quantitative imaging tasks, such as T1 [40] and T2 [41] mapping, where signal models based on Bloch equations are used to describe signal intensity changes over time. The proposed sampling strategy and temporal feature fusion may be useful to obtain better multi-contrast images. Furthermore, with the emergence of quantitative multi-parametric MRI [77], sampling and reconstructing multi-contrast images together in one sequence can be an effective strategy, since multi-contrast images that are intrinsically registered in one scan have redundancy in both spatial and temporal dimensions, which can be utilized to regularize the image series during reconstruction. Our future work will extend LARO to other mGRE and multi-contrast MRI tasks.

CHAPTER 4. mcLARO: MULTI-CONTRAST LEARNED ACQUISITION AND RECONSTRUCTION OPTIMIZATION FOR SIMULTANEOUS QUANTITATIVE MULTI-PARAMETRIC MAPPING

4.1 Abstract

A pulse sequence was developed by interleaving inversion recovery and T2 magnetization preparations and single-echo and multi-echo gradient echo acquisitions, which sensitized k-space data to T1, T2, T2* and magnetic susceptibility. The proposed mcLARO used a deep learning framework to optimize both the multi-contrast k-space under-sampling pattern and the image reconstruction based on image feature fusion. The proposed mcLARO method with $R = 8$ under-sampling was validated in a retrospective ablation study using fully sampled data as reference and evaluated in a prospective study using separately acquired conventionally sampled quantitative maps as reference standard. The retrospective ablation study showed improved image sharpness of mcLARO on the reconstructed images compared to the baseline network without multi-contrast sampling pattern optimization or image feature fusion, and negligible bias and narrow 95% limits of agreement on regional T1, T2, T2* and QSM values were obtained by the under-sampled reconstructions compared to the fully sampled reconstruction. The prospective study showed small or negligible bias and narrow 95% limits of

agreement on regional T1, T2, T2* and QSM values by mcLARO (5:39 mins) compared to reference scans (40:03 mins in total).

4.2 Introduction

For developing MRI pulse sequences and image reconstructions in fast quantitative multi-parametric mapping, in addition to T1 and T2 relaxation time, there has been an increasing interest in incorporating multi-echo gradient echo (mGRE) acquisition into multi-contrast sequences to allow T2* and quantitative susceptibility mapping (QSM) [78-80]. QSM [6] is a post-processing technique which estimates the tissue local field from the total field derived from the GRE phase data [43, 44] by applying background field removal [60] and performs the dipole field inversion to calculate the tissue susceptibility map [45]. In the brain, QSM can provide a quantitative measure of local susceptibility sources in both healthy and pathological tissues including endogenous deoxyheme and ferritin iron, myelin, and calcium, as well as exogenous gadolinium- or iron-based contrast agents [71, 81, 82]. QSM has been applied in multiple sclerosis [81], stroke and small vessel disease [83], and neurodegenerative disorders including amyotrophic lateral sclerosis [84], Parkinson's disease [85, 86] and Alzheimer's disease [87].

Recent works incorporating T2* and QSM into multi-parametric mapping include MP2RAGEME [78], Multitasking [79] EPTI [80] and BUDA-SAGE [88]. A common acquisition strategy of these methods is to combine magnetization

preparations (e.g., inversion recovery (IR) for T1 weighting and T2prep for T2 weighting) with an mGRE readout using k-space under-sampling. Images are reconstructed using parallel imaging methods such as SENSE [17] or GRAPPA [16], or low-rank denoising [89] and multitasking [77]. While promising, these methods suffer from relatively long scan time [78, 79], low SNR on QSM due to the short last echo time [79], and thick slices with limited coverage [80], which limits their clinical utility.

Recently, deep learning approaches have been applied to k-space under-sampling pattern optimization [1, 7], image reconstruction [2, 8, 9, 11, 50, 90, 91], biophysical inverse problems [12, 15, 65, 67, 92-94] and image post-processing [95-98] in MRI. For the under-sampling pattern optimization, LOUPE [1] and its extension LOUPE-ST [7] learned an optimal variable density k-space under-sampling pattern through back propagation, where a probabilistic density function of k-space data was updated to improve reconstructed image quality. For image reconstruction, MoDL [50] and VarNet [2] incorporated the parallel imaging forward model into the unrolled reconstruction networks, where convolutional denoisers were learned from fully sampled images to help reduce noise and aliasing artifacts from under-sampled reconstruction. In addition to the single-echo k-space imaging involved in the above methods, k-t imaging with multiple echoes, contrasts or frames has been accelerated using deep learning as well [8, 9, 52, 91].

In this work, we extend our prior work, learned acquisition and reconstruction optimization (LARO) [8, 9] for QSM acceleration, to the multi-parametric mapping acceleration by 1) developing an IR and T2-prepared single and multi-echo GRE sequence for simultaneous T1w, T2w and T2*w signal acquisition, 2) building a multi-contrast under-sampling pattern and unrolled image reconstruction network optimization for accelerated imaging, and 3) deriving T1 and T2 maps using dictionary matching and T2* and QSM maps using multi-echo GRE signal fitting. The resulting method is named mcLARO: Multi-Contrast Learned Acquisition and Reconstruction Optimization.

4.3 Method

4.3.1 Pulse sequence design

Figure 1a shows the proposed multi-contrast pulse sequence inspired by the MP2RAGEME [78] and 3D-QALAS [99, 100] designs. A module consisting of a non-selective inversion pulse followed by single-echo (N_{GRE} TRs) and multi-echo (N_{mGRE} TRs, each N_E echoes) GRE readouts was used to sensitize T1, T2* and magnetic susceptibility. A second module consisting of a T2prep pulse [101, 102] followed by a single-echo GRE readout was used for T2 relaxation measurement. Acquisition parameters for the proposed sequence are listed in Table S1.

4.3.2 *K-space sampling*

Similar to the prospective under-sampling strategy in LARO [9], a radial fan-beam sampling scheme [62] is used for both fully sampled and variable density under-sampled scans in the proposed sequence. During the fully sampled scan with 258×160 $k_y - k_z$ acquisition matrix, k-space locations are divided into 244 fan-beam segments with 128 TRs in each segment for one repetition of the sequence, yielding $(244 * 128)/(258 * 160) = 75.7\%$ elliptical k-space coverage to acquire fully sampled data. At each repetition, in-and-out (k-space center in the middle of the segment), reverse-centric (k-space center at the end of the segment), and centric (k-space center at the beginning of the segment) ordering strategies are applied to the inversion recovery (IR) prepped single-echo, multi-echo, and T2 prepped single-echo acquisitions, respectively. The total scan time of the fully sampled data is 34:30 mins. The under-sampling pattern follows the same fan-beam strategy with sparsely sampled k-space locations. An $R = 8$ under-sampling pattern was implemented into the proposed sequence with 40 repetitions, resulting in $(40 * 128)/(258 * 160) = 12.40\%$ sampling ratio with a total scan time of 5:39 mins. More details regarding the fan-beam sampling strategy can be found in Figure 2 in [9].

4.3.3 *Optimized multi-contrast reconstruction*

A deep ADMM network (Figure 2a) proposed in [9] is used for image reconstruction by unrolling an ADMM iterative scheme of multi-contrast images, where single and

multi-echo images are reconstructed together. A multi-contrast feature fusion module (Figure 2c) is proposed by extending the temporal feature fusion module in [9] to aggregate features across single-echo and multi-echo contrasts during reconstruction. First, the temporal feature fusion module proposed in [9] is used to extract the features of the multi-echo images s_j ($j = 1, 2, \dots, N_E$) for T2* and QSM, where a recurrent convolutional network including convolutional layers $N_m(\cdot)$ and $N_h(\cdot)$ for s_j and h_j is used to generate the j -th echo s_j 's hidden state feature h_j recurrently after Rectified Linear Unit (ReLU) activation:

$$h_j = \text{ReLU}\left(N_m(s_j) + N_h(h_{j-1})\right). \quad [4.1]$$

This recurrent network attempts to implicitly capture the echo dynamics and fuse features from the preceding echoes. Second, another convolutional layer $N_s(\cdot)$ is used to extract features of the single-echo images s_{N_E+1} , s_{N_E+2} and s_{N_E+3} , corresponding to the two inversion recovery and the single T2 prepared images, respectively:

$$h_{N_E+1:3} = N_s(s_{N_E+1:3}). \quad [4.2]$$

Finally, the feature maps of all echoes are updated by fusing h_j and $h_{N_E+1:3}$:

$$\begin{aligned} h_j &= h_j + h_{N_E+1} + h_{N_E+2} + h_{N_E+3} \quad (j = 1, 2, \dots, N_E), \\ h_{N_E+1:3} &= h_1 + h_{N_E+1:3}. \end{aligned} \quad [4.3]$$

After the multi-contrast feature fusion, all feature maps are concatenated along the channel dimension and fed into a denoising network based on U-Net [68] to generate

denoised multi-contrast images.

4.3.4 Optimized multi-contrast sampling pattern

A sampling pattern optimization module (Figure 2b) proposed in [9] is used to optimize an $R = 8$ under-sampling pattern for each echo from the fully sampled k-space data. This module updates the variable density of the under-sampling pattern by learning a probabilistic density distribution that the under-sampling pattern is generated from. Specifically, 2D variable density Cartesian sampling patterns in the $k_y - k_z$ plane as shown in Figure 2b are used to retrospectively under-sample the fully sampled k-space data during the sampling pattern optimization process, where for the j -th contrast ($j = 1, 2, \dots, N_E + 3$), learnable weights w_j generate a probabilistic density pattern P_j through sigmoid transformation with a slope parameter $a = 0.25$:

$$P_j(w_j) = \frac{1}{1 + e^{-a \cdot w_j}}. \quad [4.4]$$

Then a binary under-sampling pattern U_j is generated via stochastic sampling from P_j with indicator function $\mathbf{1}_x$ and sample z from uniform distribution on $[0, 1]$:

$$U_j(w_j) = \mathbf{1}_{z < P_j(w_j)}. \quad [4.5]$$

A straight-through estimator [26] is used to overcome the zero gradient problem when backpropagating through Eq. 2:

$$\frac{d\mathbf{1}_{z < P_j(w_j)}}{dw_j} \rightarrow \frac{dP_j(w_j)}{dw_j}. \quad [4.6]$$

4.3.5 Data acquisition and processing

All sequences were run on a 3T GE scanner with a 32-channel head coil. Fully sampled k-space data were acquired in 13 healthy subjects following an IRB approved protocol. Voxel size was $0.75 \times 0.75 \times 1 \text{ mm}^3$ with imaging parameters listed in Table S1. Coil compression [56] was applied to the original 32-coil k-space data, generating 8 virtual coils to save GPU memory. A coil sensitivity map was then estimated with ESPIRiT [36] using a centric $20 \times 20 \times 20$ self-calibration k-space region. Fully sampled multi-contrast images were computed by taking inverse Fourier transform of multi-coil k-space data and combining them using the obtained coil sensitivity maps to provide labels for network training and result validation. 8/1/4 subjects (2560/320/1280 2D coronal slices) were used as training, validation, and test datasets, respectively. K-space data were also retrospectively sampled on the same test subjects using the learned $R = 8$ under-sampling pattern.

Under-sampled k-space data were acquired in the same 4 test healthy subjects following an IRB approved protocol, using the same imaging parameters as above while using the under-sampling pattern obtained during training on the previous healthy subjects. The same data processing was applied to the prospectively under-sampled k-space data and used as additional test data.

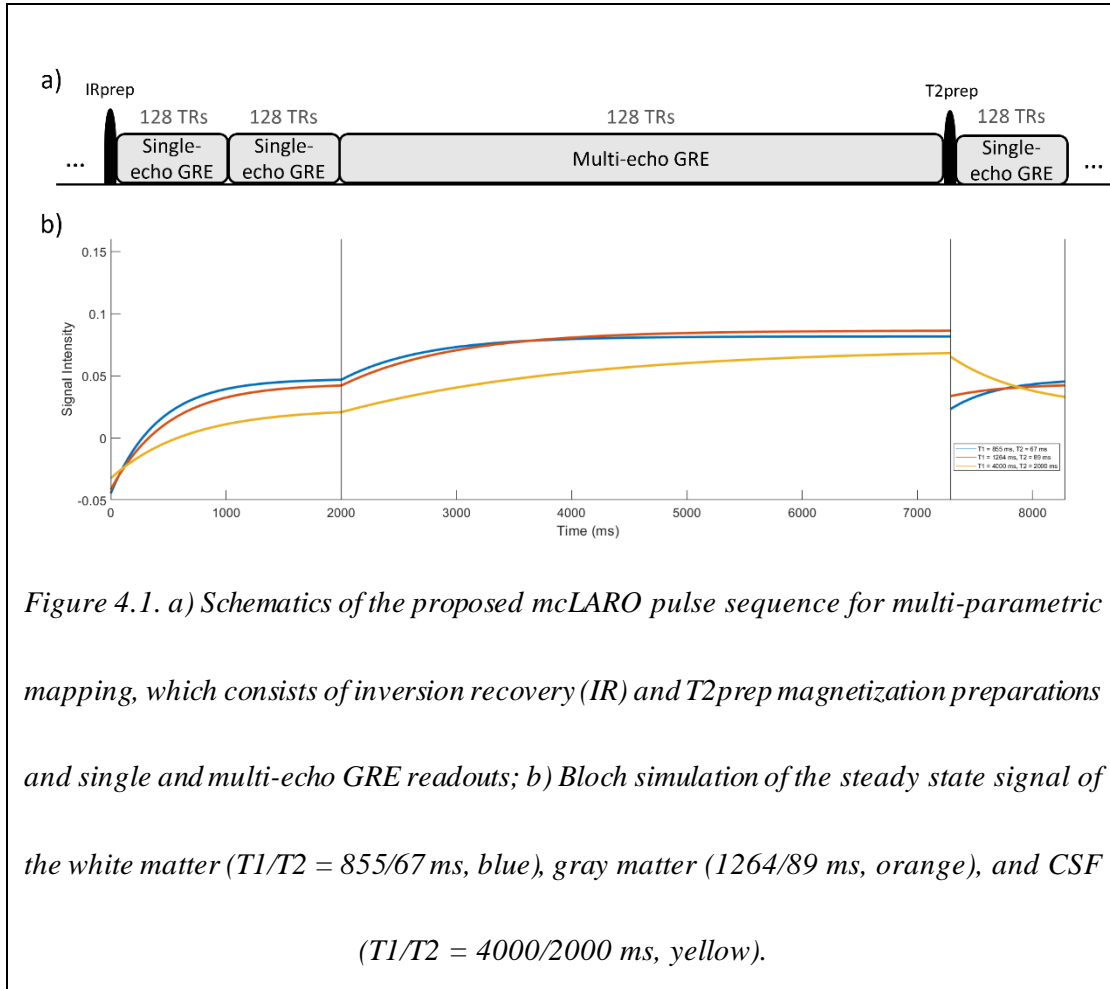
T1 and T2 maps were calculated by dictionary matching. The dictionary containing a 4-time-point transverse magnetization for the mCLARO sequence was generated using

a numerical Bloch simulation with sequence parameters in Table S1 (assuming on-resonance condition) and T1 values (ms) in [100:10:2000] and T2 values (ms) in [10:1:200]. QSM was calculated from the mGRE images through fitting the total field map [43, 44], removing background field [60], and solving dipole inversion [45]. T2* was calculated using the ARLO algorithm [58].

The training process consisted of two phases. In phase one, weights in the deep ADMM network and sampling pattern optimization module were updated simultaneously by maximizing a channel-wise structural similarity index measure (SSIM) [38]. In phase two, the pre-trained deep ADMM network from phase one was fine-tuned with fixed binary sampling patterns. We implemented the training in PyTorch using the Adam optimizer [37] (batch size 1, number of epochs 100 and initial learning rate 10^{-3}) on a RTX 2080Ti GPU.

4.3.6 Comparison and statistical analysis

An ablation study was conducted on the retrospectively under-sampled data to validate the efficacy of the multi-contrast feature fusion (Eq. 3) and the sampling pattern optimization of the three single-echo GRE acquisitions (Eq. 4) in mcLARO. We compared the ADMM reconstruction obtained without either of them (denoted as



“mcLARO=00”) with that obtained using only sampling pattern optimization (denoted as “mcLARO=01”) and that obtained using both (denoted as “mcLARO=11”). Multi-echo sampling pattern optimization and temporal feature fusion of mGRE images for T_2^* and QSM mapping, which had already been validated in LARO [9], were used in the ablation study. When the single-echo sampling pattern optimization was not applied, variable density sampling patterns were designed using a multi-level sampling scheme [57], where sampling pattern of each single-echo was generated independently from a manually designed probabilistic density function. A reference-free image blurriness metric [103] was used to measure reconstruction

quality (a score between 0 and 1, with lower indicating less blurring). For each test subject, the first single-echo image from the fully sampled scan was used to segment 114 regions of interest (ROIs) using FreeSurfer [104, 105]. Bland-Altman analyses [106] were performed to measure the agreement between the regional T1, T2, T2* and

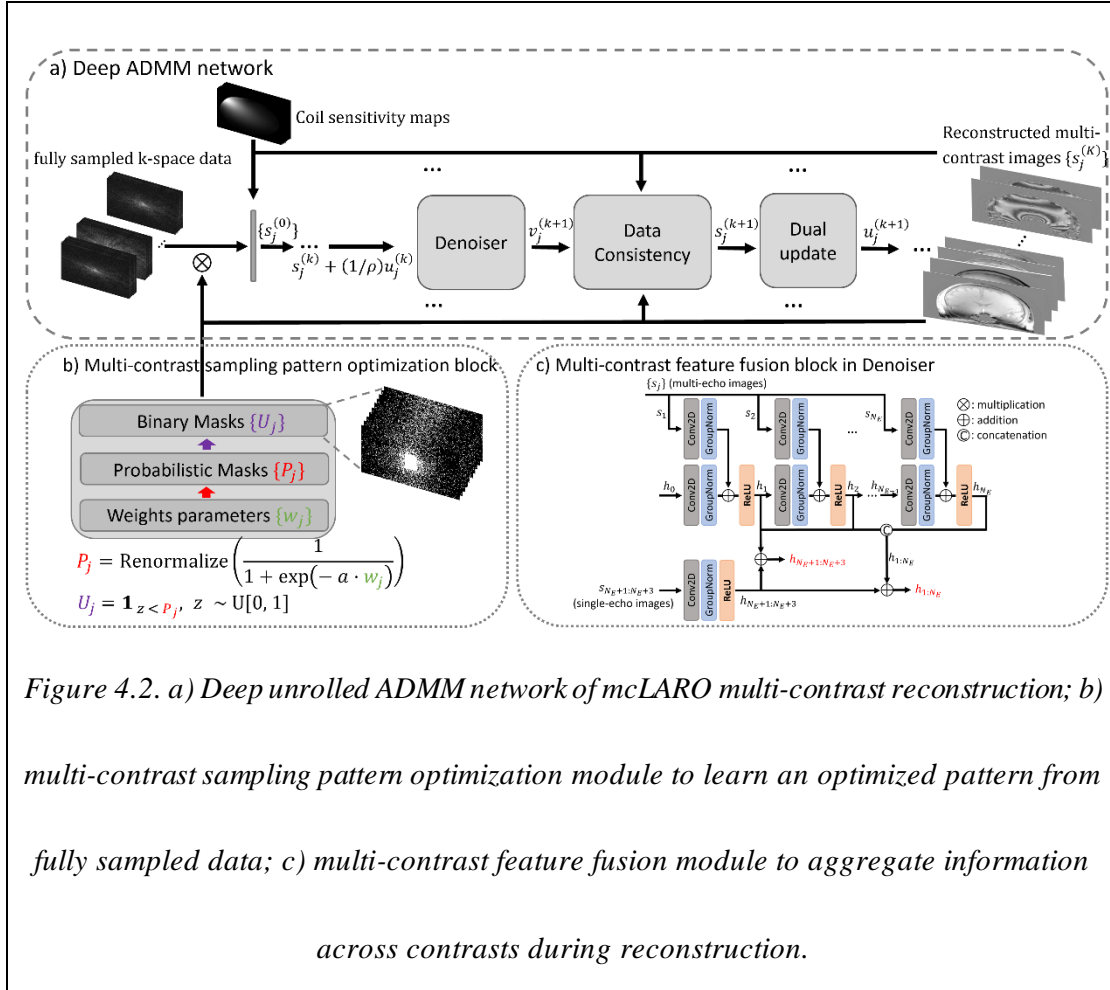


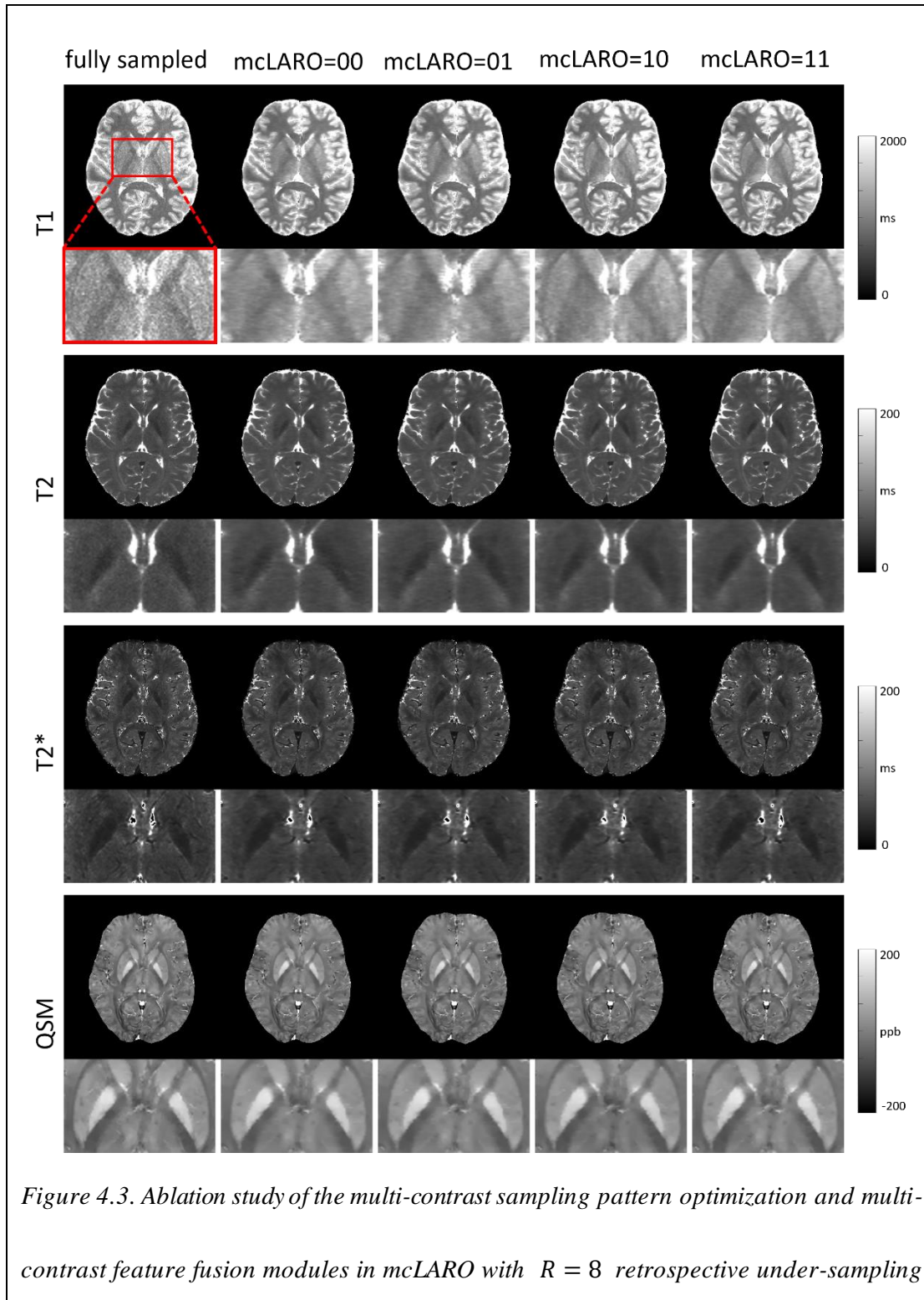
Figure 4.2. a) Deep unrolled ADMM network of mcLARO multi-contrast reconstruction; b) multi-contrast sampling pattern optimization module to learn an optimized pattern from fully sampled data; c) multi-contrast feature fusion module to aggregate information across contrasts during reconstruction.

QSM values obtained from the fully sampled and under-sampled reconstructions. Reference scans for T1, T2, T2* and QSM mapping were acquired separately using conventional sampling and compared to the mcLARO prospective experiment on the same four test subjects. The sequence parameters of the reference scans are summarized in Table S2. In each subject, 12 ROIs were manually drawn that were

contained in the slice coverage of the 2D reference scans, including anterior white matter, caudate nucleus, putamen, globus pallidus, substantia nigra, and red nucleus (one ROI in each hemisphere for each region). Bland-Altman analyses [106] were used to assess the agreement between the regional T1, T2, T2* and QSM values obtained with the reference scans and the prospectively under-sampled mcLARO scans.

4.4 Results

4.4.1 Retrospectively under-sampled ablation study

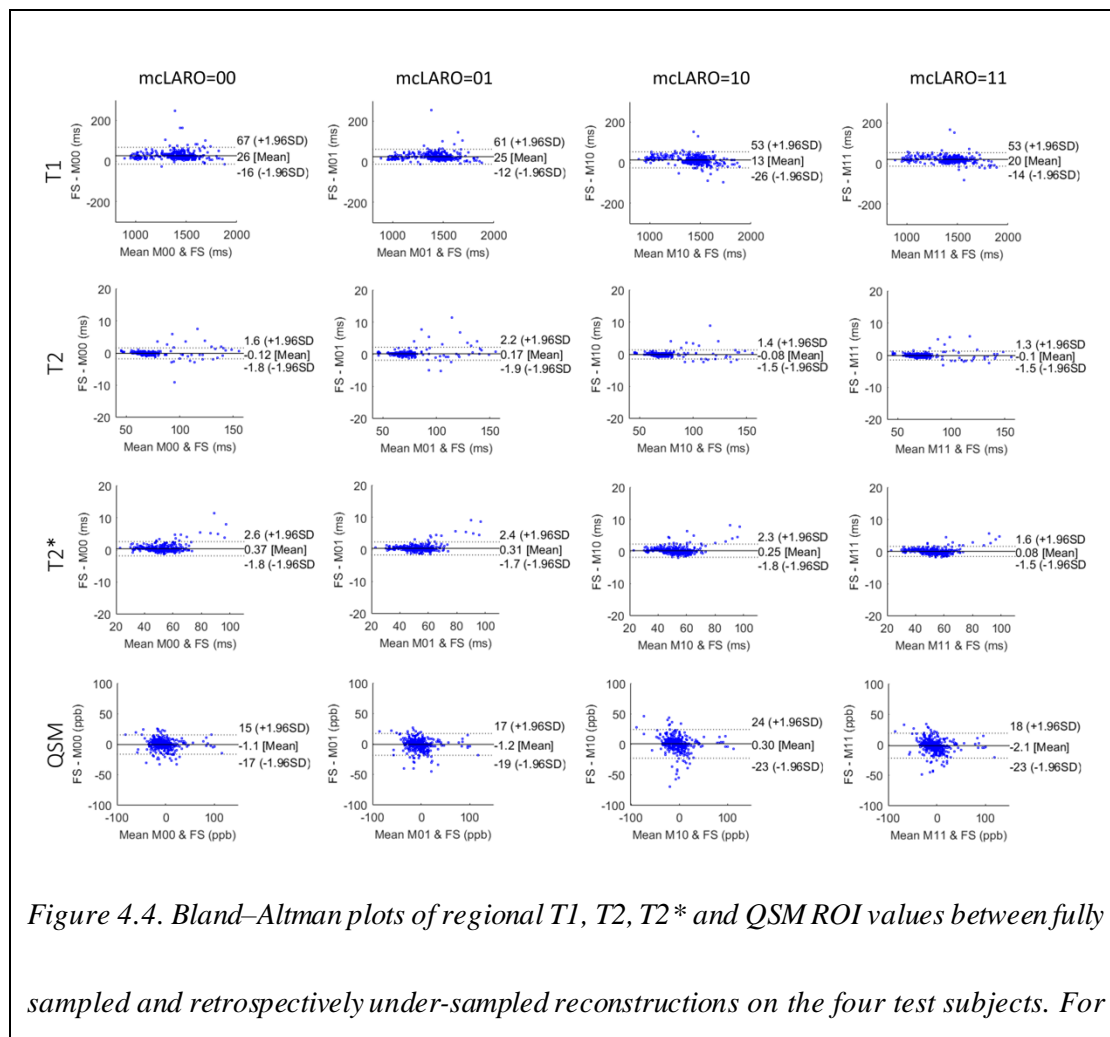


from the fully sampled data of one representative test subject. For T1 maps (1st row), the noise visible in the fully sampled reconstruction (1st column) was reduced in all under-sampled reconstructions (2nd to 5th columns). Deep grey matter regions in the zoomed in images were blurry without the two modules (mcLARO=00), but were progressively improved when the sampling pattern optimization (mcLARO=01), feature fusion (mcLARO=10) and combined (mcLARO=11) modules were applied. For T2 and T2 maps, noise in the fully sampled reconstruction was reduced in all under-sampled reconstructions. No visual differences were observed among under-sampled reconstructions of T2, T2* and QSM.*

Figure 4.3 shows an example of the quantitative maps obtained from the fully sampled and $R = 8$ retrospectively under-sampled reconstructions in one representative test subject. In the T1 map comparison (1st row), the moderate noise in the fully sampled T1 map (1st column) was reduced in the under-sampled T1 maps from the mcLARO ablation study (2nd to 4th columns). In the zoomed in T1 maps, the “mcLARO=00” reconstruction (2nd column, without the multi-contrast feature fusion or the sampling pattern optimization modules) showed blurry depictions of the putamen and thalamus. These depictions progressively improved as more modules were added in the “mcLARO=01” (3rd column, with the sampling pattern optimization module), “mcLARO=10” (4th column, with the multi-contrast feature fusion module) and “mcLARO=11” (5th column, with both modules) reconstructions.

The blurriness score of the fully sampled, mcLARO=00, mcLARO=01, mcLARO=10 and mcLARO=11 T1 maps were 0.24, 0.32, 0.31, 0.30 and 0.29, respectively, demonstrating improved image sharpness in the ablation study. For T2 and T2* maps (2nd and 3rd rows), the slight noise observed in the fully sampled maps was reduced in the under-sampled reconstructions. No visual differences were observed among under-sampled reconstructions of T2, T2* and QSM in the ablation study.

Figure 4.4 shows Bland–Altman plots of regional T1, T2, T2* and QSM values obtained with the fully sampled and under-sampled reconstructions from the four test



all the under-sampled reconstructions, negligible bias and narrow 95% limits of agreement were obtained (FS = Fully Sampled, M = mcLARO).

subjects. For all under-sampled reconstructions, negligible bias and narrow 95% limits of agreement were obtained.

4.4.2 Prospectively under-sampled reconstruction

Figure 4.5a shows $R = 8$ prospectively under-sampled mcLARO quantitative maps of one test subject (1st row) and reference scans (2nd row), demonstrating good visual agreement of all the quantitative maps obtained with mcLARO and reference scans. Please note that the visualized anatomy is only approximately similar as head motion may have occurred between acquisitions. Figure 4.5b shows Bland–Altman plots of regional T1, T2, T2* and QSM values obtained from the four test subjects,

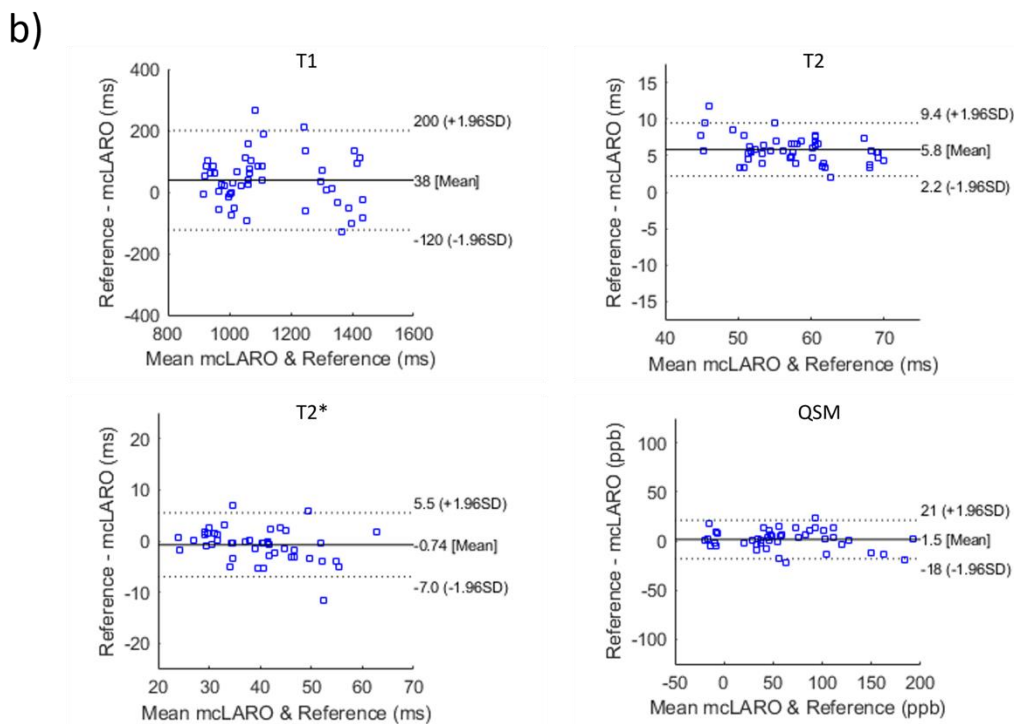
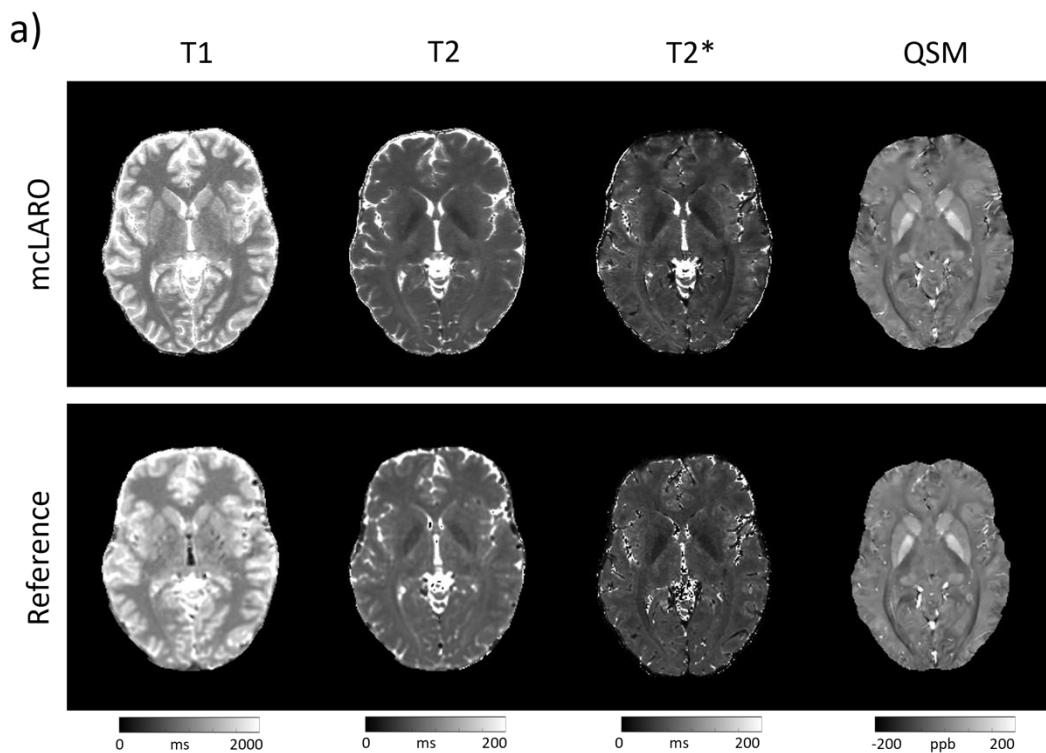


Figure 4.5. a) mcLARO and reference multi-parametric maps. Similar multi-parametric maps were derived from mcLARO compared to the reference. b) Bland–Altman plots of

regional T1, T2, T2 and QSM values obtained with the proposed mcLARO and reference methods from four test subjects. Small or negligible bias and narrow 95% limits of agreement were achieved by mcLARO.*

demonstrating small or negligible bias and narrow 95% limits of agreement.

4.5 Discussion and Conclusion

We developed mcLARO as a new learning-based framework for fast whole brain sub-millimeter T1, T2, T2* and QSM mapping in a single scan. Our ablation study showed the efficacy of the multi-contrast sampling pattern optimization and temporal feature fusion in mcLARO. Our prospective experiment showed comparable quantitative values of mcLARO in the selected ROIs with respect to the reference quantitative scans.

Based the LARO [9] method for mGRE sampling pattern optimization, the k-space sampling pattern in mcLARO, which included both single and multi-echo GRE acquisitions, was optimized independently for each echo and contrast. An optimized spatial incoherency of the learned sampling pattern in each echo was achieved by updating the probabilistic sampling density in Eq. 4 during back-propagation to minimize reconstruction error with respect to the fully sampled images. This was verified by our ablation study in Figure 4.3, where incorporating the sampling pattern optimization module improved the sharpness of the putamen and thalamus (4th and 5th columns of T1 maps in Figure 4.3).

Multi-contrast images acquired by the proposed sequence were naturally co-registered and shared similar structural information, which was utilized by the proposed multi-contrast feature fusion module in Figure 4.2c. Multi-echo feature fusion has been proposed in LARO [9] using a recurrent convolutional module. Based on LARO, multi-contrast image features from all the contrasts were similarly aggregated in mcLARO. Improved putamen and thalamus depiction (3rd and 5th columns of T1 maps in Figure 4.3) shows the effectiveness of the multi-contrast feature fusion. In addition, noise in the fully sampled images was suppressed in the reconstructed images (zoomed in images in Figure 4.3). This phenomenon may be explained by the noise2noise [107] experience in deep learning image restoration, where convolutional network is demonstrated to predict an averaged output from a training dataset with unbiased noise.

Prospective results in Figure 4.5 demonstrate that mcLARO in less than 6 minutes yielded comparable quantitative values to the reference quantitative scans. Compared to other quantitative multi-parametric mapping methods such as MP2RAGEME [78], MR Multitasking [79] and 3D QALAS [100], mcLARO uses a similar GRE-based IR and T2 prepped pulse sequence for contrast variations. The difference is that mcLARO is based on a learning-based framework for both sampling pattern and image reconstruction optimization. Learnable weights in mcLARO are updated to produce better spatial-temporal sampling incoherency, multi-contrast feature

aggregation and regularization to improve reconstruction quality under a high under-sampling ratio ($R = 8$). As a result, mcLARO achieves a whole brain sub-millimeter multi-parametric mapping in a shorter scan time compared to other methods, such as MP2RAGEME ($R = 2.89$) [78] and 3D-QALAS ($R = 1.7$) [100]. Recently, multi-contrast images in 3D-QALAS were reconstructed using model-based deep learning [91] where acceleration was pushed to $R = 12$. Our method differs in that additional multi-echo GRE is available and a sampling pattern is learned for each contrast. Future work includes pushing mcLARO acceleration to higher under-sampling ratio, such as $R = 12$.

There are some limitations of mcLARO. First, only a limited number of echoes are acquired to capture contrast variation due to magnetization relaxation (Figure 4.1a). A more suitable way may be time-resolved sampling, such as in MR Multitasking [79] and 3D-EPTI [108], where k-space centers are acquired more frequently to capture the variation. Deep learning has been used for time-resolved imaging with subspace learning [109]. Future work may include applying time-resolved acquisition and deep subspace reconstruction to mcLARO. Second, the long scan time of the fully sampled data in mcLARO may introduce motion artifacts, including motion blurring[110].

Self-supervised learning via training directly on under-sampled data may replace the possibly motion-corrupted fully sampled labels [69], but direct motion estimation may be needed to reducing blurring[111]. Future work includes exploring self-supervised

learning strategies in mcLARO. Third, the study subject sample size is very limited. mcLARO prospective study was not applied to patients with pathology not seen in training. The study organ was limited to the brain, and body QSM would require chemical shift correction[112], in addition to motion compensation. Future work also includes testing the generalization ability of mcLARO in organs outside the brain and on patients with new pathology.

CHAPTER 5. FINE: FIDELITY IMPOSED NETWORK EDIT FOR SOLVING ILL-POSED IMAGE RECONSTRUCTION

5.1 Abstract

Deep learning (DL) is increasingly used to solve ill-posed inverse problems in medical imaging, such as reconstruction from noisy and/or incomplete data, as DL offers advantages over conventional methods that rely on explicit image features and hand engineered priors. However, supervised DL-based methods may achieve poor performance when the test data deviates from the training data, for example, when it has pathologies not encountered in the training data. Furthermore, DL-based image reconstructions do not always incorporate the underlying forward physical model, which may improve performance. Therefore, in this work we introduce a novel approach, called fidelity imposed network edit (FINE), which modifies the weights of a pre-trained reconstruction network for each case in the testing dataset. This is achieved by minimizing an unsupervised fidelity loss function that is based on the forward physical model. FINE is applied to two important inverse problems in neuroimaging: quantitative susceptibility mapping (QSM) and under-sampled image reconstruction in MRI. Our experiments demonstrate that FINE can improve reconstruction accuracy.

5.2 Introduction

Image reconstruction from noisy and/or incomplete data is often solved with regularization of various forms, which can be formulated as maximum a posteriori (MAP) probability estimation [113]. Traditionally, these regularizations promote desired properties with explicitly extracted image features, such as image gradients or wavelet coefficients [114-117]. Deep learning (DL) using a convolutional neural network (CNN) of many layers has demonstrated superior capability in capturing image features compared to explicit feature extraction and achieved tremendous success in a wide range of computer vision applications [118, 119][cite]. Accordingly, CNNs have recently been used in image reconstruction [120-122].

A fundamental concern on the performance of a trained DL model in predicting outcome for previously unseen test data is the generalization error [123]. While CNNs can perform well with low generalization errors, their robustness remain concerning, with open questions [124], including their susceptibilities to adversarial attacks [125]. Considering image reconstruction as a very high dimensional regression task, generalization errors may inevitably occur at some voxels in CNN based image reconstruction. It is therefore important to investigate the performance of CNN-based image reconstructions when test data deviate from training dataset, due to for example abnormal morphology or the presence of pathology, or when test data contains adversarial noise.

To improve the robustness of network-based image reconstructions, the use of the underlying physical model of the forward problem has been explored. One approach is to use the network output as a regularization in the standard MAP optimization reconstruction of the test data [126], which maintains data fidelity of the test data but may suffer when the network output is not sufficiently close to the true solution.

Another approach is to incorporate the physical model into the network architecture [3, 127], which can improve reconstruction accuracy and reduce generalization error.

In this paper, building on the U-Net architecture [25] as the reconstruction network, we propose to update the weights of a pre-trained U-Net for each case in the test dataset by minimizing an unsupervised fidelity loss function. The fidelity loss is defined according to the forward physical model and data noise property. We refer to this method as fidelity imposed network edit (FINE). We report FINE results on two neuroimaging reconstruction problems using U-Net, quantitative susceptibility mapping (QSM) [128] and MRI reconstruction from under-sampled k-space data.

5.3 Theory

A major challenge in medical image reconstruction is to invert an ill-posed system matrix A of a known physical process in the presence of data noise n :

$$y = Ax + n, \tag{5.1}$$

where x is the desired image and y the measured data. For example, in QSM, the

dipole kernel is zero on the cone surface defined by the magic angle, making the inversion from measured magnetic field to susceptibility source ill-posed [45, 128, 129]. In under-sampled image reconstruction, the sampling mask contains many zeroes, making reconstruction of under-sampled data ill-posed. Additional prior knowledge is required to obtain a solution. The MAP inference approach provides an optimal estimation according to the measured data noise property and prior knowledge. Gaussian noise is observed in MRI complex data and is a widely-used approximate model for various other data. This leads to the common Bayesian reconstruction under Gaussian noise:

$$\hat{x} = \underset{x}{\operatorname{argmin}} \frac{1}{2} \|W(Ax - y)\|_2^2 + R(x), \quad [5.2]$$

where W is the square root of the inverse of the noise covariance matrix, $R(x)$ is a regularization term that characterizes prior knowledge. The first term in Eq.2 is referred to as data fidelity. Eq.2 can be solved using numerical optimization procedures, such as the quasi-Newton method that iteratively linearizes the problem with each linear problem solved by the conjugate gradient method. Common choices for $R(x)$ include sparsity enforcement, such as Total Variation (TV) [27] or the L1 norm in an appropriate wavelet domain [28]. These types of priors are critical for solving the ill-posed inverse problem. However, they can also limit the quality of the reconstruction, such as introducing artificial blockiness.

Fundamentally, regularization promotes desired image features, for which DL may be better suited than conventional explicit feature extraction. A data-to-image neural network model $\phi(\cdot; \Theta_0)$ with Θ_0 the network weights can be trained in a supervised fashion based on training data consisting of pairs $\{\alpha_i, \beta_i\}$, with α_i the ground-truth image and β_i the input data. The weights at each convolutional layer, along with non-linear activation functions, may be regarded as a collection of feature extractors for the desired image reconstruction [118, 130]. The large number of weights in DL may explain its advantage over explicit feature extraction that uses a single or few weights [131, 132]. Given a case in the test dataset or a test data point y , one can use this model to compute a reconstruction by evaluating the model on the observed measurement vector:

$$\hat{x} = \phi(y; \Theta_0). \quad [5.3]$$

The supervised learning strategy described above may perform poorly if there is a structural change in the test data, such as a certain pathology that is not present in the training dataset. To improve the robustness of DL-based reconstruction, it has been proposed to treat the network output in Eq. 3 as a regularization in Eq. 2 penalizing the L2 difference between the network output and the final optimized solution [126]:

$$\hat{x} = \underset{x}{\operatorname{argmin}} \frac{1}{2} \|W(Ax - y)\|_2^2 + \lambda \|x - \phi(y; \Theta_0)\|_2^2. \quad [5.4]$$

We refer to this reconstruction as DL with L2 regularization (DLL2). In another

recently proposed approach, the physical model is incorporated into the network architecture solving a quasi-newton optimization scheme [3, 127].

In this paper, we use a U-Net model as the reconstruction network and propose to exploit the data fidelity term directly in adapting the model through backpropagation without any explicit supervision. Specifically, the desired image x is reconstructed by editing the weights of a pre-trained U-Net under the guidance of data fidelity for a given test data point y . The network weights Θ are initialized with Θ_0 (obtained with supervised training) and are updated using the physical model of the imaging system as follows:

$$\hat{\Theta} = \operatorname{argmin}_{\Theta} L(y; \Theta) = \|W(A\phi(y; \Theta) - y)\|_2^2. \quad [5.5]$$

Then the output of the updated network is the reconstruction of x with both data fidelity and deep learning regularization:

$$\hat{x} = \phi(y; \hat{\Theta}). \quad [5.6]$$

We refer to this approach as “fidelity imposed network edit (FINE)” for solving an ill-posed inverse problem using deep learning and imaging physics.

5.4 Method

In this paper, we applied the proposed FINE to two inverse problems in MRI: QSM and under-sampled image reconstruction. Data were acquired following an IRB

approved protocol. All images used in this work were de-identified to protect privacy of human participants. Data and code are available to interested researchers upon request.

5.4.1 QSM

First, we applied FINE to QSM [128], which is ill-posed because of zeroes at the magic angle in the dipole kernel. Consequently, streaking artifacts appear in the image domain after un-regularized dipole inversion [129]. The Bayesian approach has been widely used to address this issue. One example is the Morphology Enabled Dipole Inversion (MEDI) method [45], which employs the following cost function:

$$\hat{\chi} = \underset{\chi}{\operatorname{argmin}} \frac{1}{2} \|W(d * \chi - f)\|_2^2 + \lambda \|M_G \nabla \chi\|_1, \quad [5.7]$$

with χ the susceptibility distribution to solve, f the field measurement, d the dipole kernel. The regularization is a weighted total variation, with ∇ the gradient operator, M_G a binary edge mask determined from the magnitude image [45] which enforces morphological consistency between magnitude and susceptibility.

Data acquisition and pre-processing

MRI was performed on 6 healthy subjects using a 3T system (GE, Waukesha, WI) with a multi-echo 3D gradient echo (GRE) sequence. Detailed imaging parameters included FA = 15°, FOV = 25.6 cm, TE1 = 5.0 ms, TR = 39 ms, #TE = 6, ΔTE = 4.6 ms, acquisition matrix = 256×256×48, voxel size = 1×1×3 mm³, BW = ±62.5 kHz.

The local tissue field was estimated using non-linear fitting across multi-echo phase data [116] followed by graph-cut based phase unwrapping [133] and background field removal [60]. GRE imaging was repeated at 5 different orientations per subject for COSMOS reconstruction [134], which was used as the gold standard for brain QSM.

A second data set was obtained by performing GRE MRI on 8 patients with intracerebral hemorrhage (ICH) and 8 patients with multiple sclerosis (MS) at the standard supine orientation. ICH patient data was acquired using the same scanner and imaging parameters as above. MS patient data was acquired using a 3T system (Magnetom Skyra, Siemens Healthcare, Erlangen, Germany) and imaging parameters included $FA = 15^\circ$, $FOV = 24.0$ cm, $TE_1 = 6.69$ ms, $TR = 49$ ms, $\#TE = 10$, $\Delta TE = 4.06$ ms, acquisition matrix = $256 \times 256 \times 48$, voxel size = $1 \times 1 \times 3$ mm³, $BW = 260$ Hz/Px.

A third data set was obtained by resampling the 2016 QSM challenge data [135] to $1 \times 1 \times 3$ mm³ voxel size to be consistent with our experimental setting.

A final data set was obtained by simulating 6 ICH brains. This was done by segmenting 6 hemorrhagic lesions from the patients of the second data set above (reconstructed using MEDI) and combining it with the 6 susceptibility maps from the multi-orientation data set described above (reconstructed using COSMOS). The corresponding local fields were generated using the dipole convolution forward

model, followed by adding Gaussian noise.

Dipole inversion network

We implemented a 3D U-Net [4, 136], a fully convolutional network architecture, for mapping from the local tissue field f to susceptibility distribution. The convolutional kernel size was $3 \times 3 \times 3$. 5 of the 6 healthy subjects with COSMOS data were used for training, with augmentation by in-plane rotation of $\pm 15^\circ$. Each 3D volume data was divided into patches of size $64 \times 64 \times 32$, giving a total number of 12025 patches for training. 20% of these patches were randomly chosen as a validation set during training. We employed the same combination of loss function as in [4] in training the network with Adam optimizer [37] (initial learning rate: 10^{-3} , epochs: 40), resulting in a 3D U-Net $\phi(\cdot; \Theta_0)$.

Fidelity Imposed Network Edit (FINE) for QSM

After pre-training the network using 3D patches described above, for a given test data, a whole local field volume f was fed into the network, and the network weights Θ_0 from pre-training were used to initialize the following minimization:

$$\hat{\Theta} = \underset{\Theta}{\operatorname{argmin}} \|W(d * \phi(f; \Theta) - f)\|_2^2. \quad [5.8]$$

This minimization essentially fine-tuned the pre-trained dipole inversion network $\phi(f; \Theta)$ to produce an output adapted for a given test field data f that is consistent with the forward dipole model. Eq. 8 was minimized using Adam [37] with

initial learning rate 10^{-4} . FINE was stopped when the relative change of the unsupervised fidelity loss between two consecutive iterations fell below 5×10^{-3} .

The final reconstruction of the fine-tuned network was $\hat{\chi} = \phi(f; \hat{\Theta})$.

FINE was compared with MEDI (Eq. 7) with $\lambda = 0.001$ [45] and with DLL2 (Eq. 4):

$$\hat{\chi} = \underset{\chi}{\operatorname{argmin}} \frac{1}{2} \|W(d * \chi - f)\|_2^2 + \lambda_2 \|\chi - \phi(f; \Theta_0)\|_2^2, \quad [5.9]$$

with $\lambda_2 = 0.01$.

Data analysis

Root mean square error (RMSE), which measures general reconstruction error, high-frequency error norm (HFEN), which measures the similarity at high spatial frequencies [61], and structural similarity index (SSIM), which quantifies image intensity, structural and contrast similarity between pairs of image patches [38], are used to quantify reconstruction accuracy on data with COSMOS or synthetic ground truth. For the healthy subjects, cross-validation was performed in which each COSMOS brain was selected as test data, leaving the other 5 brains as training dataset, resulting in 6 pre-trained U-Nets. U-Net trained by the first 5 healthy subjects was applied to the remaining experiments. For the MS patients, lesions were manually segmented by an experienced neuroradiologist (S.Z.) based on the corresponding T2FLAIR maps which were spatially registered to the magnitude of the GRE data. Deming regression [137] of all lesion mean values across patients were employed

between MEDI and the other three methods to get each pair’s linear relationship. For ICH patients, hemorrhagic lesions were segmented manually and their mean susceptibilities for each reconstruction method were calculated and compared. A reference-free metric to measure the blurring in images [138] was used to quantify tissue susceptibility reconstruction quality surrounding each hemorrhage (scores between 0 and 1, the less the better in terms of blur perception). For simulated ICH brains, the reconstructed QSM was compared with synthetic ground truth in terms of RMSE, HFEN and SSIM.

5.4.2 Under-sampled reconstruction

Second, we applied FINE to MRI reconstruction with under-sampled data. T2 weighted (T2w) images were retrospectively under-sampled. A compressive sensing reconstruction using Total Variation (TV) regularization was used to reconstruct images from the under-sampled k-space data:

$$\hat{u} = \underset{u}{\operatorname{argmin}} \|UFu - b\|_2^2 + \lambda \|\nabla u\|_1, \quad [5.10]$$

where U is the binary k-space under-sampling pattern, F the Fourier Transform operator, b the measured under-sampled k-space data, ∇ the 2D gradient operator, λ a regularization parameter and u the image to be solved.

Data acquisition and pre-processing

We obtained real-valued T2w axial images of 237 MS patients and 5 glioma patients,

with 256×184 matrix size and $1mm^2$ resolution. For each MS patient, we extracted 50 axial 2D images from each volume, giving a total number of 11850 images. For 5 glioma patients, we extracted 44 images with glioma tumors. The intensity range of each image was normalized to range $[0, 1]$. We obtained complex-valued T2w sagittal images of fully-sampled subjects used in MoDL [3] as another dataset for experiments, with 256×232 matrix size and $1mm^2$ resolution. A natural image dataset [139] resized to 256×184 , which contained coast, forest highway, city center, mountain, open country, street and tall building images, was also used in our experiments as another training data set.

Under-sampled reconstruction network

2D U-Net [25] was used as the network architecture for mapping from $A^H b$ (where $A = UF$ is the system matrix) to a fully sampled T2w image, where U was chosen as a variable-density Cartesian random sampling pattern [140]. Two 2D U-Nets were employed, one for real-valued image reconstruction and the other for complex-valued image reconstruction, with complex-valued images represented by two separate real and imaginary channels, similar to [120]. The network was trained using a 3×3 convolutional kernel. We used the L_1 difference between the network output and target image as the loss function and the Adam optimizer [37] (initial learning rate: 10^{-3} , epochs: 100). For real-valued image reconstruction, 8800 images from 176 MS patients were used for training and 2200 images from 44 MS patients were used for

validation. 850 images from the remaining 17 MS patients and 44 images with tumor from glioma patients formed two test datasets. A variable-density sampling pattern in real-valued dataset was generated with acceleration factor 3.24. For complex-valued image reconstruction, we used the same training/test dataset as in MoDL [3], yielding training data dimensions in rows \times columns \times slices \times coils as $256 \times 232 \times 360 \times 12$ and test data dimensions as $256 \times 232 \times 160 \times 12$. The same variable-density sampling patterns used in MoDL [3] were applied here, resulting in an acceleration factor of 6. We used the same symbol $\phi(\cdot; \Theta_0)$ to represent both trained 2D U-Nets for conciseness.

Fidelity Imposed Network Edit (FINE) for under-sampled reconstruction

Test data b for a test subject was obtained by under-sampling an axial T2w image of the subject using the same sampling pattern as in the pre-training step. Similar to Eq. 8, we initialized the network weights Θ using Θ_0 and updated them using the following minimization:

$$\hat{\Theta} = \underset{\Theta}{\operatorname{argmin}} \|UF\phi(A^H b; \Theta) - b\|_2^2, \quad [5.11]$$

which was solved using Adam with initial learning rate 10^{-4} . FINE was stopped when the relative change of the data fidelity between two consecutive iterations fell below 10^{-4} . The final FINE reconstruction for the T2w image was $\hat{u} = \phi(A^H b; \hat{\Theta})$.

FINE reconstruction was compared with TV (Eq. 10) with $\lambda = 0.001$, U-Net, and

DLL2 (Eq. 4):

$$\hat{u} = \underset{u}{\operatorname{argmin}} \frac{1}{2} \|UFu - b\|_2^2 + \lambda_2 \|u - \phi(A^H b; \Theta_0)\|_2^2, \quad [5.12]$$

with $\lambda_2 = 0.01$, and MoDL with 10 repetitions of sub-blocks [3].

Data analysis

Peak signal-to-noise ratio (PSNR) and SSIM are used to quantify reconstruction accuracy on all data. To test the stability of FINE with respect to the choice of network structure and optimizer details, we repeated FINE reconstructions with different initial learning rates (2×10^{-4} and 5×10^{-5}), a second solver, RMSprop [141], and a second network structure, consisting of 5 convolutional layers with 32 channels in layers 2-4 and ReLU activations. To test the dependency of FINE's performance on the initial training dataset, we pre-trained multiple networks on either natural or MR images with a range of training sizes. To test the generalization ability of FINE compared to MoDL with respect to various test data noise levels, we applied FINE and MoDL to the MS test dataset with simulated Gaussian noise described above. To test the stability of FINE against adversarial attacks, we constructed various levels of adversarial noise following [142] and compared TV regularization reconstruction, U-Net, and FINE - the proposed method. Different levels of adversarial noise were selected from the intermediate solutions during the adversarial noise construction procedure as proposed in [142].

5.5 Results

5.5.1 QSM

Healthy subjects

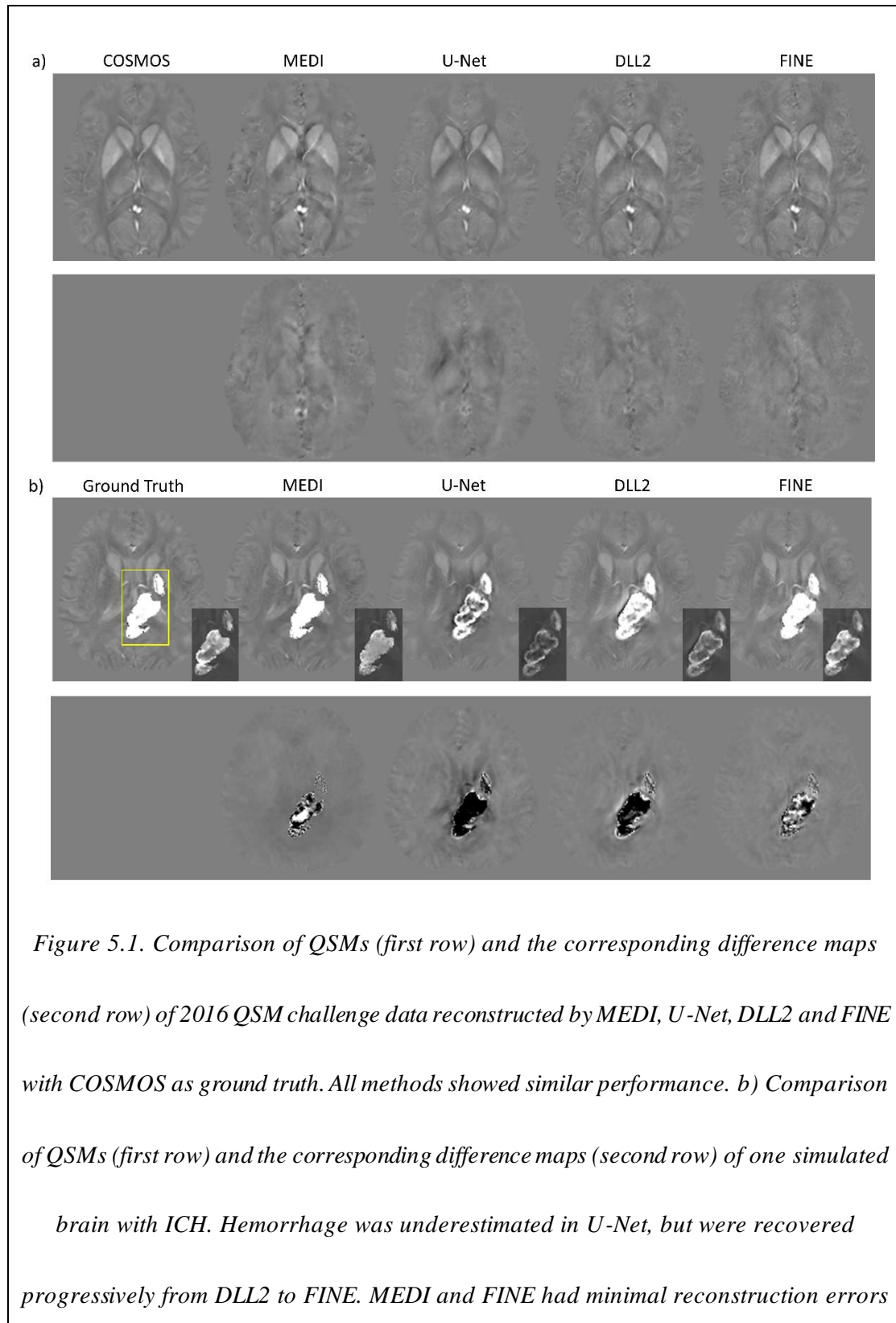
QSMs of 2016 QSM challenge data reconstructed by MEDI, U-Net, DLL2 and FINE are displayed in Figure 5.1a, with COSMOS as ground truth. The RMSE was 69.08, 74.19, 53.34 and 53.44, for MEDI, U-Net, DLL2 and FINE respectively. The corresponding SSIM was 0.9060, 0.9321, 0.9503 and 0.9483, respectively. The corresponding HFEN was 70.25, 65.47, 50.21 and 51.00, respectively. Figure 5.2 shows the median relative change of the weights per layer in U-Net structure between Θ of FINE and Θ_0 of U-Net reconstruction in Figure 5.1a. In this case, FINE changed predominantly the weights in high-level layers of U-Net (layers 1 through 5 and layers 17 through 21). Quantitative metrics averaged among cross-validation experiments on COSMOS dataset are shown in Table 5.1, with FINE demonstrating consistently good performance.

Simulated ICH brains

QSMs of one simulated brain with ICH reconstructed by MEDI, U-Net, DLL2 and FINE are displayed in Figure 5.1b, with the simulated brain as ground truth.

Hemorrhage was underestimated in U-Net, but were recovered progressively from DLL2 to FINE. MEDI and FINE had minimal reconstruction errors among all four methods. Quantitative metrics of all 6 simulated brains are shown in Table 5.2, with

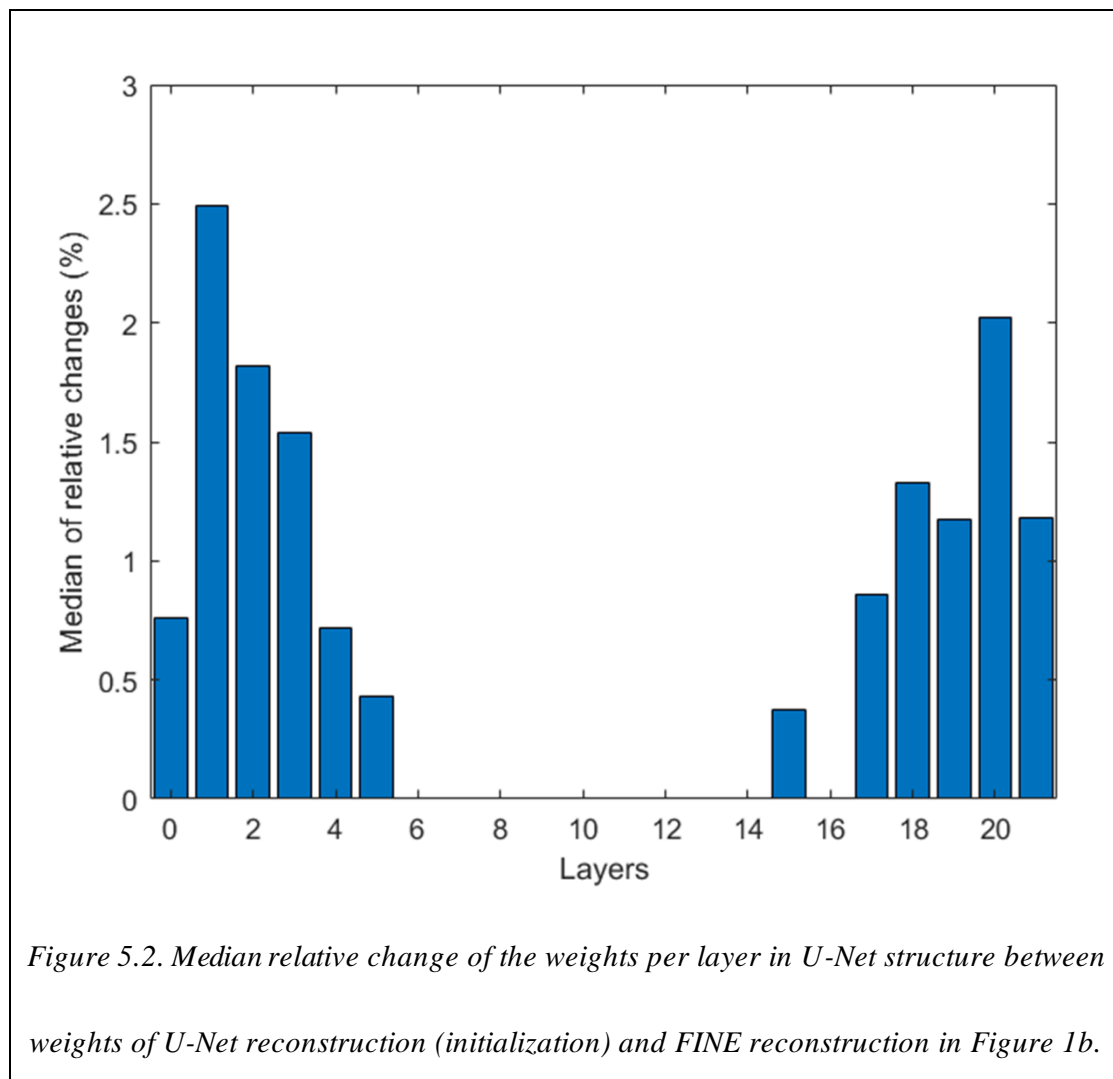
FINE demonstrating one of the best performances. Mean susceptibility values (ppm)



among all four methods. All images were displayed using a [-0.3, 0.3] ppm window except in insets in the third row, which used [-0.6, 1.5] ppm.

of hemorrhage lesions on 6 simulated ICH brains from each reconstruction method and ground truth were calculated, giving mean susceptibility values \pm standard deviations: 0.57 ± 0.10 , 0.27 ± 0.05 , 0.41 ± 0.07 , 0.60 ± 0.11 and 0.64 ± 0.10 for MEDI, U-Net, DLL2, FINE and ground truth, respectively.

MS patients



FINE changed predominantly the weights in high-level layers of U-Net (layers 1 through 5 and layers 17 through 21).

QSMs reconstructed by MEDI, U-Net, DLL2 and FINE for two representative MS patients are displayed in Figure 5.3a. MS lesions were depicted using four methods (solid arrows). Compared to MEDI, U-Net reconstruction showed reduced lesion contrast, which was improved using DLL2 and FINE. Deming regression of lesion susceptibilities between MEDI and each of the other three methods are shown in Figure 5.3b. Regression slopes for FINE (1.05, $R^2=0.8$) and DLL2 (0.96, $R^2=0.79$) were closer to unity than for U-Net (0.88, $R^2=0.74$). In addition, the fine structure of

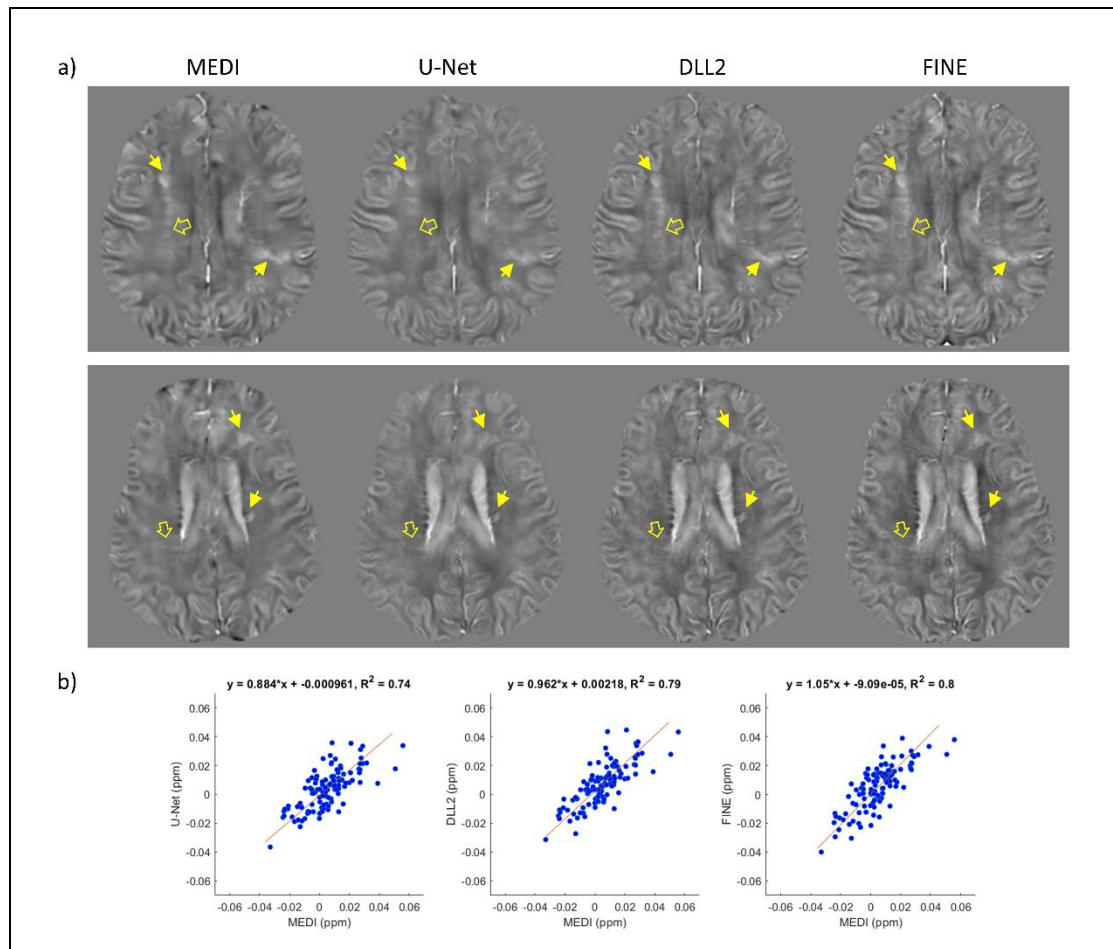
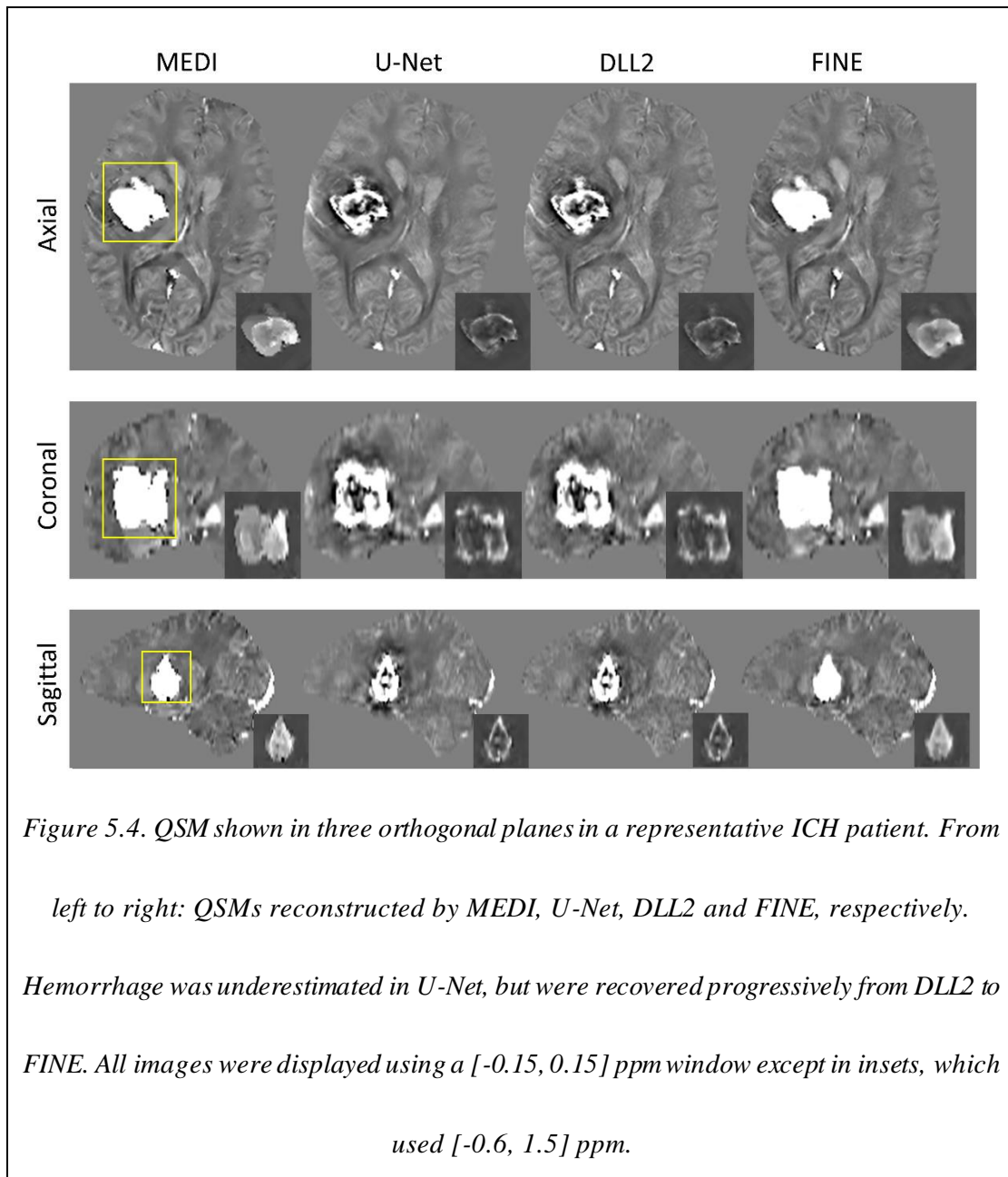


Figure 5.3. a) representative axial images from two MS patients, showing that FINE improves lesion appearance in reference to MEDI. From left to right: QSMs reconstruction by MEDI, U-Net, DLL2 and FINE, respectively. Lesions (solid arrows) near the ventricle were underestimated in U-Net, but were recovered progressively from DLL2 to FINE. The fine structure of periventricular veins was shown more clearly on FINE and DLL2, as compared to MEDI or U-Net (hollow arrows). Despite the merits, some shadow artifacts near the CSF were introduced in FINE. b) Deming regressions of all patients' lesion mean values between MEDI and the DL based three methods, showing FINE improves the lesion susceptibility accuracy in reference to MEDI. All images were displayed using a [-0.15, 0.15] ppm window.

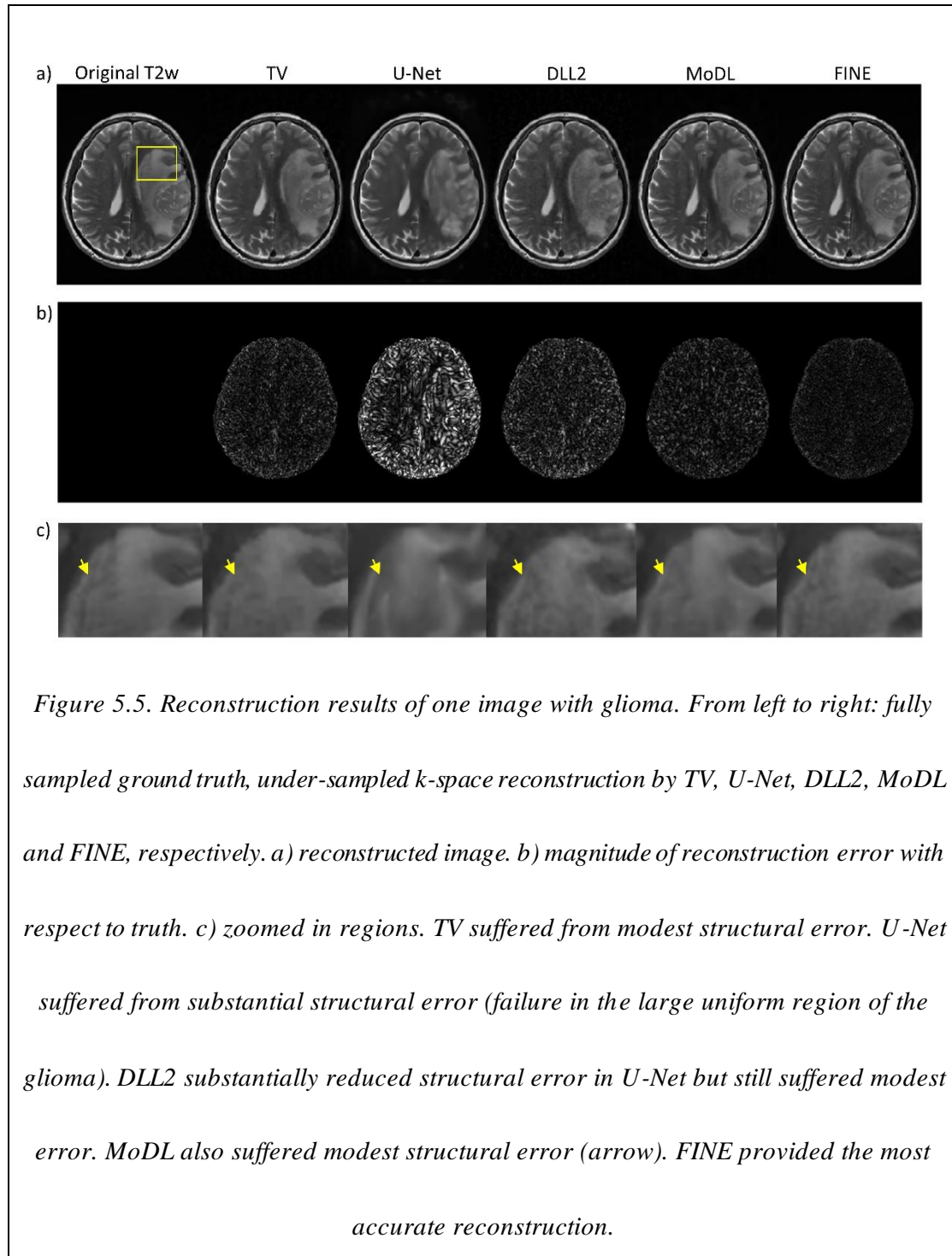
periventricular veins was shown more clearly on FINE and DLL2, as compared to MEDI or U-Net (hollow arrows). Despite the merits above, some shadow artifacts were introduced at the boundary of CSF in FINE.

ICH patients



For ICH patients, QSMs reconstructed by MEDI, U-Net, DLL2 and FINE for a representative ICH patient are displayed in Figure 5.4. Hemorrhage was underestimated in U-Net, but were recovered progressively from DLL2 to FINE. Mean susceptibility values (ppm) of hemorrhage lesions on 8 ICH patients from each reconstruction method were calculated, giving mean susceptibility values \pm standard

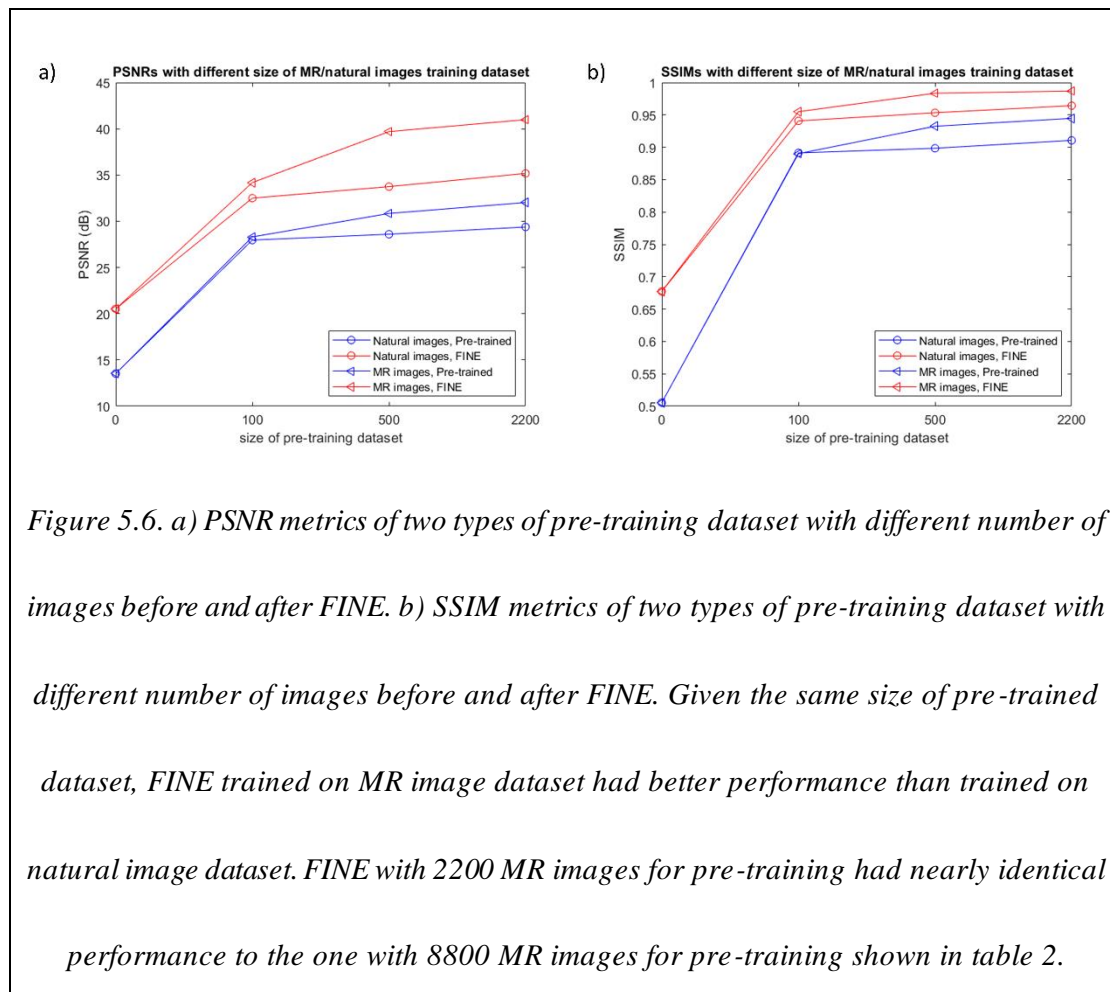
deviations: 0.63 ± 0.09 , 0.33 ± 0.10 , 0.36 ± 0.10 and 0.55 ± 0.09 for MEDI, U-Net, DLL2 and FINE, respectively. In contrast to MEDI, which showed the highest mean susceptibility



values inside lesions, U-Net and DLL2 had considerable underestimation of lesion susceptibility, while FINE gave results closest to MEDI. The blurring scores of tissues surrounding hemorrhagic lesions were 0.18 ± 0.02 , 0.22 ± 0.03 , 0.18 ± 0.02 and 0.18 ± 0.01 for MEDI, U-Net, DLL2 and FINE, respectively. MEDI, DLL2 and FINE had comparable sharpness surrounding hemorrhages, while brain tissue of U-Net surrounding hemorrhages was blurrier compared to that of the other three methods.

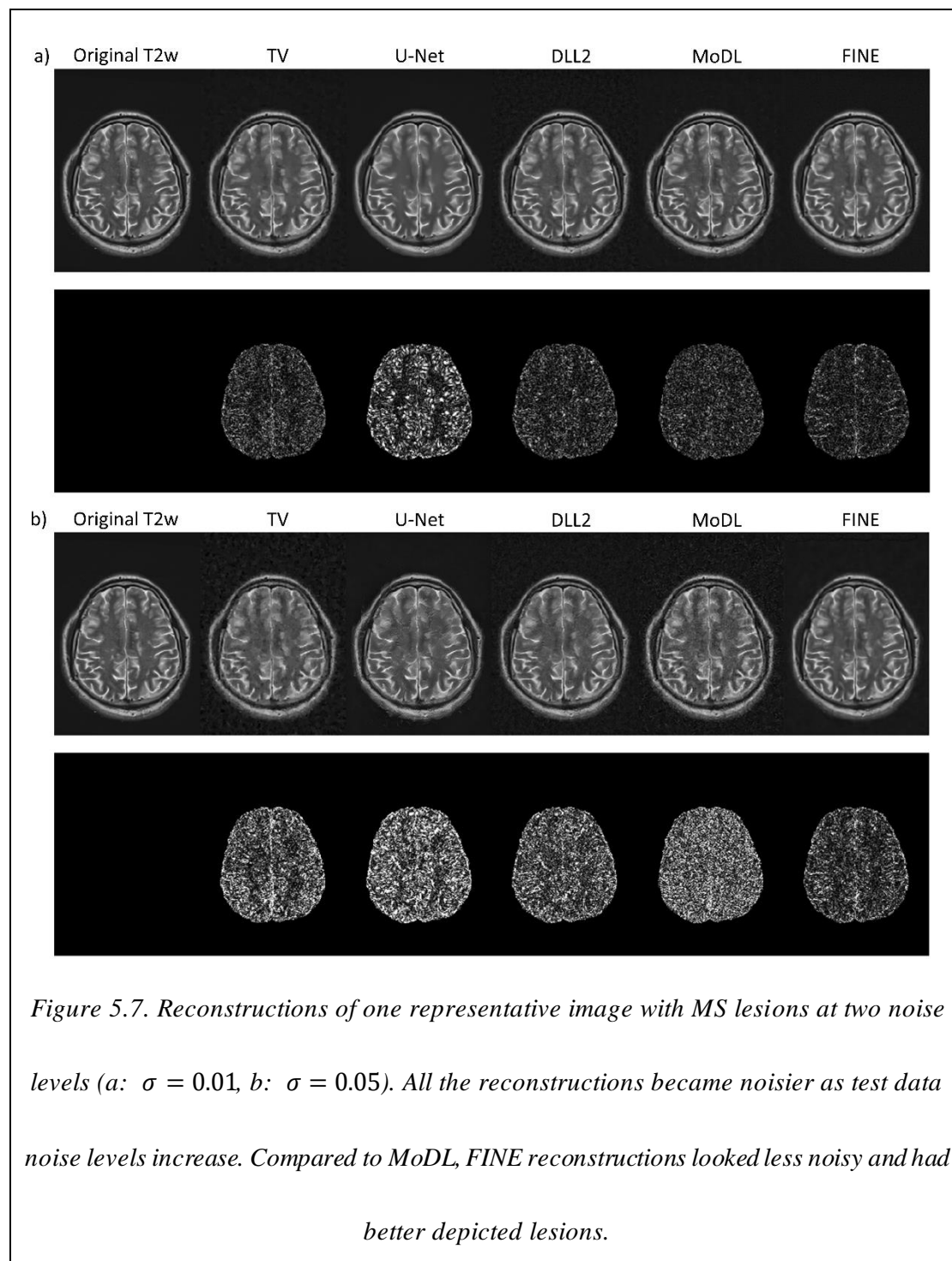
5.5.2 Under-sampled reconstruction

Single-channel real-valued image reconstruction



T2w axial images with glioma reconstructed by TV, U-Net, DLL2, MoDL and FINE are displayed in Figure 5.5. TV suffered from modest structural error. U-Net suffered from substantial structural error (failure in the large uniform region of the glioma). DLL2 substantially reduced structural error in U-Net but still suffered modest error. MoDL also suffered modest structural error (arrow). FINE provided the most accurate reconstruction. Quantitative metrics regarding PSNR and SSIM of MS and glioma test datasets are shown in Tables 5.3 and 5.4, with FINE demonstrating the best performance.

Using the Adam solver with different initial learning rates (2×10^{-4} and 5×10^{-5}), or using a different solver (RMSprop) with initial learning rate 1×10^{-4} yielded



similar results on the MS test dataset, with average PSNRs: 40.30 ± 1.85 , 39.97 ± 1.85 and 39.86 ± 1.58 , respectively and average SSIMs: 0.9858 ± 0.0056 , 0.9868 ± 0.0051 and 0.9863 ± 0.0048 , respectively. Using a different structure for the pre-

Table 5.1. RMSE, SSIM and HFEN for various QSM reconstructions averaged among cross-validation experiments in healthy subjects, with COSMOS as the ground truth reference (denotes statistical significance for the comparison between MEDI/U-Net/DLL2 and FINE; $p < 0.05$).*

	RMSE	SSIM	HFEN
MEDI	$43.19 \pm 2.59^*$	$0.9645 \pm 0.0036^*$	$34.29 \pm 3.29^*$
U-Net	$41.32 \pm 1.81^*$	$0.9737 \pm 0.0015^*$	$40.90 \pm 1.87^*$
DLL2	30.70 ± 2.34	0.9853 ± 0.0020	30.07 ± 2.51
FINE	31.36 ± 1.81	0.9861 ± 0.0017	29.38 ± 1.90

trained network (5 convolutional layers) resulted in higher error on the MS dataset, with average PSNR of 37.22 ± 2.19 and SSIM of 0.9710 ± 0.0117 . Changes in PSNR and SSIM (Table 5.3) by changing optimizers and learning rates were not statistically significant ($p > 0.05$), while those induced by a network architecture change were significant ($p < 0.05$). This indicates that the encoder-decoder structure of U-Net with low dimensional latent features was more efficient in image-to-image generation task.

Multi-channel complex-valued image reconstruction

The PSNR and SSIM of the TV, U-Net, DLL2, MoDL and FINE reconstructions in the complex-valued multi-coil T2w sagittal test images are shown in Table 5.5, indicating FINE and MoDL had the best performance.

Table 5.2. RMSE, SSIM and HFEN for various QSM reconstructions of 6 simulated ICH brains (denotes statistical significance for the comparison between MEDI/U-Net/DLL2 and FINE; $p < 0.05$).*

	RMSE	SSIM	HFEN
MEDI	27.13 ± 8.10	0.9256 ± 0.0312	20.18 ± 9.96
U-Net	$64.04 \pm 5.99^*$	0.9380 ± 0.0195	$63.37 \pm 8.19^*$
DLL2	$49.06 \pm 3.93^*$	0.9371 ± 0.0231	$48.99 \pm 7.05^*$
FINE	25.67 ± 2.79	0.9480 ± 0.0310	25.53 ± 4.15

Dependency of FINE performance on initial training dataset

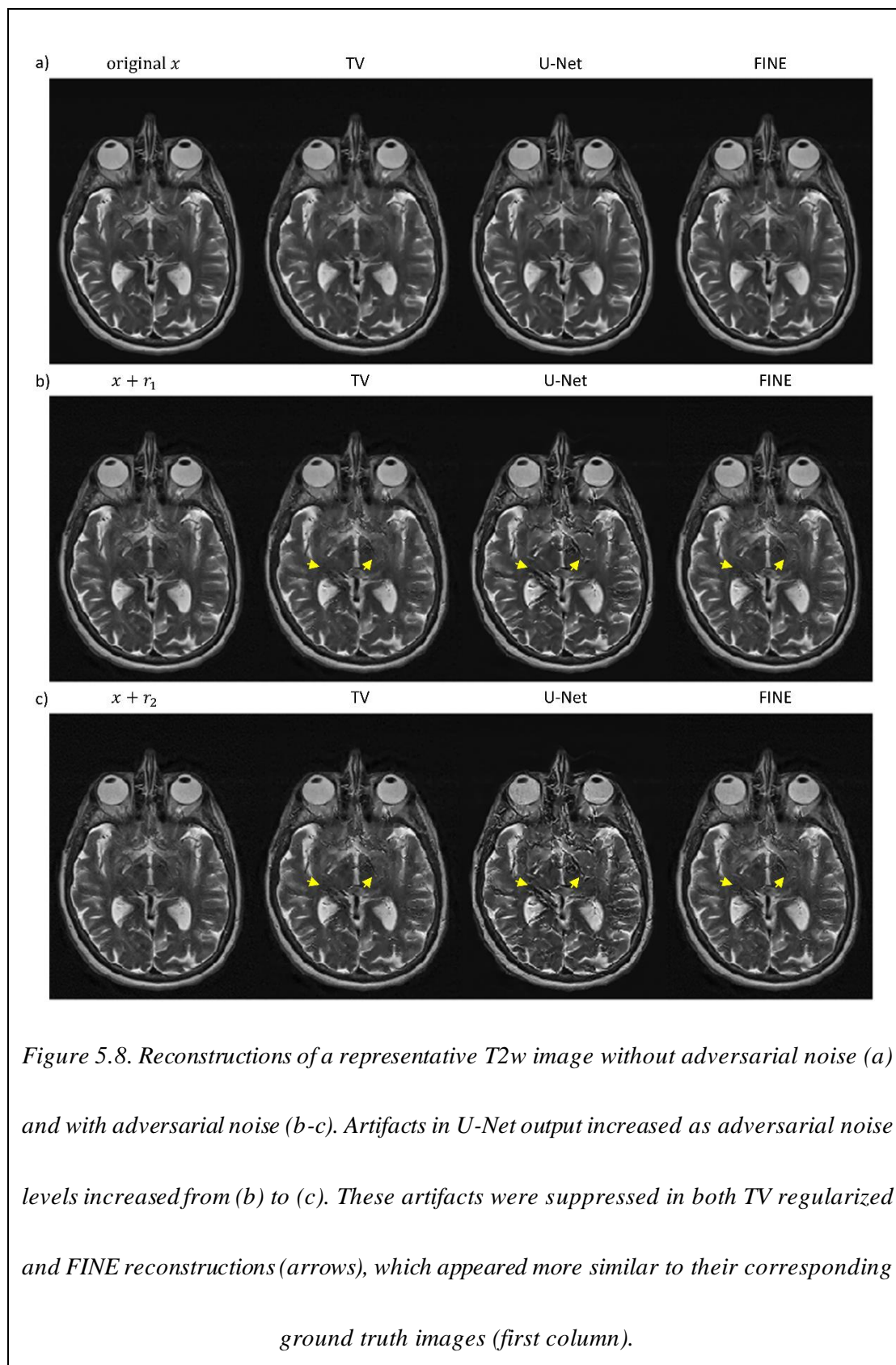
Figure 5.6 shows the reconstruction performance on the MS test dataset in terms of PSNR and SSIM as a function of training dataset type and size. The performance of FINE was improved as the size of the training dataset increased, whether training was performed on MR or natural images. In addition, the performance of FINE trained on natural images was below that of FINE trained on MR images, but was slightly better than end-to-end mapping trained on natural images without using FINE. It's worth noting that FINE trained on 2200 MR images had nearly identical performance as that

<p><i>Table 5.3. PSNR and SSIM for real-valued T2w MS patient test dataset reconstruction. (* denotes statistical significance for the comparison between TV/U-Net/DLL2/MoDL and FINE; $p < 0.05$).</i></p>		
	PSNR (dB)	SSIM
TV	$38.11 \pm 2.62^*$	$0.9791 \pm 0.0090^*$
U-Net	$32.55 \pm 1.57^*$	$0.9493 \pm 0.0144^*$
DLL2	$37.17 \pm 1.78^*$	$0.9765 \pm 0.0078^*$
MoDL	40.98 ± 2.94	0.9874 ± 0.0063
FINE	40.52 ± 1.86	0.9869 ± 0.0051

trained on 8800 MR images (Table 5.2), which indicates that FINE could reach optimal performance with less than 2200 pre-trained MR images.

Dependency of FINE performance on noise.

MoDL and FINE reconstructions on test data with added Gaussian noise ($\sigma = 0.01$



and 0.05) were deployed and reconstruction results of a representative T2w image

<p><i>Table 5.4. PSNR and SSIM for real-valued T2w Glioma patient test dataset reconstruction. (* denotes statistical significance for the comparison between TV/U-Net/DLL2/MoDL and FINE; $p < 0.05$).</i></p>		
	PSNR (dB)	SSIM
TV	$38.48 \pm 2.16^*$	$0.9756 \pm 0.0098^*$
U-Net	$31.79 \pm 1.46^*$	$0.9228 \pm 0.0229^*$
DLL2	$36.64 \pm 1.57^*$	$0.9653 \pm 0.0115^*$
MoDL	40.57 ± 2.28	0.9838 ± 0.0076
FINE	40.88 ± 2.15	0.9831 ± 0.0080

with MS lesions are shown in Figure 5.7. MoDL reconstructions appeared noisier than FINE and MS lesions contrast appeared higher in FINE. Quantitative metrics regarding PSNR and SSIM are shown in Table 5.6. Compared to MoDL, FINE showed similar performance for $\sigma = 0.01$, and improved performance for $\sigma = 0.05$.

Stability of FINE performance against adversarial attack

Two levels of adversarial noises ($|r_1| < |r_2|$) were generated on a specific T2w image of pre-trained U-Net, and FINE was applied after U-Net’s outputs. Reconstructions are shown in Figure 5.8 along with TV method as a comparison. Compared to U-Net

Table 5.5. PSNR and SSIM for complex-valued T2w test dataset reconstruction. (denotes statistical significance for the comparison between TV/U-Net/DLL2/MoDL and FINE; $p < 0.05$).*

	PSNR (dB)	SSIM
TV	$39.52 \pm 1.66^*$	$0.9867 \pm 0.0041^*$
U-Net	$28.75 \pm 1.95^*$	$0.9206 \pm 0.0259^*$
DLL2	$38.95 \pm 2.22^*$	$0.9853 \pm 0.0062^*$
MoDL	43.16 ± 1.59	$0.9922 \pm 0.0026^*$
FINE	42.93 ± 2.53	0.9898 ± 0.0051

outputs that suffered from adversarial attacks, FINE was able to effectively reduce those artifacts.

5.6 Discussion and Conclusion

Our results indicate that the proposed approach of fidelity imposed network edit (FINE) can be effective in reducing errors when using neural network models to solve ill-posed inverse problems in medical image reconstruction. FINE improves the fidelity of test data by adapting the weights of a pre-trained CNN through backpropagation according to the physical model for each case in the test dataset.

Table 5.6. PSNR and SSIM of MoDL and FINE reconstructions on MS test dataset with noise $\sigma = 0.01$ and 0.05 . (denotes statistical significance for the comparison between MoDL and FINE; $p < 0.05$).*

	$\sigma = 0.01$		$\sigma = 0.05$	
	PSNR (dB)	SSIM	PSNR (dB)	SSIM
TV	$36.03 \pm 1.79^*$	$0.9713 \pm 0.0095^*$	$29.89 \pm 1.09^*$	$0.9092 \pm 0.0214^*$
U-Net	$32.19 \pm 1.57^*$	$0.9463 \pm 0.0152^*$	$28.27 \pm 0.91^*$	$0.8777 \pm 0.0274^*$
DLL2	$36.54 \pm 1.66^*$	$0.9718 \pm 0.0090^*$	$30.52 \pm 0.94^*$	$0.9092 \pm 0.0226^*$
MoDL	37.64 ± 1.77	$0.9757 \pm 0.0085^*$	$28.00 \pm 0.54^*$	$0.8558 \pm 0.0319^*$
FINE	37.51 ± 1.39	0.9795 ± 0.0058	31.57 ± 1.74	0.9428 ± 0.0170

Therefore, FINE offers two distinct benefits in solving the ill-posed inverse problem

of reconstruction: the implicit regularization achieved via a pre-trained neural network model, and the physical model defined data fidelity. Compared to a conventional reconstruction with explicit total variation regularization, a supervised CNN (U-Net) reconstruction, and a CNN (U-Net) reconstruction with further explicit regularization, FINE can provide more accurate reconstruction as exemplified in QSM and under-

sampled reconstruction (Figures 5.1, 5.3, 5.4 and 5.5).

It is observed in FINE that updating network weights on test data improves the fidelity of the reconstruction. This FINE approach is closely related to prior work, deep image prior, which trains a DL network from scratch on a single data for inverse problems of denoising, super-resolution, and inpainting [143]. However, in FINE, the network is initialized to a pre-trained network, rather than trained from scratch and the iterative updating is stopped when the relative change in fidelity loss reaches a threshold. When to stop updating weights of a network remains an empirical question, which should be carefully evaluated for a given application and network structure; This work was done on U-Net networks for QSM and under-sampled image reconstruction. This FINE approach is also related to transfer learning that first trains a DL network on a base dataset and then uses the trained weights to initialize training on a target dataset [144]. However, in transfer learning, once the updated weights are found, they are fixed for the test datasets. Moreover, they require ground-truth/labels for the target dataset during training. In contrast, FINE updates the weights for each case in a test dataset using a loss function that is different from that in the initial training and is based on the forward physical model. Additionally, it does not require ground-truth/labels for the target datasets.

The fidelity term in FINE is used in a generalized sense that it includes the physical forward model and other data characteristics. The core objective of FINE is to reduce

the generalization error in the neural network based reconstruction, which may stem from discrepancies, such as pathologies and abnormal morphology between training and test data. Increasing noise levels in the test data often results in decreasing PSNR and SSIM of the network reconstruction, which can be improved by FINE. The inadequacy of the commonly used U-Net can be improved by incorporating the physical model in a CNN as in MoDL (Aggarwal et al., 2019; Schlemper et al) or in iterative projections using many CNN sub-blocks [145]. However, MoDL still suffers from possible discrepancies between training and test data. As FINE updates network weights with respect to test data, FINE can outperform MoDL at high noise levels in the under-sampled reconstruction application we considered. However, FINE may not address U-Net's structural inferiority to MoDL in the low noise case in Figure 5.7.

There is substantial neuroimaging interest in QSM [72], including studies of the metabolic rate of oxygen consumption [146], brain tumor [147], deep brain stimulation [148], multiple sclerosis [149], cerebral cavernous malformation [150], Alzheimer's disease [87], Parkinson's disease [151], Huntington's disease [152], and magnetic nanocarrier biodistribution [71]. As QSM needs prior information to execute the ill-posed dipole inversion, seeking a better image feature for regularizing reconstruction has continuously been a major development effort [46, 129, 135].

Mathematically, regularization should project out or suppress the streaking artifacts associated with granular noise and shadow artifacts associated with smooth model

errors [129]. Streaking artifacts have been effectively reduced using L1-type regularizations, but these techniques suffer from staircase artifacts or blockiness. Shadow artifacts have yet to be effectively suppressed, partly due to white matter magnetic anisotropy [59, 153]. These QSM reconstruction challenges may be addressed more effectively using sophisticated and complex image features [135]. Deep neural networks promise to provide the desired but indescribable complex image features. U-Nets have been used to map the tissue field into QSM [4, 5]. However, limited to the training data, these networks may not properly reconstruct new patterns not encountered in the training dataset. This is exemplified in Figure 5.4, where the hemorrhage, which was not present in training datasets obtained in healthy subjects, cannot be properly reconstructed by U-Net. MoDL overcoming structural limitation in U-Net and FINE overcoming network's lack of fidelity of test data should be explored in future QSM reconstruction.

Similar to QSM, image reconstruction from noisy under-sampled k-space data in MRI is also an ill-posed inverse problem and requires suitable regularizations to suppress artifacts associated with the under-sampling pattern. L1-type regularizations for MAP inference based reconstruction have been shown to be effective in suppressing noise-like artifacts, but image quality suffers from blockiness. Using data fidelity with CNN image reconstructions have shown improvement in highly under-sampled data [3, 127]. FINE promises improvements in image reconstruction of test data that differs

from the training set. The MRI under-sampling rate may be further increased in imaging situations of redundancy, including multiple contrasts [154], various magnetization preparations [155], and navigator motion tracking [156]. Deep neural network reconstruction with FINE as demonstrated here may be very promising to accelerate these imaging tasks.

There are several limitations present in this work. First, FINE was shown to improve image reconstruction compared to neural network based reconstructions. However, the effectiveness of FINE has to be assessed for specific training regimes and network architectures. Network structures incorporating the physical forward model may be preferred for image reconstruction. FINE improvements on such network are yet to be demonstrated and may be limited to reducing effects of discrepancy between training and test data. Second, FINE updates iteratively the network weights by minimizing the fidelity loss of the test data. While FINE achieved high quality image reconstruction across data sets tested in this work, which included various pathologies and/or noise levels not seen in the training data, early stopping is necessary to avoid overfitting to noise. This was achieved using a stopping criterion based on the relative change between iterations and a fixed threshold. While empirical, this criterion led to good performance of FINE reconstructions in the various data sets used in this work. Third, the computational cost of FINE is much higher than a single pass through a deep neural network, due to the additional network updating based on the iterative

optimization. The computational cost may be reduced by updating a subset of layers instead of the entire network in the optimization, as in transfer learning [157].

In summary, for each test case, data fidelity is used to update the neural network weights to improve reconstruction quality. This fidelity imposed network edit (FINE) strategy promises to be useful for solving ill-posed inverse problems in medical imaging.

CHAPTER 6. HOBIT: HYBRID OPTIMIZATION BETWEEN ITERATIVE AND NETWORK FINE-TUNING RECONSTRUCTIONS FOR FAST QUANTITATIVE SUSCEPTIBILITY MAPPING

6.1 Abstract

A Hybrid Optimization Between Iterative and network fine-Tuning (HOBIT) reconstruction method is proposed to solve quantitative susceptibility mapping (QSM) inverse problem in MRI. In HOBIT, a convolutional neural network (CNN) is first trained on healthy subjects' data with gold standard labels. Domain adaptation to patients' data with hemorrhagic lesions is then deployed by minimizing fidelity loss on the patient training dataset. During test time, a fidelity loss is imposed on each patient test case, where alternating direction method of multiplier (ADMM) is used to split the time consuming fidelity imposed network update into iterative reconstruction and network update subproblems alternatively in ADMM, and only a subnet of the pre-trained CNN is updated during the process. Compared to the method FINE where such fidelity imposing strategy was initially proposed to solve QSM, HOBIT achieved both performance gain of reconstruction accuracy and vast reduction of computational time.

6.2 Introduction

Quantitative susceptibility mapping (QSM) is an imaging contrast in MRI to quantify tissue magnetic susceptibility values from estimated local tissue field data [43]. QSM provides biomarkers for tissues with iron, calcium and gadolinium[46] concentrations which can be used for clinical diagnosis, such as multiple sclerosis [158], intracranial calcifications and hemorrhages [83]. QSM is computed by inverting the following forward process:

$$\mathbf{b} = \mathbf{F}^H \mathbf{D} \mathbf{F} \chi + \mathbf{n} \quad [6.1]$$

where \mathbf{b} is the estimated local tissue field from magnetic resonance phase imaging, χ is the tissue susceptibility to compute, \mathbf{F} is the Fourier transform, \mathbf{D} is the dipole kernel in k-space and \mathbf{n} is the additive noise (assuming i.i.d. Gaussian for each voxel). With single orientation sampling, the dipole inversion problem from local field \mathbf{b} to susceptibility χ is ill-posed since the zero-cone in the k-space dipole kernel produces dipole-incompatible field, which results in streaking and shadow artifacts of susceptibility [129].

Various methods have been proposed to resolve the ill-posedness of dipole inversion. Direct method truncated k-space division (TKD) modified the dipole kernel near the zero-cone to add dipole-incompatible field components [159]. Iterative method morphology enabled dipole inversion (MEDI) introduced a weighted total variation

regularization to suppress the streaking artifacts [45]. Oversampling method calculation of susceptibility through multiple orientation sampling (COSMOS) eliminated the zero-cone of the dipole kernel by a combination of multi-oriented fields [134]; therefore, COSMOS has been regarded as the gold standard susceptibility map. With the advance of convolutional neural network (CNN), deep learning (DL) has been introduced in QSM. A first deep learning method QSMnet built a 3D U-Net for field-to-susceptibility mapping using COSMOS as the training dataset, and was reported to perform better than TKD and MEDI [4]. Another deep learning method DeepQSM trained U-Net with synthetic field-susceptibility pairs [5]. Since then, more architectures have been proposed based on the backbone U-Net, xQSM [160] and folded attention U-Net [66].

Compared to conventional methods, DL QSM methods usually achieve fast and accurate reconstructions on test dataset, but when tested on the cases with pathologies not encountered during training, such as intracranial calcifications and hemorrhages with extreme susceptibility values, generalization error may be enlarged in those regions. The generalization error could show up as severely under-estimated susceptibility values of lesions in DL QSM. To overcome such limitation, several methods were proposed to improve the domain adaptation ability of DL QSM.

QSMnet+ augmented the training dataset to a wider range of susceptibility in order to generalize the network better [161]. Probabilistic dipole inversion (PDI) adapted the

pre-trained network to different patient datasets using variational inference [14, 15]. Fidelity imposed network edit (FINE) deployed the fidelity loss of dipole inversion on each test case so that the generalization error of unseen lesions could be reduced [11].

As one of the effective domain adaptation methods for DL QSM, FINE combines the advantageous robustness of iterative methods and implicit regularization of DL methods. Despite such merit, significantly increased computational time is needed for FINE, which hinders its practical usage. In the work, we analyze existing issues of FINE and attempt to resolve them all with a newly proposed method derived from FINE: Hybrid Optimization Between Iterative and network fine-Tuning (HOBIT) reconstruction for fast QSM. We deployed ablation study of HOBIT and compared it with MEDI, QSMnet, QSMnet+, FINE and PDI on both in vivo and simulated hemorrhagic datasets. Superior reconstruction performance was achieved in HOBIT and reconstruction speed was vastly accelerated compared to FINE.

6.3 Method

6.3.1 Issues in FINE

In FINE, a 3D U-Net [136] was pre-trained on the multi-orientation dataset of healthy subjects with COSMOS as labels to do supervised learning. When tested on each patient data without label, FINE adapted the pre-trained weights by minimizing the following fidelity loss in an unsupervised fashion:

$$\|W(F^H D F \chi - b)\|_2^2 \quad [6.2]$$

until the relative change of fidelity loss between two consecutive epochs fell below $5 \times e^{-3}$, where W is the square root of the inverse of the noise covariance matrix.

The vanilla FINE above has three major issues:

- When performing FINE in subject, pathology-related domain adaptation information is not inherited when performing FINE in other subjects that have a similar pathology.
- The whole network update of FINE is redundant, as lots of weights seldom change during network update (Figure 8.2 in FINE [11]).
- Network update leads to slow update of the output susceptibility, requiring hundreds of epochs to converge.

In the next section, we attempt to tackle the three issues above using the proposed method.

6.3.2 HOBIT

In HOBIT, we design a network architecture as shown in Figure 6.1, where a first dipole inversion network 3D U-Net f_θ maps local field input b to susceptibility output χ_0 , then a slimmer network g_ψ consisting of five convolutional layers maps

χ_0 and b to the final susceptibility output χ_1 . COSMOS dataset of healthy subjects are used to pre-train f_θ and g_ψ with the following loss function:

$$\min_{\theta, \psi} \sum_{i=1}^{N_C} \|\chi_0^{(i)} - \chi_T^{(i)}\|_1 + \|\chi_1^{(i)} - \chi_T^{(i)}\|_1 \quad [6.3]$$

where $\chi_T^{(i)}$ is the i -th label/target from a total of N_C COSMOS data points, $\chi_0^{(i)}$ and $\chi_1^{(i)}$ are predictions of f_θ and g_ψ . After pre-training, the following steps are deployed to resolve the three major issues of FINE described in section 6.1 point-by-point:

- Domain adaptation to the patient dataset is accomplished by fine-tuning the COSMOS pre-trained network with a fidelity loss function on the patient training dataset:

$$\min_{\theta, \psi} \sum_{i=1}^{N_P} \|W^{(i)}(F^H D F \chi_0^{(i)} - b^{(i)})\|_2^2 + \|W^{(i)}(F^H D F \chi_1^{(i)} - b^{(i)})\|_2^2 \quad [6.4]$$

where $W^{(i)}$ and $b^{(i)}$ are the i -th noise weighting matrix and input local field from a total of N_P patient data points. Then during test per case, network refinement starts from those domain adapted weights.

- After domain adaptation using Eq.8.4, f_θ is fixed and only g_ψ is refined for each test case in the patient test dataset.
- Rewrite minimization of network reparametrized fidelity loss

$$\frac{1}{2} \|W(F^H D F g_\psi(\chi_0, b) - b)\|_2^2 \text{ as:}$$

$$\begin{aligned} \min_{\psi, \chi} \quad & \frac{\alpha}{2} \|W(F^H DF \chi - b)\|_2^2 + \frac{1-\alpha}{2} \|W(F^H DF g_\psi(\chi_0, b) - b)\|_2^2 \\ \text{s.t.} \quad & \chi = g_\psi(\chi_0, b), \end{aligned} \quad [6.5]$$

where $0 \leq \alpha \leq 1$. Convert the constrained optimization problem in Eq. 6.5 as the augmented Lagrangian format:

$$\begin{aligned} \min_{\psi, \chi} \quad & \frac{\alpha}{2} \|W(F^H DF \chi - b)\|_2^2 + \frac{1-\alpha}{2} \|W(F^H DF g_\psi(\chi_0, b) - b)\|_2^2 \\ & + \frac{\rho}{2} \|\chi - g_\psi(\chi_0, b) + \mu\|_2^2 - \frac{\rho}{2} \|\mu\|_2^2, \end{aligned} \quad [6.6]$$

where ρ is the penalty parameter and μ is the dual variable. Eq. 6.6 is then solved using alternating direction method of multiplier (ADMM) [30] iteratively in three subproblems:

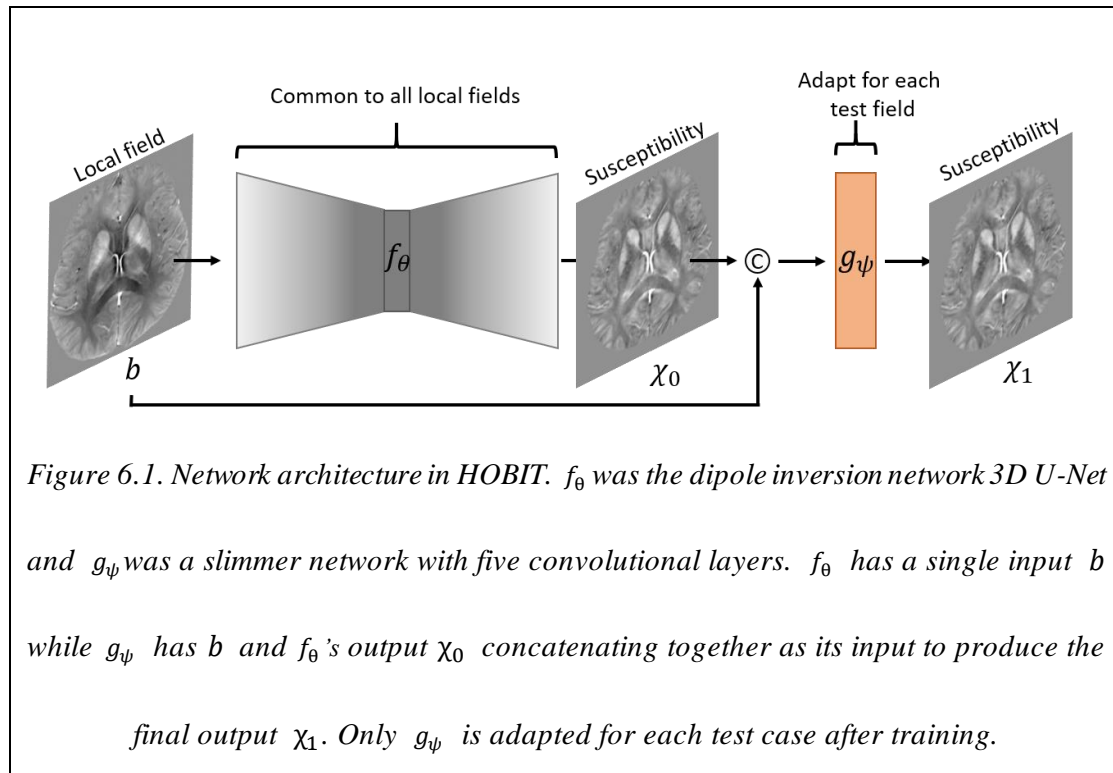
$$\begin{aligned} \chi^{n+1} &= \arg \min_{\chi} \frac{\alpha}{2} \|W(F^H DF \chi - b)\|_2^2 + \frac{\rho}{2} \|\chi - g_{\psi^n}(\chi_0, b) + \mu^n\|_2^2, \\ \psi^{n+1} &= \arg \min_{\psi} \frac{1-\alpha}{2} \|W(F^H DF g_\psi(\chi_0, b) - b)\|_2^2 + \frac{\rho}{2} \|\chi^{n+1} - g_\psi(\chi_0, b) + \mu^n\|_2^2 \\ \mu^{n+1} &= \mu^n + \chi^{n+1} - g_{\psi^{(n+1)}}(\chi_0, b), \end{aligned} \quad [6.7a - c]$$

where subproblem Eq. 6.7a is the network output regularized least square problem which can be approximated with a few conjugate gradient (CG) iterations, subproblem Eq. 6.7b is the L2 regularized nonlinear least square problem with network reparametrization, which can be solved using first order adaptive gradient descent algorithm such as Adam [37].

6.4 Results

6.4.1 Data acquisition and preprocessing

Multi-echo 3D gradient echo (MGRE) sequence was performed on 7 healthy subjects using a 3T GE scanner with 5 brain orientations, $256 \times 256 \times 48$ acquisition matrix and $1 \times 1 \times 3 \text{ mm}^3$ voxel size. After data acquisition, raw field data of each scan



was estimated via non-linear least square fitting of multi-echo phase data using Levenberg–Marquardt algorithm [44]. Phase wraps of raw field data were unwrapped using graph-cut based spatial phase unwrapping algorithm [162]. Background field of raw field data was then removed using projection onto dipole fields [60] to obtain local tissue field data b as network's input. COSMOS gold standard as pre-training

label was computed by aggregating multi-orientated local fields to do dipole inversion [134]. MGRE sequence was also performed on 7 intracerebral hemorrhagic (ICH) patients with single orientation and same scanning parameters as COSMOS dataset. Image processing procedures as above were deployed on ICH dataset, except for the COSMOS reconstruction step. Data were acquired following an IRB approved protocol.

For COSMOS pre-training in Eq. 6.3, data of 5/2 subjects (25/10 brain volumes) were used as training/validation datasets with $\pm 15^\circ$ in-plane rotations for augmentation.

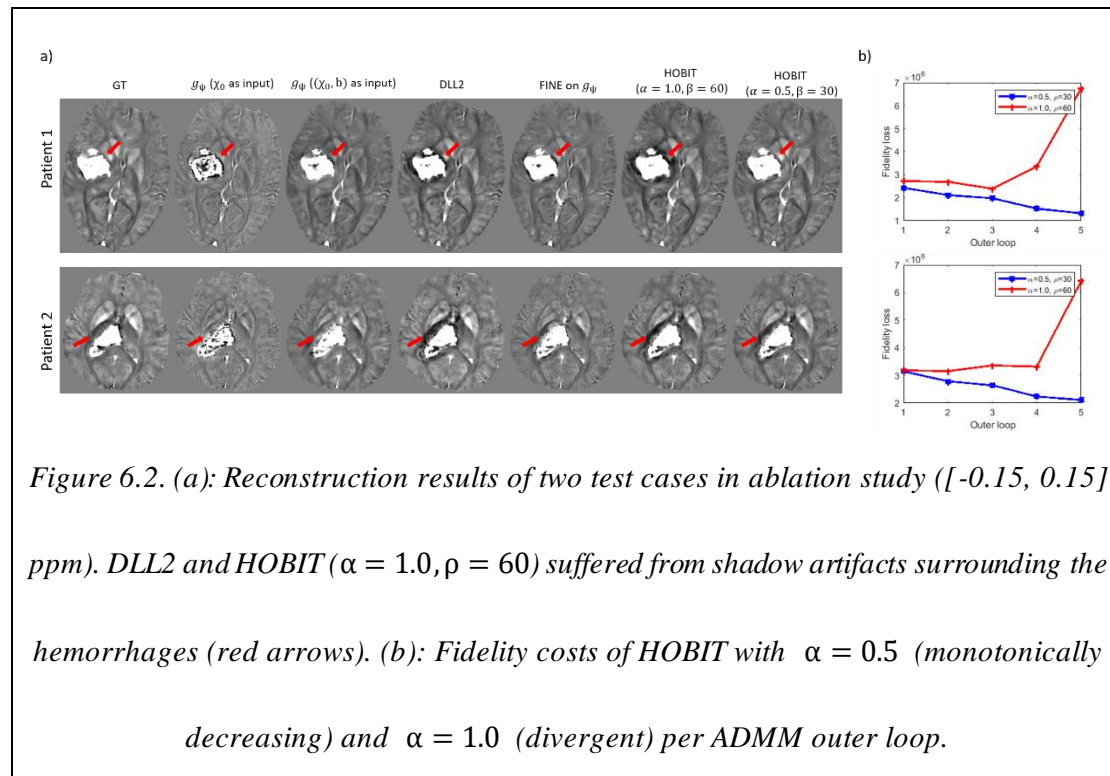
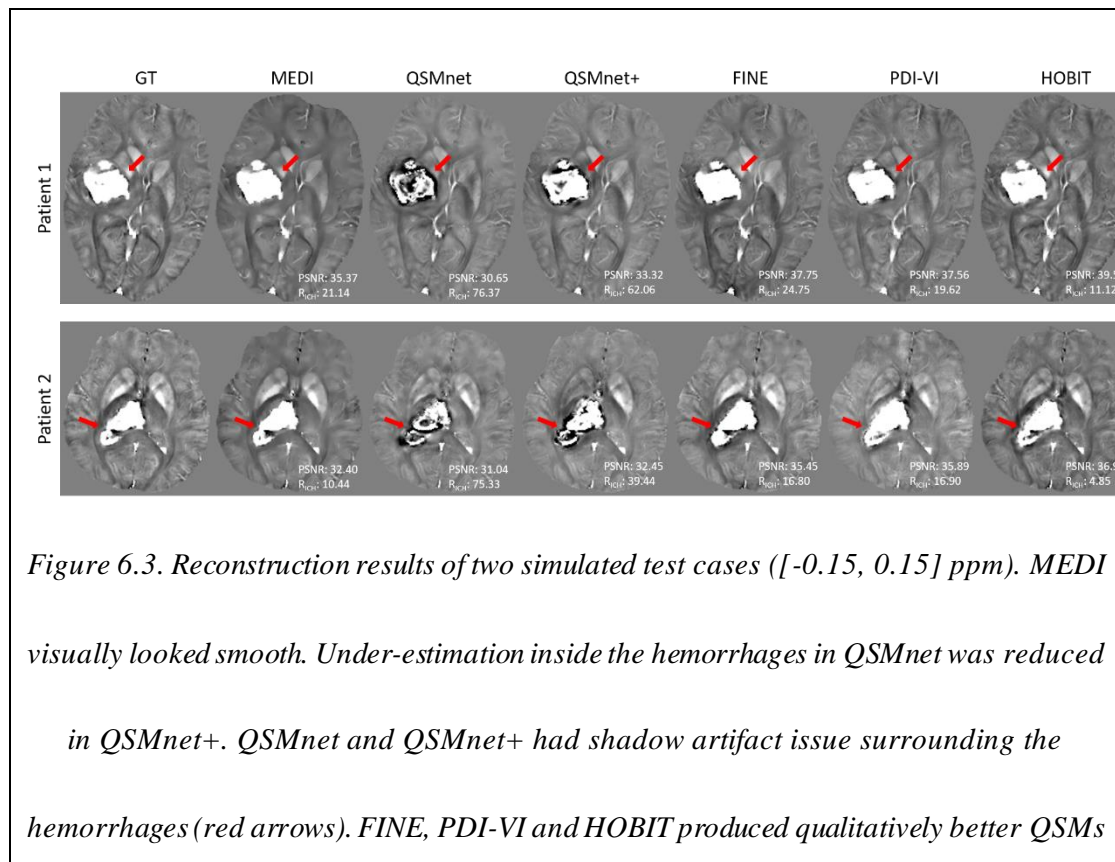


Figure 6.2. (a): Reconstruction results of two test cases in ablation study ($[-0.15, 0.15]$ ppm). DLL2 and HOBIT ($\alpha = 1.0, \rho = 60$) suffered from shadow artifacts surrounding the hemorrhages (red arrows). (b): Fidelity costs of HOBIT with $\alpha = 0.5$ (monotonically decreasing) and $\alpha = 1.0$ (divergent) per ADMM outer loop.

Brain volumes were divided into 3D patches with patch size $64 \times 64 \times 32$ and extraction step $21 \times 21 \times 11$, generating 12074/5748 patches for training/validation.

For ICH patient domain adaptation in Eq.6.4, whole brain volume data from 4/1

subjects were used as training/validation datasets. Data from the remaining 2 patients were used as in vivo ICH test dataset. Simulated local fields were also obtained by applying forward model Eq. 6.1 to FINE reconstructed QSMs of ICH validation and test datasets, where 5 simulated local fields with different samples of Gaussian noise n were generated on each ICH patient, yielding 5/10 volumes as simulated ICH validation/test datasets. The purpose of these simulated ICH datasets was to provide ground truth (GT) for both ablation study on HOBIT and quantitative comparison among different methods. Peak signal-to-noise ratio (PSNR), root-mean-square error (RMSE), structural similarity index measure (SSIM) [38], high-frequency error norm (HFEN) [61] and shadow artifact quantification metric of ICH (R_{ICH})



than the other methods.

[163] were used as quantitative metrics to evaluate reconstruction accuracy.

6.4.2 Implementation details and ablation study

For network training, f_{θ} and g_{ψ} were first trained with loss Eq. 6.3 on the COSMOS dataset using Adam optimizer [37] (learning rate 10^{-3} , 60 epochs). f_{θ} and g_{ψ} were then adapted to the ICH patient data with loss Eq. 6.4 on the in vivo ICH dataset using Adam optimizer (learning rate 10^{-3} , 200 epochs). In HOBIT, the number of outer loops in ADMM was fixed as 5, the relative change threshold of CG in Eq. 7 was 10^{-10} with a maximum of 100 iterations, and the number of gradient descent in Eq. 6.8 was 4 using Adam optimizer (learning rate 10^{-3}). To determine the optimal α and ρ in Eqs. 6.7a and 6.7b, we applied a grid search of α ($[0,1]$, interval 0.1) and ρ ($[10,100]$, interval 10) on the simulated ICH

Table 6.1. Average quantitative metrics of 10 test simulated brains reconstructed by different methods in ablation study. Overall, HOBIT ($\alpha = 0.5, \rho = 30$) performed the best.

	PSNR (\uparrow)	RMSE (\downarrow)	SSIM (\uparrow)	HFEN (\downarrow)	R_{ICH} ($\% \downarrow$)
g_ψ (χ_0 as input)	31.63	68.28	0.9733	65.19	40.18
g_ψ ((χ_0, b) as input)	33.65	57.29	0.9765	55.51	24.80
DLL2	37.91	35.04	0.9854	30.84	27.66
FINE on g_ψ	36.64	40.80	0.9711	41.89	9.81
HOBIT ($\alpha = 1.0, \rho = 60$)	35.88	44.20	0.9834	45.78	33.57
HOBIT ($\alpha = 0.5, \rho = 30$)	38.29	33.98	0.9834	32.12	7.99

validation dataset, yielding the optimal parameters $\alpha = 0.5$ and $\rho = 30$.

For ablation study, we compared HOBIT against a few methods below on the

simulated ICH test dataset. These methods included direct inference of domain adapted g_ψ without and with input local field concatenation (denoted as $g_\psi(\chi_0$ as input) and $g_\psi((\chi_0, b)$ as input)), iterative reconstruction with g_ψ as L2 regularization ($\mu^n = 0$ in Eq. 6.7a, $\alpha = 1, \rho = 60$, denoted as DLL2), FINE on domain adapted g_ψ using fidelity loss Eq. 6.2 (denoted as FINE on g_ψ), and HOBIT with $\alpha = 1.0$ and $\rho = 60$. Reconstruction results of two test cases are shown in Figure 6.2a. Quantitative metrics are shown in Table 6.1. All the methods resolved the under-estimation issue inside the hemorrhagic lesions. Compared to HOBIT with optimal $\alpha = 0.5$ and $\rho = 30$, DLL2 and HOBIT with $\alpha = 1.0$ and $\rho = 60$ suffered from shadow artifacts surrounding the hemorrhagic lesions (red arrows in Figure 6.2a, while g_ψ and FINE on g_ψ suffered from sub-optimal reconstruction accuracy. Fidelity costs Eq. 6.2 of HOBITs with two sets of parameters after each outer loop in ADMM are shown in Figure 6.2b. HOBIT with optimal $\alpha = 0.5$ and $\rho = 30$ had monotonically decreasing fidelity cost. In contrast, HOBIT with $\alpha = 1.0$ and $\rho = 60$ suffered from divergence issue of fidelity cost.

6.4.3 Simulated ICH

HOBIT was compared with other dipole inversion methods on the simulated ICH test dataset. Reconstruction results of two test cases are shown in Figure 6.3. MEDI reconstructed piecewise constant QSMs which visually looked smooth. QSMnet had under-estimation issue inside the hemorrhages, which was reduced in QSMnet+. Both

QSMnet and QSMnet+ had shadow artifact issue surrounding the hemorrhages (red arrow in Figure 6.3). FINE, PDI-VI and HOBIT produced qualitatively better QSMs than the other methods. Quantitative metrics and computational time of each method are shown in Table 6.2. HOBIT had the overall best accuracy among all the methods. In terms of computational time per subject, QSMnet, QSMnet+ and PDI achieved the fastest GPU time of less than 1s, while HOBIT was the fastest iterative method compared to MEDI ($\times 3.1$) and FINE ($\times 31.6$).

6.4.4 *In vivo ICH*

HOBIT was also compared with other methods on the in vivo ICH test dataset. In this dataset, no ground truth was provided as label; therefore, QSMs were compared qualitatively. Reconstruction results are shown in Figure 6.4. Similar to the simulation results in section 6.3, MEDI produced smooth QSMs on the in vivo test data too.

QSMnet suffered from under-estimation inside the hemorrhagic lesions while QSMnet+ suffered from severe shadow artifacts surrounding the lesions (red arrows in Figure 6.4). FINE, PDI-VI and HOBIT had visually similar QSMs including hemorrhages without under-estimation and shadow artifacts and overall susceptibilities without over-smoothness.

6.5 Discussion and Conclusion

Motivated by analyzing and solving existing issues of FINE, we proposed HOBIT as

a novel hybrid iterative and DL reconstruction method for fast QSM. Ablation study showed the necessity of each building block/step in HOBIT for performance improvement. Experiments on both in vivo and simulated ICH test datasets showed that HOBIT achieved over 30 times acceleration on computational time than FINE. Meanwhile, superior reconstruction accuracy was obtained compared to the other methods including FINE.

CHAPTER 7. PHYSICS-BASED NETWORK FINE-TUNING FOR ROBUST QUANTITATIVE SUSCEPTIBILITY MAPPING FROM HIGH-PASS FILTERED PHASE

7.1 Abstract

Susceptibility-weighted imaging (SWI) has been used in clinical diagnosis to visualize the presence of susceptibility sources such as veins, calcifications and hemorrhage. The induced change in the tissue field can be sensitized by gradient echo (GRE) MRI. SWI is a post-processing method for GRE data designed to visualize these changes but does not provide a measurement of the underlying susceptibility. In the past decade, quantitative susceptibility mapping (QSM) has been developed with the express purpose to quantify tissue susceptibility by solving an ill-posed dipole inversion problem from GRE phase data. While phase is often available together with SWI, it is not suitable for conventional QSM reconstruction methods because this phase has been high-pass filtered (HPFP) as the part of the standard SWI pipeline. To nevertheless allow a quantitative analysis of this data, convolutional neural networks (CNN) have been proposed to predict QSM from HPFP images. Promising results demonstrate the feasibility of CNN-based HPFP to QSM prediction, but the generalization ability of these pre-trained networks remain to be evaluated. In this study, we tackle two common generalization issues that arise when using a pre-trained

network to predict QSM from HPFP: a) data with unseen voxel sizes and b) data with unknown high-pass filters which may be different from training. A network fine-tuning step based on a high-pass filtering dipole convolution forward model is proposed to reduce generalization error of the pre-trained network. A progressive Unet architecture is proposed to improve prediction accuracy without increasing fine-tuning computational cost. The proposed method shows improved robustness compared to the pre-trained network without fine-tuning when test dataset deviates from the training.

7.2 Introduction

Susceptibility-weighted imaging (SWI) [164] is an MRI method to visualize susceptibility sources which affect the tissue-induced magnetic field, such as veins, calcifications and hemorrhage. SWI is obtained by combining a high-pass filtered phase (HPFP) and magnitude images of gradient-echo (GRE) data to improve the visualization of tissue susceptibility differences. The HPFP image is computed as the angle of the complex division of the original GRE by its low-pass filtered version. This operation suppresses the background field which predominantly consists of low spatial frequency components and impedes clear visualization of the local tissue details [165]. SWI has been used in clinical applications such as stroke, cerebrovascular disease and neurodegenerative disorders [166].

Although SWI has been widely applied for clinical practice, it does not allow a direct quantitative measurement of the underlying tissue susceptibility. A technique, called quantitative susceptibility mapping (QSM) [6], has been proposed to map tissue susceptibility by solving a dipole inversion problem from unfiltered complex GRE data. Typically in QSM reconstruction, the tissue-induced field map is first obtained by fitting the phase of complex multi-echo GRE signal [43, 44], after which background field removal is performed on the resulting total field map [60, 167-169]. Then a regularized dipole inversion is performed to estimate the underlying tissue susceptibility distribution [170-173].

To date, a large amount of SWI HPFP data has been collected for which the underlying complex GRE data is no longer available. Despite potential interest in their quantitative analysis, accumulated HPFP images are incompatible with QSM reconstruction due to the removal of the low spatial frequency components of the tissue field, which is known to be a suboptimal method for the removal of background field as it removes some of the tissue field as well. Thanks to the rapid development of convolutional neural networks (CNNs) in medical imaging, there is an increasing interest in recovering QSM from HPFP data in SWI using CNNs [174-176]. In one approach, a 3D Unet [68, 136] was applied to recover unfiltered phase data from HPFP data and compute QSM using the recovered phase data [175]. A second approach reconstructs QSM directly from HPFP data, either using a network

architecture with an edge prior and a cross dense block [174] or a generative adversarial network (GAN)[176]. These promising results were obtained with the assumption that training and test data were acquired with the same imaging parameters. However, generalization errors may manifest when inference is attempted on data from a different acquisition protocol, e.g., with different voxel size [174] and a different or unknown high-pass filter [175].

To address the issue of generalization errors of the pre-trained HPFP-to-QSM network, we propose to incorporate the forward model combining dipole convolution and high-pass filtering operations into the network for test-time fine-tuning [7, 12]. We also design a network architecture called “Progressive Unet” which consists of concatenating multiple Unets during forward pass and fine-tuning only the last Unet for back-propagation. Using a Progressive Unet, we observed an improved performance with similar computational cost for fine-tuning compared to the standard Unet implementation.

7.3 Method

7.3.1 Data acquisition and preprocessing

Data were acquired following an IRB approved protocol. All images used in this work were de-identified to protect the privacy of human participants.

Retrospective HPFP data

Multi-echo 3D GRE data acquired in 30 multiple sclerosis (MS) patients on a clinical 3T scanner (Siemens Healthineers) were retrospectively analyzed. The acquisition parameters were as follows: FA=15°, FOV = 24.0 cm, TE1 = 6.3 ms, TR = 50.0 ms, #TE = 10, ΔTE = 4.1 ms, acquisition matrix = 320 × 320 × 48, voxel size = 0.75 × 0.75 × 3 mm³. The tissue field was estimated using non-linear fitting of the multi-echo phase data [44], followed by phase unwrapping and background field removal [60]. QSM was reconstructed using Morphology Enabled Dipole Inversion (MEDI) [170]. The HPFP f_{HPF} at TE4 = 22.7 ms was computed retrospectively as the phase of the original complex image of slice c divided by its Hann low-pass filtering H_{FC} (·):

$$f_{HPF} = \angle \left(\frac{c}{H_{FC}(c)} \right), \quad [7.1]$$

18/2/10 of 30 patients were used as training/validation/test datasets. 3D patches with patch size 128*128*32 and extraction step size 90*90*10 were extracted for training and validation. Whole 3D volumes were fed into the network for testing.

Prospective HPFP data

3D GRE data was acquired prospectively in 9 healthy volunteers with both single-echo (TE = 22.7 ms, TR = 50.0 ms) and multi-echo acquisitions using the same 3T Siemens scanner and imaging parameters identical to the retrospective HPFP dataset. HPFP and SWI images from the single-echo GRE data were generated prospectively

by the scanner software with unknown high-pass filter parameters. QSM was reconstructed from the multi-echo GRE data using the same pipeline as the retrospective HPFP dataset. This formed another test set with prospective HPFP inputs and the corresponding QSM references.

Network pre-training and fine-tuning

Network pre-training

Inspired by [177], a progressive 3D Unet architecture with sequentially concatenated $K = 4$ Unets was constructed to predict QSM from HPFP (Figure 7.1). Nth Unet predicted an intermediate QSM_n from the input consisting of QSM_{n-1} generated by preceding Unet unit and the original HPFP. The purpose of such architecture was to progressively refine the network prediction in an iterative way, mimicking the numerical optimization scheme with iterative update of target solution. In the progressive Unet, a sum of L_1 losses between the output of each Unet and the QSM label was used to train the network with Adam optimizer [37] with learning rate $1e-3$ and 100 epochs on an RTX2080Ti GPU. In 3D Unet, each convolutional layer consisted of 3D convolution, batch normalization [178] and ReLU activation operations. Four levels of down-sampling with 32, 64, 128, and 256 output channels were used in 3D Unet to extract multiscale features.

Physics-based fine-tuning

During testing, the last Unet in the pre-trained network was fine-tuned using the

following high-pass filtering dipole convolution forward model on the whole 3D volume:

$$loss_{FT} = \left\| \angle \left(\frac{m \cdot e^{i(d*x)}}{H_{FC}(m \cdot e^{i(d*x)})} \right) - f_{HPF} \right\|_2^2, \quad (2)$$

where m is the magnitude image at the corresponding SWI echo time, d is the dipole kernel, x is the QSM output of the last Unet with fixed input HPFP f_{HPF} and QSM from the preceding Unet. As a result, f_{HPF} is used in both network input and fine-tuning loss function in a self-supervised fashion. During fine-tuning, the relative cutoff frequency FC in $H_{FC}(\cdot)$ was selected as 1/2 of the largest in-plane matrix dimension (320). The loss function in Eq. 2 was backpropagated until the input of the last Unet to update the pre-trained weights of the last Unet alone. Adam optimizer with 1e-4 learning rate was used and fine-tuning was terminated when the relative change of $loss_{FT}$ in Eq. 2 between two consecutive iterations fell below 5×10^{-3} [7] or started to fluctuate. Because the network weights for the last Unet are updated specifically for the test data in question, network inference has an increased computational cost (12s per case on average) compared to a conventional Unet (0.6s per case on average), where only a single pass through the network (with fixed weights) is required.

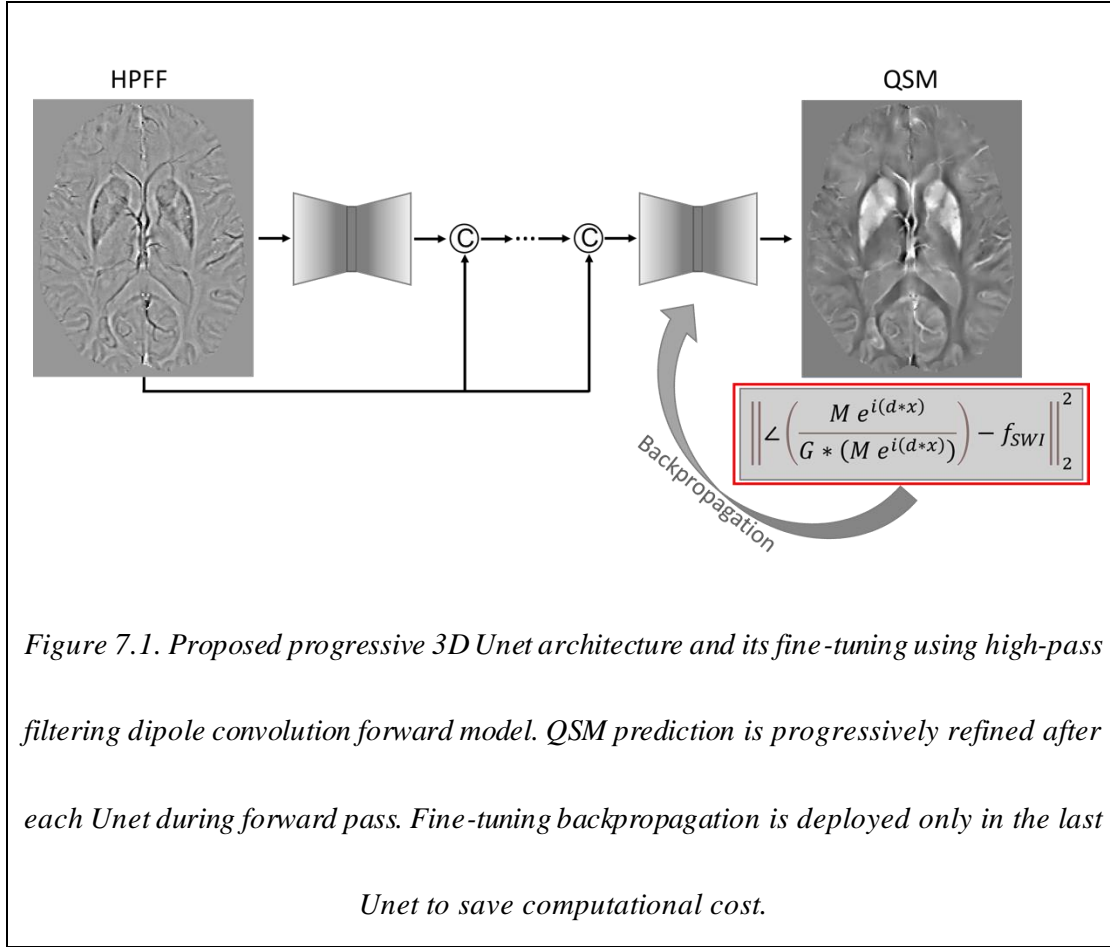
7.3.2 Experiments

Retrospective HPFP dataset with various FCs

To test how physics-based fine-tuning can improve the generalization ability of the pre-trained network to unknown Hann filters not seen during training, HPFP test data with various FC s (1/4, 3/8, 1/2, 5/8 and 3/4) in the Hann filters was calculated. Same QSM labels were used to compute network prediction accuracy. During fine-tuning, FC in Eq. 2 was fixed as 1/2 when tested on HPFP test data generated with any FC , simulating practical situation of a priori unknown cutoff frequency.

Retrospective HPFP dataset with various voxel sizes

To test the generalization ability to voxel sizes not seen during training, multi-echo complex GRE data with the original in-plane voxel size 0.75×0.75 mm² (matrix size: 320×320) was resampled to in plane voxel sizes 0.577×0.577 mm², 0.938×0.938 mm², and 1.25×1.25 mm² (matrix sizes 416×416 , 256×256 , and 192×192 , respectively), while slice thickness was kept the same. Resampling was



implemented as k-space zero-padding or truncation of the original complex data.

QSM labels for each voxel size were computed from the resampled data following the same processing pipeline as the original data. During fine-tuning, voxel size used in the dipole kernel d in Eq. 2 was modified accordingly.

Prospective HPFP dataset

To test the generalization ability of the proposed physics-based fine-tuning to unknown high-pass filtering process, HPFP and magnitude images computed by the scanner software from the single-echo GRE data were used in the fine-tuning loss Eq. 2 and the same HPFP image was also fed into the network as input. The relative cut-

off frequency FC in Eq. 2 was fixed to $1/2$. QSM from the multi-echo GRE data was used as reference for comparison.

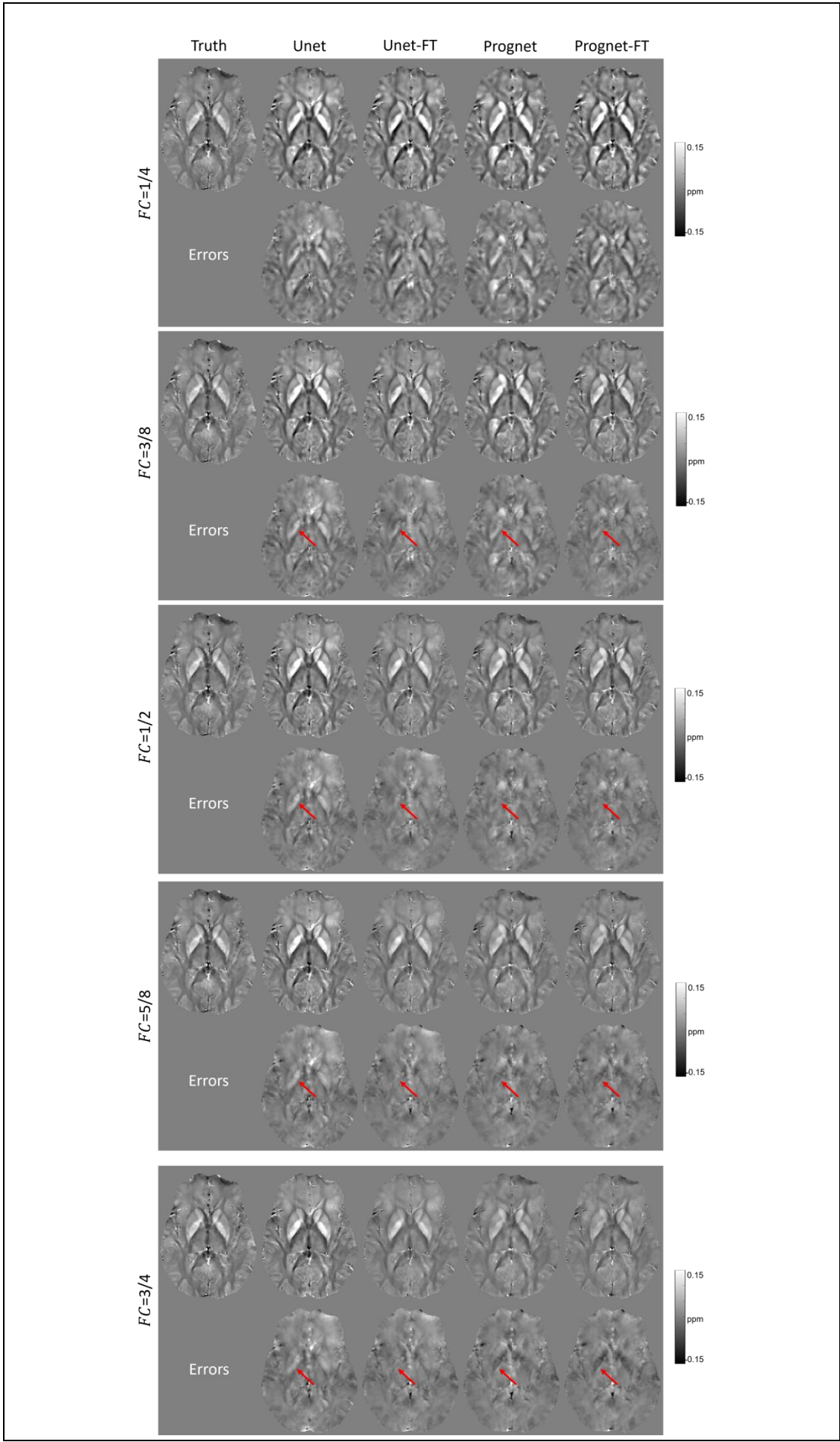


Figure 7.2. Retrospective HPFP test case with cutoff frequency $FCs = 1/4, 3/8, 1/2, 5/8$ and $3/4$ in Hann filters. $FC = 1/2$ was used in the training dataset as well as fine-tuning loss function Eq. 2. At $FC = 1/2$, visible over-estimation of GP in Unet reconstruction was reduced in Unet-FT, Prognnet and Prognnet-FT reconstructions (red arrows). At $FC = 3/8$, moderate image blurring and GP over-estimation in Unet and Prognnet reconstructions were mitigated by Unet-FT and Prognnet-FT (red arrows). At $FC = 1/4$, excessive image blurring was observed in Unet, Unet-FT, Prognnet and Prognnet-FT reconstructions. At $FC = 5/8$ and $3/4$, GP over-estimation in Unet was reduced in Unet-FT (red arrows). Slight under-estimation of GP was observed in Prognnet and Prognnet-FT (red arrows).

Performance comparison

The proposed progressive Unet with physics-based fine-tuning (Prognnet-FT) was compared to the pre-trained progressive Unet (Prognnet), pre-trained Unet (Unet) and Unet with physics-based fine-tuning (Unet-FT). For both retrospective HPFP datasets, root mean squared error (RMSE), peak signal-to-noise ratio (PSNR), structure similarity index (SSIM) and high-frequency error norm (HFEN) metrics were used to quantify the QSM reconstruction accuracy [135] with boxplots for demonstration. For the prospective HPFP dataset, regions of interest (ROIs) in the left and right caudate nuclei (CN), globus pallidus (GP) and putamen (PU) were manually segmented and mean susceptibility values of these ROIs were computed and compared.

7.4 Results

Figure 7.2 shows the predicted QSMs of one retrospective HPFP test case with $FC = 1/4, 3/8, 1/2, 5/8$ and $3/4$. At $FC = 1/2$ (i.e., FC used for training), a visible over-estimation of GP was observed in Unet reconstruction but was reduced in Unet-FT, Prognet and Prognet-FT reconstructions (red arrows). At $FC = 3/8$, Unet and Prognet reconstructions suffered from moderate blurring besides GP over-estimation (red arrows), but both issues were mitigated by Unet-FT and Prognet-FT. At $FC = 1/4$,

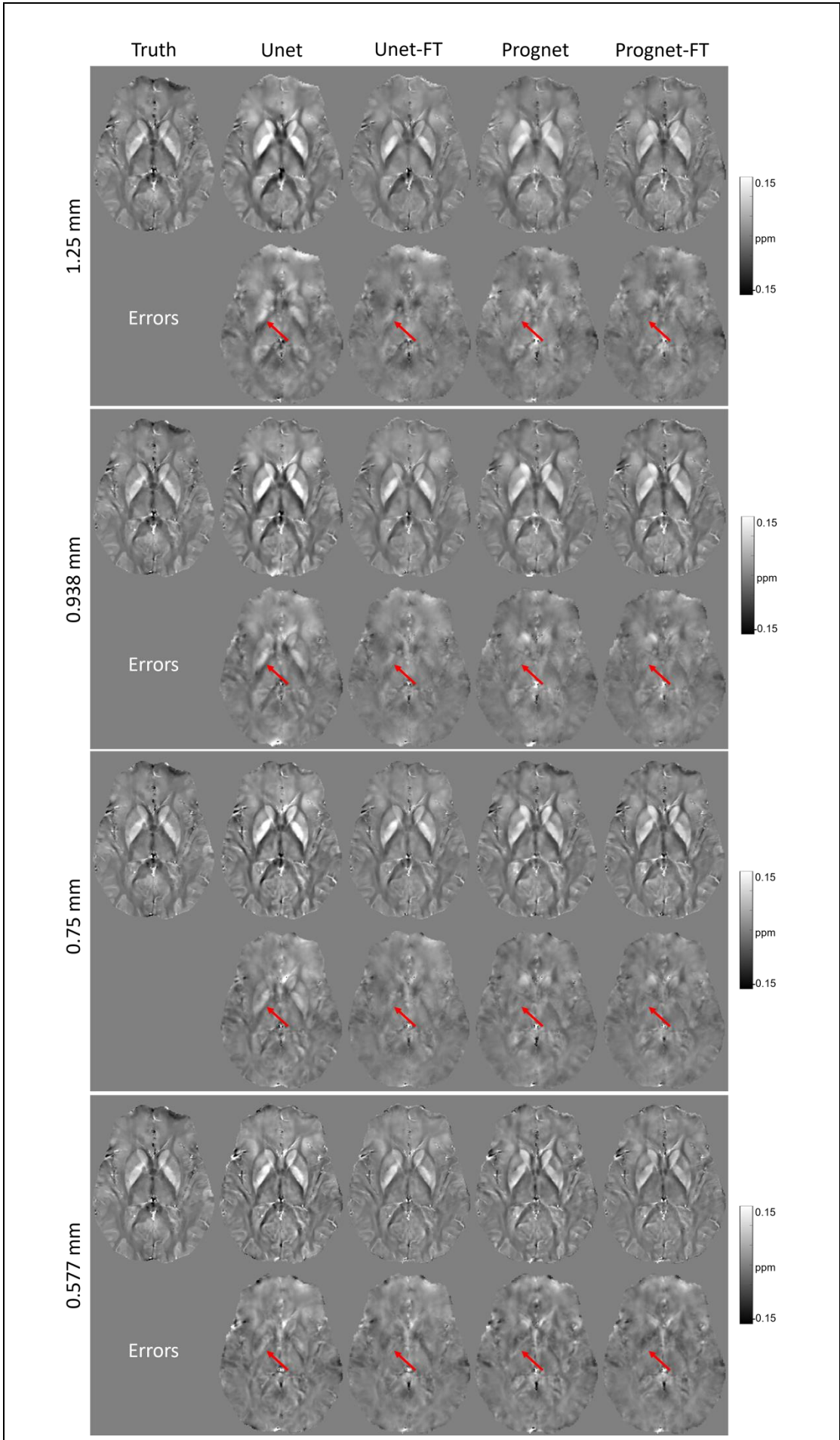


Figure 7.3. Retrospective HPFP test case with isotropic in-plane voxel sizes = 0.577, 0.75, 0.938 and 1.25 mm. Voxel size = 0.75 mm was used for training. At voxel size = 0.75 mm, visible over-estimation of GP in Unet reconstruction was reduced in Unet-FT, Prognnet and Prognnet-FT reconstructions (red arrows). Besides GP over-estimation, increased image blurring were observed in Unet and Prognnet as the test case voxel size increased (0.938 and 1.25 mm), but were reduced in Unet-FT and Prognnet-FT. Prognnet reconstruction was less blurry than Unet. At voxel size = 0.577 mm, slight blurriness was observed in Unet and Prognnet but was reduced in Unet-FT and Prognnet-FT.

all methods suffered from large performance degradation with excessive image blurring where fine-tuning was not able to improve the image quality. At $FC = 5/8$ and $3/4$, GP over-estimation was also observed in Unet but was reduced in Unet-FT (red arrows). Slight under-estimation of GP was observed in Prognnet and Prognnet-FT (red arrows). Figure 7.4a shows the boxplot of quantitative metrics across 10 test subjects with different FC s. At $FC = 3/8, 1/2, 5/8$ and $3/4$, the reconstruction accuracy of Unet and Prognnet was consistently improved in Unet-FT and Prognnet-FT with physics-based fine-tuning. Prognnet slightly outperformed Unet both before and after fine-tuning. At $FC = 1/4$, the reconstruction accuracy of Unet and Prognnet was dramatically decreased compared to the other FC s and fine-tuning resulted in worse accuracy.

Figure 7.3 shows the predicted QSMs of one retrospective HPFP test case with

isotropic in-plane voxel size = 0.577, 0.75, 0.938 and 1.25 mm. At voxel size = 0.75 mm voxel size (i.e., voxel size used for training), a visible over-estimation of GP was observed in Unet reconstruction but was reduced in Unet-FT, Prognnet and Prognnet-FT reconstructions (red arrows). At voxel size = 0.938 and 1.25 mm, besides GP over-estimation in Unet reconstruction, increased image blurring was also observed with increased voxel size, while Unet-FT managed to reduce the blurriness and GP over-estimation. Prognnet reconstruction was less blurry than Unet and was improved in

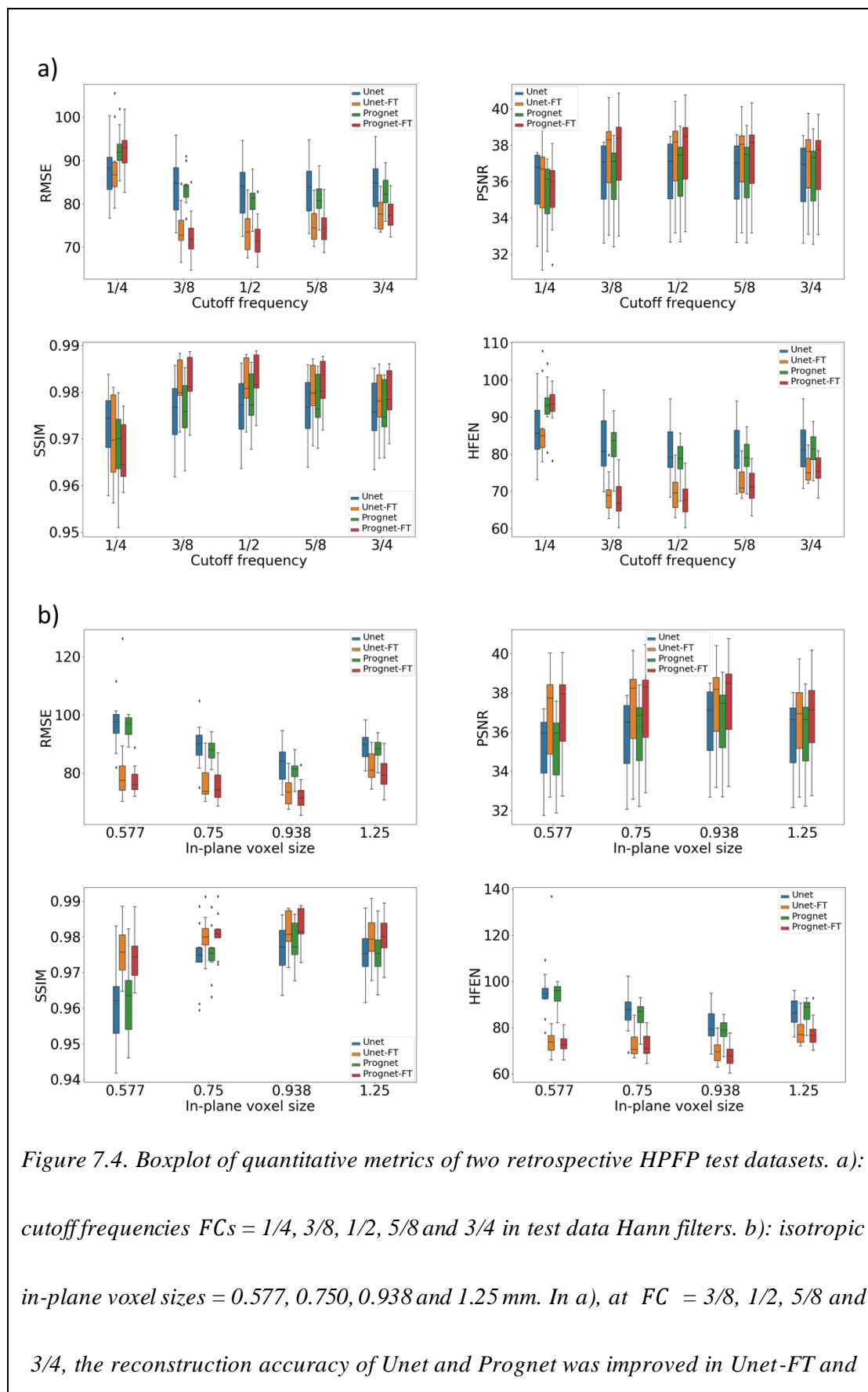


Figure 7.4. Boxplot of quantitative metrics of two retrospective HPFP test datasets. a): cutoff frequencies $FCs = 1/4, 3/8, 1/2, 5/8$ and $3/4$ in test data Hann filters. b): isotropic in-plane voxel sizes = 0.577, 0.750, 0.938 and 1.25 mm. In a), at $FC = 3/8, 1/2, 5/8$ and $3/4$, the reconstruction accuracy of Unet and Prognet was improved in Unet-FT and

Prognnet-FT. Prognnet slightly outperformed Unet both before and after fine-tuning. At $FC = 1/4$, all methods suffered from performance degradation and fine-tuning resulted in worse accuracy. In b), at all voxel sizes, the reconstruction accuracy of Unet and Prognnet was improved in Unet-FT and Prognnet-FT. Prognnet slightly outperformed Unet both before and after fine-tuning.

Prognnet-FT. At voxel size = 0.577 mm, slight blurriness was observed in Unet and Prognnet and was reduced associated with application of fine-tuning. Figure 7.4b shows the boxplot of quantitative metrics across 10 test subjects with different in-plane voxel sizes. Reconstructions of Unet and Prognnet were consistently improved after physics-based fine-tuning at all voxel sizes tested in the experiment. Prognnet slightly outperformed Unet both before and after fine-tuning at all voxel sizes.

Figure 7.5a shows the predicted QSMs of two prospective HPFP test cases. For both cases, Unet and Prognnet visually appeared blurry compared to the reference QSMs. The blurring was suppressed after fine-tuning in Unet-FT and Prognnet-FT. Figure 7.5b shows the comparison of average ROI values across 9 test subjects. Unet and Unet-FT had under-estimation in CN and GP, while Prognnet and Prognnet-FT had slight under-estimation in CN.

7.5 Discussion and Conclusion

In the present work we propose a physics-based network fine-tuning method to improve the generalization ability of reconstructing QSM from HPFP data using deep

learning. Experiments in both retrospective and prospective in vivo data demonstrate improved QSM reconstruction accuracy after fine-tuning when test dataset imaging and postprocessing parameters deviate from those encountered during training.

The major contribution of our work is the utilization of the forward physical model or fidelity loss for test time fine-tuning to reduce generalization errors of deep learning. Such fidelity imposed network edit (FINE) approach was proposed in prior

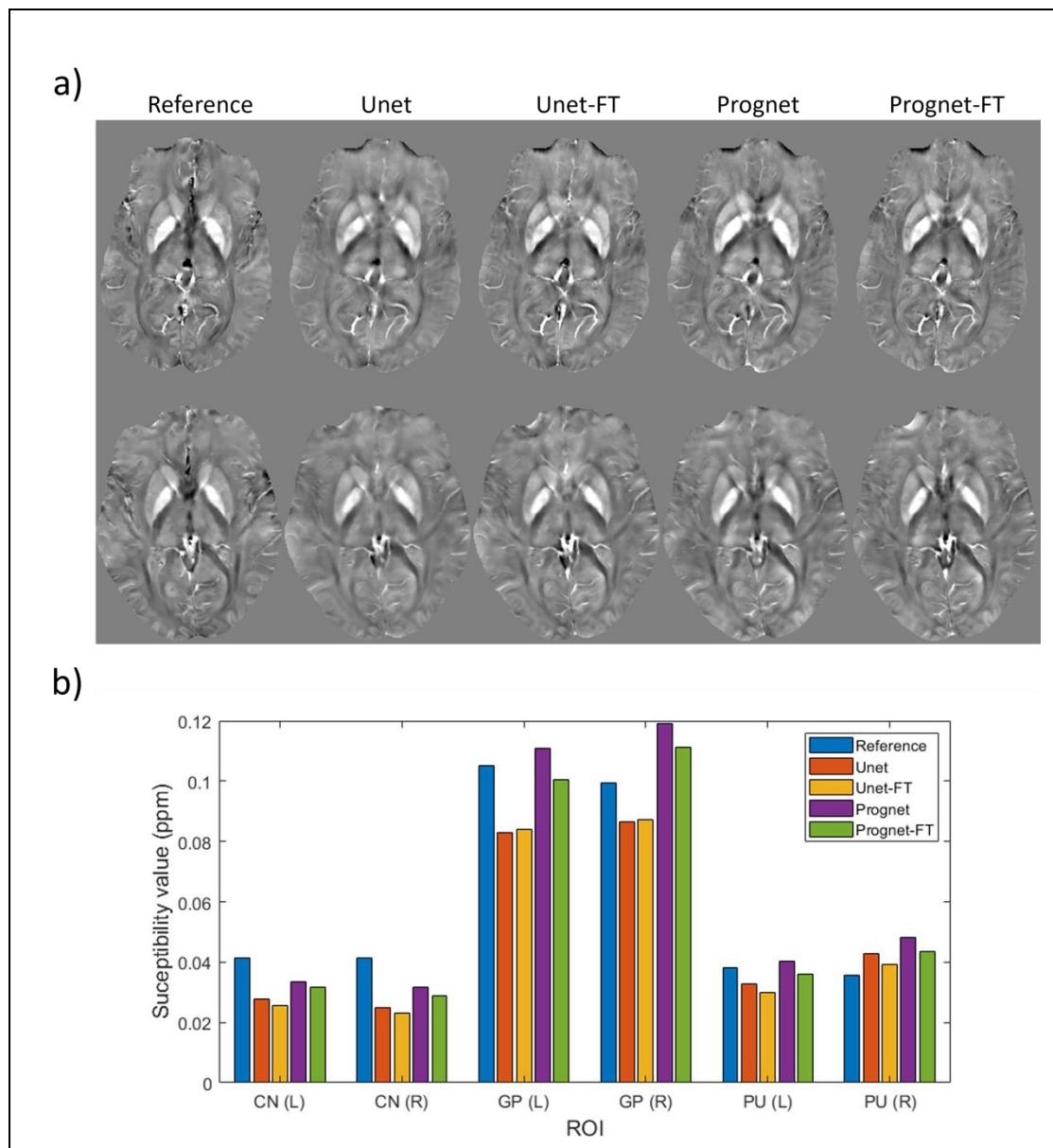


Figure 7.5. a) predicted QSMs of two prospective HPFP test cases and b) ROIs analysis averaged over 9 test cases. In a), compared to the reference QSMs, blurriness for both cases in Unet and Prognet was reduced after fine-tuning in Unet-FT and Prognet-FT. In b), all four methods had slight under-estimation in CN. Unet and Unet-FT had additional under-estimation in GP.

work [7] for ill-posed dipole inversion using deep learning [4, 14, 15, 90, 179, 180], and has been applied to related inverse problems such as water-fat separation [67]. Compared to dipole inversion, QSM reconstruction from HPFP data is a more ill-posed inverse problem, due to properties of both the dipole kernel and the inherent incompleteness of the input data (Eq. 2). Unets have been used to map the filtered tissue field into QSM [174-176]. However, depending on the training data, these networks may not properly reconstruct features not encountered in the training dataset (for instance, different voxel sizes), or when the test data was generated with unknown filter parameters. The proposed fine-tuning step is designed to reduce generalization errors due to such domain shifts and overcome network's lack of fidelity in the test data.

In the present work we show that network fine-tuning results in improved accuracy of QSM reconstruction from HPFP data under small-to-moderate deviations of filter parameters relative to the training data ($FC = 3/8$ and $5/8$ in Figures 7.2 and 7.4a). Possible explanation to this insensitivity is that high-pass filter parameters typically selected in practical setting impose very aggressive filtering, preserving only

sparse details such as phase edges. Therefore, the exact detail of the low frequency suppression may be less important, leading to a low inconsistency between measured HPFP data and data predicted by a possibly inaccurate forward model. However, such explanation does not hold with more information filtered out ($FC = 1/4$ in Figures 7.2 and 7.4a), where under such a large test case deviation, excessive blurring in Unet and Prognnet reconstructions was even exaggerated by fine-tuning, leading to worse reconstruction accuracy.

Another advantage of the proposed approach is the progressive network architecture integrating the advantages of deep learning feature extraction and classical optimization iterative scheme. To this end, the identical Unet blocks were stacked successively to mimic the iterative steps of optimization algorithms [177]. By combining a few refining modules, the quality of the susceptibility distribution image derived from the incomplete HPFP data might be progressively improved through module iterations. Additionally, compared to Unet, the progressive Unet architecture does not increase the computational cost of the physics-based fine-tuning as only the last refining module is updated during test time. Our results suggest that such progressive architecture yields higher reconstruction accuracy compared to Unet in both pre-trained and fine-tuned networks.

There are several limitations present in this work. First, the effectiveness of the progressive architecture needs to be assessed with respect to the number of the repeating

units. Second, the computational cost of fine-tuning (12s per case on average) is higher than a single pass (0.6s per case on average) through a deep neural network due to the additional network updating based on the iterative optimization. Efficiency of fine-tuning also requires further analysis. Third, unrolled architecture needs to be investigated as another strategy incorporating physical model into deep learning. Unrolled network architectures have become popular in QSM-related research, with applications in multi-echo gradient echo sequence acceleration [9, 53, 180] and dipole inversion [181-183]. Unrolled networks are inspired by classical optimization schemes replacing hand-crafted regularizations with deep learning modules [184]. As a result, unrolled networks leverage both the advantages of forward physical model incorporation and progressive architecture. Future work should also include implementation of the unrolled architecture for QSM reconstruction from HPFP data.

In summary, the physics-based fine-tuning strategy promises to be useful for solving ill-posed high-pass filtered dipole inversion inverse problem and reduce generalization errors of end-to-end neural networks.

CHAPTER 8. PDI: PROBABILISTIC DIPOLE INVERSION FOR ADAPTIVE QUANTITATIVE SUSCEPTIBILITY MAPPING

8.1 Abstract

A learning-based posterior distribution estimation method, Probabilistic Dipole Inversion (PDI), is proposed to solve the quantitative susceptibility mapping (QSM) inverse problem in MRI with uncertainty estimation. In PDI, a deep convolutional neural network (CNN) is used to represent the multivariate Gaussian distribution as the approximate posterior distribution of susceptibility given the input measured field. Such CNN is first trained on healthy subjects via posterior density estimation, where the training dataset contains samples from the true posterior distribution. Domain adaptations are then deployed on patient datasets with new pathologies not included in pre-training, where PDI updates the pre-trained CNN's weights in an unsupervised fashion by minimizing the Kullback–Leibler divergence between the approximate posterior distribution represented by CNN and the true posterior distribution from the likelihood distribution of a known physical model and pre-defined prior distribution. Based on our experiments, PDI provides additional uncertainty estimation compared to the conventional MAP approach, while addressing the potential issue of the pre-trained CNN when test data deviates from training. Our code is available at https://github.com/Jinwei1209/Bayesian_QSM.

8.2 Introduction

Quantitative susceptibility mapping (QSM) [6] is an image contrast in MRI to measure the underlying tissue apparent magnetic susceptibility, which enables quantification of specific biomarkers such as iron, calcium and gadolinium [46]. The forward model of QSM in three dimensional image space is:

$$b = d * \chi + n \quad [8.1]$$

where χ is the tissue susceptibility, b is the measured local magnetic field, d is the spatial dipole convolution kernel, and n is the measurement noise. Dipole convolution can also be defined in k-space (Fourier space) as follows:

$$b = F^H D F \chi + n \quad [8.2]$$

where F is the Fourier transform operator and D is the point-wise multiplication operator with the dipole kernel in k-space. The k-space formulation is more computationally efficient because of the fast Fourier transform, so Eq. 8.2 is often implemented in practice. The standard deviation (SD) of the Gaussian noise n is obtained by computing the variance of the least squares fit of the magnetic field b from the acquired multi-echo data [43]. The problem is to recover χ from b due to the ill-posedness of the dipole kernel in QSM [46]. Two representative methods have been proposed to solve the QSM inverse problem. The first one is called COSMOS

(calculation of susceptibility through multiple orientation sampling) [134]. COSMOS relies on multiple orientation scans to calculate the susceptibility map with high accuracy. As a result, it has been used as the gold standard reference when developing new QSM algorithms. However, the drawback of COSMOS is that it requires at least three orientation scans, which is infeasible for clinical use. Another method called MEDI (morphology enabled dipole inversion) [45] was proposed to solve the QSM problem with a single orientation scan. MEDI uses a morphology-related regularization term and solves the following optimization problem:

$$\hat{\chi} = \underset{\chi}{\operatorname{argmin}} \frac{1}{2} \|W(F^H D F \chi - b)\|_2^2 + \lambda \|M_G \nabla \chi\|_1, \quad [8.3]$$

where W is derived from the observation noise covariance matrix, λ is the tunable parameter of weighted total variation (TV) regularization with binary weighting matrix M of susceptibility's spatial gradients which only penalizes regions outside the brain tissue edges in order to suppress image-space artifacts introduced by dipole inversion. With efficient numerical solvers, MEDI generates reasonable susceptibility maps compared to COSMOS as a reference and requires only single orientation scan. From the Bayesian point of view, Eq. 8.3 belongs to the maximum a posteriori probability (MAP) estimation problem with the likelihood distribution defined as a multivariate Gaussian:

$$p(b|\chi) = \mathcal{N}\left(b \mid F^H D F \chi, \Sigma(b|\chi)\right) \quad [8.4]$$

where $n \sim \mathcal{N}(0, \Sigma_{(b|\chi)})$ with $\Sigma_{(b|\chi)}$ diagonal, and the prior distribution defined as the Laplace of the spatial gradient:

$$p(\chi) \propto e^{-\lambda \|\mathcal{M}\nabla\chi\|_1} \quad [8.5]$$

Based on Bayes’s rule, the full posterior distribution $p(\chi|b)$ given the measured local field b can also be estimated in principle, which will quantify the uncertainty in the solutions delivered and may have some clinical implications. In this paper, motivated by the posterior distribution estimation problem in QSM and advances in deep learning based density estimation techniques, we introduce a set of neural network parameterized distributions to learn an approximate posterior distribution of susceptibility χ for any given b with an adaptive training strategy. We validate our method on both healthy subjects and patients and show good performance of the proposed method. This paper is extended from previously published work [15] at MIDL 2020. The additions include a detailed methodology section, comparisons to PDI-VI0 as another baseline in Figures 8.4 and Table 8.1, an experiment on multiple sclerosis patients in Figure 8.3, amortized versus subject-specific variational inference in Figure 8.5 and 8.6, uncertainty estimation evaluation in Figure 8.7, and the discussion section.

8.3 Related Work

In recent years, posterior distribution estimation in imaging inverse problems has

become a new topic in medical imaging [185, 186], in which variance of a random variable is provided from posterior distribution to measure the uncertainty of the solution. However, posterior distribution estimation requires a complicated or even intractable integral from Bayes formula. Therefore, approximate inference methods are used to reduce the computational cost and intractability of the problem. Markov chain Monte Carlo (MCMC) [187] and variational inference (VI [188]) are two classes of approximate inference approaches to the Bayesian estimation problem. In MCMC, Markov chain based sampling methods are used to generate random samples from the true posterior distribution in order to represent an empirical distribution which resembles the true distribution. MCMC is general in that it is able to achieve the exact inference given infinite computational time. However, in imaging inverse problems, the computational cost of MCMC for Bayesian estimation is often several magnitudes higher than that of the optimization method of MAP estimation, because of the curse of dimensionality [189]. In addition, convergence of Markov chain is hard to diagnose, raising concerns on the quality of the samples.

An alternative approach is to use VI, in which an approximate distribution is proposed with tractable function form and unknown parameters, and an optimization algorithm is used (for example, expectation-maximization (EM) algorithm [190]) to learn these parameters by minimizing the divergence between the true and approximate posterior distributions. After convergence, the approximate posterior distribution is expected to

represent the true posterior distribution. Compared to MCMC, VI is fairly efficient as the inference problem is reduced to the optimization problem with respect to the distribution parameters. However, VI may make the model less expressive and thus lead to suboptimal performance. Although more complicated approximate function has a better representation ability in some cases, it introduces higher computational cost. Such accuracy-computation trade-off cannot be achieved easily as the inference performance depends on the tricky design of the approximate distribution form.

Due to advances in deep learning in the past few years, using deep neural network as the approximate function has become a new trend in VI. This is especially true for generative models such as variational auto-encoder (VAE) [191, 192], in which an encoder network is built to approximate the latent variable distribution conditioned on the observed data and a decoder network is built to represent the observed data distribution conditioned on the latent variable. In addition, because of the generalization ability of a deep neural network with millions of trainable weights, amortized formulation with regularization is applied on the training dataset to learn the network weights for faster inference on the test dataset than classic VI per data, but at the expense of lower precision [193]. As a result, this leads to a new trade-off between inference speed and amortization accuracy.

Another topic related to posterior distribution estimation with deep learning are the deep generative models trained with maximum likelihood, such as autoregressive

[194] and flow models [195]. In these models, neural network parameterized models are built to deploy tractable maximum likelihood training and generate new samples after training. If the parameterized model family is highly expressive with enough training samples, maximum likelihood training is expected to learn parameters which fit to the true data density well and generate new data with high fidelity.

Autoregressive and flow models differ from VAE in that exact likelihood is evaluated in the former while approximate evaluation is applied for the latter. Such tractable inference makes training simpler but models less expressive, except for flow models which provide a combination of tractability and high expressiveness.

In this work, we propose to solve the posterior distribution estimation problem in QSM using a neural network parameterized distribution family by combining posterior density estimation from samples with posterior distribution approximation via VI for domain adaptation. Assuming multivariate Gaussian represented by a CNN as the posterior distribution of susceptibility given the input local field, a COSMOS [134] dataset of field susceptibility pairs were used as samples from the true posterior distribution to train such CNN with an MAP loss function. Applying the likelihood in Eq. 4 and prior in Eq. 5, the pre-trained CNN was adapted using VI posterior distribution approximation on different patient datasets which only contained input measured fields. Compared to MAP estimation MEDI [45] in Eq. 8.3 and other deep learning QSM methods, QSMnet [4] and FINE [11], the proposed method estimated

the full posterior distribution of susceptibility with uncertainty quantification, while achieving domain adaptations on various datasets.

8.4 Method

Based on the assumption that the pattern from field b to $p(\chi|b)$ is recoverable, a general distribution $p_{data}(\chi|b)$ for any given b can be approximated with a learning-based approach. To accomplish that, a set of parameterized distributions $q_{\psi}(\chi|b)$ using a neural network with parameters ψ are introduced and learned on a cohort of datasets including healthy subjects and patients. In this work, we assume a multivariate Gaussian distribution with diagonal covariance matrix as the approximate posterior distribution, i.e., $q_{\psi}(\chi|b) = \mathcal{N}(\mu_{(\chi|b)}, \Sigma_{(\chi|b)})$, and use a dual-decoder network architecture (Figure 8.1) extended from 3D U-Net [136] to represent $q_{\psi}(\chi|b)$, with dual decoder’s outputs representing mean $\mu_{(\chi|b)}$ and variance $\Sigma_{(\chi|b)}$ maps.

8.4.1 Posterior Density Estimation

The modeling process consists of two steps. The first step employs the COSMOS dataset. Since COSMOS provides gold standard QSM images based on multiple orientation scans, we can treat COSMOS field-susceptibility data pairs as the samples from the true posterior data distribution. Given the large number of samples, they define an empirical distribution as follows:

$$\hat{p}_{data}(\chi|\mathbf{b}) = \frac{1}{N} \sum_{i=1}^N \mathbf{1}[\chi = \chi_i | \mathbf{b} = \mathbf{b}_i] \quad [8.6]$$

where (\mathbf{b}_i, χ_i) is the i -th susceptibility-field data pair sampled from $p_{data}(\chi|\mathbf{b})$ with total N samples, and $\mathbf{1}[\cdot]$ is the indicator function. We use Kullback–Leibler (KL) divergence as the loss function to measure the distance between the empirical distribution defined by the COSMOS samples and the parameterized approximate distribution defined by the network, i.e., $\text{KL}[\hat{p}_{data}(\chi|\mathbf{b})||q_{\psi}(\chi|\mathbf{b})]$ which is equivalent to the following loss function:

$$\text{KL}[\hat{p}_{data}(\chi|\mathbf{b})||q_{\psi}(\chi|\mathbf{b})] = \sum_{i=1}^N -\log q_{\psi}(\chi_i|\mathbf{b}_i) + H(\hat{p}_{data}) \quad [8.7]$$

where the first term computes the expectation of negative log posterior density with respect to the empirical distribution and the second term is the entropy of the empirical distribution. Since the second term does not include the learnable parameters ψ , only the first term is used during parameter learning. Notice that training using this loss function is equivalent to maximizing the parametrized approximate posterior distribution by fitting to the dataset. Inserting $q_{\psi}(\chi|\mathbf{b}) = \mathcal{N}(\mu_{\{\chi|\mathbf{b}\}}, \Sigma_{\{\chi|\mathbf{b}\}})$ into the first term of Eq. 8.7 and removing the second term of entropy, we get the loss function of posterior density estimation with the COSMOS dataset:

$$\frac{1}{N} \sum_{i=1}^N -\log q_{\psi}(\chi_i|\mathbf{b}_i) = \frac{1}{N} \sum_{i=1}^N \frac{1}{2} (\chi_i - \mu_{\chi|\mathbf{b}_i})^T \Sigma_{\chi|\mathbf{b}_i}^{-1} (\chi_i - \mu_{\chi|\mathbf{b}_i}) + \frac{1}{2} \ln |\Sigma_{\chi|\mathbf{b}_i}|. \quad [8.8]$$

We refer to $q_\psi(\chi|b)$ trained with the COSMOS dataset as Probabilistic Dipole Inversion (PDI).

8.4.2 VI Domain Adaptation

After training with the COSMOS dataset using Eq. 8.8 and obtaining the learned parameters ψ^o , we can simply estimate $p(\chi|b)$ as $q_{\psi^o}(\chi|b)$ given a test local field b . However, for a new test dataset that deviate from the COSMOS training dataset such as containing a new pathology, inferior outputs may be produced. To address this issue, $q_{\psi^o}(\chi|b)$ can be adapted by deploying VI on a subset of the new test dataset with only local field data needed in the loss function. Specifically, the pre-trained approximation network $q_\psi(\chi|b)$ with initial weights ψ^o can be fine-tuned by minimizing the KL divergence between $p(\chi|b)$ and $q_\psi(\chi|b)$:

$$\begin{aligned}
& KL[q_\psi(\chi|b)||p(\chi|b)] \\
&= E_q [\log q_\psi(\chi|b) - \log p(\chi|b)] \\
&= E_q [\log q_\psi(\chi|b) - \log p(\chi, b)] + \log p(b) \\
&= KL[q_\psi(\chi|b)||p(\chi)] - E_q [\log p(b|\chi)] \tag{8.9}
\end{aligned}$$

where the first term in the last equation imposes the approximate posterior to be similar to the prior, which works as the regularization term for training, and the second term encourages data consistency in the likelihood with the QSM forward

model. Constant term $\log p(b)$ is omitted in the last equation. Inserting the prior distribution in Eq. 8.5 and the likelihood distribution in Eq. 8.4 into the KL divergence in Eq. 8.9:

$$\begin{aligned}
KL[q_\psi(\chi|b)||p(\chi|b)] &= -\frac{1}{2} \ln \Sigma_{\chi|b} + \frac{1}{2K} \sum_{k=1}^K \lambda |M\nabla \chi_k|_1 \\
&+ \frac{1}{2K} \sum_{k=1}^K (F^H DF \chi_k - b)^T \Sigma_{b|\chi}^{-1} (F^H DF \chi_k - b) \quad [8.10]
\end{aligned}$$

where $-\frac{1}{2} \ln \Sigma_{\chi|b}$ is derived from the entropy of $q_\psi(\chi|b)$ in $KL[q_\psi(\chi|b)||p(\chi|b)]$, $-E_q[\ln p(\chi)]$ and $-E_q[\log p(b|\chi)]$ are approximated through Monte Carlo (MC) sampling with K samples χ_k 's from $q_\psi(\chi|b)$. The reparameterization strategy can be used to implement back-propagation [191], where samples from the standard Normal distribution were used to generate samples from the predicted susceptibility distribution by scaling and translating operations, in order to make the predicted susceptibility mean and variance map learnable through back-propagation. In VI domain adaptation, Eq. 8.10 is minimized across the new subjects. Once trained, the adapted $q_\psi(\chi|b)$ can be used to predict $\mu_{(\chi|b)}$ and $\Sigma_{(\chi|b)}$ for new test subject directly, which is the so-called amortized VI. We refer to the fine-tuned approximate distribution with Eq. 8.10 as PDI-VI. Amortized VI can also be deployed without any COSMOS pre-training, in which only the target dataset with single orientation local field maps is needed to learn the probabilistic dipole inversion network using Eq.

8.10. We refer to amortized VI without COSMOS pre-training as PDI-VI0.

The amortized formulation of VI in Eq. 8.10 achieves fast inference during test time compared to the classic VI per case, but potentially at the expense of suboptimal performance [193]. This inference suboptimality can be explained as the *inference gap*, which can be decomposed as follows:

$$\underbrace{KL[q_{\psi^*}(\chi|b)||p(\chi|b)]}_{\text{Approximation gap}} + \underbrace{KL[q_{\psi}(\chi|b)||p(\chi|b)] - KL[q_{\psi^*}(\chi|b)||p(\chi|b)]}_{\text{Approximation gap}} \quad [8.11]$$

where ψ and ψ^* are obtained by amortized and subject-specific VIs of Eq. 8.10. As a result, $KL[q_{\psi}(\chi|b)||p(\chi|b)]$ is decomposed into the two terms above: the approximation gap and the amortization gap. The approximation gap is determined by the capacity of the parameterized model family $q_{\psi}(\chi|b)$ to approximate the true posterior distribution. The amortization gap is determined by the ability of the learned variational parameters ψ to generalize to a new test case. Initialized with the pre-trained PDI from Eq. 8.8, we deployed and compared both amortized and subject-specific VI for QSM posterior distribution estimation.

8.4.3 Relation to VAE

The proposed VI domain adaptation strategy in Eq. 8.9 resembles the unsupervised variational auto-encoder [191]. In VAE, the auto-encoder architecture is used to learn both the approximate inference network as the encoder for the latent space variable z conditioned on the input data x , and the generative network as the decoder of data x

given samples of z . x is expected to be reconstructed from z . Evidence lower bound (ELBO) is used to approximate the log density of data x by training the encoder and decoder simultaneously, where the optimal encoder of ELBO is the true posterior distribution of z given x , at which point the ELBO is tight and equals the log density of data x .

In the proposed PDI-VI strategy for QSM, the approximate posterior distribution is also a neural network "encoder" from the input field b to the "latent" susceptibility χ , whereas the "decoder" is no longer a neural network and does not need to be trained. Instead, this "decoder" is the likelihood distribution from the forward dipole convolution model with additive Gaussian noise in Eq. 8.4. In addition, the prior distribution of the "latent" variable χ in Eq. 8.5 also comes from the domain knowledge of solving the QSM inverse problem. From physics-based likelihood and prior distributions, the same ELBO loss function in Eq. 8.9 is applied. Therefore, the proposed PDI-VI combines the modeling principle of distribution approximation and learning in VAE with the domain knowledge from medical physics in QSM.

8.4.4 Network Architecture

The proposed network architecture of $q_{\psi}(\chi|b)$ is shown in Figure 8.1. This network is inspired by the widely used U-Net [25] for image-to-image mapping tasks in the biomedical deep learning field. The extension of the proposed architecture is to have

one downsampling and two upsampling paths, where each upsampling path generates the mean or variance map from the same compressed feature maps. Skip concatenations between downsampling and upsampling are applied for spatial information sharing and better gradient back-propagation. Loss functions in Eqs. 8.8 and 8.10 are used for training on COSMOS and other datasets. For the loss function in Eq. 8.10, Monte Carlo sampling with reparameterization strategy is applied to stochastically optimize $q_{\psi}(\chi|b)$. The 3D convolutional kernel size is $3 \times 3 \times 3$. The numbers of filters from the highest feature level to the lowest are 32, 64, 128, 256 and 512. Batch normalization [178] after each convolutional layer, and max pooling operation for downsampling and deconvolutional operation for upsampling are used.

8.5 Results

8.5.1 Data Acquisition and Preprocessing

MRI was performed on 7 healthy subjects with 5 brain orientations using a 3T scanner (GE, Waukesha, WI) equipped with a multi-echo 3D gradient echo (GRE) sequence. The acquisition matrix was $256 \times 256 \times 48$ and voxel size was $1 \times 1 \times 3$ mm³. The input local tissue field data b was generated by sequentially deploying non-linear fitting across multi-echo phase data [43], graph-cut based phase unwrapping [162] and background field removal [60]. A reference QSM reconstruction was obtained using COSMOS [134]. Two other datasets were obtained by performing single

orientation GRE MRI on 9 patients with multiple sclerosis (MS) and 7 patients with intracerebral hemorrhage (ICH), which were acquired using the same scanning parameters and image processing procedures as above, except for the COSMOS reconstruction step. Data were acquired following an IRB approved protocol.

For the COSMOS dataset, data from 4/1 subjects (20/5 brain volumes) were used as the training/validation dataset, with augmentation by in-plane rotation of 15° . The brain volume data in the training and validation dataset was divided into 3D patches with patch size $64 \times 64 \times 32$ and extraction step $21 \times 21 \times 1$, generating 9659/2874 patches for training/validation. Data from the remaining 2 subjects (10 brain volumes in total) were used for testing. For the MS patient dataset, data from 6/1 subjects were used as the training/validation dataset and data from the remaining 2

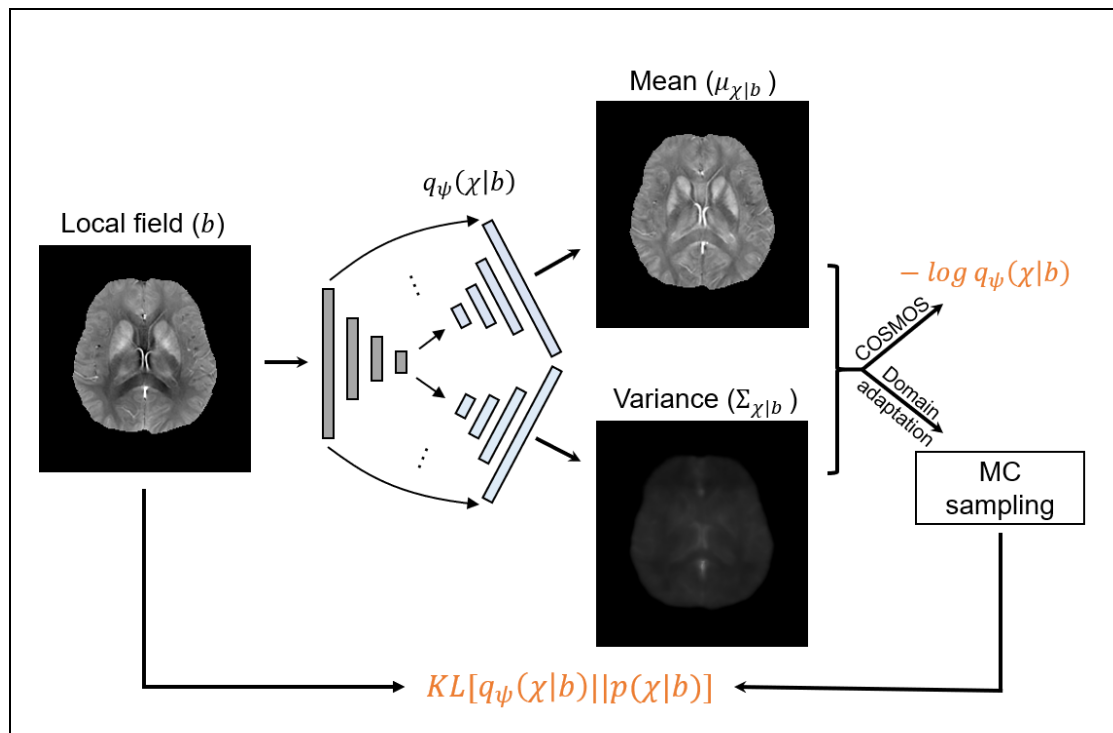
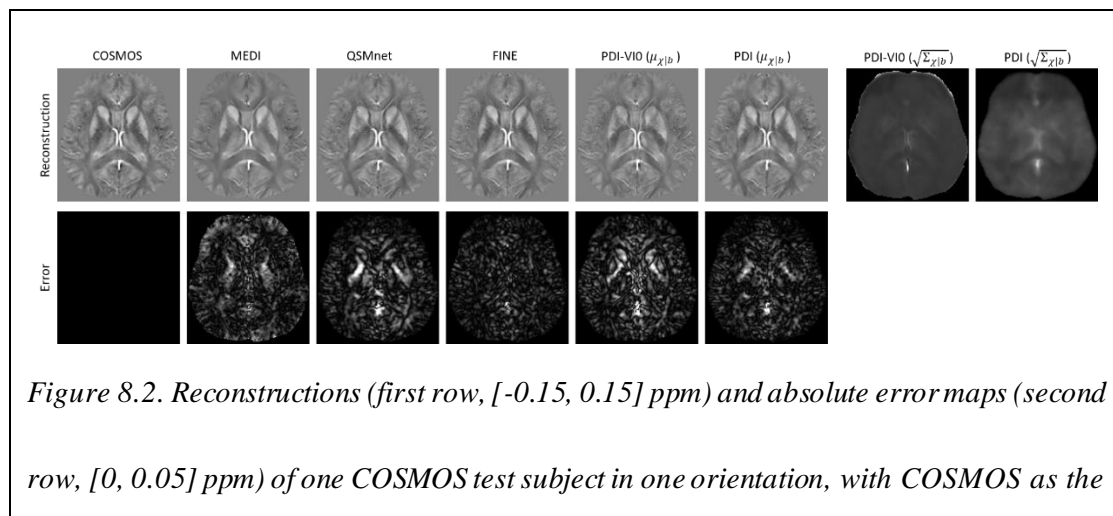


Figure 8.1. The network architecture of the proposed method. Two upsampling paths' outputs represent mean and variance maps of susceptibility. The COSMOS dataset was used to perform posterior density estimation in Eq. 8.8. Domain adaptation VI with MC sampling in Eq. 8.10 were applied on other datasets.

subjects were used for testing. For the ICH patient dataset, data from 4/1 subjects were used as the training/validation dataset and data from the remaining 2 subjects were used for testing.

8.5.2 Implementation Details

The loss function in Eq. 8.8 was applied for posterior density estimation on the COSMOS dataset with Adam optimizer [37] (learning rate: 10^{-3} , Number of epochs: 60), yielding a trained network $q_{\psi^0}(\chi|b)$, denoted as PDI. Initialized with ψ^0 , VI domain adaptations using the loss function in Eq. 8.10 were deployed on both MS and ICH datasets with Adam optimizer (learning

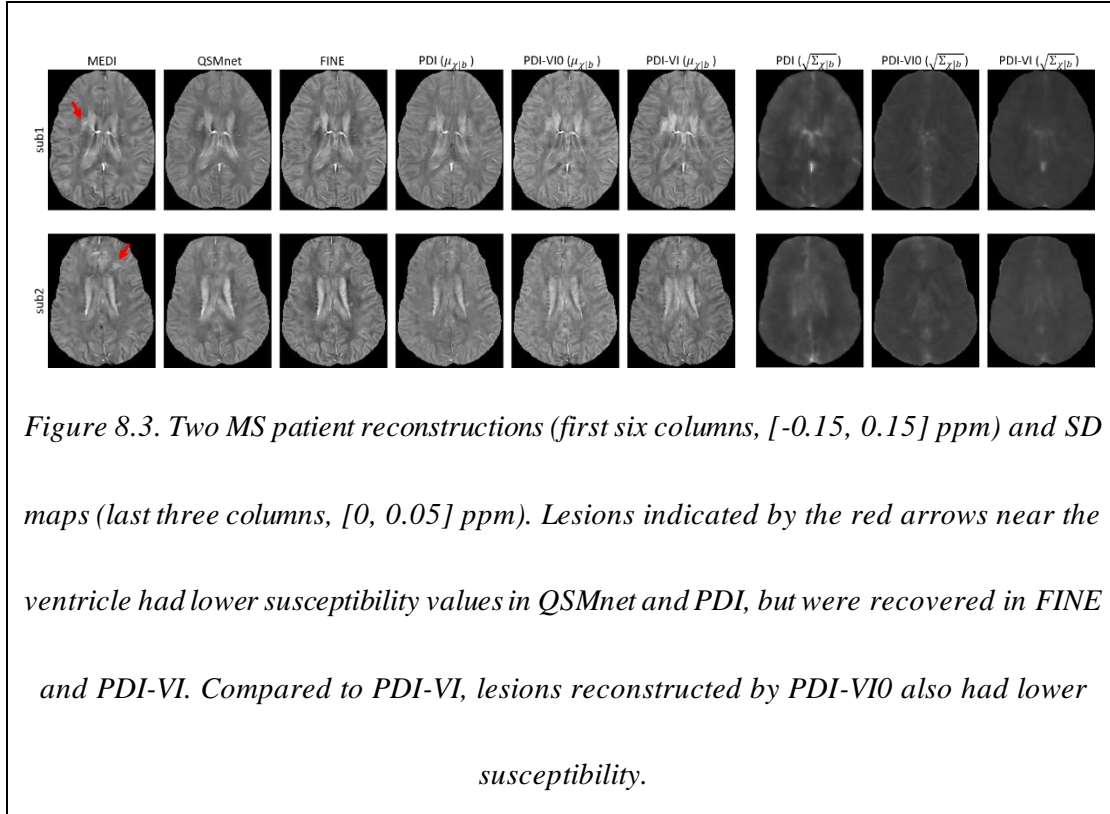


gold standard. FINE achieved the lowest reconstruction error, while the other methods had comparable results. SD maps of PDI, PDI-VI0 and PDI-VI (third row, [0, 0.05] ppm) showed high uncertainties at the sagittal sinus and globus pallidus, which was consistent with their error maps.

rate: 10^{-3} , Number of epochs: 100), denoted as PDI-VI. VIs using Eq. 8.10 and without ψ^0 initialization were also performed and compared for all datasets (Adam [37] learning rate: 10^{-3} , Number of epochs: 100), denoted as PDI-VI0. MC sampling size K in VI was chosen as 5 due to limited GPU memory. The hyperparameter λ in Eq. 8.10 was chosen as 20 to balance the streaking artifact suppression and over-smoothing effect of TV regularization. While training and validation were implemented using 3D patches, whole brain volumes were fed into the network during COSMOS testing and all VI experiments. We implemented the proposed method using PyTorch (Python 3.6) on an RTX 2080Ti GPU.

8.5.3 COSMOS Dataset

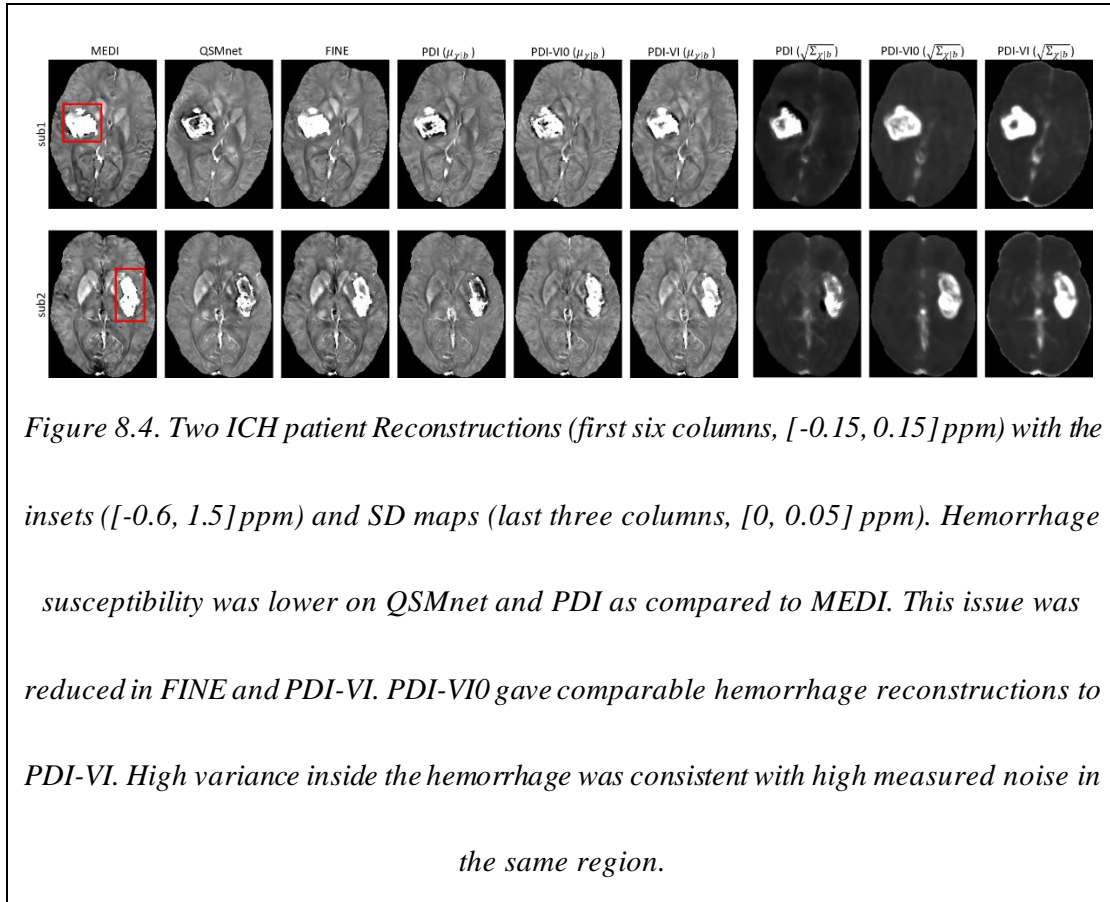
For the COSMOS test dataset, we compared PDI (Eq. 8.8), PDI-VI0 (Eq. 8.10 without PDI pre-training) and PDI-VI (Eq. 8.10 with PDI pre-training) to MAP estimation MEDI and two deep learning reconstructions



QSMnet and FINE. Reconstruction maps of one orientation from one test subject are shown in Figure 8.2. Quantitative metrics of each reconstruction method averaged among 10 test brains are shown in Table 8.1. FINE gave the best overall quantitative results with the expense of significantly increased computational time. The other methods had comparable results. All deep learning methods achieved fast inference time on GPU except FINE. In Figure 8.2, error maps of PDI, PDI-VI0 and PDI-VI's mean outputs $\mu_{\chi|b}$ matched their SD outputs, with high uncertainty/error located at the sagittal sinus and globus pallidus. The SD output of PDI-VI0 and PDI-VI were sharper than PDI with lower white-grey matter variation.

8.5.4 Patient Datasets

The reconstruction maps of two MS patients in the test dataset are shown in Figure 8.3. Lesions indicated by the red arrows had susceptibility values lower in QSMnet and PDI than in MEDI, but were recovered in FINE and PDI-VI. Compared to PDI-



VI, lesions reconstructed by PDI-VI0 also had lower susceptibility, which qualitatively indicated the advantage of the COSMOS dataset pre-training for PDI-VI.

The QSMs for two ICH patients in the test dataset are shown in Figure 8.4. Compared to MEDI and FINE which had hyperintensity inside the hemorrhage, both QSMnet and PDI had lower susceptibility inside this region, which might result from the fact

that such pathology was not encountered during training. After amortized VI domain adaptation, susceptibility value inside the hemorrhage was recovered in PDI-VI.

Shadow artifacts surrounding the hemorrhage were also reduced in PDI-VI from PDI.

PDI-VI0 yielded hemorrhage reconstructions that were comparable to PDI-VI. High

SD map inside the reconstructed hemorrhage as shown in the last three columns of

Figure 8.4 implied high reconstruction uncertainty of this region.

8.5.5 Amortized vs Subject-specific VI

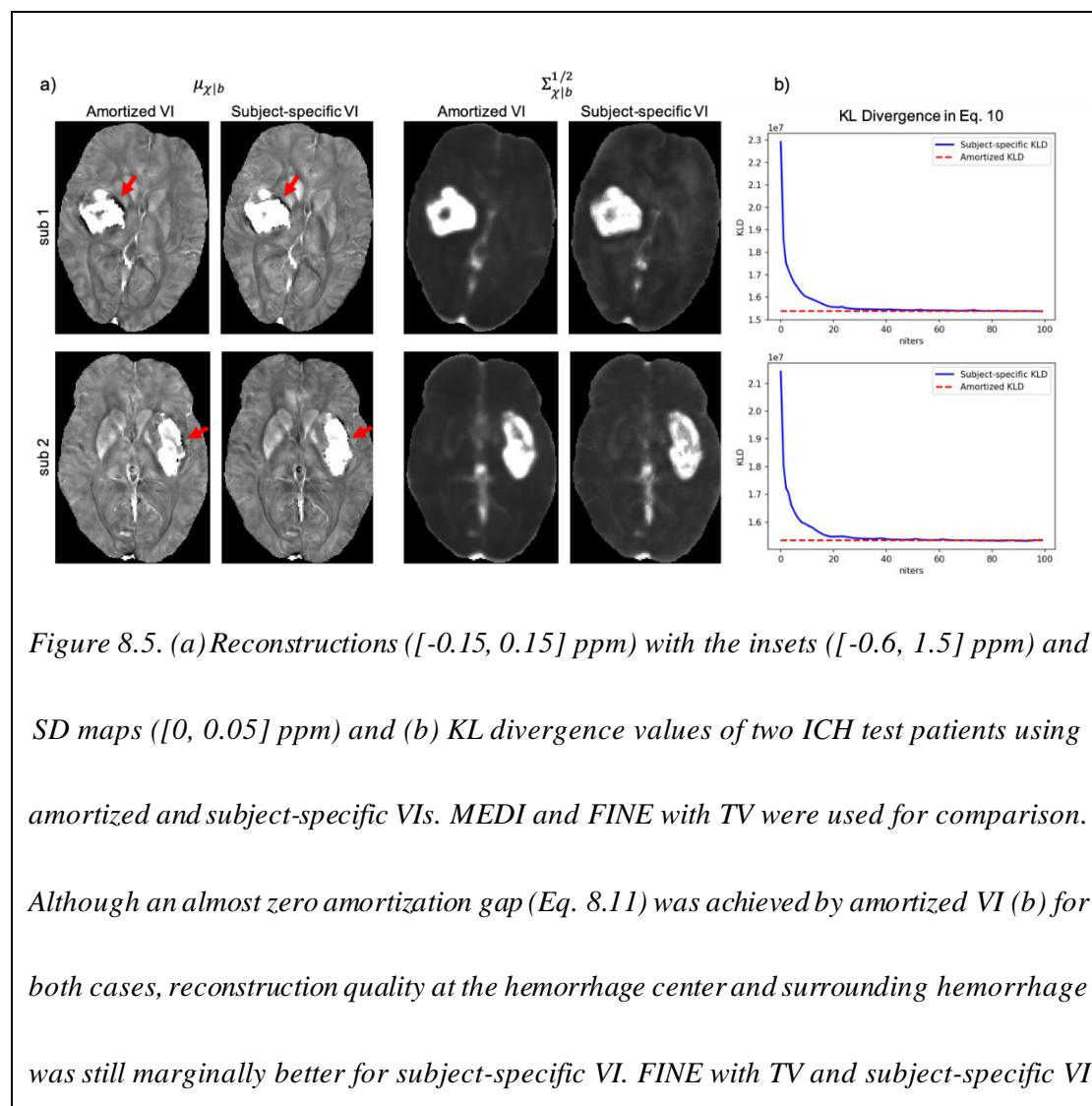
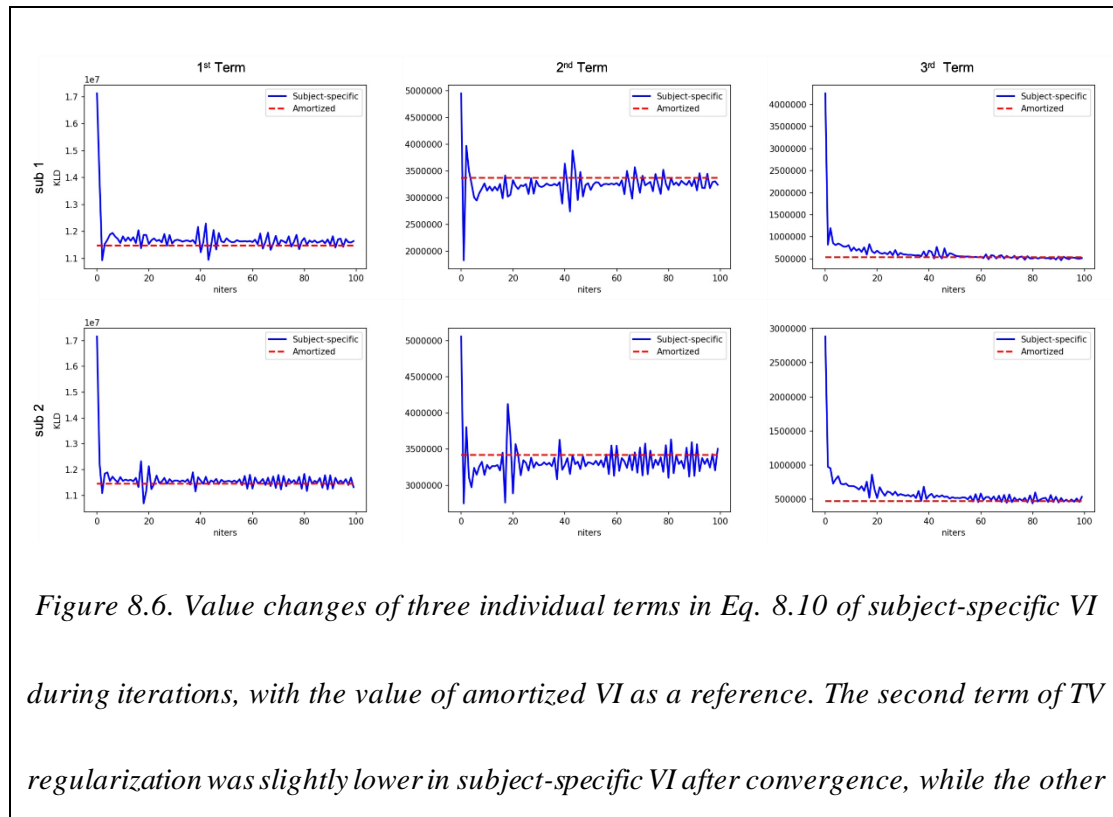


Figure 8.5. (a) Reconstructions ($[-0.15, 0.15]$ ppm) with the insets ($[-0.6, 1.5]$ ppm) and SD maps ($[0, 0.05]$ ppm) and (b) KL divergence values of two ICH test patients using amortized and subject-specific VIs. MEDI and FINE with TV were used for comparison. Although an almost zero amortization gap (Eq. 8.11) was achieved by amortized VI (b) for both cases, reconstruction quality at the hemorrhage center and surrounding hemorrhage was still marginally better for subject-specific VI. FINE with TV and subject-specific VI

achieve comparably image quality.

The inference gap in Eq. 8.11 was investigated on two ICH test cases shown in Figure 8.5, where subject-specific VI using Eq. 8.10 initialized from the weights of PDI was deployed with 100 iterations for convergence. MAP estimations in Eq. 8.3 of iterative reconstruction MEDI and network parametrized reconstruction FINE with TV ($\lambda = 20, 100$ iterations) were also deployed for comparison. As demonstrated in Figure 8.5a, both amortized and subject-specific VIs recovered the susceptibility value inside the hemorrhage from PDI in Figure 8.4. Compared to amortized VI, the susceptibility values at the center of hemorrhage (insets in Figure 8.5a) were further recovered and shadow artifacts surrounding the hemorrhage (red arrows in Figure 8.5) were reduced

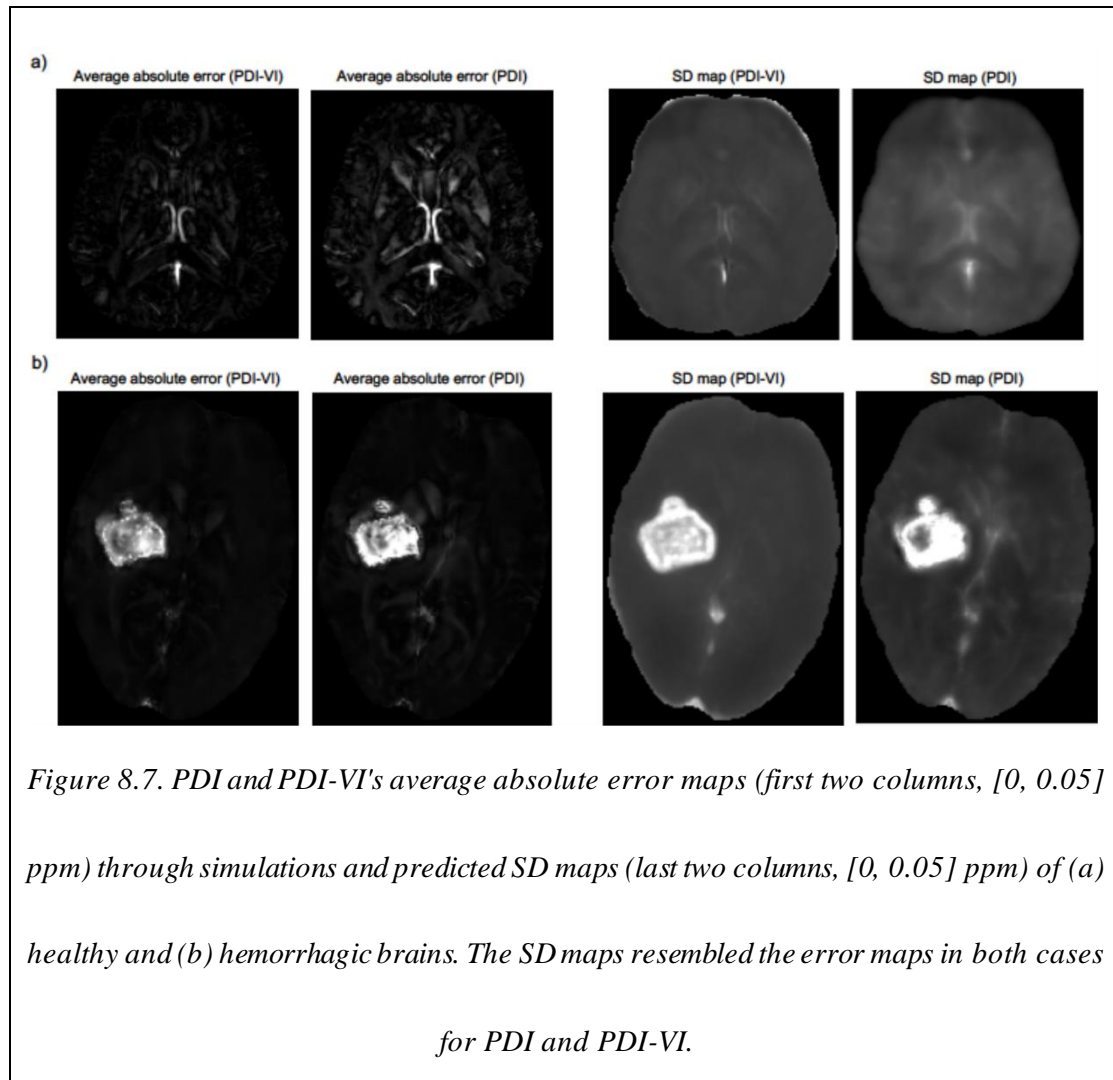


two terms were similar between amortized and subject-specific VIs.

in subject-specific VI. In addition, subject-specific VI had similar reconstructions to MEDI and FINE with TV for both test cases, which confirmed that the mean susceptibility map by subject-specific VI equals the MAP susceptibility maps by MEDI and FINE with TV. Figure 8.5b shows that KL divergence of Eq. 8.10 during subject-specific VIs converged to the value of amortized VIs with almost zero amortization gap (Eq. 8.11). Figure 8.6 shows the value changes of three individual terms in Eq. 8.10 during subject-specific VI iterations, where the second term ($\frac{1}{2K} \sum_{k=1}^K \lambda |M \nabla \chi_k|_1$) was slightly lower on average than the one of amortized VI for both test cases, which might contribute to the improvement of shadow artifact reduction.

8.5.6 Uncertainty Map Evaluation

To evaluate uncertainty estimation performance of the predicted SD map, absolute



error maps of PDI and PDI-VI's mean predictions to the ground truth susceptibilities were computed via simulation, then correlation between susceptibility SD and error maps was examined. Local field inputs were simulated from (a) COSMOS test data in

Table 8.1. Average quantitative metrics of 10 test COSMOS brains reconstructed by different methods. FINE gave the best reconstruction at the expense of significantly increased computational time. The other methods had comparable results.

	PSNR (\uparrow)	RMSE (\downarrow)	SSIM (\uparrow)	HFEN (\downarrow)	GPU time (s)
MEDI	46.39	41.16	0.9569	31.30	17.54
QSMnet	46.35	41.29	0.9705	43.31	0.60
FINE	48.12	33.66	0.9789	31.97	65.42
PDI	47.77	35.08	0.9772	35.17	0.61
PDI-VI0	46.05	42.74	0.9704	42.27	0.61
PDI-VI	46.31	41.51	0.9707	40.58	0.61

Figure 8.2 and (b) FINE reconstruction of the ICH patient in Figure 8.4a through multi-echo data synthesization with additive noise, nonlinear field fitting and phase unwrapping. Details of the simulation steps are shown in Appendix A. Such simulation was repeated 100 times to generate 100 local fields as inputs to PDI and PDI-VI. 100 mean maps of PDI and PDI-VI were predicted accordingly to compute the average absolute errors. Figure 8.7 shows the average absolute error maps and

predicted SD maps of PDI and PDI-VI. In Figure 8.7a, large errors in the cerebral veins and sagittal sinus were reflected in the predicted SD maps for both PDI and PDI-VI, while in Figure 8.7b, large errors in the hemorrhage were also predicted in PDI and PDI-VI's SD maps, which demonstrates good correlation between the error map and the predicted SD map of the proposed method for uncertainty estimation.

8.6 Discussion and Conclusion

The adaptive learning strategy proposed in this paper tackles the domain adaptation challenge in medical imaging with deep learning from a probabilistic distribution refinement point of view. Since the high quality COSMOS samples are acquired only from healthy subjects, posterior density estimation with COSMOS samples may not generalize well to the patients with pathology not covered by the COSMOS dataset. As a result, even though the COSMOS pre-trained PDI performs well on COSMOS test dataset from the same distribution (Figure 8.2), inferior mapping happens evidenced by lower susceptibility values for lesions when applying PDI to the patients directly (Figures 8.3 and 8.4). Based on the distribution approximation principle, the pre-trained density estimation network PDI needs fine-tuning in order to fit to the patient data distribution as well. VI with KL divergence as a measure of similarity between two distributions is used for approximate distribution refinement, which helps reduce the generalization error of PDI (Figure 8.3 and 8.4). However, in terms of other domain generalizations such as different imaging resolutions, PDI-VI with

KL divergence loss function for weight adjustment has not been tested and may suffer in accuracy, which will be explored in the future work. Another domain adaptation method FINE works better than PDI-VI (Figure 8.4) to reduce generalization error of the pre-trained network, since FINE fits to every test case by minimizing the fidelity loss, which has the major drawback of significantly increased computational time (Table 8.1).

The relationship between PDI-VI (Eq. 8.9) and VAE [191] is described in the methods section. The key point is that the generative network (the decoder) from latent variable to data in VAE is replaced by a physics-based likelihood model (Eq. 4) in PDI-VI. This implies a general way of learning the posterior distribution of image data conditioned on the measured signal for any imaging modality, where a specific forward imaging model is used to form the "decoder" and only the "encoder" is learned with input measured signals in an unsupervised fashion like VAE. The training strategy of PDI-VI utilizes both widely available measured signals in clinic and well-defined imaging physical models to improve the reconstruction fidelity of the trained model. When gold standard reconstructions are available for training, as in the COSMOS dataset, combining direct conditional density estimation using high quality images with VI domain adaptation on measured input signals could improve the performance of VI trained on the measured signals alone (Figure 8.3).

PDI defines a set of parameterized distributions using a neural network and learns

these parameters from samples to approximate the true distribution, where the expressiveness of the distribution family affects their approximation ability. The network architecture (Figure 8.1) is inspired by 3D U-Net, which was originally proposed for medical image segmentation tasks and has also been successfully used in deep QSM reconstructions [4, 5, 11], therefore such architecture should be expressive enough for field-to-susceptibility mapping. The COSMOS experiment indicates satisfactory image-to-image mapping ability of the proposed architecture (Figure 8.2 and Table 8.1). The simulation experiment verifies correlation between the predicted SD map and the error map, indicating reasonable uncertainty quantification of PDI and PDI-VI. Despite such merits, the choice of variational posterior form in this work is simply a Gaussian distribution with diagonal covariance matrix, which is known as the mean field approximation for modeling and calculation simplicity in classic VI. This factorized Gaussian does not consider correlation between voxels in the reconstructed susceptibility map, but in view of the forward convolution operation (Eq. 8.1) which aggregates the global susceptibility into the measured field at each location, taking into account the dependency between local voxels in the susceptibility map may make the variational posterior more expressive. Possible options could be improving the Gaussian posterior with a non-diagonal covariance matrix and using an autoregressive [194] or flow-based [195] model to capture the dependency.

The prior distribution of susceptibility (Eq. 8.5) used in PDI-VI comes from MEDI,

where weighted TV regularization was used to suppress streaking artifacts appeared on QSM dipole inversion. In general, the prior distribution $p(x)$ captures the density of data x from a prior knowledge, where higher quality data x has a higher density value. In this sense, estimating the density from sufficient data may build a more comprehensive prior distribution and therefore become more efficient to regularize the inverse problem solution. In fact, learning the prior density for MAP estimation of the imaging inverse problem has been explored by [196] and [197], where VAE and PixelCNN++ [198] were deployed to learn the explicit prior distribution of MR images. These deep prior approaches inspire us to extend our work in the future by learning and evaluating a prior density from data and inserting them into Eqs. 8.9 and 8.10 for VI.

The inference gap (Eq. 8.11) summarizes two types of errors when applying the amortized inference strategy. Amortized VI has the advantage of fast inference during test time. However, it has slightly worse visual quality inside and surrounding the hemorrhage than subject-specific VI (Figure 8.5a). Even though an almost zero amortization gap was achieved (Figure 8.5b), the regularization term of KL divergence (Eq. 8.10) was still better imposed in subject-specific VI, which may contribute to its better reconstruction of the hemorrhage. However, such advantage comes at a cost of extra inference time. To accelerate the inference speed of subject-specific VI, optimizing the initialization of variational parameters is useful to reduce

the number of VI optimization steps. Meta-learning [195, 199] may be applied to optimize the optimization process of VI per data, where a learner can be designed during pre-training to learn an inference algorithm that generalizes well to the data of interest.

CHAPTER 9. FUTURE DIRECTIONS AND CONCLUSION

9.1 Future Directions

Using physics-based deep learning methods to solve data sampling, image reconstruction and biophysical inverse problems such as QSM is an active research area in MRI. Future work based on this thesis includes both continuing methodological development and clinical applications:

9.1.1 LARO for CMRO₂ mapping

It has been shown to be feasible to map the cerebral metabolic rate of oxygen (CMRO₂) by estimating the oxygen extraction fraction (OEF) from complex mGRE data [200]. mGRE acceleration is accomplished by LARO in chapter 3. Future work includes accelerating arterial spin labeling (ASL) sequence using LARO to obtain cerebral blood flow (CBF) for CMRO₂, or/and developing a hybrid sequence combining mGRE and ASL acquisition in a single scan.

9.1.2 mcLARO for Susceptibility Source Separation

Susceptibility source separation can be solved based on a R2' model of positive and negative susceptibility sources [201]. T1, T2, T2* and QSM mapping by mcLARO in chapter 4 is a time-efficient sequence for both R2' mapping and mGRE complex signal acquisition. Future work includes validating mcLARO with susceptibility source separation.

9.1.3 SPARKLING sampling + LARO

In LARO, binary sampling pattern is generated from the learned probabilistic sampling density through independent Bernoulli sampling at each phase encoding location. However, it has been shown that a locally uniform k-space coverage improved reconstruction performance [202], which has not been considered in LARO yet. Future work includes combining LARO with SPARKLING.

9.1.4 Probabilistic diffusion models + LARO

There is currently an increasing interest in adopting denoising diffusion probabilistic models (DDPMs) into deep learning MR reconstruction [203, 204]. Future work also includes combining LARO with DDPM for LARO.

9.2 Conclusion

This thesis focused on solving MR data sampling, image reconstruction and QSM inverse problem using physics-based deep learning methods. Results showed that deep learning methods with physical models managed to improve the performance of the above tasks.

REFERENCES

- [1] C. D. Bahadir, A. Q. Wang, A. V. Dalca, and M. R. Sabuncu, "Deep-learning-based optimization of the under-sampling pattern in MRI," *IEEE Transactions on Computational Imaging*, vol. 6, pp. 1139-1152, 2020.
- [2] K. Hammernik, T. Klatzer, E. Kobler, M. P. Recht, D. K. Sodickson, T. Pock, and F. Knoll, "Learning a variational network for reconstruction of accelerated MRI data," *Magnetic resonance in medicine*, vol. 79, no. 6, pp. 3055-3071, 2018.
- [3] H. K. Aggarwal, M. P. Mani, and M. Jacob, "MoDL: Model-Based Deep Learning Architecture for Inverse Problems," *IEEE transactions on medical imaging*, vol. 38, no. 2, pp. 394-405, 2019.
- [4] J. Yoon, E. Gong, I. Chatnuntawech, B. Bilgic, J. Lee, W. Jung, J. Ko, H. Jung, K. Setsompop, and G. Zaharchuk, "Quantitative susceptibility mapping using deep neural network: QSMnet," *NeuroImage*, vol. 179, pp. 199-206, 2018.
- [5] K. G. B. Rasmussen, M. J. Kristensen, R. G. Blendal, L. R. Ostergaard, M. Plocharski, K. O'Brien, C. Langkammer, A. Janke, M. Barth, and S. Bollmann, "DeepQSM-Using Deep Learning to Solve the Dipole Inversion for MRI Susceptibility Mapping," *Biorxiv*, pp. 278036, 2018.
- [6] L. de Rochefort, T. Liu, B. Kressler, J. Liu, P. Spincemaille, V. Lebon, J. Wu, and Y. Wang, "Quantitative susceptibility map reconstruction from MR phase data using bayesian regularization: validation and application to brain imaging," *Magnetic Resonance in Medicine: An Official Journal of the International Society for Magnetic Resonance in Medicine*, vol. 63, no. 1, pp. 194-206, 2010.
- [7] J. Zhang, H. Zhang, A. Wang, Q. Zhang, M. Sabuncu, P. Spincemaille, T. D. Nguyen, and Y. Wang, "Extending LOUPE for K-space Under-sampling Pattern Optimization in Multi-coil MRI." pp. 91-101.
- [8] J. Zhang, H. Zhang, C. Li, P. Spincemaille, M. Sabuncu, T. D. Nguyen, and Y.

- Wang, "Temporal Feature Fusion with Sampling Pattern Optimization for Multi-echo Gradient Echo Acquisition and Image Reconstruction." pp. 232-242.
- [9] J. Zhang, P. Spincemaille, H. Zhang, T. D. Nguyen, C. Li, J. Li, I. Kovanlikaya, M. R. Sabuncu, and Y. Wang, "LARO: Learned Acquisition and Reconstruction Optimization to accelerate Quantitative Susceptibility Mapping," *NeuroImage*, pp. 119886, 2023.
- [10] J. Zhang, T. D. Nguyen, E. Solomon, C. Li, Q. Zhang, J. Li, H. Zhang, P. Spincemaille, and Y. Wang, "mcLARO: Multi-Contrast Learned Acquisition and Reconstruction Optimization for simultaneous quantitative multi-parametric mapping," *arXiv preprint arXiv:2304.03458*, 2023.
- [11] J. Zhang, Z. Liu, S. Zhang, H. Zhang, P. Spincemaille, T. D. Nguyen, M. R. Sabuncu, and Y. Wang, "Fidelity imposed network edit (FINE) for solving ill-posed image reconstruction," *Neuroimage*, vol. 211, pp. 116579, 2020.
- [12] J. Zhang, H. Zhang, P. Spincemaille, T. Nguyen, M. R. Sabuncu, and Y. Wang, "Hybrid optimization between iterative and network fine-tuning reconstructions for fast quantitative susceptibility mapping." pp. 870-880.
- [13] J. Zhang, A. Dimov, C. Li, H. Zhang, T. D. Nguyen, P. Spincemaille, and Y. Wang, "Physics-based network fine-tuning for robust quantitative susceptibility mapping from high-pass filtered phase," *arXiv preprint arXiv:2305.03844*, 2023.
- [14] J. Zhang, H. Zhang, M. Sabuncu, P. Spincemaille, T. Nguyen, and Y. Wang, "Probabilistic Dipole Inversion for Adaptive Quantitative Susceptibility Mapping," *arXiv preprint arXiv:2009.04251*, 2020.
- [15] J. Zhang, H. Zhang, M. Sabuncu, P. Spincemaille, T. Nguyen, and Y. Wang, "Bayesian learning of probabilistic dipole inversion for quantitative susceptibility mapping." pp. 892-902.
- [16] M. A. Griswold, P. M. Jakob, R. M. Heidemann, M. Nittka, V. Jellus, J. Wang, B. Kiefer, and A. Haase, "Generalized autocalibrating partially parallel

- acquisitions (GRAPPA),” *Magnetic Resonance in Medicine: An Official Journal of the International Society for Magnetic Resonance in Medicine*, vol. 47, no. 6, pp. 1202-1210, 2002.
- [17] K. P. Pruessmann, M. Weiger, M. B. Scheidegger, and P. Boesiger, “SENSE: sensitivity encoding for fast MRI,” *Magnetic Resonance in Medicine: An Official Journal of the International Society for Magnetic Resonance in Medicine*, vol. 42, no. 5, pp. 952-962, 1999.
- [18] M. Lustig, D. Donoho, and J. M. Pauly, “Sparse MRI: The application of compressed sensing for rapid MR imaging,” *Magnetic Resonance in Medicine: An Official Journal of the International Society for Magnetic Resonance in Medicine*, vol. 58, no. 6, pp. 1182-1195, 2007.
- [19] M. Murphy, M. Alley, J. Demmel, K. Keutzer, S. Vasanawala, and M. Lustig, “Fast ℓ_1 -SPIRiT compressed sensing parallel imaging MRI: scalable parallel implementation and clinically feasible runtime,” *IEEE transactions on medical imaging*, vol. 31, no. 6, pp. 1250-1262, 2012.
- [20] R. Otazo, D. Kim, L. Axel, and D. K. Sodickson, “Combination of compressed sensing and parallel imaging for highly accelerated first-pass cardiac perfusion MRI,” *Magnetic resonance in medicine*, vol. 64, no. 3, pp. 767-776, 2010.
- [21] F. Knoll, C. Clason, C. Diwoky, and R. Stollberger, “Adapted random sampling patterns for accelerated MRI,” *Magnetic resonance materials in physics, biology and medicine*, vol. 24, pp. 43-50, 2011.
- [22] J. P. Haldar, and D. Kim, “OEDIPUS: An experiment design framework for sparsity-constrained MRI,” *IEEE transactions on medical imaging*, vol. 38, no. 7, pp. 1545-1558, 2019.
- [23] B. Gözcü, R. K. Mahabadi, Y.-H. Li, E. Ilıcak, T. Cukur, J. Scarlett, and V. Cevher, “Learning-based compressive MRI,” *IEEE transactions on medical imaging*, vol. 37, no. 6, pp. 1394-1406, 2018.
- [24] J. Schlemper, J. Caballero, J. V. Hajnal, A. Price, and D. Rueckert, "A deep

cascade of convolutional neural networks for MR image reconstruction." pp. 647-658.

- [25] O. Ronneberger, P. Fischer, and T. Brox, "U-Net: Convolutional Networks for Biomedical Image Segmentation," *Medical Image Computing and Computer-Assisted Intervention, Pt Iii*, vol. 9351, pp. 234-241, 2015.
- [26] Y. Bengio, N. Léonard, and A. Courville, "Estimating or propagating gradients through stochastic neurons for conditional computation," *arXiv preprint arXiv:1308.3432*, 2013.
- [27] S. Osher, M. Burger, D. Goldfarb, J. Xu, and W. Yin, "An iterative regularization method for total variation-based image restoration," *Multiscale Modeling & Simulation*, vol. 4, no. 2, pp. 460-489, 2005.
- [28] D. L. Donoho, "Nonlinear solution of linear inverse problems by wavelet-vaguelette decomposition," *Applied and computational harmonic analysis*, vol. 2, no. 2, pp. 101-126, 1995.
- [29] J. Dennis, John E, and J. J. Moré, "Quasi-Newton methods, motivation and theory," *SIAM review*, vol. 19, no. 1, pp. 46-89, 1977.
- [30] S. Boyd, N. Parikh, E. Chu, B. Peleato, and J. Eckstein, "Distributed optimization and statistical learning via the alternating direction method of multipliers," *Foundations and Trends® in Machine learning*, vol. 3, no. 1, pp. 1-122, 2011.
- [31] A. Chambolle, and T. Pock, "A first-order primal-dual algorithm for convex problems with applications to imaging," *Journal of mathematical imaging and vision*, vol. 40, pp. 120-145, 2011.
- [32] B. Colson, P. Marcotte, and G. Savard, "An overview of bilevel optimization," *Annals of operations research*, vol. 153, pp. 235-256, 2007.
- [33] G. Hinton, N. Srivastava, and K. Swersky, "Neural networks for machine learning," *Coursera, video lectures*, vol. 264, no. 1, pp. 2146-2153, 2012.

- [34] K. He, X. Zhang, S. Ren, and J. Sun, "Deep residual learning for image recognition." pp. 770-778.
- [35] D. Ulyanov, A. Vedaldi, and V. Lempitsky, "Instance normalization: The missing ingredient for fast stylization," *arXiv preprint arXiv:1607.08022*, 2016.
- [36] M. Uecker, P. Lai, M. J. Murphy, P. Virtue, M. Elad, J. M. Pauly, S. S. Vasanawala, and M. Lustig, "ESPIRiT—an eigenvalue approach to autocalibrating parallel MRI: where SENSE meets GRAPPA," *Magnetic resonance in medicine*, vol. 71, no. 3, pp. 990-1001, 2014.
- [37] D. P. Kingma, and J. Ba, "Adam: A method for stochastic optimization," *arXiv preprint arXiv:1412.6980*, 2014.
- [38] Z. Wang, A. C. Bovik, H. R. Sheikh, and E. P. Simoncelli, "Image quality assessment: from error visibility to structural similarity," *IEEE transactions on image processing*, vol. 13, no. 4, pp. 600-612, 2004.
- [39] F. Knoll, K. Bredies, T. Pock, and R. Stollberger, "Second order total generalized variation (TGV) for MRI," *Magnetic resonance in medicine*, vol. 65, no. 2, pp. 480-491, 2011.
- [40] R. Deichmann, "Fast high-resolution T1 mapping of the human brain," *Magnetic Resonance in Medicine: An Official Journal of the International Society for Magnetic Resonance in Medicine*, vol. 54, no. 1, pp. 20-27, 2005.
- [41] S. C. Deoni, T. M. Peters, and B. K. Rutt, "High-resolution T1 and T2 mapping of the brain in a clinically acceptable time with DESPOT1 and DESPOT2," *Magnetic Resonance in Medicine: An Official Journal of the International Society for Magnetic Resonance in Medicine*, vol. 53, no. 1, pp. 237-241, 2005.
- [42] H. Yu, A. Shimakawa, C. A. McKenzie, E. Brodsky, J. H. Brittain, and S. B. Reeder, "Multiecho water-fat separation and simultaneous R estimation with multifrequency fat spectrum modeling," *Magnetic Resonance in Medicine: An Official Journal of the International Society for Magnetic Resonance in*

Medicine, vol. 60, no. 5, pp. 1122-1134, 2008.

- [43] B. Kressler, L. De Rochefort, T. Liu, P. Spincemaille, Q. Jiang, and Y. Wang, "Nonlinear regularization for per voxel estimation of magnetic susceptibility distributions from MRI field maps," *IEEE transactions on medical imaging*, vol. 29, no. 2, pp. 273-281, 2009.
- [44] T. Liu, C. Wisnieff, M. Lou, W. Chen, P. Spincemaille, and Y. Wang, "Nonlinear formulation of the magnetic field to source relationship for robust quantitative susceptibility mapping," *Magnetic resonance in medicine*, vol. 69, no. 2, pp. 467-476, 2013.
- [45] J. Liu, T. Liu, L. de Rochefort, J. Ledoux, I. Khalidov, W. Chen, A. J. Tsiouris, C. Wisnieff, P. Spincemaille, and M. R. Prince, "Morphology enabled dipole inversion for quantitative susceptibility mapping using structural consistency between the magnitude image and the susceptibility map," *Neuroimage*, vol. 59, no. 3, pp. 2560-2568, 2012.
- [46] Y. Wang, and T. Liu, "Quantitative susceptibility mapping (QSM): decoding MRI data for a tissue magnetic biomarker," *Magnetic resonance in medicine*, vol. 73, no. 1, pp. 82-101, 2015.
- [47] B. Zhao, W. Lu, T. K. Hitchens, F. Lam, C. Ho, and Z. P. Liang, "Accelerated MR parameter mapping with low-rank and sparsity constraints," *Magnetic resonance in medicine*, vol. 74, no. 2, pp. 489-498, 2015.
- [48] X. Peng, L. Ying, Y. Liu, J. Yuan, X. Liu, and D. Liang, "Accelerated exponential parameterization of T2 relaxation with model-driven low rank and sparsity priors (MORASA)," *Magnetic resonance in medicine*, vol. 76, no. 6, pp. 1865-1878, 2016.
- [49] T. Zhang, J. M. Pauly, and I. R. Levesque, "Accelerating parameter mapping with a locally low rank constraint," *Magnetic resonance in medicine*, vol. 73, no. 2, pp. 655-661, 2015.
- [50] H. K. Aggarwal, M. P. Mani, and M. Jacob, "MoDL: Model-based deep learning architecture for inverse problems," *IEEE transactions on medical*

imaging, vol. 38, no. 2, pp. 394-405, 2018.

- [51] J. Schlemper, J. Caballero, J. V. Hajnal, A. N. Price, and D. Rueckert, "A deep cascade of convolutional neural networks for dynamic MR image reconstruction," *IEEE transactions on Medical Imaging*, vol. 37, no. 2, pp. 491-503, 2017.
- [52] C. Qin, J. Schlemper, J. Caballero, A. N. Price, J. V. Hajnal, and D. Rueckert, "Convolutional recurrent neural networks for dynamic MR image reconstruction," *IEEE transactions on medical imaging*, vol. 38, no. 1, pp. 280-290, 2018.
- [53] Y. Gao, M. Cloos, F. Liu, S. Crozier, G. B. Pike, and H. Sun, "Accelerating quantitative susceptibility and R2* mapping using incoherent undersampling and deep neural network reconstruction," *NeuroImage*, vol. 240, pp. 118404, 2021.
- [54] S. Gu, S. Levine, I. Sutskever, and A. Mnih, "Muprop: Unbiased backpropagation for stochastic neural networks," *arXiv preprint arXiv:1511.05176*, 2015.
- [55] S. H. Chan, X. Wang, and O. A. Elgendy, "Plug-and-play ADMM for image restoration: Fixed-point convergence and applications," *IEEE Transactions on Computational Imaging*, vol. 3, no. 1, pp. 84-98, 2016.
- [56] T. Zhang, J. M. Pauly, S. S. Vasanawala, and M. Lustig, "Coil compression for accelerated imaging with Cartesian sampling," *Magnetic resonance in medicine*, vol. 69, no. 2, pp. 571-582, 2013.
- [57] B. Roman, A. Hansen, and B. Adcock, "On asymptotic structure in compressed sensing," *arXiv preprint arXiv:1406.4178*, 2014.
- [58] M. Pei, T. D. Nguyen, N. D. Thimmappa, C. Salustri, F. Dong, M. A. Cooper, J. Li, M. R. Prince, and Y. Wang, "Algorithm for fast monoexponential fitting based on auto-regression on linear operations (ARLO) of data," *Magnetic resonance in medicine*, vol. 73, no. 2, pp. 843-850, 2015.

- [59] Z. Liu, P. Spincemaille, Y. Yao, Y. Zhang, and Y. Wang, "MEDI+ 0: morphology enabled dipole inversion with automatic uniform cerebrospinal fluid zero reference for quantitative susceptibility mapping," *Magnetic resonance in medicine*, vol. 79, no. 5, pp. 2795-2803, 2018.
- [60] T. Liu, I. Khalidov, L. de Rochefort, P. Spincemaille, J. Liu, A. J. Tsiouris, and Y. Wang, "A novel background field removal method for MRI using projection onto dipole fields," *NMR in Biomedicine*, vol. 24, no. 9, pp. 1129-1136, 2011.
- [61] S. Ravishankar, and Y. Bresler, "MR image reconstruction from highly undersampled k-space data by dictionary learning," *IEEE transactions on medical imaging*, vol. 30, no. 5, pp. 1028-1041, 2010.
- [62] P. Spincemaille, T. D. Nguyen, and Y. Wang, "View ordering for magnetization prepared steady state free precession acquisition: application in contrast-enhanced MR angiography," *Magnetic Resonance in Medicine: An Official Journal of the International Society for Magnetic Resonance in Medicine*, vol. 52, no. 3, pp. 461-466, 2004.
- [63] P. Spincemaille, Z. X. Hai, L. Cheng, M. Prince, and Y. Wang, "Motion artifact suppression in breath hold 3D contrast enhanced magnetic resonance angiography using ECG ordering." pp. 739-742.
- [64] J. Kim, T. D. Nguyen, J. Zhang, S. A. Gauthier, M. Marcille, H. Zhang, J. Cho, P. Spincemaille, and Y. Wang, "Subsecond accurate myelin water fraction reconstruction from FAST-T2 data with 3D UNET," *Magnetic Resonance in Medicine*, 2022.
- [65] J. Cho, J. Zhang, P. Spincemaille, H. Zhang, S. Hubertus, Y. Wen, R. Jafari, S. Zhang, T. D. Nguyen, and A. V. Dimov, "QQ-NET—using deep learning to solve quantitative susceptibility mapping and quantitative blood oxygen level dependent magnitude (QSM+ qBOLD or QQ) based oxygen extraction fraction (OEF) mapping," *Magnetic Resonance in Medicine*, vol. 87, no. 3, pp. 1583-1594, 2022.
- [66] H. Zhang, J. Zhang, R. Wang, Q. Zhang, P. Spincemaille, T. D. Nguyen, and Y. Wang, "Efficient Folded Attention for Medical Image Reconstruction and

Segmentation,” *Proceedings of the AAAI Conference on Artificial Intelligence*, vol. 35, no. 12, pp. 10868-10876, 05/18, 2021.

- [67] R. Jafari, P. Spincemaille, J. Zhang, T. D. Nguyen, X. Luo, J. Cho, D. Margolis, M. R. Prince, and Y. Wang, “Deep neural network for water/fat separation: supervised training, unsupervised training, and no training,” *Magnetic resonance in medicine*, vol. 85, no. 4, pp. 2263-2277, 2021.
- [68] O. Ronneberger, P. Fischer, and T. Brox, "U-net: Convolutional networks for biomedical image segmentation." pp. 234-241.
- [69] B. Yaman, S. A. H. Hosseini, S. Moeller, J. Ellermann, K. Uğurbil, and M. Akçakaya, “Self-supervised learning of physics-guided reconstruction neural networks without fully sampled reference data,” *Magnetic resonance in medicine*, vol. 84, no. 6, pp. 3172-3191, 2020.
- [70] Y. Wang, and T. Liu, “Quantitative susceptibility mapping (QSM): Decoding MRI data for a tissue magnetic biomarker,” *Magn Reson Med*, vol. 73, no. 1, pp. 82-101, Jan, 2015.
- [71] T. Liu, P. Spincemaille, L. de Rochefort, R. Wong, M. Prince, and Y. Wang, “Unambiguous identification of superparamagnetic iron oxide particles through quantitative susceptibility mapping of the nonlinear response to magnetic fields,” *Magn Reson Imaging*, vol. 28, no. 9, pp. 1383-9, Nov, 2010.
- [72] Y. Wang, P. Spincemaille, Z. Liu, A. Dimov, K. Deh, J. Li, Y. Zhang, Y. Yao, K. M. Gillen, A. H. Wilman, A. Gupta, A. J. Tsiouris, I. Kovanlikaya, G. C. Chiang, J. W. Weinsaft, L. Tanenbaum, W. Chen, W. Zhu, S. Chang, M. Lou, B. H. Kopell, M. G. Kaplitt, D. Devos, T. Hirai, X. Huang, Y. Korogi, A. Shtilbans, G. H. Jahng, D. Pelletier, S. A. Gauthier, D. Pitt, A. I. Bush, G. M. Brittenham, and M. R. Prince, “Clinical quantitative susceptibility mapping (QSM): Biometal imaging and its emerging roles in patient care,” *J Magn Reson Imaging*, vol. 46, no. 4, pp. 951-971, Oct, 2017.
- [73] Y. Zhang, S. A. Gauthier, A. Gupta, J. Comunale, G. Chia-Yi Chiang, D. Zhou, W. Chen, A. E. Giambrone, W. Zhu, and Y. Wang, “Longitudinal change in magnetic susceptibility of new enhanced multiple sclerosis (MS) lesions

measured on serial quantitative susceptibility mapping (QSM),” *J Magn Reson Imaging*, vol. 44, no. 2, pp. 426-32, Aug, 2016.

- [74] R. Jafari, S. Sheth, P. Spincemaille, T. D. Nguyen, M. R. Prince, Y. Wen, Y. Guo, K. Deh, Z. Liu, and D. Margolis, “Rapid automated liver quantitative susceptibility mapping,” *Journal of Magnetic Resonance Imaging*, vol. 50, no. 3, pp. 725-732, 2019.
- [75] Y. Wen, T. D. Nguyen, Z. Liu, P. Spincemaille, D. Zhou, A. Dimov, Y. Kee, K. Deh, J. Kim, and J. W. Weinsaft, “Cardiac quantitative susceptibility mapping (QSM) for heart chamber oxygenation,” *Magnetic resonance in medicine*, vol. 79, no. 3, pp. 1545-1552, 2018.
- [76] Y. Wen, J. W. Weinsaft, T. D. Nguyen, Z. Liu, E. M. Horn, H. Singh, J. Kochav, S. Eskreis-Winkler, K. Deh, and J. Kim, “Free breathing three-dimensional cardiac quantitative susceptibility mapping for differential cardiac chamber blood oxygenation—initial validation in patients with cardiovascular disease inclusive of direct comparison to invasive catheterization,” *Journal of Cardiovascular Magnetic Resonance*, vol. 21, no. 1, pp. 1-13, 2019.
- [77] A. G. Christodoulou, J. L. Shaw, C. Nguyen, Q. Yang, Y. Xie, N. Wang, and D. Li, “Magnetic resonance multitasking for motion-resolved quantitative cardiovascular imaging,” *Nature biomedical engineering*, vol. 2, no. 4, pp. 215-226, 2018.
- [78] M. W. Caan, P. L. Bazin, J. P. Marques, G. de Hollander, S. O. Dumoulin, and W. van der Zwaag, “MP2RAGEME: T1, T2*, and QSM mapping in one sequence at 7 tesla,” *Human brain mapping*, vol. 40, no. 6, pp. 1786-1798, 2019.
- [79] T. Cao, S. Ma, N. Wang, S. Gharabaghi, Y. Xie, Z. Fan, E. Hogg, C. Wu, F. Han, and M. Tagliati, “Three-dimensional simultaneous brain mapping of T1, T2, and magnetic susceptibility with MR Multitasking,” *Magnetic Resonance in Medicine*, vol. 87, no. 3, pp. 1375-1389, 2022.
- [80] F. Wang, Z. Dong, T. G. Reese, B. Bilgic, M. Katherine Manhard, J. Chen, J. R. Polimeni, L. L. Wald, and K. Setsompop, “Echo planar time-resolved

imaging (EPTI)," *Magnetic resonance in medicine*, vol. 81, no. 6, pp. 3599-3615, 2019.

- [81] C. Wisnieff, S. Ramanan, J. Olesik, S. Gauthier, Y. Wang, and D. Pitt, "Quantitative susceptibility mapping (QSM) of white matter multiple sclerosis lesions: interpreting positive susceptibility and the presence of iron," *Magnetic resonance in medicine*, vol. 74, no. 2, pp. 564-570, 2015.
- [82] A. V. Dimov, Z. Liu, P. Spincemaille, M. R. Prince, J. Du, and Y. Wang, "Bone quantitative susceptibility mapping using a chemical species-specific R2* signal model with ultrashort and conventional echo data," *Magn Reson Med*, vol. 79, no. 1, pp. 121-128, Jan, 2018.
- [83] W. Chen, W. Zhu, I. Kovanlikaya, A. Kovanlikaya, T. Liu, S. Wang, C. Salustri, and Y. Wang, "Intracranial calcifications and hemorrhages: characterization with quantitative susceptibility mapping," *Radiology*, vol. 270, no. 2, pp. 496-505, 2014.
- [84] A. D. Schweitzer, T. Liu, A. Gupta, K. Zheng, S. Seedial, A. Shtilbans, M. Shahbazi, D. Lange, Y. Wang, and A. J. Tsiouris, "Quantitative susceptibility mapping of the motor cortex in amyotrophic lateral sclerosis and primary lateral sclerosis," *AJR Am J Roentgenol*, vol. 204, no. 5, pp. 1086-92, May, 2015.
- [85] C. Langkammer, L. Pirpamer, S. Seiler, A. Deistung, F. Schweser, S. Franthal, N. Homayoon, P. Katschnig-Winter, M. Koegl-Wallner, and T. Pendl, "Quantitative susceptibility mapping in Parkinson's disease," *PLoS One*, vol. 11, no. 9, pp. e0162460, 2016.
- [86] M. Azuma, T. Hirai, K. Yamada, S. Yamashita, Y. Ando, M. Tateishi, Y. Iryo, T. Yoneda, M. Kitajima, Y. Wang, and Y. Yamashita, "Lateral Asymmetry and Spatial Difference of Iron Deposition in the Substantia Nigra of Patients with Parkinson Disease Measured with Quantitative Susceptibility Mapping," *AJNR Am J Neuroradiol*, vol. 37, no. 5, pp. 782-8, May, 2016.
- [87] J. Acosta-Cabronero, G. B. Williams, A. Cardenas-Blanco, R. J. Arnold, V. Lupson, and P. J. Nestor, "In vivo quantitative susceptibility mapping (QSM)

in Alzheimer's disease," *PloS one*, vol. 8, no. 11, pp. e81093, 2013.

- [88] Z. Zhang, J. Cho, L. Wang, C. Liao, H. G. Shin, X. Cao, J. Lee, J. Xu, T. Zhang, and H. Ye, "Blip up-down acquisition for spin- and gradient-echo imaging (BUDA-SAGE) with self-supervised denoising enables efficient T2, T2*, para- and dia-magnetic susceptibility mapping," *Magnetic Resonance in Medicine*, 2022.
- [89] A. Bustin, G. Lima da Cruz, O. Jaubert, K. Lopez, R. M. Botnar, and C. Prieto, "High-dimensionality undersampled patch-based reconstruction (HD-PROST) for accelerated multi-contrast MRI," *Magnetic resonance in medicine*, vol. 81, no. 6, pp. 3705-3719, 2019.
- [90] H. Zhang, J. Zhang, R. Wang, Q. Zhang, P. Spincemaille, T. D. Nguyen, and Y. Wang, "Efficient folded attention for medical image reconstruction and segmentation." pp. 10868-10876.
- [91] J. Cho, B. Gagoski, T. H. Kim, Q. Tian, R. Frost, I. Chatnuntawech, and B. Bilgic, "Wave-Encoded Model-Based Deep Learning for Highly Accelerated Imaging with Joint Reconstruction," *Bioengineering*, vol. 9, no. 12, pp. 736, 2022.
- [92] Z. Liu, J. Zhang, S. Zhang, P. Spincemaille, T. Nguyen, and Y. Wang, "Quantitative susceptibility mapping using a deep learning prior." p. 4933.
- [93] J. Zhang, H. Zhang, M. Sabuncu, P. Spincemaille, T. Nguyen, and Y. Wang, "Probabilistic dipole inversion for adaptive quantitative susceptibility mapping," *Machine Learning for Biomedical Imaging*, vol. 1, no. MIDL 2020 special issue, pp. 1-19, 2021.
- [94] J. Kim, T. D. Nguyen, J. Zhang, S. A. Gauthier, M. Marcille, H. Zhang, J. Cho, P. Spincemaille, and Y. Wang, "Subsecond accurate myelin water fraction reconstruction from FAST-T2 data with 3D UNET," *Magnetic Resonance in Medicine*, vol. 87, no. 6, pp. 2979-2988, 2022.
- [95] H. Zhang, T. D. Nguyen, J. Zhang, M. Marcille, P. Spincemaille, Y. Wang, S. A. Gauthier, and E. M. Sweeney, "QSMRim-Net: Imbalance-aware learning

for identification of chronic active multiple sclerosis lesions on quantitative susceptibility maps,” *NeuroImage: Clinical*, vol. 34, pp. 102979, 2022.

- [96] H. Zhang, J. Zhang, C. Li, E. M. Sweeney, P. Spincemaille, T. D. Nguyen, S. A. Gauthier, Y. Wang, and M. Marcille, “ALL-Net: Anatomical information lesion-wise loss function integrated into neural network for multiple sclerosis lesion segmentation,” *NeuroImage: Clinical*, vol. 32, pp. 102854, 2021.
- [97] H. Zhang, J. Zhang, R. Wang, Q. Zhang, S. A. Gauthier, P. Spincemaille, T. D. Nguyen, and Y. Wang, "Geometric loss for deep multiple sclerosis lesion segmentation." pp. 24-28.
- [98] H. Zhang, J. Zhang, Q. Zhang, J. Kim, S. Zhang, S. A. Gauthier, P. Spincemaille, T. D. Nguyen, M. Sabuncu, and Y. Wang, "RsaNet: Recurrent slice-wise attention network for multiple sclerosis lesion segmentation." pp. 411-419.
- [99] S. Kvernby, M. J. B. Warntjes, H. Haraldsson, C.-J. Carlhäll, J. Engvall, and T. Ebbers, “Simultaneous three-dimensional myocardial T1 and T2 mapping in one breath hold with 3D-QALAS,” *Journal of Cardiovascular Magnetic Resonance*, vol. 16, no. 1, pp. 1-14, 2014.
- [100] S. Fujita, A. Hagiwara, M. Hori, M. Warntjes, K. Kamagata, I. Fukunaga, C. Andica, T. Maekawa, R. Irie, and M. Y. Takemura, “Three-dimensional high-resolution simultaneous quantitative mapping of the whole brain with 3D-QALAS: an accuracy and repeatability study,” *Magnetic resonance imaging*, vol. 63, pp. 235-243, 2019.
- [101] J. H. Brittain, B. S. Hu, G. A. Wright, C. H. Meyer, A. Macovski, and D. G. Nishimura, “Coronary angiography with magnetization-prepared T2 contrast,” *Magnetic resonance in medicine*, vol. 33, no. 5, pp. 689-696, 1995.
- [102] T. D. Nguyen, P. Spincemaille, J. W. Weinsaft, B. Y. Ho, M. D. Cham, M. R. Prince, and Y. Wang, “A fast navigator-gated 3D sequence for delayed enhancement MRI of the myocardium: comparison with breathhold 2D imaging,” *J Magn Reson Imaging*, vol. 27, no. 4, pp. 802-8, Apr, 2008.

- [103] F. Crete, T. Dolmiere, P. Ladret, and M. Nicolas, "The blur effect: perception and estimation with a new no-reference perceptual blur metric." pp. 196-206.
- [104] B. Fischl, D. H. Salat, E. Busa, M. Albert, M. Dieterich, C. Haselgrove, A. Van Der Kouwe, R. Killiany, D. Kennedy, and S. Klaveness, "Whole brain segmentation: automated labeling of neuroanatomical structures in the human brain," *Neuron*, vol. 33, no. 3, pp. 341-355, 2002.
- [105] R. S. Desikan, F. Ségonne, B. Fischl, B. T. Quinn, B. C. Dickerson, D. Blacker, R. L. Buckner, A. M. Dale, R. P. Maguire, and B. T. Hyman, "An automated labeling system for subdividing the human cerebral cortex on MRI scans into gyral based regions of interest," *Neuroimage*, vol. 31, no. 3, pp. 968-980, 2006.
- [106] D. Giavarina, "Understanding bland altman analysis," *Biochemia medica*, vol. 25, no. 2, pp. 141-151, 2015.
- [107] J. Lehtinen, J. Munkberg, J. Hasselgren, S. Laine, T. Karras, M. Aittala, and T. Aila, "Noise2Noise: Learning image restoration without clean data," *arXiv preprint arXiv:1803.04189*, 2018.
- [108] F. Wang, Z. Dong, T. G. Reese, B. Rosen, L. L. Wald, and K. Setsompop, "3D Echo Planar Time-resolved Imaging (3D-EPTI) for ultrafast multi-parametric quantitative MRI," *NeuroImage*, vol. 250, pp. 118963, 2022.
- [109] C. M. Sandino, F. Ong, S. S. Iyer, A. Bush, and S. Vasanawala, "Deep subspace learning for efficient reconstruction of spatiotemporal imaging data."
- [110] Y. Wang, T. M. Grist, F. R. Korosec, P. S. Christy, M. T. Alley, J. A. Polzin, and C. A. Mistretta, "Respiratory blur in 3D coronary MR imaging," *Magn Reson Med*, vol. 33, no. 4, pp. 541-8, Apr, 1995.
- [111] Y. Wang, P. J. Rossman, R. C. Grimm, A. H. Wilman, S. J. Riederer, and R. L. Ehman, "3D MR angiography of pulmonary arteries using real-time navigator gating and magnetization preparation," *Magn Reson Med*, vol. 36, no. 4, pp. 579-87, Oct, 1996.

- [112] A. V. Dimov, T. Liu, P. Spincemaille, J. S. Ecanow, H. Tan, R. R. Edelman, and Y. Wang, "Joint estimation of chemical shift and quantitative susceptibility mapping (chemical QSM)," *Magn Reson Med*, vol. 73, no. 6, pp. 2100-10, Jun, 2015.
- [113] G. Gindi, M. Lee, A. Rangarajan, and I. G. Zubal, "Bayesian reconstruction of functional images using anatomical information as priors," *IEEE Transactions on Medical Imaging*, vol. 12, no. 4, pp. 670-680, 1993.
- [114] K. T. Block, M. Uecker, and J. Frahm, "Undersampled radial MRI with multiple coils. Iterative image reconstruction using a total variation constraint," *Magnetic Resonance in Medicine*, vol. 57, no. 6, pp. 1086-98, Jun, 2007.
- [115] J. A. Fessler, "Model-based image reconstruction for MRI," *IEEE Signal Processing Magazine*, vol. 27, no. 4, pp. 81-89, 2010.
- [116] B. Kressler, L. De Rochefort, T. Liu, P. Spincemaille, Q. Jiang, and Y. Wang, "Nonlinear regularization for per voxel estimation of magnetic susceptibility distributions from MRI field maps," *IEEE transactions on medical imaging*, vol. 29, no. 2, pp. 273-281, 2010.
- [117] M. Lustig, D. Donoho, and J. M. Pauly, "Sparse MRI: The application of compressed sensing for rapid MR imaging," *Magnetic Resonance in Medicine*, vol. 58, no. 6, pp. 1182-95, Dec, 2007.
- [118] Y. LeCun, Y. Bengio, and G. Hinton, "Deep learning," *nature*, vol. 521, no. 7553, pp. 436, 2015.
- [119] I. Goodfellow, Y. Bengio, and A. Courville, *Deep learning*, Cambridge, Massachusetts: The MIT Press, 2016.
- [120] C. D. Bahadir, A. V. Dalca, and M. R. Sabuncu, "Learning-based Optimization of the Under-sampling Pattern in MRI." pp. 780-792.
- [121] C. M. Hyun, H. P. Kim, S. M. Lee, S. Lee, and J. K. Seo, "Deep learning for undersampled MRI reconstruction," *Physics in Medicine & Biology*, vol. 63,

no. 13, pp. 135007, 2018.

- [122] K. H. Jin, M. T. McCann, E. Froustey, and M. Unser, "Deep convolutional neural network for inverse problems in imaging," *IEEE Transactions on Image Processing*, vol. 26, no. 9, pp. 4509-4522, 2017.
- [123] S. Shalev-Shwartz, and S. Ben-David, *Understanding machine learning : from theory to algorithms*, New York, NY, USA: Cambridge University Press, 2014.
- [124] D. Jakubovitz, R. Giryes, and M. R. D. Rodrigues, "Generalization Error in Deep Learning," *arXiv*, vol. arXiv:1808.01174, 2018.
- [125] C. Szegedy, W. Zaremba, I. Sutskever, J. Bruna, D. Erhan, I. Goodfellow, and R. Fergus, "Intriguing properties of neural networks," *arXiv*, vol. arXiv:1312.6199, 2014.
- [126] S. Wang, Z. Su, L. Ying, X. Peng, S. Zhu, F. Liang, D. Feng, and D. Liang, "Accelerating magnetic resonance imaging via deep learning." pp. 514-517.
- [127] J. Schlemper, J. Caballero, J. V. Hajnal, A. N. Price, and D. Rueckert, "A deep cascade of convolutional neural networks for dynamic MR image reconstruction," *IEEE transactions on Medical Imaging*, vol. 37, no. 2, pp. 491-503, 2018.
- [128] L. de Rochefort, T. Liu, B. Kressler, J. Liu, P. Spincemaille, V. Lebon, J. Wu, and Y. Wang, "Quantitative susceptibility map reconstruction from MR phase data using bayesian regularization: validation and application to brain imaging," *Magnetic resonance in medicine*, vol. 63, no. 1, pp. 194-206, 2010.
- [129] Y. Kee, Z. Liu, L. Zhou, A. Dimov, J. Cho, L. De Rochefort, J. K. Seo, and Y. Wang, "Quantitative susceptibility mapping (QSM) algorithms: mathematical rationale and computational implementations," *IEEE Transactions on Biomedical Engineering*, vol. 64, no. 11, pp. 2531-2545, 2017.
- [130] A. Krizhevsky, I. Sutskever, and G. E. Hinton, "Imagenet classification with deep convolutional neural networks." pp. 1097-1105.

- [131] M. D. Zeiler, and R. Fergus, "Visualizing and understanding convolutional networks." pp. 818-833.
- [132] H. Lee, R. Grosse, R. Ranganath, and A. Y. Ng, "Convolutional deep belief networks for scalable unsupervised learning of hierarchical representations." pp. 609-616.
- [133] J. Dong, T. Liu, F. Chen, D. Zhou, A. Dimov, A. Raj, Q. Cheng, P. Spincemaille, and Y. Wang, "Simultaneous phase unwrapping and removal of chemical shift (SPURS) using graph cuts: application in quantitative susceptibility mapping," *IEEE transactions on medical imaging*, vol. 34, no. 2, pp. 531-540, 2015.
- [134] T. Liu, P. Spincemaille, L. de Rochefort, B. Kressler, and Y. Wang, "Calculation of Susceptibility Through Multiple Orientation Sampling (COSMOS): A Method for Conditioning the Inverse Problem From Measured Magnetic Field Map to Susceptibility Source Image in MRI," *Magnetic Resonance in Medicine*, vol. 61, no. 1, pp. 196-204, Jan, 2009.
- [135] C. Langkammer, F. Schweser, K. Shmueli, C. Kames, X. Li, L. Guo, C. Milovic, J. Kim, H. Wei, and K. Bredies, "Quantitative susceptibility mapping: report from the 2016 reconstruction challenge," *Magnetic resonance in medicine*, vol. 79, no. 3, pp. 1661-1673, 2018.
- [136] Ö. Çiçek, A. Abdulkadir, S. S. Lienkamp, T. Brox, and O. Ronneberger, "3D U-Net: learning dense volumetric segmentation from sparse annotation." pp. 424-432.
- [137] R. F. Martin, "General Deming regression for estimating systematic bias and its confidence interval in method-comparison studies," *Clinical chemistry*, vol. 46, no. 1, pp. 100-104, 2000.
- [138] F. Crete, T. Dolmieri, P. Ladret, and M. Nicolas, "The blur effect: perception and estimation with a new no-reference perceptual blur metric." p. 64920I.
- [139] A. Oliva, and A. Torralba, "Modeling the shape of the scene: A holistic representation of the spatial envelope," *International journal of computer*

vision, vol. 42, no. 3, pp. 145-175, 2001.

- [140] M. Uecker, F. Ong, J. I. Tamir, D. Bahri, P. Virtue, J. Y. Cheng, T. Zhang, and M. Lustig, "Berkeley advanced reconstruction toolbox." p. 2486.
- [141] T. Tieleman, and G. Hinton, "Lecture 6.5-rmsprop: Divide the gradient by a running average of its recent magnitude," *COURSERA: Neural networks for machine learning*, vol. 4, no. 2, pp. 26-31, 2012.
- [142] V. Antun, F. Renna, C. Poon, B. Adcock, and A. C. Hansen, "On instabilities of deep learning in image reconstruction-Does AI come at a cost?," *arXiv preprint arXiv:1902.05300*, 2019.
- [143] D. Ulyanov, A. Vedaldi, and V. Lempitsky, "Deep image prior." pp. 9446-9454.
- [144] J. Yosinski, J. Clune, Y. Bengio, and H. Lipson, "How transferable are features in deep neural networks?." pp. 3320-3328.
- [145] M. Mardani, E. Gong, J. Y. Cheng, S. S. Vasanawala, G. Zaharchuk, L. Xing, and J. M. Pauly, "Deep Generative Adversarial Neural Networks for Compressive Sensing MRI," *IEEE transactions on medical imaging*, vol. 38, no. 1, pp. 167-179, 2019.
- [146] J. Zhang, T. Liu, A. Gupta, P. Spincemaille, T. D. Nguyen, and Y. Wang, "Quantitative mapping of cerebral metabolic rate of oxygen (CMRO₂) using quantitative susceptibility mapping (QSM)," *Magnetic Resonance in Medicine*, vol. 74, no. 4, pp. 945-952, 2015.
- [147] A. Deistung, F. Schweser, B. Wiestler, M. Abello, M. Roethke, F. Sahm, W. Wick, A. M. Nagel, S. Heiland, H.-P. Schlemmer, M. Bendszus, J. R. Reichenbach, and A. Radbruch, "Quantitative Susceptibility Mapping Differentiates between Blood Depositions and Calcifications in Patients with Glioblastoma," *PLoS ONE*, vol. 8, no. 3, pp. e57924, 2013.
- [148] A. Dimov, W. Patel, Y. Yao, Y. Wang, R. O'Halloran, and B. H. Kopell, "Iron concentration linked to structural connectivity in the subthalamic nucleus:

- implications for deep brain stimulation,” *J Neurosurg*, pp. 1-8, Jan 18, 2019.
- [149] W. Chen, S. A. Gauthier, A. Gupta, J. Comunale, T. Liu, S. Wang, M. Pei, D. Pitt, and Y. Wang, “Quantitative susceptibility mapping of multiple sclerosis lesions at various ages,” *Radiology*, vol. 271, no. 1, pp. 183-92, Apr, 2014.
- [150] H. Tan, T. Liu, Y. Wu, J. Thacker, R. Shenkar, A. G. Mikati, C. Shi, C. Dykstra, Y. Wang, P. V. Prasad, R. R. Edelman, and I. A. Awad, “Evaluation of iron content in human cerebral cavernous malformation using quantitative susceptibility mapping,” *Invest Radiol*, vol. 49, no. 7, pp. 498-504, Jul, 2014.
- [151] Y. Murakami, S. Kakeda, K. Watanabe, I. Ueda, A. Ogasawara, J. Moriya, S. Ide, K. Futatsuya, T. Sato, K. Okada, T. Uozumi, S. Tsuji, T. Liu, Y. Wang, and Y. Korogi, “Usefulness of quantitative susceptibility mapping for the diagnosis of Parkinson disease,” *AJNR Am J Neuroradiol*, vol. 36, no. 6, pp. 1102-8, Jun, 2015.
- [152] J. M. van Bergen, J. Hua, P. G. Unschuld, I. A. Lim, C. K. Jones, R. L. Margolis, C. A. Ross, P. C. van Zijl, and X. Li, “Quantitative Susceptibility Mapping Suggests Altered Brain Iron in Premanifest Huntington Disease,” *AJNR Am J Neuroradiol*, vol. 37, no. 5, pp. 789-96, May, 2016.
- [153] C. Wisnieff, T. Liu, P. Spincemaille, S. Wang, D. Zhou, and Y. Wang, “Magnetic susceptibility anisotropy: cylindrical symmetry from macroscopically ordered anisotropic molecules and accuracy of MRI measurements using few orientations,” *Neuroimage*, vol. 70, pp. 363-376, 2013.
- [154] J. Huang, C. Chen, and L. Axel, “Fast multi-contrast MRI reconstruction,” *Med Image Comput Comput Assist Interv*, vol. 15, no. Pt 1, pp. 281-8, 2012.
- [155] T. D. Nguyen, L. de Rochefort, P. Spincemaille, M. D. Cham, J. W. Weinsaft, M. R. Prince, and Y. Wang, “Effective motion-sensitizing magnetization preparation for black blood magnetic resonance imaging of the heart,” *J Magn Reson Imaging*, vol. 28, no. 5, pp. 1092-100, Nov, 2008.
- [156] Y. Wang, P. J. Rossman, R. C. Grimm, A. H. Wilman, S. J. Riederer, and R. L.

- Ehman, "3D MR angiography of pulmonary arteries using realtime navigator gating and magnetization preparation," *Magnetic resonance in medicine*, vol. 36, no. 4, pp. 579-587, 1996.
- [157] H.-C. Shin, H. R. Roth, M. Gao, L. Lu, Z. Xu, I. Nogues, J. Yao, D. Mollura, and R. M. Summers, "Deep convolutional neural networks for computer-aided detection: CNN architectures, dataset characteristics and transfer learning," *IEEE transactions on medical imaging*, vol. 35, no. 5, pp. 1285-1298, 2016.
- [158] C. Langkammer, T. Liu, M. Khalil, C. Enzinger, M. Jehna, S. Fuchs, F. Fazekas, Y. Wang, and S. Ropele, "Quantitative susceptibility mapping in multiple sclerosis," *Radiology*, vol. 267, no. 2, pp. 551-559, 2013.
- [159] K. Shmueli, J. A. de Zwart, P. van Gelderen, T. Q. Li, S. J. Dodd, and J. H. Duyn, "Magnetic susceptibility mapping of brain tissue in vivo using MRI phase data," *Magnetic Resonance in Medicine: An Official Journal of the International Society for Magnetic Resonance in Medicine*, vol. 62, no. 6, pp. 1510-1522, 2009.
- [160] Y. Gao, X. Zhu, B. A. Moffat, R. Glarin, A. H. Wilman, G. B. Pike, S. Crozier, F. Liu, and H. Sun, "xQSM: quantitative susceptibility mapping with octave convolutional and noise-regularized neural networks," *NMR in Biomedicine*, vol. 34, no. 3, pp. e4461, 2021.
- [161] W. Jung, J. Yoon, S. Ji, J. Y. Choi, J. M. Kim, Y. Nam, E. Y. Kim, and J. Lee, "Exploring linearity of deep neural network trained QSM: QSMnet+," *Neuroimage*, vol. 211, pp. 116619, 2020.
- [162] J. Dong, T. Liu, F. Chen, D. Zhou, A. Dimov, A. Raj, Q. Cheng, P. Spincemaille, and Y. Wang, "Simultaneous phase unwrapping and removal of chemical shift (SPURS) using graph cuts: application in quantitative susceptibility mapping," *IEEE transactions on medical imaging*, vol. 34, no. 2, pp. 531-540, 2014.
- [163] Z. Liu, Y. Kee, D. Zhou, Y. Wang, and P. Spincemaille, "Preconditioned total field inversion (TFI) method for quantitative susceptibility mapping," *Magnetic resonance in medicine*, vol. 78, no. 1, pp. 303-315, 2017.

- [164] E. M. Haacke, Y. Xu, Y. C. N. Cheng, and J. R. Reichenbach, "Susceptibility weighted imaging (SWI)," *Magnetic Resonance in Medicine: An Official Journal of the International Society for Magnetic Resonance in Medicine*, vol. 52, no. 3, pp. 612-618, 2004.
- [165] E. M. Haacke, S. Mittal, Z. Wu, J. Neelavalli, and Y.-C. Cheng, "Susceptibility-weighted imaging: technical aspects and clinical applications, part 1," *American Journal of Neuroradiology*, vol. 30, no. 1, pp. 19-30, 2009.
- [166] S. Mittal, Z. Wu, J. Neelavalli, and E. M. Haacke, "Susceptibility-weighted imaging: technical aspects and clinical applications, part 2," *American Journal of neuroradiology*, vol. 30, no. 2, pp. 232-252, 2009.
- [167] F. Schweser, A. Deistung, B. W. Lehr, and J. R. Reichenbach, "Quantitative imaging of intrinsic magnetic tissue properties using MRI signal phase: an approach to in vivo brain iron metabolism?," *Neuroimage*, vol. 54, no. 4, pp. 2789-807, Feb 14, 2011.
- [168] J. Fang, L. Bao, X. Li, P. C. M. van Zijl, and Z. Chen, "Background field removal using a region adaptive kernel for quantitative susceptibility mapping of human brain," *J Magn Reson*, vol. 281, pp. 130-140, Aug, 2017.
- [169] H. Sun, and A. H. Wilman, "Background field removal using spherical mean value filtering and Tikhonov regularization," *Magn Reson Med*, vol. 71, no. 3, pp. 1151-7, Mar, 2014.
- [170] T. Liu, J. Liu, L. De Rochefort, P. Spincemaille, I. Khalidov, J. R. Ledoux, and Y. Wang, "Morphology enabled dipole inversion (MEDI) from a single-angle acquisition: comparison with COSMOS in human brain imaging," *Magnetic resonance in medicine*, vol. 66, no. 3, pp. 777-783, 2011.
- [171] K. Shmueli, J. A. de Zwart, P. van Gelderen, T. Q. Li, S. J. Dodd, and J. H. Duyn, "Magnetic susceptibility mapping of brain tissue in vivo using MRI phase data," *Magn Reson Med*, vol. 62, no. 6, pp. 1510-22, Dec, 2009.
- [172] S. Wharton, and R. Bowtell, "Whole-brain susceptibility mapping at high field: A comparison of multiple- and single-orientation methods,"

Neuroimage, vol. 53, no. 2, pp. 515-525, Nov 1, 2010.

- [173] S. Wharton, A. Schafer, and R. Bowtell, "Susceptibility mapping in the human brain using threshold-based k-space division," *Magn Reson Med*, vol. 63, no. 5, pp. 1292-304, May, 2010.
- [174] Z. Lu, J. Li, C. Wang, R. Ge, L. Chen, H. He, and J. Shi, "S2Q-Net: Mining the High-Pass Filtered Phase Data in Susceptibility Weighted Imaging for Quantitative Susceptibility Mapping," *IEEE Journal of Biomedical and Health Informatics*, 2022.
- [175] C. Kames, J. Doucette, C. Birkl, and A. Rauscher, "Recovering SWI-filtered phase data using deep learning," *Magnetic Resonance in Medicine*, vol. 87, no. 2, pp. 948-959, 2022.
- [176] V. Beliveau, C. Birkl, A. Stefani, E. R. Gizewski, and C. Scherfler, "HFP-QSMGAN: QSM from homodyne-filtered phase images," *Magnetic Resonance in Medicine*, 2022.
- [177] D. Ren, W. Zuo, Q. Hu, P. Zhu, and D. Meng, "Progressive image deraining networks: A better and simpler baseline." pp. 3937-3946.
- [178] S. Ioffe, and C. Szegedy, "Batch normalization: Accelerating deep network training by reducing internal covariate shift." pp. 448-456.
- [179] S. Bollmann, K. G. B. Rasmussen, M. Kristensen, R. G. Blendal, L. R. Østergaard, M. Plochanski, K. O'Brien, C. Langkammer, A. Janke, and M. Barth, "DeepQSM-using deep learning to solve the dipole inversion for quantitative susceptibility mapping," *Neuroimage*, vol. 195, pp. 373-383, 2019.
- [180] J. Zhang, H. Zhang, C. Li, P. Spincemaille, M. Sabuncu, T. D. Nguyen, and Y. Wang, "Temporal feature fusion with sampling pattern optimization for multi-echo gradient echo acquisition and image reconstruction." pp. 232-242.
- [181] K.-W. Lai, M. Aggarwal, P. van Zijl, X. Li, and J. Sulam, "Learned proximal networks for quantitative susceptibility mapping." pp. 125-135.

- [182] D. Polak, I. Chatnuntawech, J. Yoon, S. S. Iyer, C. Milovic, J. Lee, P. Bachert, E. Adalsteinsson, K. Setsompop, and B. Bilgic, “Nonlinear dipole inversion (NDI) enables robust quantitative susceptibility mapping (QSM),” *NMR in Biomedicine*, vol. 33, no. 12, pp. e4271, 2020.
- [183] R. Feng, J. Zhao, H. Wang, B. Yang, J. Feng, Y. Shi, M. Zhang, C. Liu, Y. Zhang, and J. Zhuang, “MoDL-QSM: Model-based deep learning for quantitative susceptibility mapping,” *NeuroImage*, vol. 240, pp. 118376, 2021.
- [184] V. Monga, Y. Li, and Y. C. Eldar, “Algorithm unrolling: Interpretable, efficient deep learning for signal and image processing,” *IEEE Signal Processing Magazine*, vol. 38, no. 2, pp. 18-44, 2021.
- [185] M. A. Chappell, A. R. Groves, B. Whitcher, and M. W. Woolrich, “Variational Bayesian inference for a nonlinear forward model,” *IEEE Transactions on Signal Processing*, vol. 57, no. 1, pp. 223-236, 2008.
- [186] A. Repetti, M. Pereyra, and Y. Wiaux, “Scalable Bayesian uncertainty quantification in imaging inverse problems via convex optimization,” *SIAM Journal on Imaging Sciences*, vol. 12, no. 1, pp. 87-118, 2019.
- [187] C. Andrieu, N. De Freitas, A. Doucet, and M. I. Jordan, “An introduction to MCMC for machine learning,” *Machine learning*, vol. 50, pp. 5-43, 2003.
- [188] C. M. Bishop, and N. M. Nasrabadi, *Pattern recognition and machine learning*: Springer, 2006.
- [189] M. Pereyra, “Maximum-a-posteriori estimation with Bayesian confidence regions,” *SIAM Journal on Imaging Sciences*, vol. 10, no. 1, pp. 285-302, 2017.
- [190] D. M. Blei, A. Kucukelbir, and J. D. McAuliffe, “Variational inference: A review for statisticians,” *Journal of the American statistical Association*, vol. 112, no. 518, pp. 859-877, 2017.
- [191] D. P. Kingma, and M. Welling, “Auto-encoding variational bayes,” *arXiv preprint arXiv:1312.6114*, 2013.

- [192] D. J. Rezende, S. Mohamed, and D. Wierstra, "Stochastic backpropagation and approximate inference in deep generative models." pp. 1278-1286.
- [193] C. Cremer, X. Li, and D. Duvenaud, "Inference suboptimality in variational autoencoders." pp. 1078-1086.
- [194] A. Van Den Oord, N. Kalchbrenner, and K. Kavukcuoglu, "Pixel recurrent neural networks." pp. 1747-1756.
- [195] L. Dinh, J. Sohl-Dickstein, and S. Bengio, "Density estimation using real nvp," *arXiv preprint arXiv:1605.08803*, 2016.
- [196] K. C. Tezcan, C. F. Baumgartner, R. Luechinger, K. P. Pruessmann, and E. Konukoglu, "MR image reconstruction using deep density priors," *IEEE transactions on medical imaging*, vol. 38, no. 7, pp. 1633-1642, 2018.
- [197] G. Luo, N. Zhao, W. Jiang, E. S. Hui, and P. Cao, "MRI reconstruction using deep Bayesian estimation," *Magnetic resonance in medicine*, vol. 84, no. 4, pp. 2246-2261, 2020.
- [198] T. Salimans, A. Karpathy, X. Chen, and D. P. Kingma, "Pixelcnn++: Improving the pixelcnn with discretized logistic mixture likelihood and other modifications," *arXiv preprint arXiv:1701.05517*, 2017.
- [199] S. Hochreiter, A. S. Younger, and P. R. Conwell, "Learning to learn using gradient descent." pp. 87-94.
- [200] J. Cho, Y. Kee, P. Spincemaille, T. D. Nguyen, J. Zhang, A. Gupta, S. Zhang, and Y. Wang, "Cerebral metabolic rate of oxygen (CMRO₂) mapping by combining quantitative susceptibility mapping (QSM) and quantitative blood oxygenation level-dependent imaging (qBOLD)," *Magnetic resonance in medicine*, vol. 80, no. 4, pp. 1595-1604, 2018.
- [201] H.-G. Shin, J. Lee, Y. H. Yun, S. H. Yoo, J. Jang, S.-H. Oh, Y. Nam, S. Jung, S. Kim, and M. Fukunaga, " χ -separation: Magnetic susceptibility source separation toward iron and myelin mapping in the brain," *Neuroimage*, vol. 240, pp. 118371, 2021.

- [202] C. Lazarus, P. Weiss, N. Chauffert, F. Mauconduit, L. El Gueddari, C. Destrieux, I. Zemmoura, A. Vignaud, and P. Ciuciu, "SPARKLING: variable-density k-space filling curves for accelerated T2*-weighted MRI," *Magnetic resonance in medicine*, vol. 81, no. 6, pp. 3643-3661, 2019.
- [203] S. U. Dar, Ş. Öztürk, Y. Korkmaz, G. Elmas, M. Özbey, A. Güngör, and T. Çukur, "Adaptive diffusion priors for accelerated mri reconstruction," *arXiv preprint arXiv:2207.05876*, 2022.
- [204] Y. Xie, and Q. Li, "Measurement-conditioned denoising diffusion probabilistic model for under-sampled medical image reconstruction." pp. 655-664.